Università degli Studi di Palermo

AREA RICERCA E INNOVAZIONE
SETTORE DOTTORATI E CONTRATTI PER LA RICERCA
U. O. DOTTORATI DI RICERCA

PhD Program in Biodiversity in Agriculture and Forestry
Department of Agricultural, Food, and Forest Sciences
AGRI-04/A — Agricultural Hydraulics and Watershed Protection

ASSESSMENT OF RAINFALL ENERGETIC CHARACTERISTICS UNDER NATURAL AND SIMULATED CONDITIONS FOR SOIL EROSION RESEARCH

Doctoral Dissertation of
Roberto Caruso

Supervisor
Prof. Francesco Giuseppe Carollo

Co-Supervisor
Dr. Maria Angela Serio

The Chair of the Doctoral Program
Prof. Riccardo Lo Bianco

2026 – XXXVIII Cycle

DOCTORATE

EXTENDED ABSTRACT

Rainfall is the primary driver of soil erosion by water, and its erosive potential depends on the size and velocity distribution of impacting raindrops. Rainfall energetic characteristics are typically estimated using optical disdrometers, specialized and costly instruments whose deployment is generally limited to dedicated research facilities and advanced monitoring stations, and therefore not widespread across standard measurement networks. As a result, these characteristics are often inferred from site-specific empirical relationships of limited accuracy, which constrain their reliable representation in erosion studies. The present doctoral research addresses these limitations through an integrated theoretical and experimental investigation of the energetic characteristics of rainfall under both natural and simulated conditions.

For natural rainfall, the study relies on an extensive database of drop-size distributions measured with an ODM 470 optical disdrometer at three Mediterranean experimental sites characterized by distinct rainfall regimes. These data were used to examine the statistical structure of raindrop size distributions and their relationship with rainfall energetic properties. The analyses showed that the Weibull distribution provides a reliable representation of natural rainfall drop size distributions in these environments, and that the theoretical relationships developed in this study for estimating rainfall kinetic power and momentum are applicable under these conditions. Within this framework, the results confirmed that rainfall intensity alone is insufficient to describe rainfall energetic characteristics, as commonly observed in the literature, whereas the Weibull parameters capture site-specific differences in drop size distributions and therefore in rainfall energetic properties.

A subset of the database collected at the Sparacia experimental site, where rainfall measurements were coupled with plot-scale soil-loss observations, was used to reassess the representation of rainfall erosivity at the event scale. The classic erosivity formulation showed limited ability to explain the variability of measured soil loss even when rainfall kinetic energy was derived from disdrometric data. A new event-scale descriptor, incorporating rainfall kinetic power and intensity at their measurement temporal resolution, yielded a substantially improved

relationship with soil loss, highlighting the importance of rainfall energy dynamics during erosive events.

Building on the Weibull-based framework, the research also advanced a patented measurement method to reconstruct rainfall energetic characteristics from three directly measurable quantities: rainfall intensity, drop concentration, and the mean diameter derived from the raindrop momentum distribution. This method enables the retrieval of Weibull parameters and the estimation of kinetic power and momentum without full disdrometric measurements. The concept relies on the analysis of electrical signals generated by piezoelectric sensing of individual raindrop impacts, offering the potential for low-cost measurement of rainfall energetic properties. Validation against disdrometric datasets confirmed the accuracy of the approach, particularly for rainfall momentum, supporting the feasibility of the patented measurement principle pending prototype development.

Furthermore, an extensive experimental program involving different types of rainfall simulators (drip-type and pressurized) supported the development of a reliable methodology for their comprehensive characterization, enabling the assessment of rainfall-intensity spatial uniformity and associated energetic parameters. Specifically, for drip-type simulators, which generate droplets with constant diameter and fall velocity under fixed operating conditions, rainfall energetic properties are inherently deterministic. For the widely used Kamphorst simulator, this implies that kinetic power and momentum depend only on rainfall intensity and fall height, enabling the development of empirical relationships expressed solely in terms of these variables. This deterministic behavior also allowed the validation, across all investigated drip-type devices, of a literature-calibrated empirical relationship for estimating raindrop fall velocity as a function of drop diameter and fall height. By contrast, pressurized simulators produce more complex rainfall fields, consisting of composite droplet sprays with a wide range of sizes and velocities that more closely resemble the variability of natural rainfall. In this study, two pressurized configurations were considered: a newly proposed simulator developed in Palermo and a previously established facility in León capable of generating terminal fall-velocity conditions. Owing to this intrinsic heterogeneity, the deterministic approaches applicable to drip-type devices are not

suitable for these simulators. Their comprehensive characterization, accounting for the spatial variability of drop size and fall velocity and their associated energetic properties, can therefore be achieved only through spatially distributed optical disdrometer measurements integrated with conventional volumetric calibration based on the Christiansen method.

Controlled laboratory investigations enabled an assessment of the Parsivel^2 optical disdrometer, designed for rainfall monitoring under natural conditions. The instrument provided reliable estimates of drop size distributions but showed limited accuracy in fall-velocity measurements. In particular, the experiments confirmed that the underestimation of raindrop velocity, well documented for natural rainfall, also occurs under simulated, non-terminal conditions. At the same time, the disdrometer-based velocity measurements allowed verification of the applicability of the above-mentioned empirical fall-velocity relationship across both drip-type and pressurized simulators, under sub-terminal as well as terminal fall conditions.

The results obtained for both natural and simulated rainfall converge toward the future development of the patented rainfall energy measurement device. Once available, the instrument will first require validation under highly controlled conditions, ensured by the fully characterized drip-type simulators. Subsequent scaling to more complex rainfall fields will be supported by the pressurized simulator configuration proposed in this work. Final verification will then be conducted under natural field conditions.

SOMMARIO ESTESO

La pioggia costituisce il principale fattore dell'erosione idrica del suolo, il cui potenziale erosivo dipende dalla distribuzione dimensionale e di velocità delle gocce di pioggia che impattano il suolo. Le caratteristiche energetiche della pioggia sono tipicamente stimate mediante disdrometri ottici, strumenti specializzati il cui impiego è generalmente limitato a strutture di ricerca dedicate e stazioni di monitoraggio avanzate e, pertanto, non diffusi nelle reti di misura pluviometriche standard. Di conseguenza, tali caratteristiche energetiche sono spesso dedotte mediante relazioni empiriche sito-specifiche di limitata accuratezza, con conseguenti incertezze nella loro rappresentazione negli studi sull'erosione. La presente ricerca di dottorato affronta queste limitazioni mediante un'indagine teorica e sperimentale integrata sulle caratteristiche energetiche della pioggia in condizioni naturali e simulate.

Per la pioggia naturale, lo studio si basa su un ampio database di distribuzioni dimensionali delle gocce di pioggia misurate con un disdrometro ottico ODM 470 in tre siti sperimentali mediterranei caratterizzati da distinti regimi pluviometrici. Tali dati sono stati utilizzati per esaminare la struttura statistica delle distribuzioni dimensionali delle gocce di pioggia e la loro relazione con le proprietà energetiche della pioggia. Le analisi hanno mostrato che la distribuzione di Weibull fornisce una rappresentazione affidabile delle distribuzioni dimensionali delle gocce di pioggia naturali in questi ambienti. Inoltre, le relazioni teoriche sviluppate in questo studio, a partire dalla distribuzione di Weibull, stimano con precisione la potenza cinetica e la quantità di moto della pioggia in ambiente mediterraneo. In questo quadro, i risultati hanno confermato che la sola intensità di pioggia è insufficiente a descrivere le caratteristiche energetiche della pioggia, come comunemente osservato in letteratura, mentre i parametri della distribuzione di Weibull colgono le differenze sito-specifiche nelle distribuzioni dimensionali delle gocce e, di conseguenza, nelle proprietà energetiche della pioggia.

Un sottoinsieme del database raccolto nel sito sperimentale di Sparacia, in cui le misure di pioggia erano accoppiate con misure contemporanee di perdita di suolo a scala di parcella, è stato utilizzato per riesaminare la rappresentazione dell'erosività della pioggia alla scala di evento. La formulazione classica dell'erosività, basata su

un descrittore globale di intensità, ha mostrato una limitata capacità di spiegare la variabilità della perdita di suolo misurata, anche quando l'energia cinetica della pioggia è stata derivata da dati disdrometrici. Al contrario, un nuovo descrittore che combina potenza cinetica e intensità alla loro risoluzione temporale di misura ha fornito una relazione con la perdita di suolo sostanzialmente migliorata, evidenziando l'importanza della dinamica intra-evento durante gli eventi erosivi.

Basandosi sul quadro concettuale fondato sulla distribuzione di Weibull, la ricerca ha inoltre apportato avanzamenti su un metodo di misura brevettato per ricostruire le caratteristiche energetiche della pioggia a partire da tre grandezze direttamente misurabili: intensità di pioggia, concentrazione di gocce e diametro medio derivato dalla distribuzione della quantità di moto delle gocce di pioggia. Tale metodo consente la determinazione dei parametri di Weibull e la stima della potenza cinetica e della quantità di moto senza misure disdrometriche complete. Il concetto si basa sull'analisi dei segnali elettrici generati dal rilevamento piezoelettrico degli impatti individuali delle gocce di pioggia, consentendo misure a basso costo delle proprietà energetiche della pioggia. La validazione rispetto ai dataset disdrometrici ha confermato l'accuratezza dell'approccio, in particolare per la quantità di moto della pioggia, a supporto della fattibilità del principio di misura brevettato, in attesa dello sviluppo di un prototipo.

Inoltre, un ampio programma sperimentale, comprendente diverse tipologie di simulatori di pioggia (a goccia e pressurizzati), ha supportato lo sviluppo di una metodologia affidabile per la loro caratterizzazione completa, consentendo la valutazione dell'uniformità spaziale dell'intensità di pioggia e dei parametri energetici associati. In particolare, per i simulatori a goccia, che generano gocce con diametro e velocità di caduta costanti, in condizioni operative fissate, le proprietà energetiche della pioggia sono intrinsecamente deterministiche. Per l'ampiamente utilizzato simulatore di Kamphorst, si è dimostrato che la potenza cinetica e la quantità di moto dipendono soltanto dall'intensità della pioggia e dall'altezza di caduta, consentendo lo sviluppo di relazioni empiriche espresse esclusivamente in funzione di tali variabili. Tale comportamento deterministico ha inoltre consentito, su tutti i dispositivi a goccia investigati, la validazione di una relazione empirica, calibrata su dati di letteratura, per la stima della velocità di

caduta delle gocce di pioggia in funzione del diametro e dell'altezza di caduta. Al contrario, i simulatori pressurizzati producono piogge più complesse, costituite da gocce con un ampio spettro di dimensioni e velocità, che riproducono con maggiore fedeltà la variabilità della pioggia naturale. In questo studio sono state considerate due configurazioni: un simulatore pressurizzato di nuova proposta sviluppato a Palermo e una struttura già consolidata a León (Spagna) in grado di generare condizioni di velocità terminale di caduta. A causa della loro intrinseca eterogeneità, gli approcci deterministici applicabili ai dispositivi a goccia non risultano idonei ai simulatori pressurizzati. La loro caratterizzazione completa, che tenga conto della variabilità spaziale delle distribuzioni di dimensione e di velocità di caduta delle gocce, nonché delle proprietà energetiche associate, può pertanto essere ottenuta soltanto mediante misure disdrometriche distribuite spazialmente, integrate con la calibrazione volumetrica convenzionale basata sul metodo di Christiansen.

Le indagini di laboratorio condotte in condizioni controllate hanno inoltre consentito di valutare le prestazioni di un disdrometro ottico Parsivel^2, progettato per il monitoraggio della pioggia in condizioni naturali. Lo strumento ha fornito stime affidabili delle distribuzioni dimensionali delle gocce simulate, ma ha mostrato una limitata accuratezza nella misurazione della velocità di caduta. In particolare, gli esperimenti hanno confermato che la sottostima della velocità delle gocce di pioggia, ben documentata per la pioggia naturale, si verifica anche in condizioni di pioggia simulata a velocità sub-terminali. Al contempo, le misure di velocità basate su disdrometro hanno consentito di verificare l'applicabilità della suddetta relazione empirica di velocità di caduta sia per simulatori a goccia sia per simulatori pressurizzati, in condizioni di caduta sia sub-terminali sia terminali.

I risultati ottenuti dallo studio delle piogge naturali e simulate convergono sul futuro sviluppo del dispositivo brevettato per la misura dell'energia della pioggia. Una volta disponibile, lo strumento richiederà inizialmente una validazione in condizioni altamente controllate, garantite dai simulatori a goccia completamente caratterizzati. Il successivo passaggio a campi di pioggia più complessi sarà supportato dal simulatore pressurizzato proposto in questo lavoro. La validazione conclusiva avverrà infine in condizioni di pioggia naturale.

TABLE OF CONTENTS

EXTENDED ABSTRACT I

SOMMARIO ESTESO IV

TABLE OF CONTENTS VII

1 INTRODUCTION 1

1.1 Soil Erosion Processes 1

1.1.1 Global Significance of Soil Erosion 1

1.1.2 Soil Erosion by Water 2

1.1.3 Empirical Soil Erosion Models: Limitations and Future Perspectives 4

1.1.4 Empirical Models at the Event Scale 7

1.2 Rainfall Erosivity Characterization 10

1.2.1 Drop Size Distribution 10

1.2.2 DSD Measurement Techniques 11

1.2.3 Theoretical Modelling of DSDs 16

1.2.3.1 Exponential Distribution 16

1.2.3.2 Gamma Distribution 17

1.2.3.3 Lognormal Distribution 22

1.2.3.4 Weibull Distribution 23

1.3 Simulated Rainfall 25

1.3.1 The Role of Rainfall Simulators in Soil Erosion Research 25

1.3.2 Rainfall Simulator Characterization and Validation Methods 28

1.4 Objectives of the Thesis 34

2 MATERIALS AND METHODS 36

2.1 Study Areas and Natural Rainfall Data Collection 36

2.1.1 Experimental Sites: Geographical and Climatic Context 37

2.1.2 Natural Drop Size Distribution Monitoring 40

2.1.2.1 Disdrometric Data Processing 40

2.1.2.2 Method of Moments and Statistical Evaluation of DSD Fitting using the Weibull Distribution 43

2.1.2.3 Application of Method of Moments and Weibull DSD to the Patented Measurement of Rainfall Energetic Characteristics 43

2.1.3 Plot-Scale Soil Loss Measurements at the Sparacia Experimental Site 44

2.2 Laboratory Experimental Setups for Simulated Rainfalls 46

2.2.1 Rainfall Simulators 48

2.2.1.1 Kamphorst Rainfall Simulator 48

2.2.1.2 Modified Kamphorst Rainfall Simulator 52
2.2.1.3 Drop Generator 53
2.2.1.4 Pressurized Rainfall Simulator of Palermo 54
2.2.1.5 Pressurized Rainfall Simulator of León 58
2.2.2 Parsivel² Optical Disdrometer 59
2.2.3 Rainfall Simulator Characterization Methodologies 63
2.2.3.1 Development of an Empirical Relationship to Estimate Raindrop Fall Velocity in Laboratory Conditions 63
2.2.3.2 Spatial Uniformity Assessment 65
2.2.3.3 Weighing and Photographic Techniques for Drip-Type Systems 70
2.2.3.4 Disdrometric Evaluation of Drip-Type and Pressurized Systems 74
2.3 Statistical Analysis 78

3 RESULTS AND DISCUSSION 81

3.1 Rainfall Erosivity and Soil Loss Measurements at Sparacia 82
3.2 Analysis of Natural Rainfall Using the Weibull Distribution 86
3.2.1 Reliability of Weibull distribution in reproducing Mediterranean DSDs 86
3.2.2 Theoretical Determination of Rainfall Kinetic Power and Momentum from the Weibull Distribution 91
3.2.3 Physical and Statistical Interpretation of the Weibull Shape and Scale Parameters and Sensitivity of Rainfall Energetic Estimates 95
3.2.4 Performance Comparison Between Weibull and Gamma Distributions in Estimating Rainfall Energy-Related Properties 99
3.3 Advances in the Patented Method for Measuring Rainfall Energetic Characteristics Using the Weibull Distribution 103
3.4 Characterization of Rainfall Simulators 109
3.4.1 Performance of the Kamphorst rainfall simulator 110
3.4.2 From the Modified Kamphorst Simulator to a Generalized Energetic Framework for Drip-Type Rainfall Simulators 119
3.4.3 A New Portable Rainfall Simulator for Soil Erosion Investigations 127
3.4.4 Characterization of the Pressurized Rainfall Simulator of León 141
3.4.5 Assessment of Parsivel² Reliability Under Laboratory Conditions and Extension of the Empirical Fall Velocity Relationship to Pressurized Rainfall Simulators 147
3.4.6 Validation of the Empirical Fall Velocity Relationship Under Terminal Fall Conditions 158

4 CONCLUSIONS 161

4.1 Natural Rainfall 161

4.1.1 Rainfall Erosivity and Soil Loss Measurement at the Sparacia Experimental Site 161

4.1.2 Analysis of Natural Rainfall Properties Using the Weibull Distribution 161

4.1.3 Advances in the Patented Method for Measuring Rainfall Energetic Characteristics Using the Weibull Distribution 162

4.2 SIMULATED RAINFALL 164

4.2.1 Rainfall Simulator Characterization 164

4.2.2 Raindrop Fall Velocity under Simulated Rainfall Conditions 165

4.2.3 Evaluation of the Parsivel² Disdrometer under Laboratory Conditions 165

4.3 FUTURE PERSPECTIVES 167

ACKNOWLEDGMENTS 168

A PERSONAL NOTE 169

REFERENCES 171

LIST OF SYMBOLS AND UNITS 209

ABBREVIATIONS 214

1 INTRODUCTION

1.1 Soil Erosion Processes

1.1.1 Global Significance of Soil Erosion

Soil is universally acknowledged as a vital, limited, non-renewable resource (García-Ruiz et al., 2015; Verheijen et al., 2009). It constitutes the essential foundation for the economy, society, and the environment, providing critical services such as food production, carbon storage, water filtering, and increased resilience to climate change and extreme weather events (Braimoh and Vlek, 2008; Breure et al., 2018; Keesstra et al., 2012; Kimble et al., 2000; Montanarella and Vargas, 2012; Saco et al., 2021; Smith, 2012).

However, soils in the European Union (EU) are currently in a poor condition, with degradation processes persisting and intensifying across all Member States (European Environment Agency, 2024). Over 60% of European soils are in unhealthy conditions according to the Soil Mission board estimates and the indicators presented in the European Union Soil degradation dashboard (Panagos et al., 2025).

Indeed, soil erosion is estimated at 1 billion tons per year across the EU, with water erosion affecting 24% of European soils and unsustainable practices impacting around 32% of agricultural land, posing a significant threat to soil fertility and long-term agricultural productivity (European Environment Agency, 2024). As a result, the economic consequences of soil degradation are substantial, estimated to cost the Union tens of billions of euros annually due to losses in agricultural productivity, carbon depletion, and off-site infrastructure damage (Panagos et al., 2025), highlighting the urgent need for effective mitigation measures (Boardman and Vandaele, 2023).

Within the broader context of environmental degradation and climate change, the European Green Deal establishes the ambitious goal of transforming the EU into a climate-neutral economy by 2050 (Boix-Fayos and de Vente, 2023; Di Stefano et al., 2023; Montanarella, 2020; Montanarella and Panagos, 2021). As part of this policy agenda, protecting, conserving, and restoring soil health is designated as a key priority, integral to the EU Biodiversity Strategy 2030, the Zero Pollution

Action Plan, and the Climate Change Adaptation Strategy (Depietri, 2025; Keesstra et al., 2024).

1.1.2 Soil Erosion by Water

Water erosion, driven primarily by precipitation and surface runoff, is a dominant factor in soil degradation (Centeri, 2022; García-Ruiz et al., 2017; Ketema and Dwarakish, 2021; Li and Fang, 2016).

From a physic perspective, soil erosion by water is a chain of linked sub-processes: the mechanical break up of aggregates and removal of particles at the surface (detachment), the transfer of these particles into moving water (entrainment), their movement within sheet or concentrated flow (transport), and their eventual settling when flow competence decreases (deposition) (Morgan, 2005).

The magnitude of water erosion is governed by the balance between erosive forcing (erosivity) and soil resistance (erodibility). Erosive forcing depends on rainfall and runoff characteristics, i.e., rainfall intensity, drop size distribution (DSD), fall velocity, and the hydraulic properties of overland flow (depth, velocity, shear stress), whereas soil resistance is controlled by structure and aggregation, organic matter content, texture, cohesion, bulk density, and moisture (Bryan, 2000; Cerdá, 1997; Lal, 2001; Wischmeier and Smith, 1978). Therefore, when the external stresses imposed by rainfall and runoff exceed the local soil resistance thresholds, detachment begins. The process may be detachment-limited or transport-limited, depending on the relation between sediment supply and flow transport capacity.

Although erosion is an intrinsic geomorphic process operating over geological timescales, anthropogenic disturbances such as intensive cultivation, vegetation removal, and inappropriate land management greatly accelerate detachment and transport rates, producing what is commonly termed accelerated soil erosion (Issaka and Ashraf, 2017; Lal, 2001; Leh et al., 2013; Nearing et al., 2017; Pimentel et al., 1995).

The consequences of accelerated water erosion are extensive and include: (i) on-site effects, such as nutrient depletion, deterioration of soil properties, and reduced agricultural productivity (Issaka and Ashraf, 2017; Lal, 2003; Lal et al., 2000; Osman, 2014); and (ii) off-site effects, including water quality degradation and

sedimentation of reservoirs and channels (Boardman et al., 2019; Majoro et al., 2020; Mullan, 2013).

Quantifying soil erosion at the watershed scale remains challenging because sediment yield measured at a catchment outlet represents the integrated outcome of multiple interacting processes operating across the landscape. Hillslope detachment, local deposition and temporary storage, re-entrainment, channel and bank erosion, and sediment routing within the drainage network all contribute to the final sediment flux, often obscuring the spatial origin and magnitude of gross hillslope soil loss (Morgan, 2005; Walling, 1990).

Consequently, many experimental investigations are conducted at the plot scale, where boundary conditions can be defined and soil loss measured directly using bounded plots equipped with runoff and sediment collection systems.

Plot experiments enable reproducible quantification of soil loss from a known area and allow controlled analysis of the effects of rainfall, soil, slope, and land management.

However, extrapolation to larger spatial units remains difficult because sediment delivery, connectivity, and internal redistribution processes vary with scale (Panagos et al., 2015; Walling, 1990).

Beyond spatial representativeness issues, reliable erosion assessment also requires accurate characterization of rainfall forcing. Rainfall intensity is relatively easy to measure and benefits from dense, long-established pluviometric monitoring networks.

In contrast, physically based descriptors of rainfall erosivity, such as kinetic energy or kinetic power, require detailed knowledge of raindrop size and fall velocity distributions and thus specialized instrumentation (e.g., disdrometers), which is costly and far less widely available than conventional rain gauges (Angulo-Martínez and Barros, 2015).

Consequently, rainfall energy is often estimated indirectly from intensity through empirical relationships (e.g., Brown and Foster, 1987; van Dijk et al., 2002), despite their known limitations and site specificity.

The implications of relying on intensity-based proxies for rainfall erosivity are examined in the following section.

1.1.3 Empirical Soil Erosion Models: Limitations and Future Perspectives

Currently, soil erosion modelling is predominantly characterized by empirical approaches derived from the *Universal Soil Loss Equation* (USLE) framework. The original USLE (Wischmeier, 1955; Wischmeier and Smith, 1978) and its revised versions, including the *Revised Universal Soil Loss Equations* (RUSLE) (Renard et al., 1997) and RUSLE2 (Foster, 2005; Foster et al., 2001), remain the most widely applied tools for estimating average annual soil loss. Several extensions of the USLE concept have been developed to broaden its applicability across spatial and temporal scales, such as the *Modified Universal Soil Loss Equation* (MUSLE) (Williams and Berndt, 1977) and the *Sediment Delivery Distributed* model (SEDD) (Ferro and Porto, 2000).

The USLE model was originally developed for predicting the average annual soil loss per unit area (Panagos et al., 2012). It has the following form (Wischmeier and Smith, 1978):

$$A = R\,K\,L\,S\,C\,P \tag{1}$$

in which A (t ha^{-1} yr^{-1}) is the annual average soil loss, R (MJ mm h^{-1} ha^{-1} yr^{-1}) is the rainfall erosivity factor, K (t ha h ha^{-1} MJ^{-1} mm^{-1}) is the soil erodibility factor, L (−) is the slope-length factor, S (–) is the slope-steepness factor, C (–) is the land cover and management factor, and P (–) is the soil conservation or prevention practices factor.

Nevertheless, according to the *Global Applications of Soil Erosion Modelling Tracker* (GASEMT) database (Borrelli et al., 2021), which reviews 3,030 modelling records across 126 countries, models belonging to the (R)USLE family are by far the most widely used, representing approximately 41% of total applications. The dominance of this approach is even more pronounced if USLE-derived models like the *Water and Tillage Erosion Model / Sediment Delivery Model* (WaTEM/SEDEM) (Van Oost et al., 2000), the *Erosion-Productivity Impact Calculator* (EPIC) (Williams et al., 1983), the *Soil and Water Assessment Tool* (SWAT) (Arnold et al., 1998), and the *Unit Stream Power-based Erosion Deposition* (USPED) (Mitasova et al., 1996) are included in the count.

In contrast to these empirical frameworks, physically-based models such as the *Water Erosion Prediction Project* (WEPP) (Laflen et al., 1991), the *Limburg Soil Erosion Model* (LISEM) (De Roo et al., 1996), and the *European Soil Erosion Model* (EUROSEM) (Morgan et al., 1998) have been developed to explicitly simulate the mechanics of detachment, transport, and deposition. Despite their theoretical capability to better represent spatiotemporal variability, their operational use remains significantly lower than that of empirical counterparts, accounting for only about 12% of the total entries in the GASEMT database (Borrelli et al., 2021). The limited adoption of physically based models is partly due to the fact that increasing model complexity does not necessarily yield lower uncertainties or better predictions than simpler empirical models (Alewell et al., 2019; Pampalone et al., 2025). For instance, recent comparisons have shown that WEPP does not inherently predict event soil loss from bare fallow areas better than USLE-based models like RUSLE2, often due to difficulties in accurately estimating parameters (e.g., interrill erodibility) (Kinnell, 2025).

On the other hand, the widespread adoption of the (R)USLE family models is due to their ease of application, offering a favorable compromise between modest input data requirements and reliability of estimates, especially in data-scarce environments (Alewell et al., 2019; Benavidez et al., 2018). Furthermore, these empirical models can be seamlessly integrated with Geographical Information Systems (GIS), allowing for large-scale assessments (Benavidez et al., 2018).

However, this reliance on empirical models implies significant intrinsic limitations. Firstly, the mathematical structure of the USLE was deduced using a specific reference condition, the “unit plot” (22.1 m long, 9% slope, continuous fallow), which implies that the model factors are strictly valid only within the range of the original calibration data collected primarily in the USA (Carollo et al., 2024c; Wischmeier and Smith, 1978). Consequently, applying these models to different climatic and geomorphological contexts without local calibration can lead to significant errors (Carollo et al., 2024c). Secondly, there is a fundamental discrepancy in the nature of the modeled processes: USLE-type models predict gross erosion (the total amount of soil moved), whereas most validation measurements quantify net erosion or sediment yield, ignoring the depositional

processes that occur within the catchment (Alewell et al., 2019). Finally, these models are typically limited to estimating sheet and rill erosion, systematically neglecting fundamental processes such as gully erosion, channel erosion, and mass wasting, and failing to account for sediment routing and delivery to water bodies unless coupled with specific sediment delivery ratios (Alewell et al., 2019; Benavidez et al., 2018).

Beyond these structural limitations, other fundamental critical issue lies in the parameterization of rainfall erosivity, a key driver in soil erosion modelling. Indeed, traditional empirical models simplify the estimation of the rainfall erosivity index by relying almost exclusively on rainfall intensity, I (mm h^{-1}), as a proxy to estimate the kinetic energy of a storm event (Wischmeier and Smith, 1978). This approach has been widely adopted since intensity data are readily available from standard pluviograph networks, whereas direct measurements of kinetic energy or drop size distributions require specific, expensive, and less widespread instrumentation such as disdrometers (Adirosi et al., 2023; Angulo-Martínez et al., 2016; Carollo et al., 2017, 2018b, 2023, 2024d, 2026; Johannsen et al., 2020b).

However, extensive research has demonstrated that relying solely on intensity is not sufficiently physically rigorous and is often a source of significant errors (Angulo-Martínez et al., 2016; Johannsen et al., 2020b; Mineo et al., 2019). In particular, the relationship between I and the kinetic energy per unit area and time, named kinetic power, P_n (J m^{-2} s^{-1}), is site specific, depending on storm type and climatic zone. For instance, Salles et al. (2002) and van Dijk et al. (2002) conducted critical appraisals of literature data, highlighting that empirical P_n–I relationships are highly site-specific and cannot be generalized without introducing substantial uncertainty. Similarly, Wilken et al. (2018) in Germany and Carollo et al. (2017) in Mediterranean environments demonstrated that commonly used P_n–I relationships often overestimate cumulative kinetic energy compared to direct disdrometer measurements, particularly at high intensities, confirming that intensity alone cannot adequately represent the multiple variables and microphysical processes governing raindrop formation and, consequently, the energetic characteristics of erosive precipitation.

Consequently, recent studies suggest that metrics directly based on rainfall physical impact properties, such as the rainfall kinetic power and the rainfall momentum, M (N m^{-2}), can be more reliable predictors of soil detachment. While P_n is classically used to describe detachment, early work by Rose (1960) suggested that M correlates more strongly with soil aggregate breakdown and detachment rate (Carollo et al., 2018a). This hypothesis has been supported by recent investigations across diverse climatic contexts: for instance, Lim et al. (2015) in Korea and Sanchez-Moreno et al. (2012) in Cape Verde found that rainfall momentum is a robust predictor of erosivity, often interchangeable with or superior to kinetic energy, depending on soil properties.

Both P_n and M depend on the mass and velocity of individual drops, thus they are strictly related to the rainfall Particle Size and Velocity Distribution (PSVD) (Carollo et al., 2018a, 2024d). Hence, an accurate erosivity estimation cannot disregard the detailed microphysics of precipitation.

Therefore, it is crucial to move beyond empirical intensity-based relationships and adopt an approach that directly measures and integrates the information about the PSVD (Caracciolo et al., 2012). Alternatively, information on the Drop Size Distribution (DSD) is applied to estimate the terminal velocity of raindrops using a relationship (Carollo et al., 2026).

1.1.4 Empirical Models at the Event Scale

The USLE model can also be applied at the event scale (Bagarello et al., 2020):

$$A_e = R_e\ K\ L\ S\ C\ P \tag{2}$$

where A_e (t ha^{-1}) is the event soil loss and R_e (MJ mm h^{-1} ha^{-1}) is the event rainfall erosivity index.

Following the criteria established by (Wischmeier and Smith, 1978), rainfall events are considered distinct if a minimum inter-event time of six hours without precipitation occurs. Furthermore, an event is classified as erosive if it meets specific thresholds: a cumulative rainfall depth of at least 13 mm or a peak accumulation of 6 mm within a 15-minute interval.

For each identified erosive event, R_e is computed as:

$$R_e = \left(\sum_{e=1}^{N} \frac{P_{n,e}}{I_e} h_e \right) I_{30} \quad (3)$$

in which $P_{n,e}$ (MJ ha^{-1} h^{-1}), I_e (mm h^{-1}), and h_e (mm) are the rainfall kinetic power, intensity, and depth in the e-th interval of the erosive event, respectively, N (–) is the number of time intervals within the erosive event, and I_{30} (mm h^{-1}) is the maximum 30-minute rainfall intensity, i.e., the highest average intensity recorded over any continuous 30-minute period within the event.

According to Wischmeier and Smith (1978), when $I_e \leq 76$ mm h^{-1}, the kinetic energy per unit volume of rainfall can be estimated as:

$$\frac{P_{n,e}}{I_e} = 0.119 + 0.0873 \log I_e \quad (4)$$

while for higher intensities a constant value of 0.2832 MJ ha^{-1} mm^{-1} is assumed. However, as already observed in Section 1.1.3, the $P_{n,e}/I_e$ relationship is site-specific. For instance, Carollo et al. (2023) showed that in Mediterranean environments the rainfall intensity threshold beyond which $P_{n,e}/I_e$ becomes approximately constant is about 40 mm h^{-1} at the Palermo site (Sicily, Italy) and about 100 mm h^{-1} at the Sparacia site (province of Agrigento, Sicily, Italy), two locations separated by only ~65 km in straight-line distance.

Consequently, the fixed threshold of 76 mm h^{-1} implicit in Equation (4) cannot be considered universally valid, and the relationship requires site-specific calibration. More generally, using rainfall intensity alone as a surrogate for erosive energy implies that the classical R_e index may only partially capture the physical impact characteristics of precipitation.

In addition to these limitations, the classical event-scale USLE formulation does not explicitly account for runoff generation, which directly controls sediment transport capacity at the plot scale. To overcome this limit, several runoff-based empirical extensions of the USLE have been proposed. The USLE-M incorporates the runoff coefficient into the erosivity factor, defining an event rainfall–runoff erosivity index proportional to the product of rainfall erosivity and runoff ratio (Kinnell, 1997; Kinnell and Risse, 1998). Subsequent developments led to the USLE-MM, in which soil loss is related to a power function of the runoff-weighted erosivity index, improving the representation of event-scale variability and soil

erodibility estimation in Mediterranean environments (Bagarello et al., 2013, 2010, 2008). A further theoretically supported extension is the USLE-MB, which formulates soil loss as a function of a rainfall–runoff erosivity factor derived through dimensional analysis and self-similarity theory to jointly represent rainfall detachment and flow transport processes (Bagarello et al., 2018, 2020; Pampalone et al., 2023). These runoff-driven USLE-type models demonstrate that incorporating hydrological response into the erosivity term substantially improves event soil loss prediction compared with rainfall-based formulations, while preserving the empirical structure of the original USLE approach.

Nevertheless, both the classical R_e index and its runoff-based variants ultimately rely on simplified descriptors of rainfall energy derived from intensity measurements. Extensive experimental evidence indicates that such formulations cannot fully capture the variability of erosive precipitation, since the kinetic power of rainfall depends on the full drop size and fall velocity distribution rather than on intensity alone. Consequently, further research is required to assess whether direct energy estimates derived from raindrop size and velocity spectra can provide a more physically consistent explanation of event-based soil loss.

1.2 Rainfall Erosivity Characterization

1.2.1 Drop Size Distribution

In soil erosion processes, precipitation plays a crucial role in the detachment and transport of soil particles. Traditionally, hydrological studies have relied on rainfall intensity and rainfall depth as the primary variables for characterizing rainfall events. However, several authors (Cevasco et al., 2015; Meshesha et al., 2018; Uijlenhoet and Stricker, 1999; Waldvogel, 1974) stated that these bulk parameters are insufficient for accurately describing the erosive potential of rainfall and suggested that the DSD provides a more physical basis for investigating soil erosion mechanisms.

The drop size distribution (DSD) is formally defined as the expected number of drops with diameters, D (cm), between D and $D+dD$, usually referred to a unit volume of air $N_{(D)V}$ ($cm^{-1}m^{-3}$) (Bringi et al., 2003; Gires et al., 2020; Marshall and Palmer, 1948; Uijlenhoet and Stricker, 1999) or to the unit area and time $N_{(D)}$ (cm^{-1} m^{-2} s^{-1}) (Carollo et al., 2018a; Carollo and Ferro, 2015; Janapati et al., 2023; Serio et al., 2019a; Zeng et al., 2024).

Specifically, $N_{(D)V}$ describes the static properties of the raindrop population and expresses the spatial distribution of raindrops in a unit volume of air. Thus, it is commonly employed in meteorological studies.

In contrast, hydrological studies primarily refer to $N_{(D)}$ because it also accounts for the dynamic properties of the raindrop population. In other words, $N_{(D)}$ allows determination of the energy and momentum transferred to the soil surface, which are key variables for a rigorous estimation of rainfall erosivity, defined as the capability of rainfall to detach soil particles.

Under the assumption that wind, turbulence, and raindrop interactions are negligible, the two size distributions are connected by the following relationship (Carollo and Ferro, 2015; Hall and Calder, 1993; Uijlenhoet and Stricker, 1999):

$$N_{(D)} = V_{(D)} N_{(D)V} \tag{5}$$

where $V_{(D)}$ (m s^{-1}) represents the terminal velocity of a drop with diameter D.

When measured at ground level, the DSD is the product of complex microphysical phenomena that influence drop evolution (Pruppacher and Klett, 1978, 2010). While evaporation modifies the lower end of the spectrum by depleting smaller drops, the shape of the distribution is primarily governed by the dynamic equilibrium between coalescence and breakup processes (Saha et al., 2012; Testik et al., 2011). Coalescence promotes drop growth through collisions and mergers, while breakup limits the maximum drop size and redistributes mass into smaller fragments (Saha et al., 2012; Testik et al., 2011).

Therefore, knowledge of the DSD is fundamental to accurately understanding how rainfall is composed, enabling a rigorous characterization of precipitation erosivity by integrating critical energetic parameters such as P_n and M with the conventional hydrological variables of intensity and depth (Mualem and Assouline, 1989).

1.2.2 DSD Measurement Techniques

Over the last century, several methodologies have been developed and refined to measure the DSD of rainfall, evolving from rudimentary manual techniques to sophisticated automated sensors. Early studies attempted to describe raindrop size using manual measurement techniques involving chemically treated paper, flour, or oil-coated screens (Blanchard, 1952; Defant, 1905; Wiesner, 1895). While these pioneering approaches established the foundational knowledge of rainfall physics, they were often labor-intensive, time-consuming, and required rigorous calibration.

One of the earliest techniques was the stain method, originally described by Lowe (1892). This method involves exposing sheets of chemically treated paper dusted with a water-soluble dye to rainfall for a brief interval. Upon impact, the drops react with the dye, leaving permanent marks whose diameter is a function of the drop size and the paper's thickness (Hall, 1970). Despite its widespread historical use, this method presents significant limitations: it is sensitive to paper temperature and humidity (Campos, 1999; Quinn, 1981), tends to underestimate the volume of small drops due to the overlapping of larger stains (Kincaid et al., 1996), and prevents accurate counting during prolonged sampling periods (Kathiravelu et al., 2016).

An evolution of the stain method was the raindrop spectrograph (Bowen and Davidson, 1951), a semi-automated device where falling drops were deflected by a

horizontal air current onto sensitized paper based on their mass, allowing for a continuous record of the DSD, although it remained unsuitable for very small drops (< 0.25 mm) (Bowen and Davidson, 1951).

Contemporaneously, the flour pellet method became a standard reference to characterize both natural and simulated rainfalls (Arnaez et al., 2007; Kohl, 1974; Laws and Parsons, 1943; Navas et al., 1990; Pérez-Latorre et al., 2010). By exposing a tray of flour to rainfall, the water droplets interact with the flour to form dough pellets, which are subsequently dried, sieved, and weighed. The mass of the pellets is then related to the mass of the original raindrops through calibration curves (Laws and Parsons, 1943). However, this method is only accurate for drops larger than 0.3 mm, destructive, and susceptible to wind effects (Eigel and Moore, 1983; Laws and Parsons, 1943).

To address the measurement of smaller droplets, particularly in clouds and fogs, the oil immersion method was developed (Fuchs and Petrjanoff, 1937). Drops are collected in a low-density immiscible liquid (oil) that preserves their spherical shape due to surface tension, allowing measurement via microscopy. However, this method is prone to the breakup of large drops upon impact and evaporation issues.

A major limitation shared by all these manual techniques (the stain method, the flour pellet method, and the oil method) is their inability to directly measure the fall velocity of raindrops. In this context, a significant technological advance was the photographic method, which enabled the first detailed monitoring of splash droplet production and fall velocity (Laws, 1941; Mutchler, 1971; Mutchler and Hansen, 1970; Mutchler and Larson, 1971). However, early applications were limited by light infiltration and depth-of-field issues, often restricting sampling to nighttime or requiring complex setups (Kathiravelu et al., 2016; Mason and Ramanadham, 1953).

Over time, the photographic method has effectively evolved into modern video-based rainfall measurement techniques (Yan et al., 2023). Indeed, the integration of Computer Vision (CV) and Deep Learning (DL) has transformed the optical analysis of raindrops from a manual task into an automated, real-time process. Therefore, by applying advanced algorithms, such as photometric constraints or Convolutional Neural Networks (Garg and Nayar, 2007; Yin et al., 2023), it is

possible to estimate the raindrop size and velocity and derive the information about rainfall intensity and PSVD.

However, despite being a reliable method, these video-based techniques are not widely adopted because they are subject to technical challenges similar to those of photographic methods, particularly regarding depth of field and complex background interference.

Among the diverse range of techniques available for the comprehensive microphysical characterization of precipitation, disdrometers are widely regarded as the most advanced and reliable instruments. First introduced in the mid-20th century to support radar calibration and meteorological studies, these devices were specifically designed to measure the size and fall velocity of individual hydrometeors. Over the decades, disdrometer technology has undergone substantial evolution, achieving higher sensitivity and accuracy, as well as improved discrimination capabilities through enhanced optical and signal-processing techniques, and has consequently become the standard tool for rainfall characterization (Fernández-Raga et al., 2011).

Disdrometers are generally categorized into three main types based on their physical measurement principle: impact, acoustic, and optical. Impact disdrometers, such as the Joss-Waldvogel disdrometer (JWD) (Joss and Waldvogel, 1967), infer kinetic energy from the signals generated by drops impacting a sensor surface. Although these devices are simple and suitable for erosion studies, they suffer from significant limitations. A critical issue is the *dead-time* error, in which the residual vibration of the sensor after a large drop impact masks the signals from smaller drops that follow immediately, leading to a systematic underestimation of small drops during intense rainfall (Tokay et al., 2001). Furthermore, JWD does not directly measure fall velocity, assuming that drops are falling at their theoretical terminal velocity (Gunn and Kinzer, 1949).

Alternatively, acoustic disdrometers determine rainfall parameters by recording the sound energy produced as raindrops hit a specialized liquid or solid surface, typically using piezoelectric sensors (Kathiravelu et al., 2016). These instruments offer the advantage of large sampling areas and high temporal resolution; however, their accuracy is susceptible to environmental noise, background vibrations, non-

uniform sensitivity across the piezoelectric surface, and the complex acoustic signature of splashing drops (Nystuen, 2001; Winder and Paulson, 2012).

Finally, laser optical disdrometers have emerged as the most prevalent instruments in modern research due to their non-intrusive nature and high levels of automation (Lanza et al., 2021). These devices utilize light sources, typically laser diodes, to detect particles passing through a sampling area, without influencing their behavior. Based on the underlying physical principle, they can be categorized into systems that operate on light occlusion (or extinction) and those that operate on light scattering (Angulo-Martínez et al., 2018).

In soil erosion, the most widely used devices operate on the extinction principle. They employ a horizontal laser beam and a receiver: when a drop passes through the beam, it blocks a portion of the light, reducing the output voltage at the receiver, whose attenuation is proportional to the particle's diameter (Saha and Testik, 2023). Devices like the Particle Size Velocity^2 (Parsivel^2) (OTT Hydromet GmbH, 2016) and the Laser Precipitation Monitor (LPM) (Thies CLIMA, 2010) also derive the fall velocity of each particle from the duration of the signal blockage, allowing for the generation of a complete PSVD matrix and the direct calculation of P_n and M. Conversely, other optical systems, such as the Eigenbrodt Optical Disdrometer (ODM, model 470) (Eigenbrodt GmbH & Co., 2007), function primarily as spectrometers, only measuring the DSD. In such cases, energy-related parameters must be estimated by coupling measured diameters with an assumed terminal-velocity law (e.g., Atlas et al., 1973; Atlas and Ulbrich, 1977; Beard, 1976; Ferro, 2001; Gunn and Kinzer, 1949).

A different approach is employed by optical disdrometers that use the light-scattering principle, such as the Present Weather Sensor 100 (PSW100) (Campbell Scientific, 2015). Instead of measuring blockage, it uses four laser sheets to detect light scattered by drops passing through the sampling volume with off-axis detectors. This configuration allows velocity to be determined via a *time-of-flight* method (by measuring the time delay between pulses from different light sheets) rather than by residence time.

The scientific literature provides extensive evidence of discrepancies arising not only between fundamentally different measurement principles, but also between

instruments of the same typology produced by different manufacturers, which often employ distinct internal processing algorithms and hardware geometries (Angulo-Martínez et al., 2018; Caracciolo et al., 2006; Fernández-Raga et al., 2021; Johannsen et al., 2020a; Lanza et al., 2021; Liu et al., 2013; Sheppard and Joe, 1994; Tokay et al., 2001). Therefore, the selection of the DSD or PSVD measurement technique critically impacts the determination of rainfall erosivity parameters.

Despite these instrumental uncertainties, optical disdrometers can also serve as a crucial resource for verifying the reliability of standard empirical procedures for estimating soil loss. Unlike traditional methods that rely on generalized correlations between rainfall intensity and kinetic energy, disdrometers enable direct quantification of the actual energy load impacting the soil surface. Consequently, contemporaneous measurements of (i) soil loss at the plot and event scale and (ii) rainfall characteristics, such as intensity and DSD, enable the assessment of whether erosivity indices derived from high-resolution disdrometric data provide a more accurate prediction of sediment yield compared to conventional empirical estimates.

Nevertheless, the widespread application of disdrometers remains limited by their high cost, operational complexity, and the significant effort required for data processing and maintenance. These constraints make them suitable primarily for research environments rather than for large-scale or routine monitoring of rainfall erosivity. To overcome these limitations, recent research has explored alternative approaches aimed at estimating rainfall energetic characteristics without requiring full disdrometric measurements. For instance, an innovative method and a dedicated device for the direct measurement of rainfall energy, subject to a patent (Patent No. 102018000010691), have been recently proposed.

The patented approach is based on the simultaneous detection, within a given time interval, of two easily measurable variables, namely rainfall intensity and the number of raindrops impacting a reference surface. These quantities can be obtained through a simple and low-cost system consisting of a conventional pluviograph equipped with an additional collar hosting impact sensors capable of counting the number of drop collisions. The underlying idea is to infer rainfall kinetic power and

momentum through simplified formulations, enabling the use of low-cost instrumentation while preserving adequate physical consistency.

Preliminary investigations by Serio et al. (2019b) highlighted the potential of this approach but also showed that the sole use of rainfall intensity and the number of impacts was insufficient to ensure accurate estimates of rainfall kinetic power under Mediterranean conditions. Hence, further developments were introduced by Carollo et al. (2024d), who proposed theoretical refinements to improve the method's reliability by incorporating additional information from the analysis of the rainfall momentum distribution.

These contributions demonstrated that simplified measurement strategies can potentially provide physically consistent estimates of rainfall energetic variables, while avoiding the operational complexity and costs associated with traditional disdrometric techniques.

1.2.3 Theoretical Modelling of DSDs

Several analytical functions have been proposed in the scientific literature to fit measured DSDs: the exponential distribution (Marshall and Palmer, 1948), the Gamma distribution (Ulbrich, 1983), the lognormal distribution (Mueller and Sims, 1966), and the Weibull distribution (Sekine and Lind, 1982; Weibull, 1951).

1.2.3.1 Exponential Distribution

Marshall and Palmer (1948) proposed the following negative exponential function to describe DSDs measured with a filter paper technique and relative to rainfall intensities between 1 mm h^{-1} and 23 mm h^{-1} (Uijlenhoet and Stricker, 1999):

$$N_{(D)V}dD = N_{0,V}exp(-\Lambda_V D)dD \tag{6}$$

in which $N_{(D)V}$ is the drop number concentration per unit air volume and unit diameter interval (m^{-3} cm^{-1}), and $N_{0,V}$ (m^{-3} cm^{-1}) and Λ_V (cm^{-1}) are the parameters of the exponential distribution. The slope parameter Λ_V varies with rainfall intensity according to a power law (Marshall and Palmer, 1948):

$$\Lambda_V = 4.1\, I^{-0.21} \tag{7}$$

while the intercept parameter $N_{0,V}$ was originally suggested to be constant (8×10^4 m^{-3} cm^{-1}). However, many authors proved that $N_{0,V}$ is not constant

(Donnadieu, 1980; Sekhon and Srivastava, 1971; Waldvogel, 1974). Specifically, analyzing drop size spectra measured by Laws and Parsons (1943), Ulbrich (1983) proposed the following relationship in which $N_{0,V}$ is a function of the rainfall intensity:

$$N_{0,V} = 5.1 \times 10^4 \, I^{-0.03} \tag{8}$$

Although the Marshall–Palmer distribution is widely adopted as a reference parameterization of the raindrop size distribution (Marshall and Palmer, 1948; Neuper and Ehret, 2019; Uijlenhoet, 2001), a substantial body of observational studies has documented important limitations of the single-parameter exponential form (Carbone and Nelson, 1978; Waldvogel, 1974).

In particular, the Marshall–Palmer model often misrepresents the distribution tails, tending to overestimate the number of very small and very large drops compared with field measurements (Gunn and Marshall, 1955; Sempere Torres et al., 1994; Waldvogel, 1974). Moreover, in tropical regions characterized by high-intensity rainfall, several studies report that the slope parameter Λ_V appears to reach an approximately constant value above certain intensity thresholds, a behaviour that the single-parameter exponential cannot capture (Pasqualucci, 1982; Sauvageot and Lacaux, 1995; Tokay and Short, 1996; Zhang et al., 2022).

1.2.3.2 Gamma Distribution

To address the limitations of the exponential model, Ulbrich (1983) introduced the Gamma distribution, which generalizes the Marshall-Palmer function of Equation (6) by adding a shape parameter, μ_V (–). This distribution is expressed as:

$$N_{(D)V} dD = N_{0,V} D^{\mu_V} exp(-\Lambda_V D) dD \tag{9}$$

in which $N_{0,V}$ is expressed as m^{-3} $cm^{-1-\mu}$ and Λ_V as cm^{-1}.

The shape parameter μ_V allows the distribution to model concave-downward (positive μ_V) or concave-upward (negative μ_V) spectra on a semi-logarithmic plot, providing greater flexibility in fitting experimental data. For $\mu_V = 0$, the Gamma distribution reduces to the exponential distribution given by Equation (6).

The versatility and applicability across different climatic conditions have made the Gamma distribution a standard tool for describing precipitation particles in clouds and aerosols (Blanchard, 1953; Brawn and Upton, 2008; Caton, 1966;

Chandrasekar and Bringi, 1987; Dingle and Hardy, 1962; Fu et al., 2020; Gatidis et al., 2020; Lee et al., 2023; Mineo et al., 2020; Tokay and Short, 1996; Zhang et al., 2022).

Moreover, Equation (9) is also reliable for estimating DSD per unit time and area ($N_{(D)}$). Notably, combining Equations (5) and (9), and applying an expression for the $V_{(D)}$ estimation, such as that by Atlas and Ulbrich (1977):

$$V_{(D)} = 17.67\, D^{0.67} \tag{10}$$

The following relationship is obtained:

$$N_{(D)}dD = N_0 D^{\mu} exp(-\Lambda D)dD \tag{11}$$

in which N_0 ($m^{-2}\ s^{-1}\ cm^{-1-\mu}$), μ (–), and Λ (cm^{-1}) are the three parameters of the $N_{(D)}$ distribution.

As for any parametric DSD model, macroscopic rainfall variables can be expressed in terms of the distribution parameters. For the Gamma distribution, the rainfall intensity can be expressed as a function of the three distribution parameters (Carollo et al., 2018a; Olver, 1997; Salles et al., 2002):

$$I = 3.6\frac{\pi}{6} N_0 \frac{\Gamma(4+\mu)}{\Lambda^{4+\mu}} \tag{12}$$

in which Γ is the gamma function. Equation (12) allows the determination of the N_0 parameter as a function of I, Λ, and μ:

$$N_0 = \frac{\Lambda^{4+\mu}}{3.6\frac{\pi}{6}\Gamma(4+\mu)} I \tag{13}$$

Moreover, two crucial parameters for analytically characterizing the energetic potential of a DSD, i.e., the median volume diameter, D_0 (cm), defined as the specific raindrop size that divides the total precipitation volume into two equal halves, and the median drop diameter, D_{50} (cm), defined as the median diameter of the DSD, are analytically linked to both the distribution's scale (Λ) and shape (μ) parameters (Uijlenhoet and Stricker, 1999; Ulbrich, 1983):

$$D_0 = \frac{3.67+\mu}{\Lambda} \tag{14}$$

$$D_{50} = \frac{0.67+\mu}{\Lambda} \tag{15}$$

Furthermore, the mean, $\mu_{(D)}$, and the standard deviation, $\sigma_{(D)}$, of the Gamma distribution can also be expressed as a function of the Λ and μ parameters (Uijlenhoet and Stricker, 1999):

$$\mu_{(D)} = \frac{\mu + 1}{\Lambda} \tag{16}$$

$$\sigma_{(D)} = \frac{\sqrt{\mu + 1}}{\Lambda} \tag{17}$$

Building on this analytical framework, recent studies have shown that the Gamma distribution provides a consistent way to represent observed DSD variability and to quantify the associated rainfall kinetic energy and erosivity. In particular, studies in Mediterranean environments have used these Gamma-based analytical relationships to connect the statistical characterization of DSDs to physically based estimates of rainfall erosivity (Carollo et al., 2016b, 2017, 2018a, 2018b, 2023; Carollo and Ferro, 2015; Serio et al., 2019a, 2019b).

According to Carollo and Ferro (2015), the probability, $P_{(D)}$, that the raindrop diameter is less than D can be calculated as:

$$P_{(D)} = \frac{\Lambda^{4+\mu}}{\Gamma(\mu + 1)} \int_0^D D^{\mu} \exp(-\Lambda D)\, dD \tag{18}$$

Additionally, Carollo and Ferro (2015) and Carollo et al. (2018a) theoretically deduced two relationships to estimate the rainfall kinetic power and momentum, respectively, using the Gamma distribution. The kinetic power per unit area and area can be expressed as the integral of the kinetic energy of all falling drops (Salles et al., 2002):

$$P_n = 10^{-6} \frac{\rho\pi}{12} \int_0^{\infty} {V_{(D)}}^2 D^3 N_{(D)}\, dD \tag{19}$$

in which ρ (kg m^{-3}) is the water density. Similarly, the momentum per unit time and area can be calculated by adding the contribution of single raindrops according to the following relationship:

$$M = 10^{-6} \frac{\rho\pi}{6} \int_0^{\infty} V_{(D)} D^3 N_{(D)}\, dD \tag{20}$$

To solve the integrals of Equations (19) and (20), the authors (Carollo et al., 2018a; Carollo and Ferro, 2015) adopted the velocity relationship proposed by Ferro (2001):

$$V_{(D)} = V_h[1 - \exp(-a_h D)] \quad (21)$$

where D is expressed in cm and V_h (m s^{-1}) and a_h (cm) are coefficients depending on the fall height, h (m). For natural precipitation ($h \geq 20$ m), V_h and a_h take values of 9.5 m s^{-1} and 6 cm. For smaller heights ($h < 20$ m), discrete tabulated values of V_h and a_h are provided by Ferro (2001) for h = 0.5, 0.75, 1.0, 1.5, 2.0, 2.5, 3.0, 4.0, 5.0, 6.0, and 8.0 m.

Equation (21), derived from experimental measurements reported in the literature (Blanchard, 1967; Epema and Riezebos, 1983; Gunn and Kinzer, 1949; Jayawardena and Rezaur, 2000; Laws, 1941), shows performance consistent with Equation (10) for $D < 0.55$ cm and is more reliable than Equation (10) for $D > 0.55$ cm.

By combining Equations (11), (19), and (21), and analytically solving the integral, the final expression for the kinetic power estimation, as a function of the rainfall intensity and the Gamma shape (μ) and scale (Λ) parameters, is obtained:

$$P_n = 10^{-6} \frac{9.5^2}{7.2} \rho \Lambda^{4+\mu} \left[\frac{1}{\Lambda^{4+\mu}} - \frac{2}{(6+\Lambda)^{4+\mu}} + \frac{1}{(12+\Lambda)^{4+\mu}} \right] I \quad (22)$$

Accordingly, combining Equations (11), (20), and (21), and solving the integral, the rainfall momentum can be estimated as a function of I, μ, and Λ:

$$M = 10^{-6} 2.64 \rho \left[1 - \frac{\Lambda^{4+\mu}}{(6+\Lambda)^{4+\mu}} \right] I \quad (23)$$

The theoretical derivations of Equations (22) and (23) marked a significant advancement from traditional empirical approaches, revealing that the kinetic energy per unit volume of rainfall (P_n/I) and the momentum per unit volume of rainfall (M/I) are strictly dependent on the intrinsic microphysical structure of the precipitation event (μ and Λ parameters of the DSD) (Carollo et al., 2018a; Carollo and Ferro, 2015).

The validity of this theoretical approach was rigorously tested against a large database of natural rainfall observations collected using the same optical disdrometer (Eigenbrodt, Model ODM 470) in Palermo (Italy), Sparacia (Italy), and

El Teularet (Spain) experimental sites (Carollo et al., 2016b, 2018b, 2023; Carollo and Ferro, 2015).

Further theoretical analysis by Carollo et al. (2017; 2018a) demonstrated that, under the assumption that the exponential Marshall-Palmer distribution, referred to unit area and time, is formally identical to a Gamma distribution with a shape parameter $\mu = 0.67$, the resulting P_n/I and M/I relationships theoretically depend only on the median volume diameter:

$$P_n = 10^{-6} 12.53 \rho \left[1 - \frac{2}{\left(\frac{6D_0}{4.34} + 1\right)^{4.67}} + \frac{1}{\left(\frac{12D_0}{4.34} + 1\right)^{4.67}} \right] I \qquad (24)$$

$$M = 10^{-6} 2.64 \rho [1 - (1.38 D_0 + 1)^{-4.67}] I \qquad (25)$$

Moreover, the comparison between Equation (24) and experimental (D_0, P_n/I) pairs from Bogor (Indonesia), Corvallis (Oregon, USA), El Teularet (Spain), Franklin (North Carolina, USA), Hong Kong (China), Island Beach (New Jersey, USA), Majuro Atoll (Marshall Islands), Northern Ethiopian Highlands (Ethiopia), Palermo (Italy), and Woody Island (Alaska, USA) (Carollo et al., 2017; Jayawardena and Rezaur, 2000; Mueller and Sims 1967a, 1967b, 1967c, 1967d, 1968a, 1968b; Nyssen et al., 2005) confirms that the theoretically deduced Equation (24) is site-independent. Accordingly, Carollo et al. (2018a) obtained the same conclusion by comparing Equation (25) with experimental (D_0, M/I) pairs from the same literature datasets.

Carollo et al. (2016b) and Carollo and Ferro (2015) used both the Maximum Likelihood method (ML) and the Method of Moments (MM) to estimate the shape and scale parameters of the Gamma distribution. In particular, the ML approach determines μ and Λ by maximizing the likelihood of the observed drop diameters, providing statistically efficient estimates but requiring iterative computation. Conversely, the MM was applied following two alternative formulations: in MM_1, μ and Λ are derived from the third and fourth order moments of the measured DSD, thus exploiting information linked to drop volume, while in MM_2, the parameters are obtained from the sample mean and variance of the drop diameters, allowing a closed-form analytical solution. According to the authors (Carollo et al., 2016b;

Carollo and Ferro, 2015), MM_1 is particularly suitable for hydrological and soil erosion applications, providing more physically consistent estimates in terms of rainfall water content and kinetic energy, while MM_2 is more sensitive to measurement noise and to the presence of large drops, which may lead to less stable estimates of the Gamma parameters. These findings further underscore the central role played by D_0 in characterizing rainfall erosivity.

It must be stressed that the median volume diameter is not a directly observable variable, as it can only be obtained from measured DSDs. Several authors have therefore proposed empirical formulas to infer D_0 from more readily available rainfall or radar variables (Bringi et al., 2012; Raupach, 2016; Uijlenhoet and Stricker, 1999; Westbrook et al., 2010), thereby enabling estimation of D_0 where disdrometer data are unavailable. However, such empirical estimators are typically derived from local datasets and thus retain site-specific biases and uncertainties. Consequently, using these empirical formulations to estimate D_0 introduces errors of the same nature and order previously identified for intensity-based erosivity proxies.

1.2.3.3 Lognormal Distribution

An alternative formulation to the Exponential and Gamma distributions is the Lognormal distribution (Feingold and Levin, 1986; Levin, 1961; Mueller and Sims, 1966):

$$N_{(D)V}dD = \frac{N_T}{\sqrt{2\pi\ ln\sigma_g D}} exp\left[-\frac{\ln^2\left(\frac{D}{D_g}\right)}{2\ln^2\sigma_g}\right]dD \tag{26}$$

in which N_T (m^{-3}) is the concentration of drops per unit volume of air, σ_g (–) is the geometric standard deviation, and D_g (cm) is the geometric mean diameter. Thus, its parameters have direct physical interpretations in terms of drop coalescence and breakup processes. They can be calculated as (Feingold and Levin, 1986):

$$N_T = \int_0^\infty N_{(D)V}dD \tag{27}$$

$$\ln^2\sigma = \overline{\left(\ln D - \ln D_g\right)^2} \tag{28}$$

$$\ln D_g = \overline{\ln D} \tag{29}$$

Equation (26) has been applied in several regional studies (e.g., Israel and West Africa), where lognormal functions were found to provide good fits to observed DSDs (Feingold and Levin, 1986; Markowitz, 1976; Ochou et al., 2007).

However, such performance is generally restricted to specific climatic and conditions, and its applicability is less general than that of the Gamma formulation, especially across a wide range of rainfall types and intensities.

1.2.3.4 Weibull Distribution

Another statistical formulation adopted for the raindrop size distribution fitting is the Weibull distribution (Weibull, 1951), first proposed by Sekine and Lind (1982):

$$N_{(D)}dD = N_0 \frac{\eta}{\sigma}\left(\frac{D}{\sigma}\right)^{\eta-1} exp\left[-\left(\frac{D}{\sigma}\right)^{\eta}\right] dD \tag{30}$$

where N_0 (m^{-3}), η (–), and σ (cm) are the three parameters of the Weibull distribution. When $\eta = 1$, Equation (30) is identical to the exponential distribution of Equation (6).

Using a limited dataset (Laws and Parsons, 1943; Sander, 1975; Wickerts, 1982), Sekine and Lind (1982) stated that N_0 is constant and equal to 1000 m^{-3}, while η and σ depend on I, according to the following relationships:

$$\eta = 0.26\, I^{0.44} \tag{31}$$

$$\sigma = 0.95\, I^{0.14} \tag{32}$$

A significant theoretical advancement was provided by Mualem and Assouline (1989): unlike previous models, based primarily on curve-fitting, the authors analytically derived the Weibull distribution by modeling the DSD evolution as a stochastic process of random fragmentation. Assuming the probability of drop breakup is proportional to drop volume, they demonstrated that the DSD asymptotically approaches a Weibull distribution.

Furthermore, Mualem and Assouline (1989) showed that DSDs from several geographic locations (e.g., USA, Rhodesia, Israel) tend to converge toward a common asymptotic form that is largely independent of rainfall intensity. This suggests that the Weibull distribution provides a physical representation of the

mechanisms governing DSD evolution, in contrast with empirical formulations. Consequently, this distribution appears particularly suitable for establishing a robust link between DSD and the energetic variables required for accurate soil erosion modelling.

Specifically, for the Weibull distribution, the cumulative probability $P_{(D)}$ that a raindrop diameter is smaller than a given value D can be expressed as:

$$P_{(D)} = 1 - \exp\left(-\left(\frac{D}{\sigma}\right)\right)^{\eta} \tag{33}$$

This formulation highlights that the $P_{(D)}$ depends exclusively on the scale, σ (cm), and shape, η (–), parameters of the Weibull distribution. Accordingly, the main statistical descriptors of the DSD, including the mean diameter, $\mu_{(D)}$ (cm), the standard deviation, $\sigma_{(D)}$ (cm), and the median diameter, D_{50} (cm), can also be expressed as functions of σ and η:

$$\mu_{(D)} = \frac{\sigma}{\eta}\Gamma\left(\frac{1}{\eta}\right) \tag{34}$$

$$\sigma_{(D)} = \frac{\sigma}{\eta}\left[2\eta\Gamma\left(\frac{2}{\eta}\right) - \Gamma^2\left(\frac{1}{\eta}\right)\right]^{0.5} \tag{35}$$

$$D_{50} = \sigma(log2)^{1/\eta} \tag{36}$$

More recently, Carollo et al. (2026) demonstrated that the median volume diameter, D_0 (cm), can also be expressed as a function of σ and η:

$$D_0 = \sigma\left(\frac{3}{\eta} + 0.67\right)^{1/\eta} \tag{37}$$

Equations (34)–(37) therefore indicate that the main diameter-related properties of rainfall can be fully characterized by the scale and shape parameters of the Weibull distribution.

1.3 Simulated Rainfall

1.3.1 The Role of Rainfall Simulators in Soil Erosion Research

The study of soil erosion, hydrological processes, and surface runoff dynamics requires a rigorous understanding of precipitation characteristics. However, reliance on natural rainfall for such investigations presents substantial methodological constraints due to its stochastic nature.

Natural precipitation is characterized by high spatiotemporal heterogeneity, unpredictability, and intermittency (Battany and Grismer, 2000; Meyer, 1988). This variability impedes experimental controllability and reproducibility, which are essential for establishing robust cause/effect relationships in hydrological and geomorphic analyses (Hou et al., 2026).

To address these obstacles, rainfall simulators (RS) have emerged as pivotal technological solutions. The primary importance of rainfall simulators in erosion research lies in their capability to reproduce, in a rapid and controlled way, key precipitation characteristics such as rainfall intensity, kinetic energy, and momentum (Bosio et al., 2023; Carollo et al., 2024a; Caruso et al., 2025; Iserloh et al., 2013a; Meyer, 1994; Neff, 1979; Serio et al., 2024, 2025). Therefore, applying simulated rainfall to experimental plots, under conditions that closely mimic natural events, offers a cost-effective alternative to long-term field observations, enabling researchers to collect data when and where it is needed, without relying on the unpredictability of natural storms (Neff, 1979).

RSs can be employed for a variety of applications, adapting to specific research topics including soil erosion (Hamed et al., 2002; Iserloh et al., 2013a; Mhaske et al., 2019), hydrology (Chouksey et al., 2017; Martínez-Murillo et al., 2013), water infiltration (Amerman, 1979; Ogden et al., 1997; Roth et al., 1985), runoff and sediment transport (Abudi et al., 2012; Boulange et al., 2019; Simelane et al., 2024), heritage surfaces erosion (Fernández-Raga et al., 2022; Richards et al., 2019), soil texture (Arunrat et al., 2022; Bharali, 2021), the roles of runoff and splash erosion in soil degradation and landform development (Aksoy et al., 2012; Fernández-Raga et al., 2017; Ma et al., 2022; Rodrigo-Comino, 2021), the assessment of environmental impacts (Biswas et al., 2017; Eckley and Branfireun, 2009; Saber et

al., 2019) or validating erosion models like the USLE and WEPP (Fu et al., 2012; Musa et al., 2021).

Since the first developments in the 1930s and 1940s, which initially relied on simple drop-forming devices inspired by irrigation systems, rainfall simulators have progressively evolved into increasingly refined, pressurized configurations as understanding of natural rainfall physics advanced throughout the mid-20th century (Hou et al., 2026).

In this context, researchers have developed over a hundred different models worldwide, most designed for small experimental plots (< 5 m^2, and in most cases < 1 m^2) (e.g., Abudi et al., 2012; Adams et al., 1957; Aksoy et al., 2012; Alves Sobrinho et al., 2008; Battany and Grismer, 2000; Birt et al., 2007; Blanquies et al., 2003; Bosio et al., 2023; Cerdà et al., 1997; Clarke and Walsh, 2007; Cottenot et al., 2021; Covert and Jordan, 2009; De Ploey, 1981; Etheridge, 2023; Farres, 1987; Fernández-Raga et al., 2022; Hudson, 1965; Humphry et al., 2002; Imeson, 1977; Iserloh et al., 2013a; Kamphorst, 1987; Lassu et al., 2015; Loch et al., 2001; Luk, 1985; Martínez-Mena et al., 2001; Mhaske et al., 2019; Nadal-Romero and Regüés, 2009; Neal, 1938; Norton, 1987; Poesen et al., 1990; Regmi and Thompson, 2000; Regüés and Gallart, 2004; Rončević et al., 2025; Roth et al., 1985; Serio et al., 2025; Torri et al., 1999; Vergni et al., 2018; Wilm, 1943).

The ongoing development of RSs underscores the persistent interest in these devices for soil erosion research and related hydrological studies. But it also reveals a tendency among researchers to develop *ad hoc* systems tailored to study specific hydrological and erosive processes, rather than concentrate efforts toward a *universal* simulator (Živanović et al., 2022).

For decades, the literature has emphasized the need for standardization to facilitate the comparability between experiments. This can be achieved by homogenizing rainfall characteristics such as drop size distribution, drop impact velocity, and rainfall intensity (Bubenzer, 1979; Clarke and Walsh, 2007; Lascelles et al., 2000; Ries et al., 2013; Tiller et al., 2025)

However, to date, the development of a *universal* RS appears to be a utopian goal, given the RS's broad range of applications and the prohibitive conditions for simultaneously achieving realistic values for rainfall kinetic energy, impact

velocity, distribution uniformity, and DSD characteristics (Meyer, 1994, 1988). Indeed, only a few recognized protocols have provided standardized procedures for rainfall simulator calibration, testing configuration, and data collection and analysis, and these primarily address specific research needs, such as rolled erosion control products (Advancing Standards Transforming Markets, 2019; Manning, 2021; Manning et al., 2023; Midha et al., 2017; Ricks et al., 2019)

As a result, rainfall simulators exhibit substantial variability in their hydraulic design (e.g., nozzle type, operating pressure, drop-forming mechanisms), plot configuration and scale, rainfall characteristics (including intensity range, drop-size distribution, terminal velocity, and resulting kinetic energy), spatial and temporal uniformity, and operational protocols such as calibration procedures and duration of application (Hou et al., 2026; Meyer, 1979).

Nevertheless, RSs are generally categorized by their drop-generation mechanism into two main categories: drip-type and pressurized systems (Rončević et al., 2023). Drip-type rainfall simulators (DRS) utilize capillary tubes or needles to form drops with zero initial velocity. While their simple design offers cost-effectiveness and precise control over drop size, a significant limitation is the substantial fall height required for drops to approach terminal velocity (Fernández-Raga et al., 2022; Iserloh et al., 2012; Koch et al., 2024; Laws, 1941; Meyer, 1979; Serio et al., 2024; van Boxel, 1998). This physical parameter is defined as the equilibrium speed attained when the aerodynamic drag force balances the downward force of gravity (Serio et al., 2019a). Furthermore, DRS systems are typically restricted to small-scale experimental setups and tend to produce repetitive impacts on fixed points; consequently, achieving a realistic spatial distribution often requires modifications, such as the use of meshes to induce drop breakup and randomization (Bowyer-Bower and Burt, 1989; Clarke and Walsh, 2007; Cottenot et al., 2021; Naves et al., 2020; Regmi and Thompson, 2000).

Pressurized rainfall simulators (PRS) employ pumps and spray nozzles to generate a more complex rainfall pattern composed of drops with initial velocities. Unlike drip-type systems, this mechanism allows pressurized simulators to more closely approximate the kinetic energy and momentum of natural rain, even at the limited nozzle heights typical of field or laboratory setups (Meyer, 1979). By adjusting

nozzle types and hydraulic pressure, these systems offer the flexibility to generate a wide range of rainfall intensities and drop-size distributions, representing a powerful tool for hydrology and soil-erosion research (Birt et al., 2007; Ricks et al., 2019; Serio et al., 2025). However, they require careful design and maintenance and face limitations in water-use efficiency (Aksoy et al., 2012; Rončević et al., 2025).

1.3.2 Rainfall Simulator Characterization and Validation Methods

The accurate characterization of RSs is a prerequisite for hydrological and soil erosion research, as it ensures data reliability and facilitates the reproducibility and comparability of results across studies (Iserloh et al., 2013a; Kavian et al., 2018; Koch et al., 2024; Ries et al., 2009). Common approaches for characterizing these devices, whether DRS or PRS, typically include the use of rain collectors to quantify rainfall intensity and spatial uniformity, photographic techniques to determine diameters and fall velocity of individual raindrops, and disdrometers to evaluate the PSVD (Koch et al., 2024; Zemke, 2017). However, the choice of a particular characterization method can significantly influence the measured rainfall parameters, potentially introducing variability into the results and highlighting the need for standardized protocols (Caruso et al., 2025; Green and Pattison, 2022; Isidoro et al., 2022; Lazarus et al., 2023).

The correct functioning of a simulator implies that the rainfall distribution over the investigated plot area should be as uniform as possible. Achieving a high degree of spatial uniformity over the experimental plot is not intended to reproduce the natural variability of precipitation, which is inherently non-uniform and stochastic (Lu et al., 2025). Rather, the controlled, uniform application of rainfall ensures that the same precipitation amount and characteristics are applied across all parts of the plot, thereby enabling reproducible, comparable results across trials and studies.

To assess the spatial uniformity of simulated rainfall, the use of rain collectors and the evaluation of the Christiansen Uniformity Coefficient (CUC, %) (Christiansen, 1942) are the standard methods (Carollo et al., 2025, 2024b; Iserloh et al., 2013a). CUC is defined as:

$$\mathrm{CUC} = 100\left(1 - \frac{\sum_{i=1}^{n}|I_c - I_S|}{n\, I_S}\right) \tag{38}$$

where I_c (mm h^{-1}) is the rainfall intensity of each i-th rain collector, I_S (mm h^{-1}) is the mean simulated rainfall intensity across the tested area, and n_c is the number of employed collectors. Therefore, as the CUC value approaches 100%, the rainfall pattern becomes increasingly uniform.

It is acknowledged that the number, spatial arrangement, and physical characteristics of rainfall collectors, such as their size and shape, directly affect the representation of rainfall distribution (Green and Pattison, 2022). In other words, the CUC method is susceptible to the sampling resolution, thus reflecting not only the simulator's actual performance, but also the performance of the selected testing procedure (Caruso et al., 2025).

Despite these limitations, the CUC coefficient remains the standard metric for evaluating RS performance. A threshold of 80% is commonly accepted as the benchmark for considering the simulated rainfall spatial distribution good (Esteves et al., 2000; Iserloh et al., 2013a; Mhaske et al., 2019; Salem and Meselhy, 2021). However, for large-scale plot applications, a lower threshold of 70% is often accepted since wind effects and overlapping nozzle patterns make it significantly more challenging to achieve such high degrees of spatial uniformity (Luk et al., 1993; Rodrigo-Comino, 2021)

Other authors (e.g., Fernández-Raga et al., 2022; Serio et al., 2025) also refer to the American Society of Agricultural and Biological Engineers (ASABE) classification (ASABE Standard, 2014), originally developed for irrigation systems. According to the latter, drippers and nozzles can be classified as follows: unacceptable (CUC < 60%), poor (60% ≤ CUC < 70%), fair (70% ≤ CUC < 80%), good (80% ≤ CUC < 90%), and excellent (CUC ≥ 90%).

A particularly simple and effective technique for determining the diameter of raindrops generated by DRS devices is the weighing method (Carollo et al., 2024a). Indeed, for fixed operating conditions, such as the pressure head acting on the capillary/needle and the water temperature, DRS systems typically generate drops of constant size. Consequently, by measuring the weight of a known number of raindrops and assuming a spherical drop shape, the mean raindrop diameter can be

easily determined. This approach not only provides a precise measurement but also offers a robust baseline for validating the accuracy of alternative diameter measurement techniques.

As already observed for natural rainfall (Section 1.2), characterizing the erosive potential of a precipitation event requires going beyond merely assessing rainfall intensity and the spatial uniformity of water volumes. Thus, a rigorous simulation of soil erosion processes requires replicating a realistic PSVD, which directly determines the amounts of P_n and M transferred to the soil surface.

Consequently, the validation of RS devices requires specific protocols to assess these microphysical properties. Indeed, applying standard measurement techniques to simulated rainfall presents unique challenges compared to natural precipitation, primarily due to the physical constraints of experimental setups.

A critical limitation in rainfall simulation concerns raindrop fall velocity. Specifically, simulated drops generated by DRS are released with zero initial velocity. To reach the terminal velocity typical of natural rainfall, these drops require a substantial fall height, depending on drop diameter. According to van Boxel (1998), the maximum stable diameter a droplet can attain before fragmenting is approximately 8 mm, and a fall height of roughly 10 m is required for drops of this size to achieve between 95% and 99% of their terminal velocity. Since laboratory environments and portable field setups rarely offer sufficient vertical space, the resulting droplets strike the soil with lower kinetic energy than natural rainfall.

Conversely, PRS produces drops with an initial velocity determined by the hydraulic pressure at the nozzle, facilitating the achievement of velocities closer to terminal values even under laboratory conditions and with reduced fall heights compared to gravity-driven systems (Iserloh et al., 2013a).

However, characterizing these two systems poses contrasting methodological challenges. Determining the fall velocity in DRS devices is methodologically more straightforward because drop generation is deterministic and occurs at fixed positions, unless drop fragmentation systems are employed (Clarke and Walsh, 2007; Naves et al., 2020; Regmi and Thompson, 2000). This predictability allows for the effective use of photographic methods (Carollo et al., 2024; Serio et al.,

2024). Nevertheless, manual processing of photographic data remains time-consuming, labor-intensive, and subject to operator bias (Chigier, 1983). Furthermore, errors in velocity estimation arising from frame-rate limitations, motion blur, depth-of-field constraints, perspective distortion, and uncertainties in drop identification, challenges often shared with automated image-processing techniques, can significantly propagate to kinetic energy calculation. Finally, the acquisition of high-speed image sequences is notably memory-intensive, often imposing significant constraints on data storage capacity and transfer rates.

Conversely, characterizing PRS devices is significantly more complicated. Indeed, in addition to the abovementioned sources of errors, these systems generate drops which are randomly expelled in a turbulent spray with a wide range of initial velocities and trajectories, making image-processing techniques difficult to apply due to depth-of-field issues and drop overlap (Fernández-Raga et al., 2021).

For these reasons, laser optical disdrometers are widely used to characterize rainfall simulators, as they offer continuous, automated, and reliable characterization capabilities (Kathiravelu et al., 2016). However, their application in laboratory and simulator settings is not devoid of issues. Several studies have reported significant limitations in using optical disdrometers to characterize artificial rainfall, especially under conditions of high drop concentration and variable drop-size/velocity regimes (Gires et al., 2020). Moreover, in the context of PRS, the hydraulic pressure driving the nozzle flow can induce excessive atomization: under such conditions, and particularly at elevated rainfall intensities, optical disdrometers may incur relevant measurement errors, often resulting in the systematic underestimation of drop counts and misclassification of drop sizes and velocities. These errors are primarily attributed to sampling limitations such as overlapping drops in the laser beam or signal-to-noise issues, i.e., the instrument's inability to distinguish the smallest droplets (Fraile et al., 2013).

Furthermore, a critical source of bias arises from the instruments' internal processing algorithms, which are typically developed and calibrated to characterize natural rainfall (Saha and Testik, 2023). For instance, disdrometers typically reject particles exhibiting unrealistic diameter-velocity combinations relative to standard terminal-velocity relationships (Saha and Testik, 2023). Thus, such filters can

erroneously exclude valid drops or misclassify them, leading to distorted bulk variables such as rainfall intensity and kinetic energy, underscoring the need to rigorously monitor and correct for these systematic measurement biases to ensure data reliability (Saha and Testik, 2023; Tokay et al., 2001).

Given the inherent challenges in reproducing realistic kinetic energy conditions in laboratory settings with both DRS and PRS, several studies suggest applying rainfall intensities exceeding those typically observed in nature to induce comparable erosive responses (Fazlina et al., 2018; Palmeri et al., 2025; Schiettecatte et al., 2005). While this intensity-compensation strategy can effectively align natural energetic inputs, it warrants careful consideration of the hydrological representativeness of the simulation (Dhakal and Sidle, 2004). Indeed, the application of intensities exceeding natural occurrence rates might influence soil surface dynamics, such as ponding times, infiltration, and interrill erosion (Palmeri et al., 2025; Schiettecatte et al., 2005).

Regardless of whether the experimental goal is to simulate realistic volumetric or kinetic energy conditions, the resulting DSD must approximate those observed in natural rainfall, thereby avoiding the monodisperse distributions typical of some DRS systems or the excessively atomized sprays characteristic of some PRS.

Despite the aforementioned limitations, disdrometers remain the most suitable instruments for such characterization. However, it is well-established in the literature that commonly used optical disdrometers, such as Parsivel^2 and LPM, tend to underestimate measured fall velocity values, at least under natural rainfall conditions (Angulo-Martínez et al., 2018; Johannsen et al., 2020b). Conscious of this systematic bias, researchers typically adopt two correction strategies. The first involves applying post-processing filters to the raw PSVD data to exclude diameter-velocity combinations falling outside a specific validity band (e.g., ±20%) relative to established theoretical relationships (e.g., Atlas et al., 1973; Atlas and Ulbrich, 1977; Beard, 1976; Ferro, 2001; Gunn and Kinzer, 1949). The second involves disregarding the measured velocity distribution entirely and replacing it with theoretical terminal velocity values directly derived from the measured diameters, using the same established literature relationships.

While this strategy may be justifiable for correcting instrumental underestimation with natural rainfall, it is methodologically inapplicable to laboratory rainfall simulations, where terminal velocity is not attained.

Consequently, to address this critical gap, a new relationship specifically valid for ordinary laboratory or field conditions, capable of reliably estimating the actual fall velocity of drops as a function of both the diameters measured by a disdrometer and the selected fall height, is needed to enable an accurate simulator characterization.

1.4 Objectives of the Thesis

The overall objective of this doctoral research is to improve the estimation of rainfall erosivity and related energetic properties by integrating observations from natural rainfall and laboratory-simulated precipitation. The research focuses on raindrop population descriptors, energetic variables, measurement techniques, and rainfall simulation systems, with the aim of improving the accuracy, reliability, and experimental consistency of erosion assessment methods. To achieve this general aim, the study is structured around specific objectives.

A first objective is to analyze rainfall erosivity by combining simultaneous measurements of rainfall DSD and plot-scale soil loss. The purpose is to critically assess traditional intensity-based approaches in comparison with alternative physically based methods, and to determine whether disdrometer-derived rainfall descriptors offer a more reliable representation of erosive potential.

A second objective is to verify the reliability and robustness of the Weibull distribution for describing natural DSDs detected in the Mediterranean environment. Moreover, its applicability for deriving theoretical relationships to estimate energy-related variables, such as kinetic power and momentum, is tested.

A third objective is to advance a patented method for estimating the energetic characteristics of rainfall based on simplified, easily measurable variables. The proposed approach combines rainfall intensity, the number of impacting drops, and descriptors derived from the rainfall momentum distribution, using the Weibull distribution and the Method of Moments to estimate kinetic power and momentum without requiring complete disdrometric measurements.

A fourth objective concerns the characterization of laboratory rainfall simulators operating under a wide range of experimental conditions. The study evaluates different types of simulators through an integrated approach that combines established calibration methodologies with high-resolution disdrometer measurements. Both drip-type systems, characterized by highly controlled operating conditions, and pressurized simulators, capable of generating more complex rainfall patterns under both sub-terminal and terminal-velocity conditions, are considered. Within this framework, a customized rainfall simulator was also

developed and implemented at the University of Palermo as an experimental tool for future investigations on plot-scale soil loss.

A fifth objective is to develop and validate an empirical relationship for estimating raindrop fall velocity under laboratory rainfall conditions, explicitly accounting for drop diameter and fall height. The proposed formulation is intended for sub-terminal fall-velocity regimes and is tested across a wide range of experimental configurations, including both drip-type and pressurized rainfall simulators.

A sixth and final objective is to evaluate the performance and reliability of the Parsivel^2 optical disdrometer under laboratory rainfall conditions, which differ from the natural rainfall environment for which the instrument was originally designed. The study investigates whether the limitations reported in the literature for natural rainfall measurements, particularly the tendency to underestimate raindrop fall velocities, also occur in simulated rainfall. In addition, the analysis examines the accuracy of Parsivel^2-derived rainfall descriptors, including drop counts, rainfall intensity, and drop diameter distributions, under different experimental configurations generated by both drip-type and pressurized rainfall simulators.

Therefore, the overall aim regarding simulated rainfall is to synthesize the experience gained from these diverse experimental setups and established assessment methodologies in order to propose practical guidelines for the standardized and reliable characterization of rainfall simulators.

2 MATERIALS AND METHODS

2.1 Study Areas and Natural Rainfall Data Collection

This chapter describes the experimental methodology adopted to investigate natural rainfall and its associated erosive effects. The approach integrates (i) theoretical analyses based on drop size distributions (DSDs) measured with an optical disdrometer, and (ii) investigations in which disdrometer-derived DSD measurements are combined with concurrent plot-scale soil loss observations to evaluate rainfall erosivity.

To this end, three experimental sites characterized by a Mediterranean climate were monitored: Palermo (Italy), El Teularet (Spain), and the Sparacia experimental area (Italy) (Figure 1). The Palermo and El Teularet sites were dedicated exclusively to the collection of high-resolution rainfall data, constituting the core dataset for the analysis of the Weibull distribution and the derivation of theoretical energetic relationships. Conversely, the Sparacia station provided both rainfall monitoring and direct measurements of soil loss at the plot scale, enabling a direct comparison between soil erosion and disdrometer measurements.

Figure 1. Location of the study sites: Palermo and Sparacia (Italy) and El Teularet (Spain).

2.1.1 Experimental Sites: Geographical and Climatic Context

The Palermo experimental station is located within the urban area of the city, at the Department of Agricultural, Food, and Forest Sciences of the University of Palermo (Metropolitan City of Palermo, Sicily, Italy). The site is located at an elevation of 35 m a.s.l. and is characterized by a typical Mediterranean climate, with hot, dry summers and mild, wet winters. The average annual temperatures range between 15°C and 22°C, while rainfall, mainly concentrated in autumn and winter, shows a mean annual value of 654 mm. Data collected here provided a representation of coastal rainfall regimes.

During the observation period (from June 2006 to April 2014), the site was equipped with an Eigenbrodt ODM 470 optical disdrometer (Eigenbrodt GmbH & Co., 2007) (Figure 2) for the continuous monitoring of rainfall intensity and DSDs. Although the station is also equipped with two experimental plots (2×7 m) for soil erosion measurements, these facilities were not employed in the present investigation, as the analysis at this site was restricted exclusively to disdrometric data.

Figure 2. View of the rainfall monitoring equipment at the Palermo study site (Italy).

The El Teularet experimental station is located in the Sierra de Enguera (Valencia, Valencian Community, Spain), at an elevation of approximately 760 m a.s.l. The local climate is Mediterranean. Mean annual rainfall in the study area ranges from 479 mm (recorded at the Enguera, Las Arenas meteorological station) to 590 mm (at the Enguera Confederación Hidrográfica del Jucar station). Precipitation is distributed relatively homogeneously across spring, autumn, and winter, whereas the summer season is extremely dry due to high temperatures and negligible rainfall (García-Orenes et al., 2009). Mean annual temperatures range from 12.7 °C to 14.2 °C. Despite the dry summers, this climatic setting is frequently subjected to high-intensity convective storms, particularly during transition periods, making it highly relevant for erosivity studies.

During the observation period (from July 2015 to May 2016), the station was equipped with the same optical disdrometer used at the Palermo site (Figure 3). This consistency in instrumentation ensures full comparability between the datasets collected at the two different geographical locations, minimizing potential biases due to sensor-specific functions.

Figure 3. View of the ODM 470 disdrometer at the El Teularet experimental station.

The Sparacia experimental area of the Department of Agricultural, Food, and Forest Sciences (University of Palermo) is located in the Sicilian hinterland (Cammarata, Province of Agrigento, Sicily, Italy), at an elevation of approximately 415 m a.s.l. The local climate is semiarid Mediterranean, with an average annual precipitation of roughly 700 mm. The soil is classified as a *Vertic-Haploxerept*, with a clay-dominated texture (62% clay, 33% silt, and 5% sand), making it particularly susceptible to swelling and shrinking cycles and water erosion processes.

While the Sparacia area is also equipped for monitoring hydrological processes at the watershed scale, this study focuses specifically on the plot scale. All plots are maintained in cultivated fallow, with up-and-downhill tillage conducted by a power cultivator 3–4 times per year when the soil is relatively dry.

Rainfall data are measured with a rain gauge located near the plots at 1-min intervals. Furthermore, to ensure data consistency across all experimental sites, the station was equipped with the same optical disdrometer used at Palermo and El Teularet (Figure 4) during the observation period (from March 2017 to December 2019).

Figure 4. Sparacia experimental site: detail of the disdrometer installed downstream of the plots used for event-scale soil loss measurements.

The experimental setup monitors soil loss under varying topographic conditions. Gentler gradients are examined using two plots of 22×2 m^2 (length × width) on a 9% slope. The intermediate condition is represented by a diverse set of plots on a 14.9% slope, including two plots of 18×8 m^2, two standard Wischmeier plots (22×8 m^2), two plots of 33×8 m^2, two plots of 44×8 m^2, and two plots of 11×4 m^2. Finally, steeper slopes are analyzed through four plots of 22×6 m^2: two established on a 22% slope and two on a 26% slope.

Specifically, these last four steep plots were selected for the present investigation. Between September 2017 and April 2020, 10 erosive events were monitored. For these events, 10,960 1-minute DSDs were recorded.

Therefore, event soil loss measured in these bare fallow plots served as the benchmark for comparing the predictive performance of different erosivity indices. In particular, the observed plot-scale soil loss was compared with both the standard USLE-based R_e index, in which rainfall kinetic energy is empirically estimated from the maximum 30-min rainfall intensity (I_{30}), and a new R_e^* index derived from a revised formulation in which rainfall kinetic energy and intensity are evaluated at their actual temporal resolution thanks to disdrometric measurements.

2.1.2 Natural Drop Size Distribution Monitoring

2.1.2.1 Disdrometric Data Processing

At all three experimental sites, natural rainfall characteristics were monitored using the same optical disdrometer, model ODM 470, by Eigenbrodt (Figure 5).

This instrument is particularly renowned for its reliability under high-wind conditions and adverse weather, making it suitable even for maritime applications. It consists of a U-shaped frame housing a transmitter and a receiver, defining a cylindrical control volume with a length of 120 mm and a diameter of 22 mm. A distinctive feature of the ODM series is the aerodynamically optimized housing combined with a wind vane, which aligns the instrument with the wind direction. This alignment is crucial as it keeps the cylindrical sensitive volume perpendicular to the local airflow, making the measurement independent of the particle incidence angle and immune to local up- and downdraft effects (Lempio et al., 2007). Additionally, the instrument is equipped with an internal heating system to prevent

condensation and icing on the optical lenses, ensuring continuous data quality even under high humidity or low-temperature conditions.

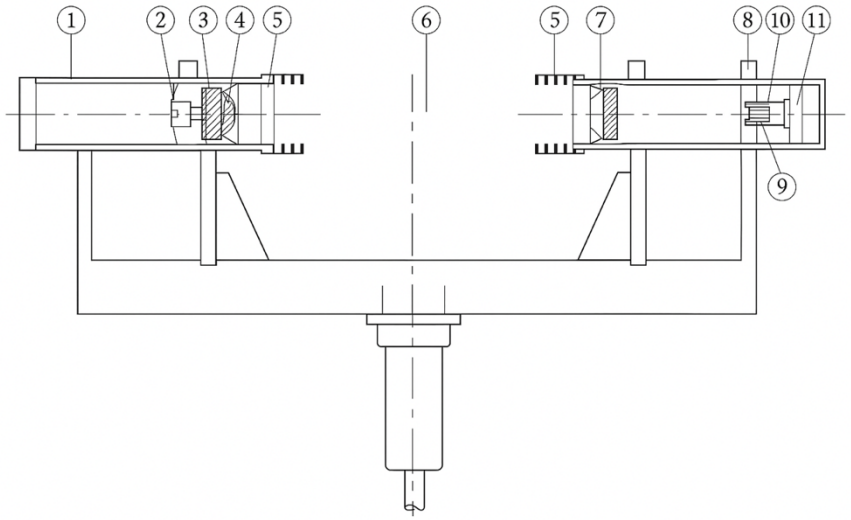

Figure 5. Cross-section of the optical disdrometer model ODM 470 by Eigenbrodt. Legend: electronics (1), light emitting diode (2), lens system (3), window (4), baffles (5), sensitive volume (6), achromatic collector lens (7), optical blend (8), photo diode (10), electronic compartment (11). Image modified from Grossklaus et al. (1998).

The measurement principle relies on light extinction. The transmitter is equipped with a 100-mW infrared diode (880 nm wavelength) and a sophisticated optical system comprising achromatic collector lenses and optical blends. This configuration ensures a highly uniform light barrier within the control volume, minimizing optical aberrations and ensuring homogeneous sensitivity throughout the sampling area. When a raindrop passes through this volume, it occludes a portion of the light beam, causing a voltage drop in the receiver proportional to the drop's cross-sectional area. The ODM 470 detects raindrops in the range of 0.50 mm to 6.00 mm, classifying each drop into 128 diameter classes with a resolution of 0.05 mm.

To optimize data acquisition, the system is controlled by an external rainfall detector with a control volume of 12×2.5 cm^2, i.e., an Infrared Sensor System (IRSS) model IRSS88 by Eigenbrodt, which activates the disdrometer upon detecting incipient rainfall (defined as at least 5 drops in 90 s) and switches it off after a 60-second dry interval. Data are then aggregated at a 1-minute temporal resolution via a Data Converter and Power Supply (DCPS) unit.

From the raw DSD measured by the instrument, the number of drops and rainfall intensity for each recorded minute can be determined directly. Moreover, to exclude rainfall events with negligible erosive power and DSDs with insufficient sample sizes, a filtering criterion was applied: only DSDs characterized by a rainfall intensity greater than 0.5 mm h^{-1} and at least 20 occupied diameter classes were retained for analysis. Specifically, the rainfall intensity measured by the ODM 470, I_{ODM} (mm h^{-1}), can be obtained as follows:

$$I_{ODM} = \frac{3.6 \times 10^9}{A_{ODM}\, t} \frac{\pi}{6} \sum_{i=1}^{128} (10D_i)^3 N_i \tag{39}$$

in which A_{ODM} (m^2) is the disdrometer sampling surface, equal to 0.00264 m^2 for the ODM 470, t (s) is the sampling interval, equal to 60s for the present investigation, N_i (–) is the number of drops of the i-th diameter class, D_i (cm) is the mean diameter of the i-th diameter class, and 3.6×10^9 is a conversion factor.

Finally, although the device records the time of flight through the control volume, it does not provide explicit drop velocity data. Consequently, to calculate the rainfall kinetic power or momentum, it is necessary to associate the measured DSD with a literature-based terminal velocity law. For the present investigation, the kinetic power related to the ODM 470 disdrometer, $P_{n,ODM}$ (J m^{-2} s^{-1}), has been determined as follows:

$$P_{n,ODM} = \frac{\pi\rho}{12\, t\, A_{ODM}} \sum_{i=1}^{128} \left(\frac{D_i}{100}\right)^3 {V_{(D)}}^2 N_i \tag{40}$$

where $V_{(D)}$ (m s^{-1}) is calculated by Equation (21).

Similarly, the rainfall momentum, M_{ODM} (N m^{-2}), is obtained from the ODM 470 raw DSD as:

$$M_{ODM} = \frac{\pi\rho}{6\, t\, A_{ODM}} \sum_{i=1}^{128} \left(\frac{D_i}{100}\right)^3 V_{(D)} N_i \tag{41}$$

From the ratio between Equations (39) and (40), multiplied by a factor of 36 to express the specific kinetic energy in the standard unit, the kinetic power per unit volume of rainfall, P_n/I (MJ ha^{-1} mm^{-1}), is obtained. In the following analyses, rainfall intensity and the derived kinetic power and momentum obtained from the measured DSD are treated as measured rainfall variables.

2.1.2.2 Method of Moments and Statistical Evaluation of DSD Fitting using the Weibull Distribution

The present investigation adopts the Weibull distribution as the theoretical framework for describing natural raindrop size distributions (DSDs) measured under Mediterranean climatic conditions. Its applicability to the large DSDs dataset is tested by evaluating both its fitting performance and its implications for estimating rainfall kinetic power and momentum.

The estimation of the Weibull parameters was performed using the Method of Moments (MM) by imposing agreement between the measured and theoretical values of both D_{50} and D_0. The same methodological framework was applied to the widely adopted Gamma distribution (Section 1.2.3.2), enabling a direct and consistent comparison between the two formulations with respect to both fitting performance and rainfall-energetic estimates.

Specifically, the goodness-of-fit of the Weibull and Gamma distributions in reproducing the observed DSDs was evaluated using the coefficient of determination (R^2), computed between the measured and modelled cumulative distributions (Section 2.3). Moreover, the agreement between measured and calculated rainfall kinetic power and momentum was quantified using the Mean Relative Error (MRE), the Mean Absolute Error (MAE), and the percentage of estimates with absolute relative error ≤ 20% (Section 2.3).

2.1.2.3 Application of Method of Moments and Weibull DSD to the Patented Measurement of Rainfall Energetic Characteristics

The Method of Moments is also adopted in this investigation as a validation and assessment tool to evaluate recent advancements in a patented method for estimating rainfall energetic characteristics from simplified, easily measurable variables, namely rainfall intensity, number of impacting drops, and representative mean drop diameters, without requiring full disdrometric information. The performance of these advancements is quantitatively evaluated using the MRE and the MAE (Section 2.3).

2.1.3 Plot-Scale Soil Loss Measurements at the Sparacia Experimental Site

Soil loss measurements were carried out following the field protocol developed and validated at the Sparacia experimental station (Carollo et al., 2016a).

To ensure consistent monitoring of soil erosion processes, the four investigated experimental plots were maintained in continuous bare fallow, using a powered cultivator to perform tillage operations up and down the slope.

During each rainfall event capable of generating surface flow, the runoff and the associated sediment load were intercepted by a collecting gutter installed at the lower end of each plot. This flow is then conveyed into a dedicated storage system consisting of a series of three metallic tanks, each characterized by known geometric dimensions and a storage capacity of approximately 1 m^3 (Figure 6a).

The total runoff volume and soil loss (A_e) were generally quantified immediately after every erosive event, defined as a rainfall event producing measurable runoff and sediment. However, in cases where consecutive rainfall events occurred within short time intervals insufficient to allow for field operations, the measurements were performed cumulatively. Consequently, in such instances, A_e represents the cumulative sediment yield produced between two successive tank emptying operations.

The accurate determination of sediment concentration is a critical aspect of the measurement protocol. Literature highlights that traditional sampling methods (e.g., bottles or beakers plunged into the suspension) often lead to significant underestimation of the actual sediment load due to incomplete mixing and vertical particle stratification (Lang, 1992; Zöbisch et al., 1996). To overcome these limitations, a custom-designed cylindrical sampler (Carollo et al., 2016a) (Figure 6b) is employed at the Sparacia station. This device consists of a 120 cm high brass cylinder (inner diameter 4.75 cm) equipped with a bottom closing valve (guillotine type) fitted with a sealing gasket. This design allows the withdrawal of a full vertical column of the suspension, thereby integrating sediment concentration across the entire water depth and minimizing errors due to stratification.

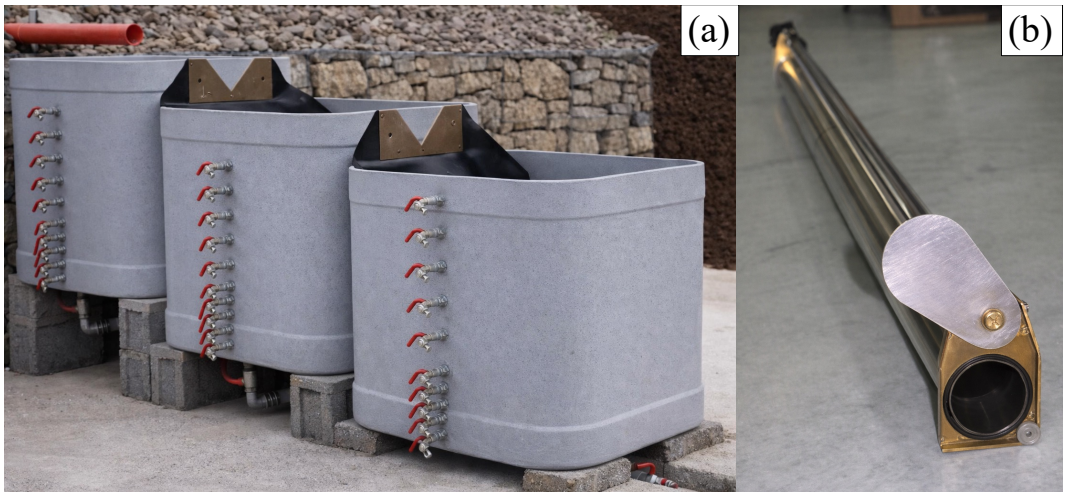

Figure 6. The storage system consisting of a series of three metallic tanks (a) and the cylindrical sampler device (b).

The specific sampling procedure involves the following steps: (i) vigorous stirring of the suspension within the tank to resuspend settled sediments; (ii) extraction of five samples from each tank using the cylindrical sampler. Statistical analysis (Carollo et al., 2016a) has demonstrated that this sample size represents the optimal compromise between measurement reliability and operational feasibility; (iii) laboratory analysis, where the collected samples are oven-dried at 105 °C for 48 hours to determine the dry weight of the solid material.

Simultaneously, the water level in each tank was measured to calculate the total stored runoff volume using the tank's geometry. Finally, the total soil loss for the event was calculated by multiplying the total stored runoff volume by the mean sediment concentration derived from the five samples.

The performance of the linear relationship between event soil loss and rainfall erosivity was evaluated using the Root Mean Square Error (RMSE) and the Nash–Sutcliffe Efficiency Index (NSEI). These metrics quantify the agreement between measured and calculated event soil loss at the Sparacia experimental site. Their formulation and interpretation are reported in Section 2.3

2.2 Laboratory Experimental Setups for Simulated Rainfalls

The experimental phase of this research also relied on two distinct laboratory facilities designed to simulate rainfall under controlled conditions.

The first facility, located at the Hydrology Laboratory of the Department of Agricultural, Food, and Forest Sciences (University of Palermo, Italy), was used to characterize in detail the energetic and hydraulic performance of both drip-type (DRS) and pressurized (PRS) rainfall simulators. A telescopic galvanized-steel support structure was installed in the laboratory (Figure 7).

Figure 7. Support structure for the DRS and PRS systems at the Hydrology Laboratory of the University of Palermo.

The structure features a 1.2 m square base and is vertically extendable up to a height of 3.2 m. This adjustable framework enabled the comprehensive characterization of DRS devices across different fall heights, h (m), thereby enabling the precise

quantification of drop diameters and fall velocities using three distinct methodologies: weighing, photographic, and disdrometric techniques. Furthermore, the same structure served as the mounting platform for developing a new PRS, enabling the testing of various nozzle configurations.

The second facility, established at the School of Industrial, Computer, and Aerospace Engineering (Department of Chemistry and Applied Physics, University of León, Spain), which hosted the author's doctoral research stay abroad, was configured for high-fall rainfall simulations with a PRS device (Figure 8).

Figure 8. View of the experimental setup at the School of Industrial, Computer, and Aerospace Engineering of the University of León.

This configuration was specifically selected to investigate simulated rainfall dynamics at velocities comparable to those of natural precipitation. Designed for studies on stone-based heritage erosion (Fernández-Raga et al., 2022; Rodríguez et al., 2023), the PRS is suspended and anchored to the walls of an internal courtyard by tensioned steel cables, enabling a substantial fall height of 10 m. The vertical walls of the courtyard help minimize wind effects and prevent droplet drift during simulations.

2.2.1 Rainfall Simulators

2.2.1.1 Kamphorst Rainfall Simulator

The Kamphorst Simulator (KS) (model 09.06) (Eijkelkamp, 2022) is a portable drip-type device originally developed at Wageningen Agricultural University for soil conservation surveys (Kamphorst, 1987).

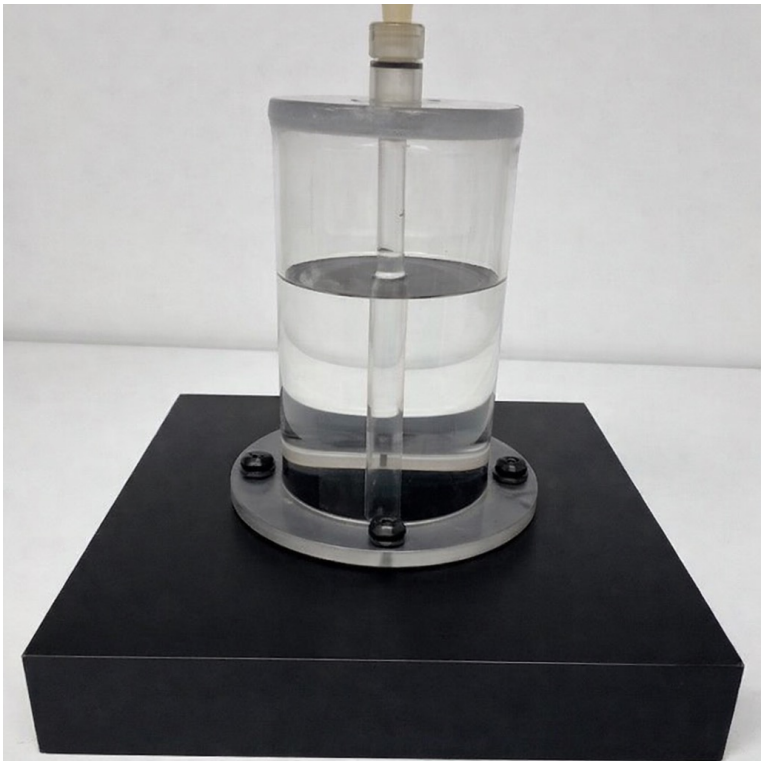

Figure 9. View of the Kamphorst rainfall simulator showing the water reservoir and the aeration tube used to set the hydraulic head on the capillary tubes. The aeration tube is shown capped (test starts upon cap removal), and the hydraulic head is set to its minimum value (aeration tube fully lowered).

It operates on a test plot with a surface area, A_{KS} (m^2), of 0.0625 m^2 (a square microplot of 0.25 m × 0.25 m) and a fixed fall height of 0.4 m. Thanks to its stainless-steel ground frame, the KS can be deployed on slopes with gradients up to 40%.

The instrument is characterized by a sprinkling head equipped with 49 glass capillary tubes positioned in a fixed grid pattern. Each capillary has a length of 10±1 mm and an inner diameter of 0.6±0.08 mm.

The simulator features a built-in pressure regulator based on the Mariotte bottle principle (Mariotte, 1686; McCarthy, 1934), designed to ensure a constant pressure head, *H* (cm), on the capillaries (Figure 10).

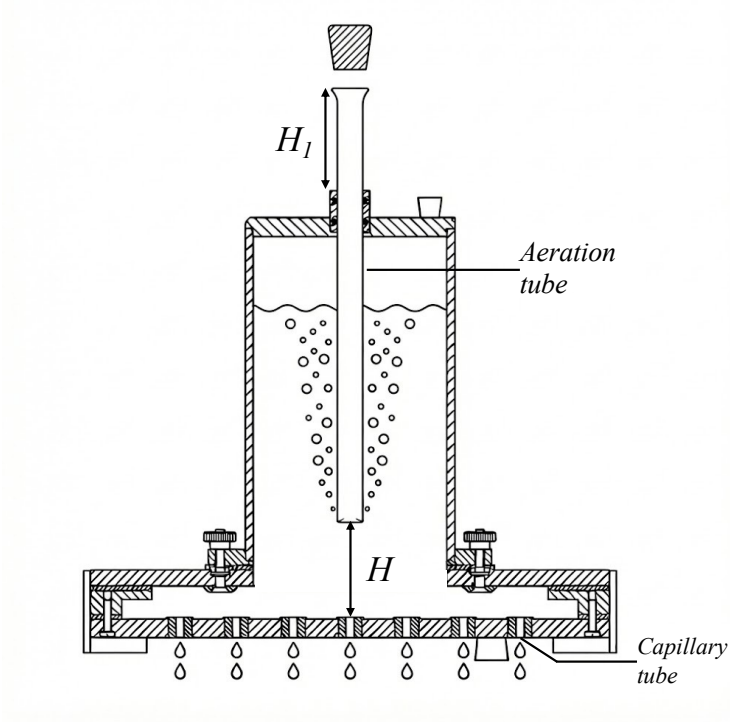

Figure 10. Vertical cross-section of the Kamphorst rainfall simulator illustrating its operation based on Mariotte's bottle principle. The diagram shows the effective pressure head (H) that governs discharge through the capillary tubes.

The system consists of a cylindrical reservoir with a capacity of 2.3 L, functioning as a sealed vessel. An aeration tube, immersed in the liquid, serves as an air-intake line. As water is discharged through the capillary tubes, it is continuously replaced by air entering through the intake. This mechanism establishes the atmospheric pressure acting on the inlet section of the 49 capillary tubes, i.e., the vertical distance between the aeration tube tip and the capillary tubes' inlets, *H* (m)

(Figure 10). Hence, moving the aeration tube up or down, H_1 (m) regulates the pressure head in the capillary tubes (Figure 10).

The pressure head regulation mechanism was originally intended to compensate for variations in water viscosity induced by temperature changes (Kamphorst, 1987), ensuring the reproducibility of experiments and the comparability of results across different research institutions. Specifically, by adjusting the aeration tube height to achieve a calibrated discharge rate of 375 ml min^{-1}, the device delivers a rainfall event with a standard intensity, I_S (mm h^{-1}), of 360 mm h^{-1} (3-minute rainfall event with a total magnitude of 18 mm). According to the manufacturer's specifications, this standard simulation should produce consistent drops characterized by a mean diameter, D, of 0.59 cm and a mass, m_D, of 1.06×10^{-4} kg. Falling from the standard height of 0.4 m, this configuration yields a kinetic power per unit time and area of about 0.4 J m^{-2} s^{-1}.

Subsequent studies by Bagarello et al. (1996) provided crucial insights into the device's hydraulic behavior and operational protocol. Based on an analysis of 238 experimental runs, the authors confirmed the laminar flow regime within the capillary tubes and established a linear calibration equation relating rainfall intensity, I_S, to the aeration tube opening, H_1 (cm), and water temperature, T (°C):

$$I_S = 2.844 + 1.010\,H_1 + 0.058\,T \tag{42}$$

Notably, they observed that the relative influence of water temperature on intensity is less relevant as the rainfall intensity increases. Furthermore, to ensure the comparability of soil loss data, Bagarello et al. (1996) emphasized the need for standardizing microplot conditions, recommending measurements on bare, untilled soil with a controlled initial moisture content (e.g., at a potential of 0.1 bar). Addressing the significant spatial variability in erosion processes observed in the field, they determined that at least 8 repetitions are required to identify a stable mean soil loss value.

To predict the rainfall intensity generated by the KS, Agosta et al. (2022) developed the following theoretical framework. Assuming that the outflow process from the capillary tubes is governed by the physical properties of the fluid (water density ρ, kg m^{-3}, and dynamic viscosity φ, kg m^{-1} s^{-1}) and the nozzle geometry (length l_c, m, and diameter d_c, m), the authors applied Bernoulli's theorem between the inlet

and outlet cross-sections of the capillary. The model explicitly incorporates Poiseuille's law to estimate the head losses, a valid assumption given that the Reynolds numbers observed in the capillaries confirm a strictly laminar flow regime. Accounting for the non-uniform velocity distribution of the fluid, i.e., applying the Coriolis coefficient, α (–), at the inlet (α_1) and outlet (α_2) sections of the capillary tubes, the resulting relationship for estimating the rainfall intensity is:

$$I_S = 3.6 \times 10^6 \frac{\pi c_n}{A_{KS}} \frac{4\varphi}{\rho} \frac{l_c}{1 - \frac{\alpha_1}{2}} \left(-1 + \sqrt{1 + \frac{g\left(1 - \frac{\alpha_1}{2}\right)(H + l_c)}{\left(\frac{16}{{d_c}^2} \frac{\varphi}{\rho} l_c\right)^2}} \right) \quad (43)$$

where n_c (–) is the number of capillary tubes (49), A_{KS} (m^2) is the plot area (0.0625 m^2), and H (m) is the pressure head. α_2 was set to 2, consistent with the theoretical value for uniform laminar flow (De Marchi, 1950). Conversely, α_1 should be set to a value between 1 and 2 to account for the interference of fluid particles entering the tubing (De Marchi, 1950); thus, α_1 was treated as a calibration parameter. Specifically, to validate the model, Agosta et al. (2022) conducted an extensive experimental campaign using two distinct simulators. They measured discharge rates under varying operating conditions (H ranging from 1 cm to 12 cm and T from 16.5°C to 30°C), for a total of 198 simulations per device. By fitting the theoretical equation to the experimental data, the authors identified a coefficient α_1 of 1.25, confirming the model's reliability in predicting rainfall intensity as a function of temperature and hydraulic head.

From a rainfall energy point of view, Iserloh et al. (2013) measured the PSVD of a KS using an LPM disdrometer under standard operating conditions (360 mm h^{-1} for three minutes, h equal to 0.4 m). Although the CUC was not evaluated, the authors observed that the KS produces a regular drop distribution that deviates from typical natural precipitation patterns, with D_{50} ranging from 5.5 to 6.5 mm. Specifically, the KS produced a kinetic power per unit time and area of 0.36 J m^{-2} s^{-1} and a momentum of 0.09 N m^{-2}.

Finally, recent investigations by Palmeri et al. (2025) examined the interaction between simulated rainfall and the soil surface using close-range photogrammetry. By generating a Digital Elevation Model (DEM) and a DEM of Difference (DoD)

before and after the simulations, the authors quantified the micro-topographic changes induced by the rainfall events. They demonstrated that, due to the fixed grid configuration of the capillary tubes, raindrops consistently impact the same points on the soil surface. This process leads to localized scouring, resulting in distinct craters directly beneath the capillary tubes, particularly under bare-soil conditions.

Within the framework of the present investigation, a preliminary verification of the discharge uniformity among the 49 capillary tubes was conducted to further characterize the KS. This was achieved by analyzing the output of a single representative capillary tube. This methodological approach was adopted to isolate individual drops, thereby simplifying the measurement setup and enabling higher precision in determining drop mass and equivalent diameter using the weighing technique, as well as drop fall velocity using the photographic technique, without interference from adjacent dripping drops (Section 2.2.3.3).

2.2.1.2 Modified Kamphorst Rainfall Simulator

To investigate the influence of capillary tubes' geometry on drop formation and explore rainfall characteristics differing from those supplied by the KS, a Modified Kamphorst Simulator (MKS) was developed by replacing the KS glass capillary tubes with stainless-steel capillary tubes (Figure 11).

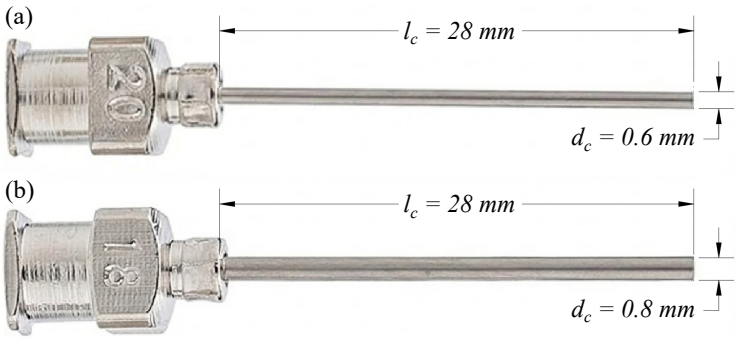

Figure 11. The stainless-steel capillary tubes employed to develop two Modified Kamphorst Simulator configurations, named MKS (a) and MKS_2 (b).

They were inserted into the KS sprinkling head and secured with hot glue to ensure stability and prevent leakage. Specifically, two distinct MKS configurations, designated MKS (Figure 11a) and MKS_2 (Figure 11b), were considered and

characterized individually. While both configurations featured a constant capillary length of 28 mm, they differ in their inner diameters: 0.6 mm for MKS and 0.8 mm for MKS_2. For both configurations, the experimental characterization followed the same single-capillary approach described in Section 2.2.1.1.

2.2.1.3 Drop Generator

To generate constant, large-diameter raindrops, a 10-liter round HDPE (high-density polyethylene) aspiration bottle, equipped with a flow-regulating spigot, named Drop Generator (DG), was employed (Figure 12).

Figure 12. View of the 10-liter HDPE aspiration bottle, named Drop Generator.

To ensure standardized drop production, strict operating conditions were established. The hydraulic head in the reservoir was maintained constant to ensure uniform pressure during droplet formation. The spigot was positioned horizontally to increase the residence time of the water volume at the outlet tip, allowing surface tension forces to sustain the formation of larger drops before detachment. Moreover, the consistency of the drop generation was verified through high-speed video analysis. Slow-motion footage was examined to confirm the production of single drops and to ensure the absence of satellite droplets (secondary fragmentation) following the detachment of the main drop. The equivalent diameter of the generated drops was determined using the ponderal technique described in Section

2.2.3.3. Specifically, raindrops with diameters ranging from 0.51 cm to 0.63 cm were generated by regulating the spigot valve.

2.2.1.4 Pressurized Rainfall Simulator of Palermo

To simulate more complex rainfall patterns, a Pressurized Rainfall Simulator was employed at the Hydrology Laboratory of the University of Palermo (Figure 13).

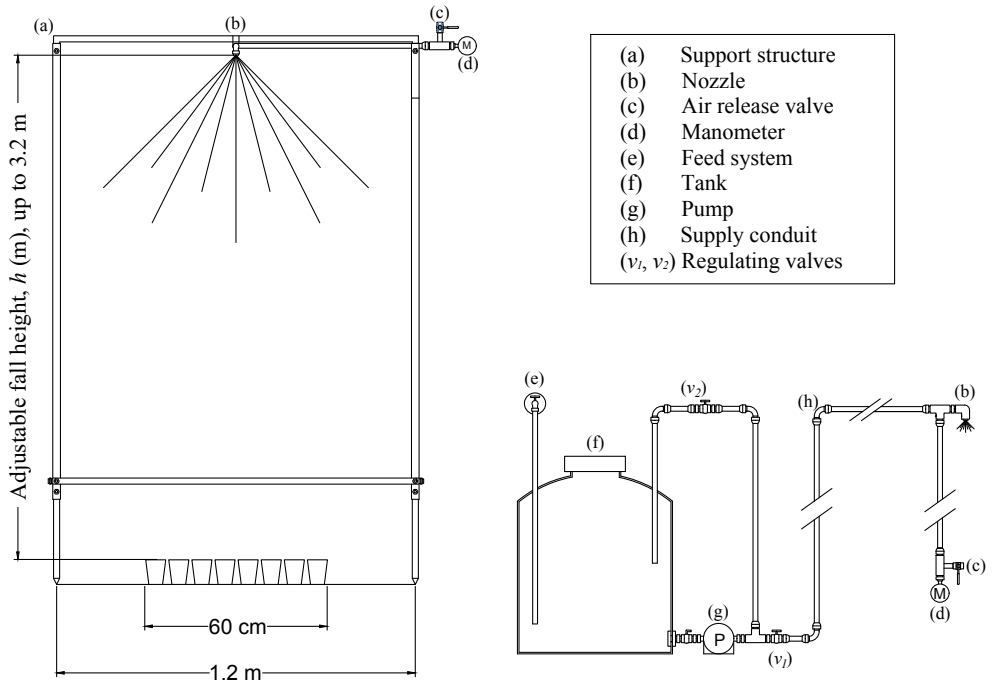

Figure 13. Experimental setup of the PRS at the University of Palermo. Left: front view of the support structure in which the nozzle is installed. Right: schematic diagram of the hydraulic system of the rainfall simulator, from the feed system to the nozzle outlet.

The experimental setup consists of a telescoping galvanized steel support structure (Figure 13a) that enables adjustment of the fall height to up to 3.2 m. The rainfall generation is achieved using axial full-cone nozzles from the Lechler 490 Series (Lechler GmbH, Metzingen, Germany) (Lechler GmbH, 2016) (Figure 13b), located at the summit of the frame. To ensure hydraulic stability and accuracy, an air release valve (Figure 13c) is installed to purge any air bubbles trapped in the circuit and is positioned adjacent to a digital manometer (model PCE-DMM 10, PCE Instruments) (Figure 13d). This specific placement of the manometer, at the same geodetic height as the nozzle, eliminates potential measurement errors attributable to hydrostatic pressure differences.

The hydraulic circuit begins with a feed system (Figure 13e) that supplies tap water to a 30 L capacity tank (Figure 13f). This connection ensures a constant water level within the reservoir, replenishing the volume discharged during the simulation. The water is then pressurized by a 12 V diaphragm centrifugal pump (model 2088-713-515, Shurflo, Roncq, France) (Figure 13g), capable of delivering a maximum pressure, P_S (bar), of 3.8 bar and a maximum flow rate, Q (L min^{-1}) of 13.2 L min^{-1}. The fluid is conveyed to the top of the structure through a rigid supply conduit (Figure 13h). Finally, the fine regulation of rainfall intensity is managed by a dual-valve system (Figure 13v_1, v_2). Valve v_1 regulates the intake from the pump, while v_2 controls the recirculation flow returning to the tank. For each fixed v_1 opening, maximum pressure occurs when v_2 is fully closed. Gradually opening v_2 diverts flow back to the tank, thereby reducing both the pressure and flow rate at the nozzle outlet.

The Lechler 490 Series nozzles (Figure 14a) were specifically selected for their high resistance to oxidation and abrasion, ensuring consistent hydraulic performance over time. Moreover, the presence of wide internal flow channels significantly minimizes the risk of clogging (Figure 14b). The nozzles generate a solid cone jet (Figure 14c) and are suitable for simulating several pressure conditions.

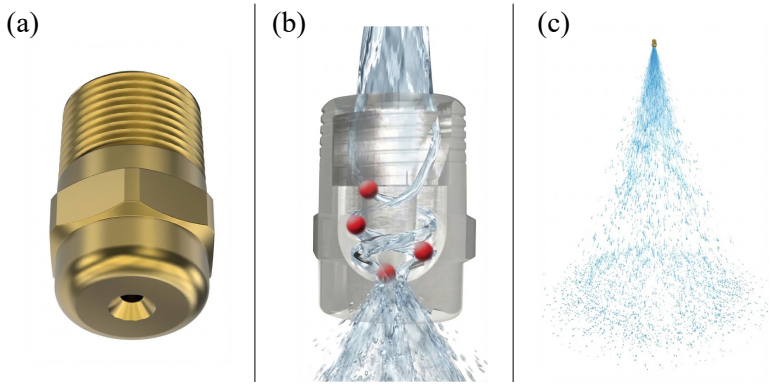

Figure 14. Lechler 490 Series nozzle (a), cross-sectional view of internal fluid dynamics (b), and example of the full cone spray pattern (c). Modified from (Lechler GmbH, 2016).

The selection of Lechler nozzles is also supported by their widespread adoption in the scientific community for both laboratory and field applications (e.g., Iserloh et al., 2012, 2013b; Lassu et al., 2015; Martinez-Mena et al., 2001; Nadal-Romero et al., 2011; Nadal-Romero and Regüés, 2009).

The developed PRS enables the interchangeability of different nozzle models, distinguished by their spray angle (from 45° to 120°) and flow rate (high-flowrate, HFR, and low-flowrate, LFR, types), allowing for the reproduction of a broad range of rainfall intensities, wetting surfaces, and energies. Table 1 summarizes the key technical characteristics of the selected nozzle models and details the relationship between operating pressure and flow rate.

Table 1. Characteristics of the selected Lechler nozzles. Source: Lechler GmbH (2016)

Spray Angle and Nozzle Model	**Type**	**Bore width (mm)**	**Flow Rate Q (L min^{-1})**						
			Pressure P (bar)						
			0.5	1	2	3	5	7	10
45°_490683	HFR	2.55	2.87	3.79	5.00	5.88	7.21	8.25	9.52
60°_490684	HFR	2.60	2.87	3.79	5.00	5.88	7.21	8.25	9.52
90°_490686	HFR	2.70	2.87	3.79	5.00	5.88	7.21	8.25	9.52
120°_490688	HFR	2.75	2.87	3.79	5.00	5.88	7.21	8.25	9.52
120°_490608	LFR	2.10	1.81	2.39	3.15	3.70	4.54	5.20	6.00

The availability of multiple nozzle configurations prompted a systematic experimental comparison under controlled conditions. Although the pressurized rainfall simulator investigated in this study was tested under laboratory conditions, this choice was made intentionally to ensure rigorous experimental control. The laboratory environment allows the isolation of the main hydraulic and microphysical variables, enables a controlled comparison among different nozzle configurations under identical boundary conditions, and helps reduce experimental uncertainty before field deployment. Within this framework, the laboratory characterization was conceived as a preparatory step to identify nozzle configurations most suitable for future plot-scale field applications, including soil loss measurements and related erosion studies.

To ensure the accuracy of the simulated rainfall and quantify potential manufacturing variability, a technological reliability assessment was conducted. For each model listed in Table 1, two separate nozzles, designated n_1 and n_2, were experimentally tested to verify their hydraulic performance consistency.

The validation process compared the experimental data with the manufacturer's theoretical hydraulic characteristic curves. According to the technical specifications, for pressures varying between 0.5 bar and 10 bar, the relationship between flow rate and pressure is described by the following power law equation (Table 1) (Lechler GmbH, 2016):

$$Q = \mathrm{a}\, P_S^{0.4} \tag{44}$$

where the coefficient a (L min^{-1} bar$^{-0.4}$) depends on the flow rate condition. Specifically, it assumes a value equal to 3.8 L min^{-1} bar$^{-0.4}$ for HFR models (45°_490683, 60°_490684, 90°_490686, 120°_490688), implying a common characteristic curve for this group, and equal to 2.4 L min^{-1} bar$^{-0.4}$ for LFR models (120°_490608), respectively (Figure 15).

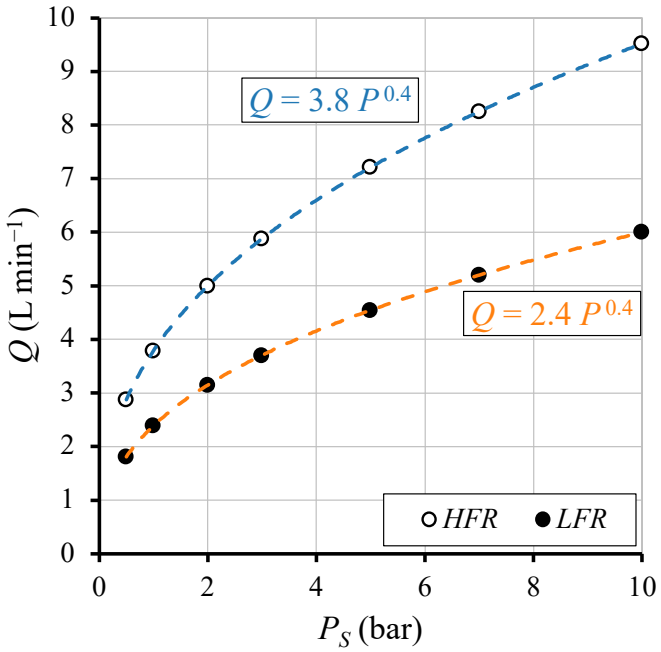

Figure 15. Relationship between flow rate, Q (L min^{-1}), and pressure, P_S (bar), for high-flow-rate (HFR) and low-flow-rate (LFR) nozzles.

Although the manufacturer specifies a standard operating range starting at 0.5 bar, preliminary simulations indicated that, for some nozzle models, these pressures produced excessive spray flow rather than the desired rainfall characteristics.

To achieve a simulated rainfall consisting of visually distinguishable single droplets, it was necessary to investigate lower operating pressures. Consequently, the experimental validation was conducted using 11 pressure values from 0.1 bar to

2.5 bar, deliberately extending below the manufacturer's lower limit to verify hydraulic behavior under the conditions of interest.

2.2.1.5 Pressurized Rainfall Simulator of León

During the author's research stay at the University of León (Spain), a second PRS was employed. Unlike the PRS of Palermo, which was specifically assembled and calibrated for this study, the PRS of León is a well-established apparatus previously employed by the local research group for investigating erosion processes on stone-based cultural heritage. Consequently, its hydraulic behavior and operational parameters have been consolidated in prior investigations (e.g., Búrdalo-Salcedo et al., 2023; Fernández-Raga et al., 2022; Rodríguez et al., 2023).

The simulator (Figure 16) is suspended by tensioned steel cables within an internal courtyard. A distinct feature of this setup is the available fall height of 10 m, which, according to the literature, should allow droplets to achieve terminal velocities significantly closer to those of natural precipitation (Beard, 1976; Gunn and Kinzer, 1949; van Boxel, 1998).

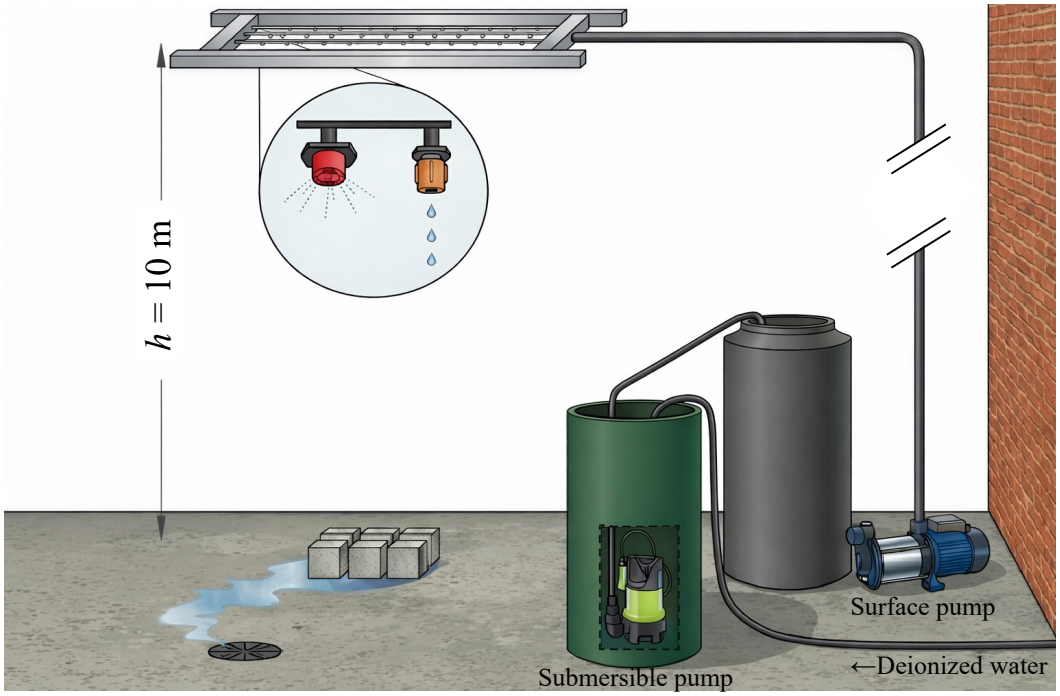

Figure 16. Scheme of the pressurized rainfall simulator located at the University of León.

The hydraulic system was designed to address specific chemical and physical constraints. Tap water was excluded to prevent calcium carbonate deposition, which

could compromise the hydraulic efficiency of the finer components over time. Therefore, deionized water was generated via a purification system (model DE7003, Wasserlab, Barbatáin, Navarra, Spain) that continuously supplied a 100 L storage tank. Water was drawn from the tank by a submersible pump (model Hidrosub AS-216, LISTA, Ehlis S.A., Illescas, Toledo, Spain) and subsequently conveyed to the main supply line at the top of the courtyard by a surface pump (model EH-125, Hidrobex, Parets del Vallés, Barcelona, Spain).

To mitigate the gradual power loss typical of surface pumps during extended operation and ensure consistent hydraulic performance, the system was automated using an Arduino-based controller. This controller managed the pump's duty cycle, programmed for a run time of 55 seconds followed by a pause of 5 seconds. This intermittent operation maintained a constant mean flow rate throughout the 5-minute simulation runs employed in this investigation.

The drop generation system (Figure 17a) consists of a metal frame supporting four independent pipes equipped with 46 emitters. Specifically, two different drippers commonly employed for gardening applications were used: 26 releasing droplets in eight peripheral directions (Figure 17b) and 20 with a single outlet (Figure 17c).

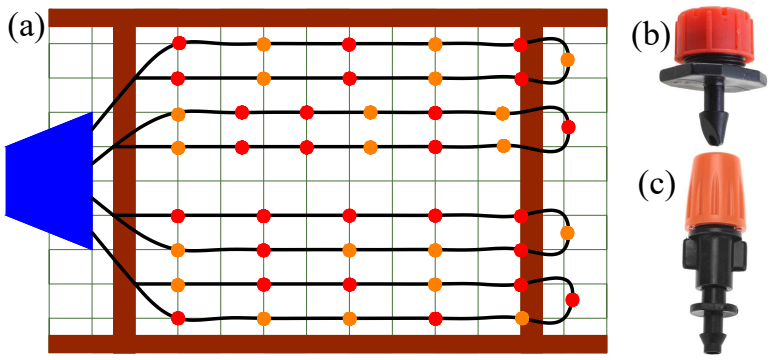

Figure 17. Drop generation system of the pressurized rainfall simulator at the University of León: 2D schematic of the frame (a) and details of the two dripper types (b, c).

2.2.2 Parsivel² Optical Disdrometer

To monitor the microphysical properties of simulated rainfalls, this study employed a Parsivel² disdrometer (OTT Hydromet GmbH, 2016) (Figure 18).

Figure 18. View of the Parsivel² optical disdrometer.

This instrument is a laser-based optical disdrometer that has become a standard tool in hydrometeorological research due to its robustness, low maintenance requirements, and ability to measure both liquid and solid precipitation.

The Parsivel² operates on the light extinction principle, featuring a transmitter unit that emits a flat, horizontal infrared laser beam (wavelength of 780 nm) toward a receiver unit. The optical path defines a sensing volume with dimensions of 180 mm in length, 30 mm in width, and approximately 1 mm in thickness, resulting in a nominal sampling area of 0.0054 m^2.

When a hydrometeor passes through this laser sheet, it occludes a portion of the beam, reducing the output voltage at the receiver. The amplitude and the duration of the voltage drop are used to derive the diameter and fall velocity of each particle, respectively (Löffler-Mang and Joss, 2000).

The raw data are classified into a matrix of 32 diameter classes, ranging from 0.2 mm to 25 mm, and 32 velocity classes, ranging from 0.2 m s^{-1} to 20 m s^{-1}. The class widths are non-uniform, increasing with particle size to span a wide range of precipitation types. Specifically, diameter class widths range from 0.125 mm to 3.0 mm, while velocity class widths vary from 0.1 m s^{-1} to 3.2 m s^{-1}.

The disdrometer relies on internal assumptions regarding raindrop geometry to determine the equivalent spherical diameter: (i) drops smaller than 1 mm are assumed to be spherical; (ii) for drops between 1 mm and 5 mm, the instrument

assumes a horizontally oriented oblate spheroid shape, with an axis ratio linearly varying from 1.0 to 0.7; for drops larger than 5 mm, the axis ratio is fixed at 0.7 (Park et al., 2017).

Compared to the previous generation, the Parsivel^2 incorporates several improvements, including the use of a more advanced laser unit yielding data less affected by measurement errors, a new splash-protection shield to minimize interference from raindrops shattering on the instrument surface, and an increased sampling frequency (from 10 kHz to 50 kHz) allowing for finer resolution in detecting fast-falling particles (Tokay et al., 2014).

Despite these advancements, the current instrument remains subject to instrumental errors, widely documented in the literature. These include the misinterpretation of multiple particles passing simultaneously as a single larger drop and the occurrence of margin fallers, i.e., drops that only partially intersect the beam and are therefore not fully detected or misclassified (Saha and Testik, 2023). Although the manufacturers state that these devices incorporate corrections for margin fallers and coincident particles, the specific methodologies employed to address these sources of error remain undisclosed (Saha and Testik, 2023).

Furthermore, a consistent finding across multiple studies is that the Parsivel^2 tends to underestimate the fall velocity of mid-sized drops (0.1–0.3 cm), which inevitably influences estimates of kinetic power and momentum. Saha and Testik (2023) described this as a *bell-shaped deviation* in velocity measurements, attributing it to the laser sensor's characteristics rather than to environmental factors such as wind. This issue becomes particularly critical at high rainfall intensities, where measurement discrepancies tend to increase (Park et al., 2017). Finally, compared with other optical disdrometers such as the LPM, the Parsivel^2 tends to record significantly fewer small drops, suggesting lower sensitivity at the lower end of the drop-size spectrum (Angulo-Martínez et al., 2018).

To mitigate the abovementioned instrumental source of error, the literature typically suggests removing particles that significantly deviate from the theoretical terminal velocity, for instance by applying a ±50% filter to empirical relationships, such as those suggested by Atlas and Ulbrich (1977), Beard (1976), and Gunn and Kinzer

(1949). However, this standard practice is inapplicable to simulated rainfall studies where the limited fall height prevents drops from reaching terminal velocity.

Moreover, to address the systematic undercounting caused by margin fallers, a geometric correction factor is commonly applied to the nominal sampling area. The effective sampling area, A_{OTT} (m^2), varies with drop diameter and is calculated as follows:

$$A_{OTT} = L_{OTT}\left(W_{OTT} - \frac{N_i}{N_{OTT}}\frac{D_i}{2}\right) \tag{45}$$

where L_{OTT} (m) and W_{OTT} (m) are respectively the Parsivel^2 laser beam length and width, N_i (–) is the number of drops recorded in the i-th diameter class, N_{OTT} (–) is the total number of drops recorded during the selected sampling interval, and D_i (m) is the mean diameter of the i-th diameter class.

Consequently, from the raw Particle Size and Velocity Distribution (PSVD), measured at desired intervals (e.g., 1 minute, 5 minutes, 10 minutes), additional information such as the rainfall intensity, I_{OTT} (mm h^{-1}), kinetic power, $P_{n,OTT}$ (J m^{-2} s^{-1}), and momentum, M_{OTT} (N m^{-2}), can be calculated.

Specifically, from the raw PSVD, the rainfall intensity can be derived as:

$$I_{OTT} = \frac{\pi}{6}\frac{3600}{t}\sum_{i=1}^{32}\frac{(10D_i)^3 N_i}{A_{OTT}\times 10^6} \tag{46}$$

in which t (s) is the sampling interval at which PSVDs are recorded, set to 60 seconds for the present investigation.

The rainfall kinetic power can be computed as:

$$P_{n,OTT} = \frac{\pi\rho}{12\,t}\sum_{i=1}^{32}\sum_{j=1}^{32}\frac{\left(\frac{D_i}{100}\right)^3 {V_j}^2 N_{ij}}{A_{OTT}} \tag{47}$$

where V_j (m s^{-1}) is the fall velocity recorded in the j-th velocity class and Nij (–) is the number of drops recorded in the i-th diameter and j-th velocity class.

Similarly, the rainfall momentum is derived from the raw Parsivel^2 PSVD as:

$$M_{OTT} = \frac{\pi\rho}{6\,t}\sum_{i=1}^{32}\sum_{j=1}^{32}\frac{\left(\frac{D_i}{100}\right)^3 V_j N_{ij}}{A_{OTT}} \tag{48}$$

2.2.3 Rainfall Simulator Characterization Methodologies

This section first describes the methodological framework adopted to develop an empirical relationship for estimating raindrop fall velocity under simulated rainfall conditions. Subsequently, the different measurement techniques and characterization methodologies employed are presented, with specific reference to each simulator type and to the experimental constraints associated with the corresponding setup.

2.2.3.1 Development of an Empirical Relationship to Estimate Raindrop Fall Velocity in Laboratory Conditions

In rainfall simulation experiments, raindrops typically fall from limited heights and therefore do not necessarily reach terminal-velocity conditions, unlike in natural precipitation. For this reason, the direct application of terminal velocity relationships commonly adopted for natural rainfall may lead to inaccurate estimates when simulating rainfalls.

This limitation underscores the need for an empirical relationship that can estimate raindrop fall velocity not only as a function of drop diameter, but also as a function of fall height. Relationships of this type have already been proposed in the literature, such as that introduced by Ferro (2001), and reported as Equation (21). However, this formulation relies on tabulated parameter values corresponding to discrete fall heights (i.e., 0.50 m, 0.75 m, 1.00 m, 1.50 m, 2.00 m, 2.50 m, 3.00 m, 4.00 m, 5.00 m, 6.00 m, 8.00 m, 20.00 m), which limits its applicability when continuous height-dependent estimates are required.

To overcome this limitation, a literature dataset providing simultaneous measurements of raindrop diameter, fall velocity, and fall height was employed. Specifically, the experimental data collected by Laws (1941) were used as the reference dataset to develop the relationship. In that study, individual water drops with D ranging from 0.1 cm to 0.6 cm were generated under controlled laboratory conditions and released from heights ranging from 0.5 m to 20 m. Diameters and fall velocities were measured using a stroboscopic photographic system in which falling drops were recorded as a sequence of discrete images on a single exposure

by means of a rotating chopper-disc and dark-field illumination, allowing velocity to be determined from the spacing between successive images (Laws, 1941).

Starting from these data, a functional formulation, similar to that proposed by (Ferro, 2001), was assumed, expressing the fall velocity of the simulated drop, V_S (m s^{-1}), as:

$$V_S = V_h[1 - \exp(-a_h D)] \tag{49}$$

where D is expressed in cm, and a_h (cm) and V_h (m s^{-1}) are empirical parameters. The analysis of the Laws (1941) dataset demonstrates that the dependence of these parameters on the fall height, h (m), could be effectively described through continuous functional relationships (Figure 19):

$$a_h = 11.43\, h^{-0.24} \tag{50}$$

$$V_h = \frac{11.50}{1 + \frac{1.65}{h^{0.80}}} \tag{51}$$

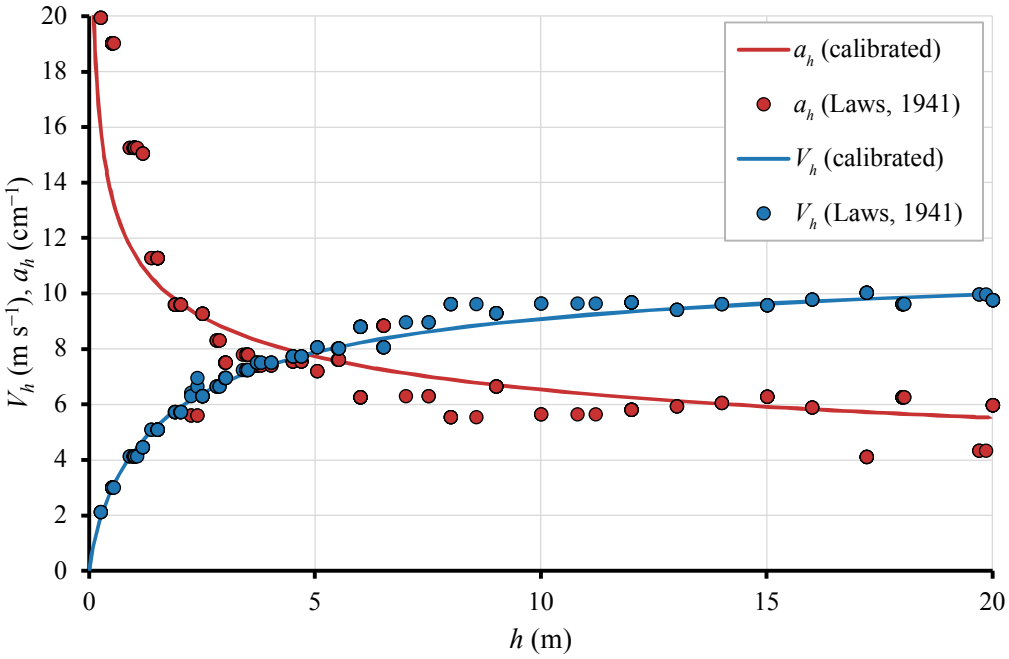

Figure 19. Dependence of a_h and V_h on the height of fall. The coefficients of determination (R^2) are equal to 0.909 and 0.986, respectively. Symbols represent experimental data from Laws (1941), while solid lines indicate the calibrated empirical relationships.

Therefore, Equation (49) can be rewritten as:

$$V_S = \frac{11.50}{1 + \frac{1.65}{h^{0.80}}}\left[1 - \exp(-11.43\, h^{-0.24} D)\right] \quad (52)$$

The reliability of this relationship was evaluated by comparing its predictions with:
(i) the calibration dataset (Laws, 1941);
(ii) independent literature data (Epema and Riezebos, 1983);
(iii) experimental fall velocity measurements collected in this study using photographic techniques for drip-type rainfall simulators, which served as an independent reference under controlled laboratory conditions;
(iv) disdrometric fall velocity measurements for pressurized rainfall simulators.

2.2.3.2 Spatial Uniformity Assessment

To assess the spatial uniformity of simulated rainfalls, the Christiansen method (Christiansen, 1942) was employed. Once the number and arrangement of rainfall collectors were defined for each configuration, the CUC was determined using Equation (38). While originally proposed for volumetric distribution, this investigation also applied this method to analyze the uniformity of rainfall kinetic power and momentum, as well as statistical DSD descriptors as $\mu_{(D)}$, $\sigma_{(D)}$, D_0, and D_{50}. To this end, the volumetric terms in Equation (38) were replaced with the corresponding energy-related or statistical variables, and the concept of rain collectors was adapted to the disdrometric sampling surfaces used in the experiments.
For KS and MKS devices, the uniformity assessment focused on verifying the homogeneity of the discharge rate across the 49 capillary tubes. A custom-made polystyrene collector rack was designed to hold 49 Falcon® polypropylene tubes with a 50 ml capacity, positioned directly under each capillary outlet (Figure 20).
Before each simulation, the collectors were weighed to establish the tare. Rainfall simulations were then performed under varying operating conditions, with water temperatures ranging from 24 °C to 27 °C and pressure head values ranging from 2 cm to 12 cm. Two repetitions were carried out for each *H-T* combination. To validate the collection efficiency, a third control run was performed by measuring the total volume discharged into a bulk tank for each *H-T* condition.

The rainfall intensity of each capillary tube was derived by relating the net weight of the collected water to the simulation time and the representative area of a single nozzle, equal to 1.276×10^{-3} m^2.

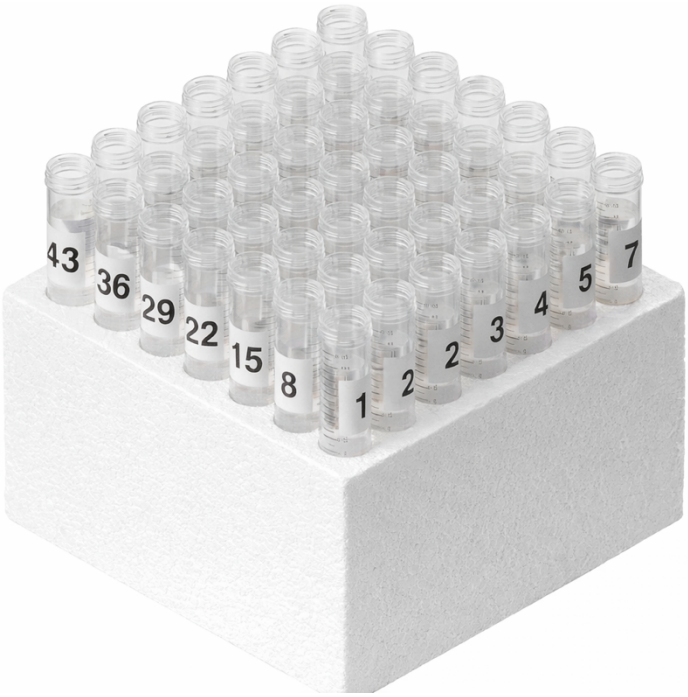

Figure 20. 3D representation of the collector system used to assess rainfall spatial uniformity across the 49 capillary tubes of the Kamphorst rainfall simulator.

This verification of discharge uniformity across the nozzle array justified the subsequent micro-physical characterization (i.e., mass, diameter, and velocity of drops) based on the analysis of a single representative capillary tube for both KS and MKS configurations. Conversely, no spatial uniformity assessment was required for the Drop Generator (DG), as it operates via a single capillary emitter.

For the PRS of Palermo, the spatial rainfall distribution was assessed using cylindrical rain collectors with a diameter of 6.35 cm and a maximum capacity of 200 cm^3 (Figure 21).

The collectors were secured on polystyrene bases to prevent displacement due to drop impact. The sampling method was carried out both on the core zone, defined as a circle of 60 cm centered on the vertical projection of the nozzle, and across six peripheral zones extending up to 1.5 m from the center (Figure 21a). Specifically, within the central 60 cm area, which corresponds to the plot size for which the simulator was originally conceived, 55 collectors were arranged concentrically

around the nozzle axis (Figure 21b). Furthermore, 17 additional collectors were positioned along each of the six radial axes to verify the simulated rainfall behavior in the area surrounding the intended experimental plot (Figure 21b). Thus, a total of 157 collectors were employed.

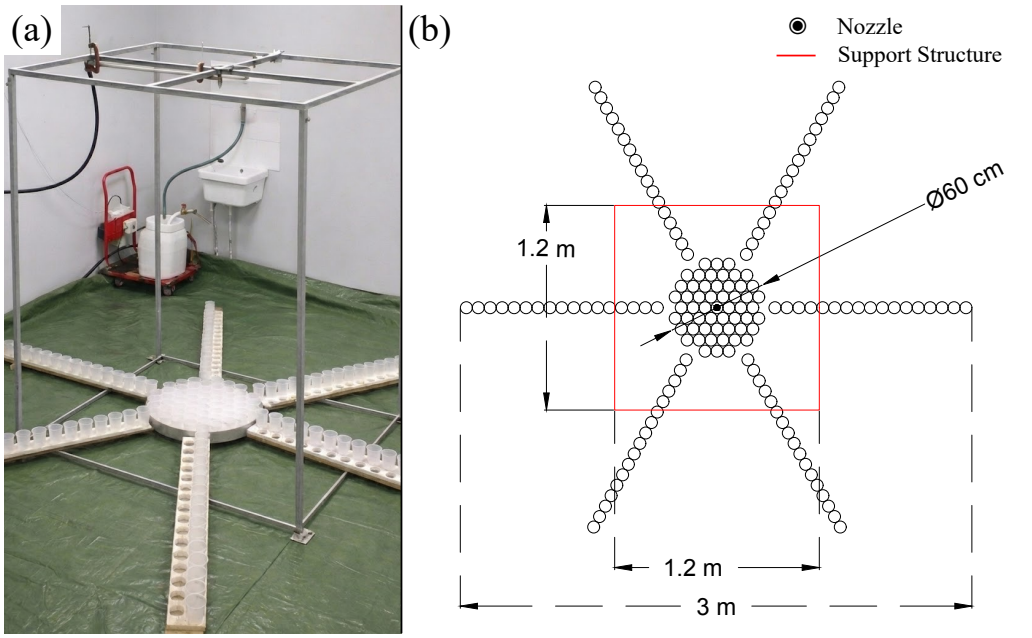

Figure 21. View of the experimental set-up employed for the volumetric calibration of the PRS in the laboratory of the University of Palermo(a) and top view of the sampling scheme showing the positions of the 157 rain collectors (b).

The volumetric tests were conducted with the fall height fixed at 1.63 m, defined as the vertical distance between the nozzle outlet and the upper surface of the rain collectors. The operating pressure was adjusted according to the nozzle characteristics, ranging from about 0.25 bar to 0.50 bar for the 120° and 90° models, and from 1.00 bar to 1.50 bar for the 45° and 60° models. These specific pressure intervals were selected to generate a simulated rainfall consisting of visually distinguishable droplets reaching the ground, thereby avoiding the formation of a spray flow or mist. In total, 20 rainfall simulations were performed, covering two distinct pressure configurations for each of the two nozzles of the five models.

The collected water volumes were quantified by weighing each rain collector before and after a precipitation interval of approximately 30 minutes, drying the external surface of each collector to ensure data accuracy and prevent measurement errors and systematic overestimation caused by water adhering to the outer surface. The mean simulated rainfall intensity, I_c, of each collector was calculated by dividing

the volume accumulated in each cup by the sampling surface of each collector and the duration of the experiment.

Subsequently, the spatial uniformity of the mean rainfall intensity, I_S, was evaluated using the CUC calculated from Equation (38). This assessment was performed at two distinct spatial scales: first, focusing strictly on the central 60 cm-diameter core; and second, extending to the entire sampled surface using the 157 rain collectors.

Furthermore, the spatial distribution of rainfall was analyzed as a function of radial distance from the nozzle axis. Specifically, for each nozzle model, the I_S trends were determined by averaging values within circular areas (Figure 22a), while the variation of the CUC was evaluated using concentric rings (Figure 22b).

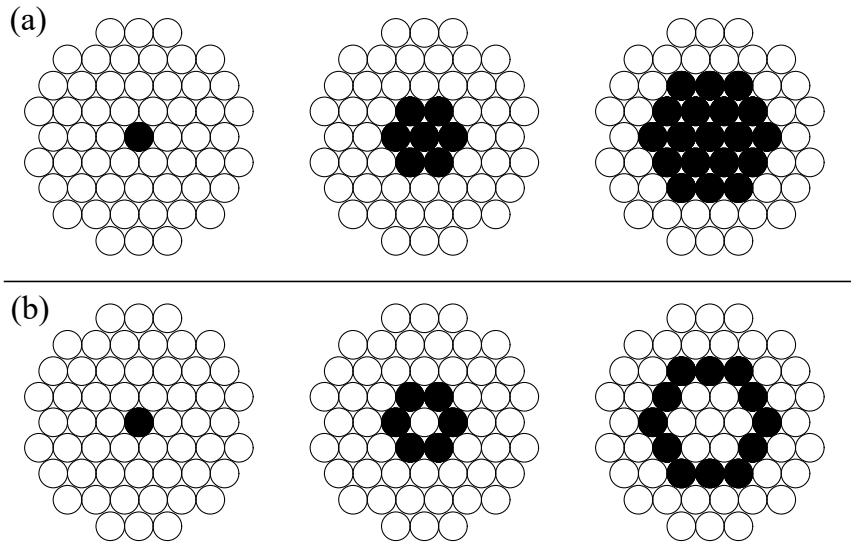

Figure 22. Examples of circular areas (a) and concentric rings (b) used to evaluate rainfall spatial distribution as a function of the distance from the nozzle.

For the volumetric calibration of the PRS at the University of León, a rectangular sampling area of 1.8 m × 1.8 m was considered. Given the laboratory floor configuration, 36 rain collectors were placed at the center of each 0.3×0.3 m tile grid (Figure 23). Due to the significant fall height and high intensities typical of this simulator, potential measurement errors caused by splash phenomena (splash-in/splash-out) were investigated. Hence, two collector types were tested: short plastic vessels (p_v), with a capacity of 0.5 L and a sampling area of 9.607×10^{-3} m^2 (Figure 23a), and tall plastic cups (p_c), with a capacity of 1 L and a sampling area

of 9.276×10^{-3} m^2 (Figure 23b). For both rainfall collector types, the larger upper diameter was used to determine the effective sampling surface.

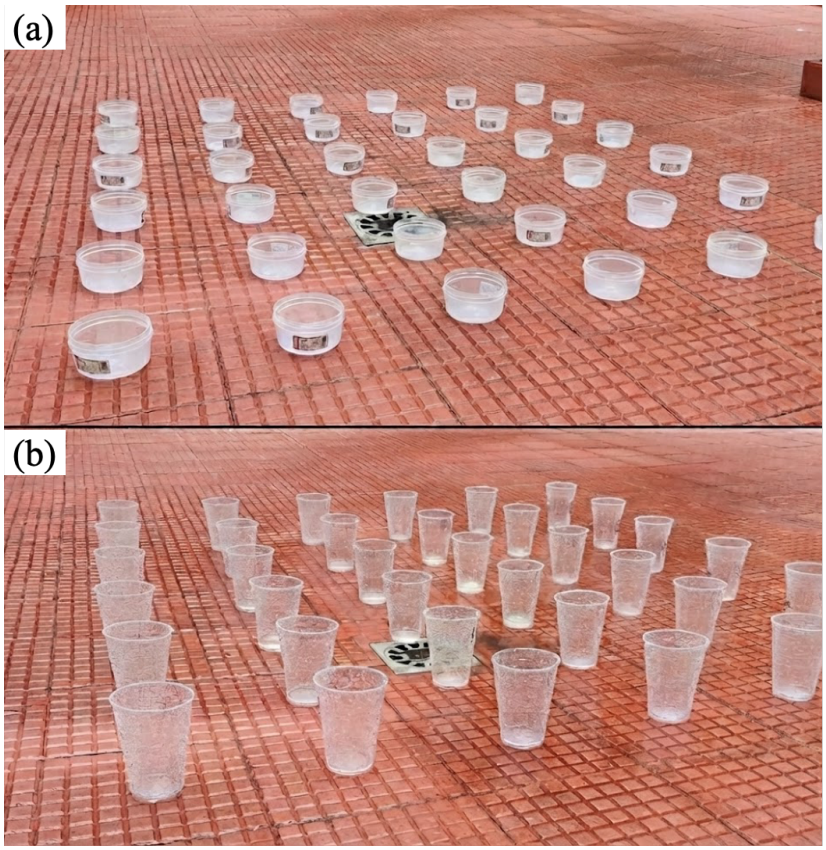

Figure 23. Rain collectors used for the volumetric calibration: plastic vessels (a) and plastic cups (b).

Three experimental treatments (T) were compared: p_v for 5 min (T1), pc for 5 min (T2), and pc for 10 min (T3). Due to their limited capacity, p_v could not be used for the 10-minute simulation.

Regarding the measurement protocol, before each rainfall simulation, the collectors were calibrated using a digital scale to establish the tare weight. After the simulation, their outer surfaces were dried to avoid measurement errors caused by external water adhesion, and the collected water volume was determined by weighing. Then, as described for the PRS of Palermo, the rainfall intensity was calculated by dividing the volume collected by each collector by the relative sampling area and time. For each treatment, three repetitions were performed, totaling 324 intensity measurements.

To statistically verify the validity of the experimental treatments adopted for rainfall spatial uniformity assessment, a two-way ANOVA with replication was performed, considering treatment and collector position as factors (Section 2.3 for statistical methodology).

Additionally, GIS software (QGIS, v. 3.34) was used to generate thematic maps for a visual evaluation of the spatial distribution.

2.2.3.3 Weighing and Photographic Techniques for Drip-Type Systems

For drip-type rainfall simulators (DRSs), weighing and photographic techniques were adopted not only for microphysical characterization purposes, but also to provide an independent experimental reference for fall velocity measurements under controlled laboratory conditions. In particular, the photographic measurements were conceived as a benchmark dataset for both validating the empirical fall velocity relationship developed in this study, Equation (52), and assessing the reliability of disdrometric measurements under non-terminal velocity conditions. To this end, a dedicated experimental setup was developed by isolating a single capillary tube, enabling controlled, repeatable measurements of individual drop properties.

Given the low fall heights tested with DRSs, it was assumed that the drops maintained a spherical shape. Consequently, by measuring the cumulative weight of a known number of drops, the mean mass of a single drop, m_D (kg), was obtained. The volume of a single drop, vol_D (m^3), was then calculated as:

$$vol_D = \frac{m_D}{\rho} \tag{53}$$

Finally, the equivalent diameter of each drop, D (cm), was derived from the volume using the geometric relationship for a sphere:

$$D = 2\sqrt[3]{\frac{3}{4}\frac{vol_D}{\pi}} \tag{54}$$

To measure the fall velocity of single drops, V_S (m s^{-1}), a high-speed imaging system was employed on the single capillary arrangement (Figure 24).

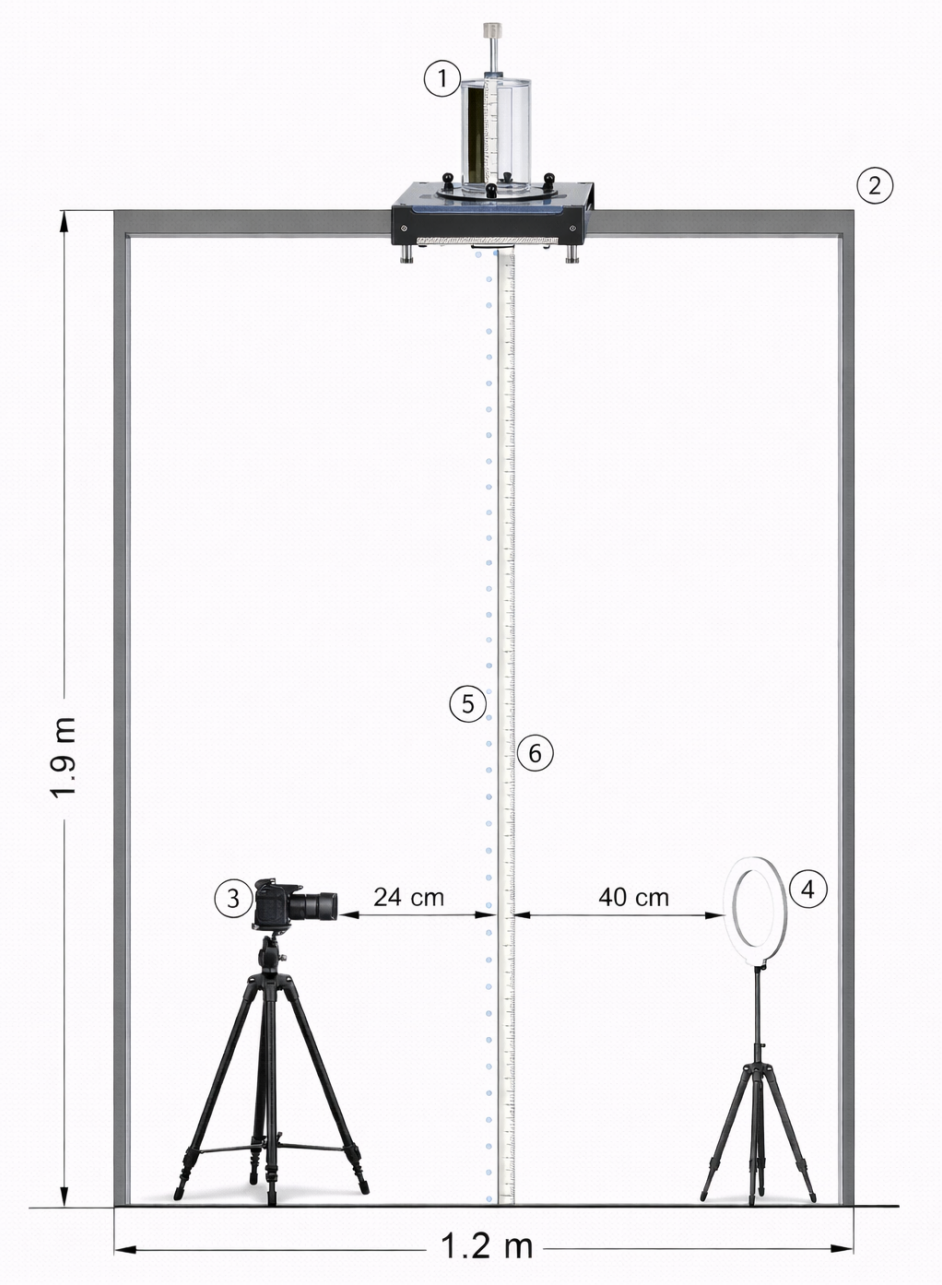

Figure 24. Front-view representation of the experimental setup employed for determining the fall velocity of single raindrops generated by drip-type rainfall simulators (DRS). The figure shows a Kamphorst simulator (1), the support structure (2), a high-frame-rate camera (3), an LED lamp (4), the vertical trajectory of individual raindrops (5), and the meter ruler with the opaque background panel used to measure the displacement of a single raindrop between two consecutive frames (6).

The setup featured a mobile phone camera capable of recording slow-motion video at 720p resolution with a frame rate of 480 frames per second (FPS). The camera was mounted on a vertically extendable tripod, leveled to ensure that the lens axis was perpendicular to the drop trajectory. A calibrated meter ruler was positioned parallel to the drop path to quantify displacement, and the distance between the

camera and the ruler was fixed at 24 cm. To maximize contrast and ensure reliable drop detection, an LED light source was positioned opposite the camera, 40 cm behind an opaque background panel. Thus, the camera was positioned at several fixed heights of fall, and videos were recorded for each explored configuration in terms of RS type and diameter.

For V_S calculation, frames containing the falling drop were extracted and imported into Computer-Aided Design software (AutoCAD®) to perform precise measurements (Figure 25).

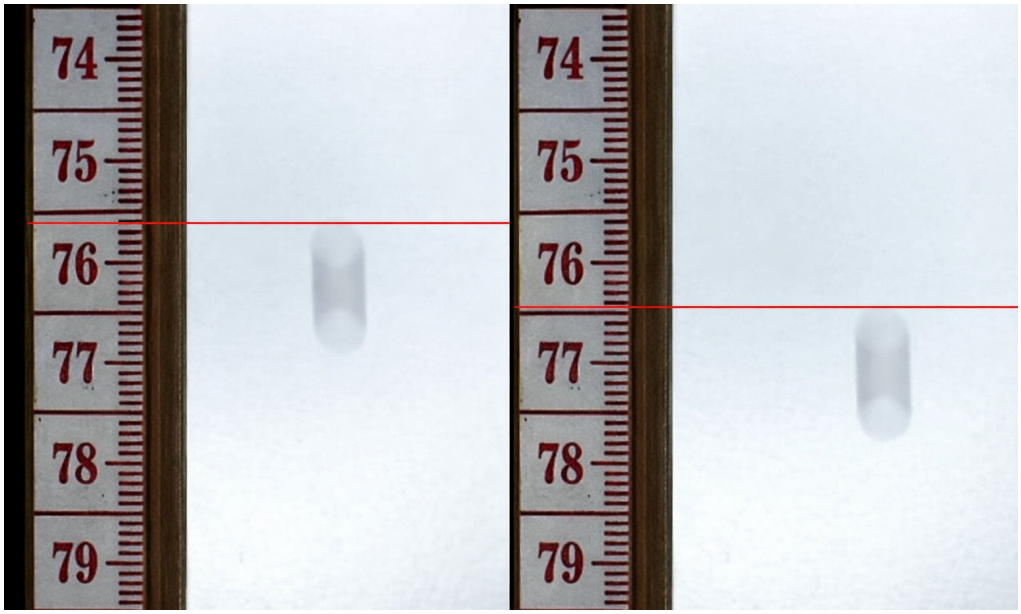

Figure 25. Two consecutive frames from a high-resolution, high-frame-rate video showing the same falling water drop. A horizontal line, drawn perpendicular to the direction of motion, is aligned with the top of the drop in both frames to measure the vertical displacement between frames.

The vertical displacement was determined by scaling the images based on the reference ruler and tracking the upper tip of the drop. The time interval between two consecutive frames was determined by the camera's frame rate (1/480 s). Therefore, for each experimental configuration (i.e., specific capillary type, pressure head, and fall height), the measurement procedure was repeated for three distinct drops to minimize random errors. Furthermore, given the high sensitivity of this manual tracking procedure to subjective interpretation, all video analyses and CAD measurements were performed by the same operator to guarantee methodological consistency.

To verify the reliability of the photographic method, the measured fall velocity, V_S, values were first compared with the theoretical maximum velocity achievable by a body falling freely in a vacuum starting from rest, V_{max} (m s^{-1}):

$$V_{max} = \sqrt{2gh} \tag{55}$$

where g (m s^{-2}) is the gravitational acceleration.

Once their reliability had been established, the measurements obtained with the photographic technique were explicitly used as a benchmark to evaluate the applicability of Equation (52) to the experimental data, and to assess the accuracy of Parsivel[2].

This specific validation was deemed necessary because the experimental conditions fall outside the instrument's standard design specifications, which are typically optimized for natural rainfall at terminal velocity.

Finally, combining m_D and V_S measurements, the rainfall kinetic power, $P_{n,D}$ (J m^{-2} s^{-1}), and momentum, M_D (N m^{-2}), of a single drop per unit time and area, were calculated as follows:

$$P_{n,D} = \frac{0.5 m_D {V_S}^2}{\sigma_c t} \tag{56}$$

$$M_D = \frac{m_D V_S}{\sigma_c t} \tag{57}$$

in which σ_c (m^2) is the sampling area assigned to the considered capillary tube and t (s) is the sampling time.

For the PRSs used in both Palermo and León, the spray-based nature of drop generation prevented the application of single-drop measurement techniques. In pressurized rainfall conditions, droplets are generated simultaneously within a three-dimensional spray volume and cannot be constrained to fall within a single, well-defined vertical plane.

As a consequence, individual drops captured by video imaging are located at varying and unknown distances from the camera along the optical axis. This variability introduces geometric and perspective distortions that compromise displacement and velocity measurements.

2.2.3.4 Disdrometric Evaluation of Drip-Type and Pressurized Systems

Disdrometric measurements were performed following different experimental protocols depending on the type of rainfall generation system, namely DRS and PRS.

For DRS devices (KS, MKS, DG), which generate individual droplets from single capillary tubes, the disdrometer was positioned beneath the outlet of the dripping device for each fall-height condition. This setup ensured that the falling droplets intercepted the geometric center of the Parsivel^2 sampling area, thereby minimizing edge effects and guaranteeing that the measured signal corresponded to a single droplet at a time.

Measurements were conducted over fixed intervals of 15 minutes, and the resulting particle size–velocity distributions (PSVDs) were assumed to be representative of the droplet generation mechanism. In other words, for each experimental condition, a specific fall height could be associated with a corresponding droplet diameter and mean fall velocity generated by the DRS device, since under identical operating conditions these systems produce droplets with consistent and repeatable characteristics.

Where required, the obtained data were used to compare disdrometric measurements with alternative measurement techniques, such as photographic methods, or with empirical relationships for estimating raindrop fall velocities.

For the PRS installed at the Hydrology Laboratory of the University of Palermo, at the present stage, the disdrometric characterization was carried out with reference to a single nozzle configuration (120°_490608). Additional measurement campaigns are planned to extend the same experimental protocol to other nozzle types that proved to be of interest from an applicative perspective, in order to broaden the characterization of the PRS.

A different measurement strategy than DRS was adopted to account for the spatial heterogeneity of the simulated rainfall. Due to the atomization process at the nozzle outlet, the simulated precipitation can be characterized by spatial variability in both drop size distribution and rainfall intensity. Consequently, the disdrometer was used to explore the spatial variability of rainfall properties within the wetted area (Figure 26).

Differently from the volumetric characterization performed using rain collectors, which covered the entire wetted surface, the disdrometric measurements were limited to the central portion of the rainfall pattern (Figure 26b).

An area spatially consistent with the central 60 cm portion (Figure 21) previously identified through volumetric measurements as the most homogeneous zone of the simulator, was investigated. Specifically, the Parsivel^2 disdrometer was sequentially positioned at 33 distinct sampling locations distributed across the entire investigated surface (Figure 26b).

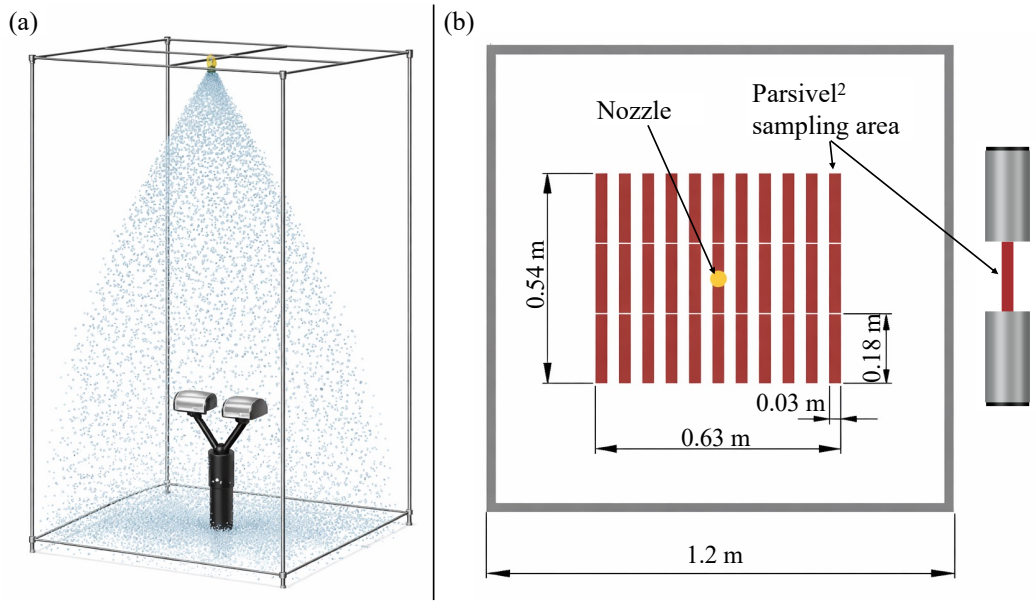

Figure 26. 3D representation of the rainfall simulation setup with the Parsivel^2 disdrometer located at the center of the wetted area generated by the PRS of Palermo (a), and the actual measurement positions used to investigate the spatial variability of rainfall properties (b).

At each sampling location, disdrometric measurements were conducted for a duration of 15 minutes, with raw particle size and velocity distributions (PSVD) recorded at a temporal resolution of 1 minute. For each sampling position, rainfall intensity, kinetic power, and momentum were computed from the measured PSVD using Equations (46), (47), and (48). The values obtained at 1-minute resolution were subsequently averaged over the 15-minute measurement interval, yielding representative estimates of the local rainfall characteristics.

The spatially distributed data of rainfall intensity, kinetic power, momentum, and diameter-related statistics (median diameter, median volume diameter, mean diameter, and standard deviation of diameters) were used both to compute the CUC

according to Equation (38) and to generate thematic maps with GIS support, aimed at providing a spatial visualization of the observed variability.

Furthermore, the applicability of the empirical relationship developed in this study for estimating the drop fall velocity as a function of diameter and height of fall, Equation (52), originally derived from single-drop measurements, was evaluated under pressurized operating conditions for the PRS of Palermo. For each drop diameter class, weighted mean fall velocities were derived from the Parsivel^2 raw PSVD and compared with the velocities predicted by Equation (52).

A similar disdrometric approach was adopted for the characterization of the PRS installed at the University of León. In this configuration, the simulator operates with a large fall height, specifically designed to promote the development of raindrop fall velocities comparable to those observed under natural precipitation conditions. Based on preliminary volumetric assessments of the rainfall spatial distribution, the disdrometric characterization was focused on a central wetted area of 1.2 m × 1.2 m (Figure 27). This area was selected because it exhibited the most homogeneous rainfall pattern in terms of intensity, while peripheral zones were characterized by larger spatial gradients.

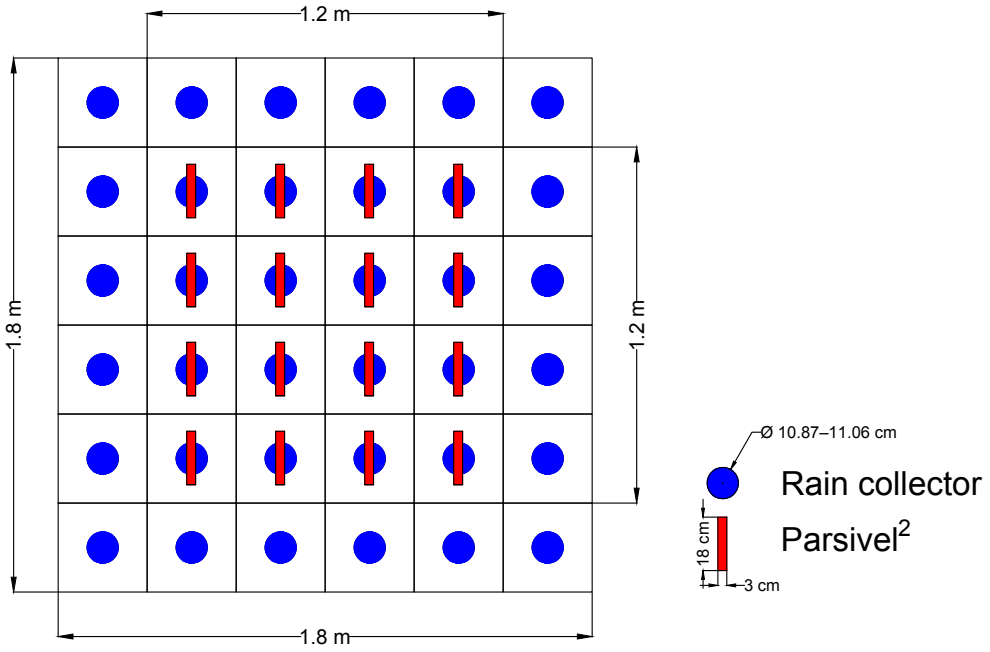

Figure 27. Schematic representation of the sampling layout, illustrating the transition from the preliminary volumetric characterization performed over a 1.8 m × 1.8 m wetted area to the disdrometric characterization, which was restricted to a smaller and more spatially uniform wetted area of 1.2 m × 1.2 m.

Disdrometric measurements were carried out by sequentially positioning the Parsivel[2] sensor at 16 different locations within the selected 1.2 m × 1.2 m area. At each sampling location, rainfall was applied for a fixed duration of 15 minutes, during which the disdrometer recorded the Particle Size and Velocity Distributions at a temporal resolution of 1 minute.

From the raw PSVD, rainfall intensity, kinetic power, and momentum were calculated using equations (46), (47), and (48), respectively, and subsequently averaged over the entire measurement duration, yielding representative values for each spatial position.

The spatial uniformity of the simulated rainfall was then evaluated by computing the CUC in terms of I_{OTT}, $P_{n,OTT}$, and M_{OTT} using Equation (38). In addition, thematic maps were generated using GIS software to visually represent the spatial variability of the investigated rainfall properties.

Finally, to verify the capability of the PRS of León to generate raindrops with fall velocities comparable to those of natural rainfall, the measured drop velocities were analyzed as a function of drop diameter. Similarly to the approach adopted for the PRS of Palermo, for each diameter class, weighted mean fall velocities were derived from the disdrometric dataset and compared with expected velocity-diameter relationships, including:

(i) the formulation proposed by Atlas et al. (1973) for natural raindrops:

$$V_{(D)} = 9.65 - 10.3 \exp\left(-0.6\frac{D}{10}\right) \tag{58}$$

(ii) the relationship developed by Ferro (2001), reported in Equation (21);

(iii) the relationship developed in this study for simulated rainfall under laboratory conditions, reported in Equation (52). In this latter case, the comparison was aimed at evaluating whether the applicability of the empirical formulation could be extended to operating conditions characterized by large fall heights, under which raindrops are expected to approach terminal velocity regimes.

2.3 Statistical Analysis

To evaluate the accuracy and reliability of the analyses carried out in this study, a set of statistical error metrics and statistical tests was adopted. These tools quantify complementary aspects of agreement between measured and estimated quantities, including systematic bias, average deviation magnitude, dispersion of errors, goodness of fit, and statistical significance of differences among experimental conditions.

Error magnitude was assessed through the Mean Relative Error (MRE), the Mean Absolute Error (MAE), and the percentage of observations characterized by an absolute relative error lower than or equal to a predefined threshold. Model–data agreement and dispersion were further evaluated using the coefficient of determination (R^2) and the Root Mean Square Error (RMSE). In addition, model predictive capability was assessed using the Nash–Sutcliffe Efficiency Index (NSEI). Statistical differences among experimental configurations were analyzed through analysis of variance (ANOVA).

In the following formulations, x_m denotes a measured reference value obtained from experimental observations, while x_c denotes the corresponding calculated or estimated value derived from empirical relationships, theoretical models, or instrument measurements under evaluation. The number of paired observations is denoted by N, whose value depends on the specific analysis performed and coincides with the sample size of the considered dataset (e.g., number of observed drop size distributions, number of rainfall events, number of measured drop fall velocities, etc.).

The MRE quantifies the average relative bias between calculated and measured values while preserving the sign of deviations. Values close to zero indicate negligible systematic bias, whereas positive or negative values denote overall overestimation or underestimation, respectively:

$$MRE = \frac{1}{N}\sum_{i=1}^{N}\frac{x_c - x_m}{x_m} \tag{59}$$

The MAE represents the average magnitude of relative deviations between calculated and measured values, regardless of sign, and is therefore indicative of overall estimation accuracy.

$$MAE = \frac{1}{N}\sum_{i=1}^{N}\left|\frac{x_c - x_m}{x_m}\right| \tag{60}$$

MRE and MAE are expressed in percentage by multiplying by 100.

To complement mean-based metrics, the proportion of observations whose absolute relative error falls within predefined accuracy bands was evaluated. In this study, thresholds of ±20% and ±10% were adopted depending on the specific application. The ±20% threshold was primarily used for natural rainfall observations, where higher variability is expected, while the ±10% threshold was mostly employed in experiments under controlled laboratory conditions.

The R^2 expresses the fraction of variance in measured data explained by the model or empirical relationship under analysis. Values approaching unity indicate strong agreement and high explanatory capability. R^2 was computed as:

$$R^2 = 1 - \frac{\sum_{i=1}^{N}(x_m - x_c)^2}{\sum_{i=1}^{N}(x_m - \overline{x_m})^2} \tag{61}$$

where $\overline{x_m}$ is the mean of measured values.

In this study, Equation (61) is applied in two main contexts. First, it is used in the validation of the empirical drop fall velocity relationship, Equation (52), where x_m and x_c represent measured and calculated fall velocities, respectively. Second, it is employed in the goodness-of-fit analysis of drop size distribution models, where x_m and x_c correspond to the measured cumulative probability $P_{(D),i}$ and calculated $P_{(D)}$ that the raindrop diameter is less than D. The cumulative probability, $P_{(D)}$, is computed using Equations (18) and (33) for the Gamma and Weibull distributions, respectively.

The RMSE measures the quadratic mean dispersion of deviations between calculated and measured values. It is sensitive to outliers and indicative of overall model performance. This indicator can be determined as:

$$RMSE = \sqrt{\frac{\sum_{i=1}^{N}(x_c - x_m)^2}{N}} \tag{62}$$

In this study, Equation (62) is used to evaluate the agreement between measured and calculated event soil loss at the Sparacia experimental site. In this application, N coincides with N_e, i.e. the number of considered rainfall events, while x_m and x_c represent measured and calculated event soil loss, respectively. Calculated soil loss is obtained from Equation (64), in which the erosivity factor R_e is determined using Equation (3) for the classical USLE formulation and Equation (65) for the new erosivity index introduced in this study (Section 3.1).

The NSEI (Nash and Sutcliffe, 1970) evaluates a model's predictive capability relative to the mean of the observed data. It provides a dimensionless measure of model performance ranging from $-\infty$ to 1. A value of 1 indicates perfect agreement, 0 indicates performance equivalent to the mean of observations, and negative values indicate performance worse than the mean predictor.

$$NSEI = 1 - \frac{\sum_{i=1}^{N}(x_m - x_c)^2}{\sum_{i=1}^{N}(x_m - \overline{x_m})^2} \tag{63}$$

In this study, Equation (63) is applied to the same soil loss evaluation performed for RMSE at the Sparacia experimental site. Therefore, $N = N_e$, and x_m and x_c denote measured and calculated event soil loss, respectively, computed as described above.

Finally, a two-way ANOVA with replication was applied exclusively to the León rainfall simulator experiments, where the specific experimental conditions adopted for rainfall spatial uniformity assessment (Section 2.2.3.2) required statistical verification of the validity of the defined experimental treatments.

The analysis evaluated whether simulated rainfall intensity differed significantly among treatments (T1–T3), which incorporate variations in collector typology and simulation duration, and among collector positions within the sampling grid. Both main effects and their interaction were tested to determine whether these factors were responsible for statistically significant deviations in the measured rainfall intensity. Statistical significance was assessed by comparing p-values at the significance level $\alpha = 0.05$.

3 RESULTS AND DISCUSSION

This chapter presents and discusses the main results of the research, which are organized into four sections that address complementary aspects of rainfall erosivity and soil erosion.

Section 3.1 investigates the relationship between event soil loss and rainfall erosivity using an experimental dataset collected at the Sparacia site. The analysis is based on a unique set of field observations in which plot-scale soil loss measurements are coupled with contemporaneous high-resolution disdrometric measurements of natural rainfall, an experimental configuration that has not been previously documented in the soil erosion literature.

Section 3.2 examines the reliability of the Weibull distribution in reproducing measured drop size distributions using an extensive disdrometric database. Closed-form analytical relationships are derived to estimate rainfall kinetic power and momentum directly from the Weibull parameters. The physical interpretation and sensitivity of these parameters are analyzed, and the Weibull formulation is compared with the classical Gamma distribution.

Section 3.3 builds on the theoretical advances in Section 3.2 to develop and validate improvements to a patented method for estimating the energetic characteristics of rainfall. Specifically, a new procedure is proposed to derive the Weibull parameters and rainfall energy descriptors from rainfall intensity and drop counts, demonstrating that accurate estimates of kinetic power and momentum can be obtained without full disdrometric measurements.

Finally, Section 3.4 provides a comprehensive characterization of the rainfall simulators employed in this study. Using combined volumetric, disdrometric, and energetic analyses, the hydraulic behavior, spatial uniformity, drop-size distributions, fall velocities, and energetic properties of drip-type and pressurized simulators are evaluated, resulting in a generalized framework for their hydrological and energetic characterization.

3.1 Rainfall Erosivity and Soil Loss Measurements at Sparacia

This section presents a field-based analysis aimed at evaluating the capability of a widely used rainfall erosivity index, specifically the classical USLE-based formulation, to reproduce measured event soil loss.

In parallel, a novel erosivity index is introduced, developed using an experimental dataset collected at the Sparacia site in which plot-scale soil loss measurements are paired with contemporaneous disdrometric observations of natural rainfall. Beyond relying on direct measurements of rainfall kinetic power, the proposed index reformulates the classical R_e concept, which in its original USLE formulation combines the maximum 30-min rainfall intensity (I_{30}) with rainfall kinetic energy empirically estimated from rainfall intensity. The new formulation instead aggregates rainfall intensity and kinetic power at the temporal resolution of the measurements, enabling a more physically consistent representation of the intra-event variability of erosive forcing and a direct evaluation of erosivity–soil loss relationships at the event scale.

Rainfall properties were monitored using the ODM 470 optical disdrometer, while soil loss was measured at the event scale across four replicated bare plots with identical soil type and land use but different slope gradients (22% and 26%). Under these conditions, for a given plot characterized by fixed soil properties, slope length, and land use, Equation (2) reduces to:

$$A_e = sR_e \tag{64}$$

where s (–) is a constant.

Figure 28 shows the relationship between the measured A_e obtained from Equation (64) and averaged over the replicated plots, and the rainfall erosivity index R_e computed according to the classical USLE formulation, Equation (3). In particular, Figure 28a reports the *calculated* R_e, in which the kinetic power per unit volume of rainfall, $P_{n,e}/I_e$, is determined according to the Wischmeier and Smith (1978) approach, Equation (4), whereas Figure 28b plots the *measured Re*, estimated using rainfall kinetic energy derived from measured raindrop size distributions, Equation (40).

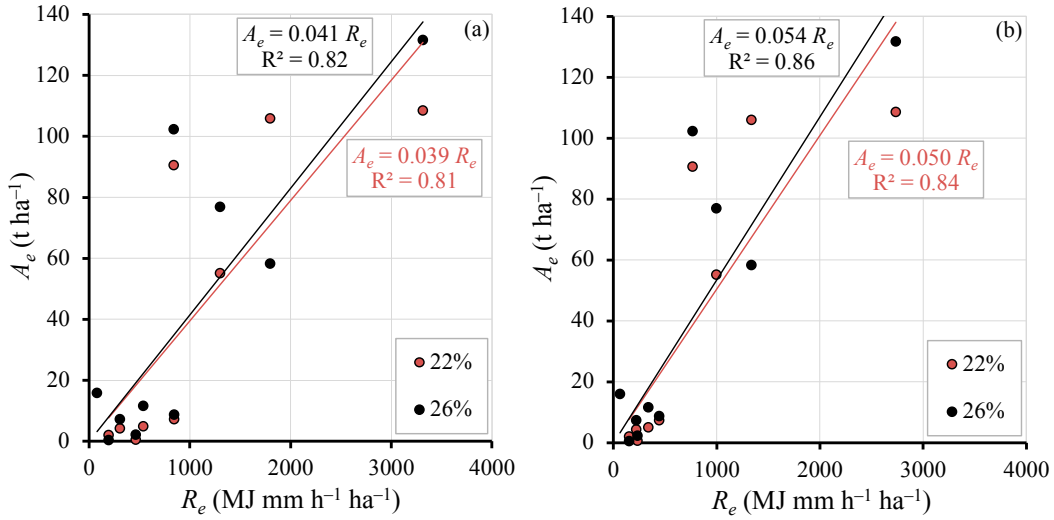

Figure 28. Relationship between the measured event soil loss, A_e, and the rainfall erosivity index, R_e, calculated using Equation (3) (a) and derived from measured raindrop size distributions (b), for the plots at 22% and 26% slope gradients.

As illustrated in Figure 28a, the pairs (*calculated* R_e; A_e) exhibit pronounced nonlinearity for both investigated slope gradients, with coefficients of determination (R^2) equal to 0.81 and 0.82 for the 22% and 26% plots, respectively. These results confirm the limited predictive capability of the USLE-based erosivity index at the event scale for the Sparacia experimental area, in agreement with previous findings reported in the literature (Bagarello et al., 2020).

The use of measured rainfall intensity and kinetic energy values leads to a slight improvement in the agreement between observed and predicted soil loss (Figure 28b). Specifically, for the 22% and 26% plots, the RMSE decreases from 25.3 t ha^{-1} to 23.8 t ha^{-1} and from 25.9 t ha^{-1} to 23.0 t ha^{-1}, respectively. Accordingly, the NSEI increases from 0.63 to 0.68 and from 0.64 to 0.77, respectively. However, computing R_e using measured rainfall kinetic energy does not substantially reduce the scatter of the data points, with R^2 values of 0.84 for the 22% plots and 0.86 for the 26% plots.

The persistence of a pronounced dispersion in the A_e-R_e relationship, even when rainfall kinetic energy is derived from direct DSD measurements, suggests that the observed variability cannot be attributed solely to uncertainties in the empirical estimation of rainfall energy. Rather, it likely reflects a limited suitability of the classical Wischmeier and Smith erosivity formulation for representing rainfall aggressiveness under the Mediterranean conditions of the Sparacia site. The USLE

erosivity index was originally developed from rainfall records in temperate regions of the United States, and its reliance on I_{30} as a representative event descriptor may be less appropriate in Mediterranean climates.

Indeed, in the classical formulation of R_e, rainfall kinetic energy is aggregated over the event and combined with a single characteristic intensity value, I_{30}, implicitly assuming that this combination adequately represents the erosive forcing of the entire rainfall event. However, such an approach does not explicitly account for the temporal variability of rainfall intensity and energy within the event.

To investigate whether a different aggregation of rainfall energy and intensity could improve the description of event soil loss, an alternative rainfall erosivity index, R_e^* (MJ mm h^{-1} ha^{-1}), was introduced. This index is defined as:

$$R_e^* = \sum_{e=1}^{k} \frac{P_{n,e}}{I_e} h_e I_e \tag{65}$$

where $P_{n,e}$, I_e, and h_e are the rainfall kinetic power, intensity, and depth measured at the same temporal resolution, set to 1-minute. Therefore, unlike the classical R_e, the proposed R_e^* aggregates the contributions of $P_{n,e}$ and I_e, representing respectively the detachment potential and the transport capacity, measured at the same temporal resolution, rather than relying on a single event-scale intensity such as I_{30}.

Figure 29 shows the relationship between the measured A_e and the alternative rainfall erosivity index, R_e^*, for both slope gradients.

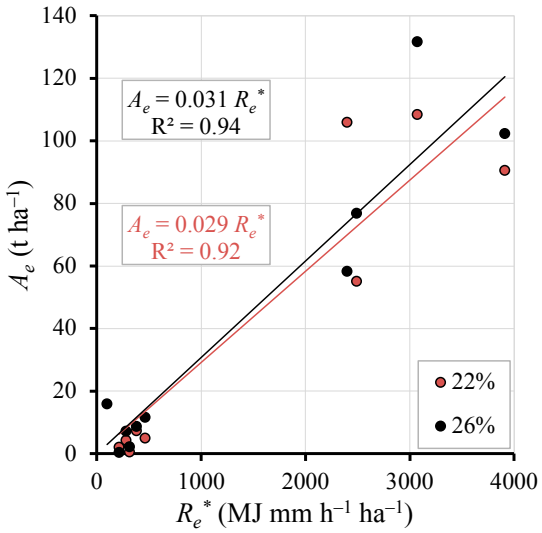

Figure 29. Relationship between the measured soil loss (A_e) and the alternative rainfall erosivity index (R_e^*) for the plots at 22% and 26% slope gradients.

Compared with the classical formulation, the use of R_e* yields a marked improvement in the linearity of the soil loss-erosivity relationship. Notably, the R^2 increases to 0.92 and 0.96 for the 22% and 26% plots, respectively, while RMSE values decrease to 16.5 t ha^{-1} and 14.9 t ha^{-1}, and NSEI values increase to 0.84 and 0.91.

Despite the improved performance of the alternative index, Figure 29 still exhibits a noticeable scattering of data points, particularly for event soil loss values exceeding approximately 60 t ha^{-1}. These high soil loss values are typically associated with long sequences of multiple erosive rainfall events at the Sparacia site, for which plot-scale soil loss measurements are inherently more uncertain.

These findings suggest that further investigations are necessary to enhance the existing database of contemporaneous soil loss measurements and rainfall microphysical observations. Expanding such datasets would enable a more robust assessment of the predictive capability of rainfall erosivity indices and support the development of improved formulations informed by future experimental evidence.

3.2 Analysis of Natural Rainfall Using the Weibull Distribution

This section presents the main theoretical and methodological advancements that support the use of the Weibull distribution to describe rainfall microphysics and estimate rainfall energetic properties in Mediterranean environments. The analysis is based on an extensive experimental dataset comprising more than 47,000 one-minute DSDs collected at the Palermo and El Teularet experimental sites, obtained using the same optical disdrometer and processed according to the methodological framework described in Section 2.1.2.

Specifically, the reliability of the Weibull distribution in reproducing measured Mediterranean DSDs is assessed through a systematic fitting analysis. Second, an analytical framework is developed, allowing rainfall kinetic power and momentum to be expressed explicitly as functions of the Weibull shape and scale parameters, providing closed-form relationships for the estimation of rainfall energetic characteristics. Third, the physical meaning of the Weibull parameters is examined, and a sensitivity analysis is carried out to evaluate how uncertainties in their estimation affect kinetic power and momentum estimates. Finally, the performance of the Weibull-based approach is compared with that of the widely used Gamma distribution, highlighting similarities in predictive accuracy and the conceptual advantages of the Weibull formulation.

3.2.1 Reliability of Weibull distribution in reproducing Mediterranean DSDs

The Weibull distribution, Equation (30), describes the raindrop population reaching a unit horizontal surface during a unit time interval. Its cumulative form is expressed as the integral function, $F_{(D)}$, of Equation (30):

$$F_{(D)} = N_0 \left(1 - exp\left[-\left(\frac{D}{\sigma}\right)^{\eta}\right]\right) \tag{66}$$

By integrating the corresponding probability density function over the entire diameter range, the total number of raindrops is obtained as:

$$N = \int_0^{\infty} N(D)\, dD = \int_0^{\infty} N_0 \frac{\eta}{\sigma}\left(\frac{D}{\sigma}\right)^{\eta-1} exp\left[-\left(\frac{D}{\sigma}\right)^{\eta}\right] dD = N_0 \tag{67}$$

This result assigns a clear physical meaning to the parameter N_0, demonstrating that it represents the total number of raindrops reaching the unit surface per unit time, rather than being a constant fitting coefficient as previously suggested in the literature by Sekine and Lind (1982).

The Weibull distribution was fitted to a total of 47,860 measured DSDs using the Method of Moments (MM) (Section 2.1.2.2) to estimate the η and σ parameters, enforcing the coincidence between the measured and theoretical values of both the median diameter, D_{50}, and the median volume diameter, D_0. Representative examples of the fitted distributions for different rainfall-intensity classes at both experimental sites are shown in Figure 30, illustrating the Weibull distribution's ability to reproduce the observed DSD shapes across a wide range of rainfall conditions.

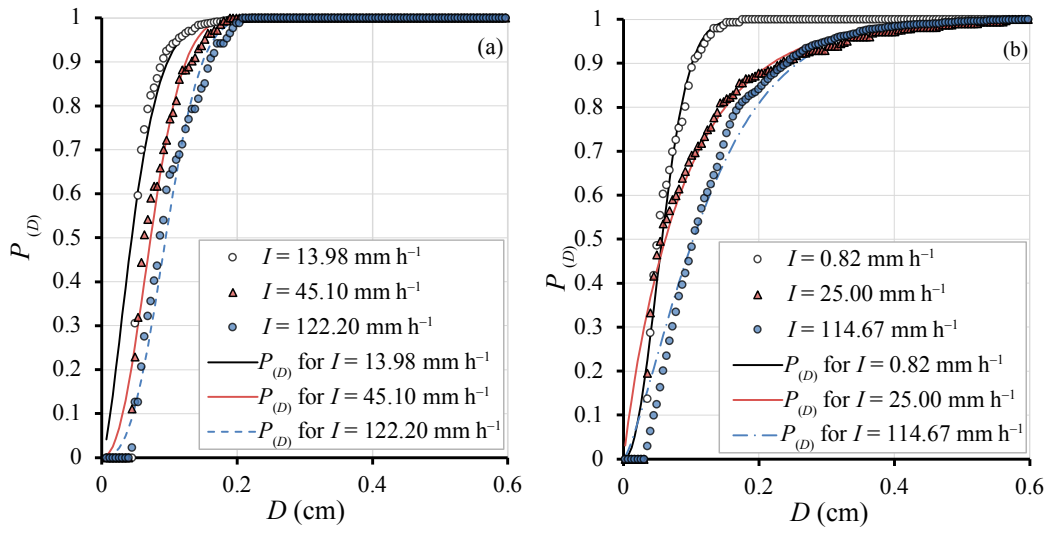

Figure 30. Examples of fitting of Weibull's distribution at Palermo (a) and El Teularet (b) experimental sites.

The fitting performance was quantified using the coefficient of determination, as defined in Equation (61). Mean R^2 values of 0.953 for Palermo and 0.962 for El Teularet were obtained, indicating a high level of agreement between the measured and modelled distributions.

To investigate the influence of rainfall intensity on fitting reliability, the DSDs were aggregated into rainfall intensity classes with an amplitude of 5 mm h^{-1}, and the corresponding mean R^2 values were computed. For each investigated experimental

site, the relationship between the mean R^2 and the mean rainfall intensity, I_{mean} (mm h^{-1}), is reported in Figure 31.

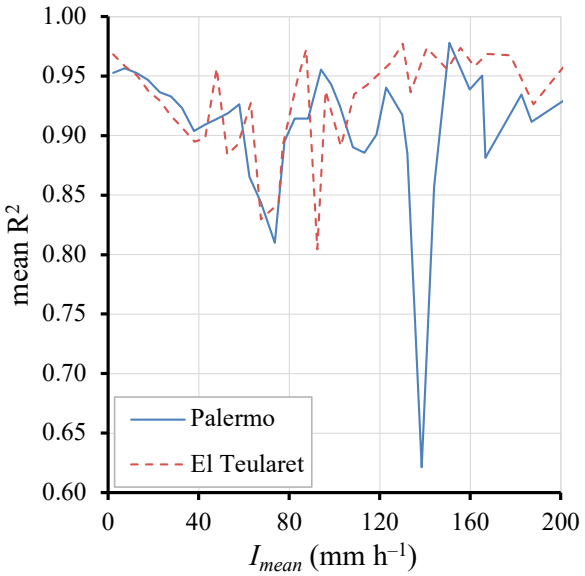

Figure 31. Relationship between the mean R^2 and I_{mean}, for each experimental site.

In agreement with Alonge and Afullo (2012), Figure 31 highlights a gradual decrease in fitting accuracy with increasing rainfall intensity up to approximately 40 mm h^{-1}, beyond which no systematic trend is observed. This behavior, consistent across both experimental sites, is primarily attributed to the reduced number of available DSD samples at high rainfall intensities (Table 2), which limits the robustness of averaged statistical indicators. Overall, DSDs poorly fitted by the Method of Moments ($R^2 < 0.8$) represent 0.58% of the entire dataset (277 DSDs), while those associated with rainfall intensities exceeding 40 mm h^{-1} account for only 0.09% of the observations (44 DSDs). This confirms that the Weibull distribution maintains a high degree of reliability even under intense rainfall conditions.

The relationship between the estimated Weibull parameters was also investigated. A very weak correlation between the shape parameter η and the scale parameter σ was observed (Figure 32), indicating that these parameters describe independent aspects of the raindrop population. This behavior is consistent across both experimental sites, as shown for Palermo (Figure 32a) and El Teularet (Figure 32b).

Table 2. Rainfall intensity classes (5 mm h^{-1} width) and corresponding mean rainfall intensity, I_{mean}, mean coefficient of determination, R^2, of the Method of Moments (MM), and number of analyzed Drop Size Distributions (DSDs) for the Palermo and El Teularet sites.

		Palermo			**El Teularet**		
Rainfall intensity range (mm h^{-1})		I_{mean} (mm h^{-1})	*Mean* R^2	Observed DSDs	I_{mean} (mm h^{-1})	*Mean* R^2	Observed DSDs
0.50	5.49	2.20	0.953	34529	2.16	0.968	3764
5.50	10.49	7.35	0.957	4998	7.73	0.958	966
10.50	15.49	12.54	0.953	1347	12.55	0.951	396
15.50	20.49	17.63	0.947	541	17.73	0.938	155
20.50	25.49	22.85	0.936	306	22.96	0.929	99
25.50	30.49	27.79	0.933	148	27.77	0.916	45
30.50	35.49	32.71	0.923	104	32.32	0.908	31
35.50	40.49	37.88	0.904	78	38.15	0.895	28
40.50	45.49	42.92	0.909	59	42.81	0.897	16
45.50	50.49	47.47	0.914	36	47.85	0.956	8
50.50	55.49	52.94	0.919	23	52.58	0.884	9
55.50	60.49	57.84	0.926	20	57.30	0.893	9
60.50	65.49	62.49	0.865	11	63.05	0.928	7
65.50	70.49	67.50	0.844	13	67.58	0.830	3
70.50	75.49	73.57	0.810	5	75.28	0.843	2
75.50	80.49	78.03	0.895	7	77.02	0.891	4
80.50	85.49	82.42	0.914	7	83.56	0.947	4
85.50	90.49	88.27	0.914	6	87.51	0.973	2
90.50	95.49	94.03	0.955	2	92.50	0.805	3
95.50	100.49	98.46	0.943	8	96.18	0.937	2
100.50	105.49	102.33	0.925	4	102.79	0.891	3
105.50	110.49	108.11	0.890	1	108.77	0.935	3
110.50	115.49	113.16	0.886	7	114.38	0.943	4
115.50	120.49	118.51	0.901	2	124.38	0.960	2
120.50	125.49	122.71	0.940	3	130.05	0.977	1
125.50	130.49	129.98	0.917	2	133.65	0.936	2
130.50	135.49	132.11	0.885	1	140.82	0.974	1
135.50	140.49	138.42	0.621	1	149.64	0.956	1
140.50	145.49	144.11	0.858	3	155.74	0.974	1
150.50	155.49	150.66	0.978	1	161.75	0.958	2
155.50	160.49	159.66	0.939	1	167.47	0.968	2
160.50	165.49	165.17	0.950	1	177.68	0.967	2
165.50	170.49	166.65	0.881	1	187.78	0.926	3
180.50	185.49	182.54	0.934	1	208.93	0.976	1
185.50	190.49	187.10	0.911	1	–	–	0
200.50	205.49	203.33	0.932	1	–	–	0

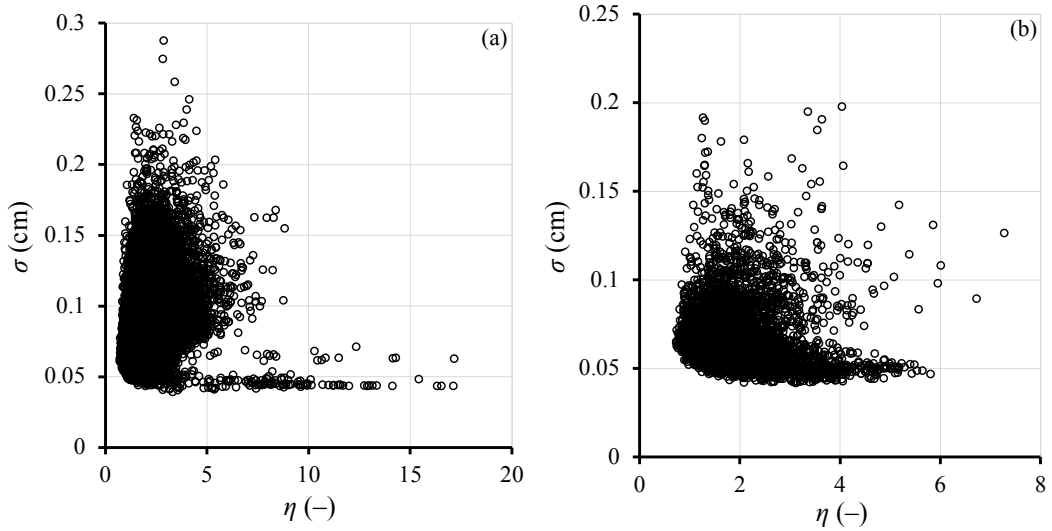

Figure 32. Relationship between the shape parameter, η, and the scale parameter, σ, of the Weibull distribution estimated from the observed drop size distributions (DSDs) using the Method of Moments (MM) for the Palermo (a) and El Teularet (b) experimental sites. Each point represents an individual DSD.

Figure 33 shows the relationship between rainfall intensity and the Weibull parameters σ (Figure 33a) and η (Figure 33b). A weak correlation is observed in both cases and at both the observed experimental sites, indicating that intensity alone is not sufficient to synthesize the microphysical structure of precipitation, as DSDs characterized by markedly different shape and scale parameters can occur under similar intensity conditions.

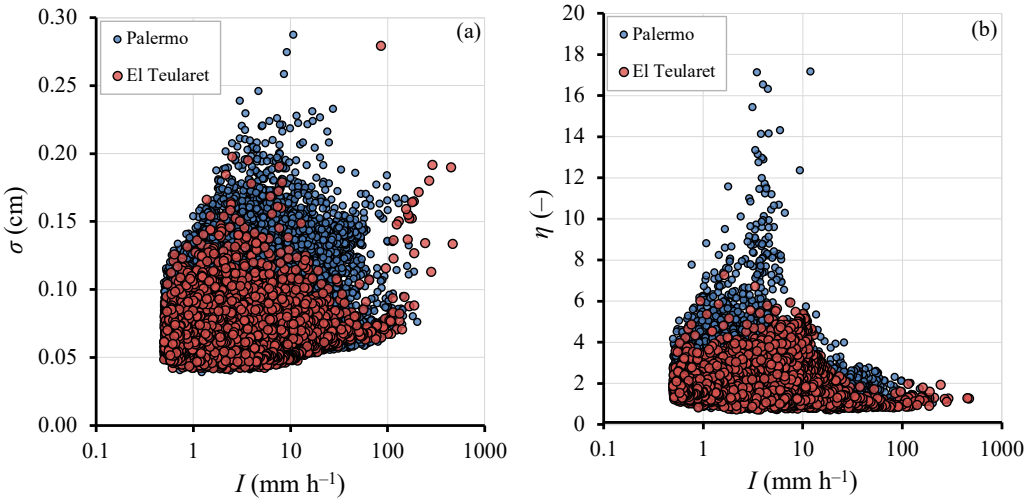

Figure 33. Relationship between rainfall intensity, I, and the Weibull scale parameter σ (a) and shape parameter η (b). Results are shown for the Palermo and El Teularet experimental sites.

These findings contradict earlier studies by Sekine and Lind (1982) that suggested a direct power-law relationship between Weibull parameters and rainfall intensity, based on datasets collected under a range of climatic conditions by Laws and Parsons (1943), Sander (1975), and Wickerts (1982). However, those datasets were obtained under climatic conditions that differ from those of the Mediterranean environment considered in this investigation. In this framework, the Weibull parameters seem to reflect intrinsic properties of raindrop populations that are largely independent of bulk rainfall descriptors.

3.2.2 Theoretical Determination of Rainfall Kinetic Power and Momentum from the Weibull Distribution

Once the reliability of the Weibull distribution in reproducing Mediterranean raindrop size distributions has been established, the distribution can be used to derive physically based relationships for estimating rainfall energetic characteristics.

Rainfall intensity can be expressed as a function of the raindrop size distribution through the volumetric flux of water (Salles et al., 2002):

$$I = 3.6\frac{\pi}{6}\int_0^\infty D^3 N_{(D)} dD \tag{68}$$

where D is expressed in cm and $N_{(D)}$ in m^{-2} s^{-1}. By substituting the Weibull distribution of Equation (30) into Equation (68) and solving the integral, rainfall intensity can be written as:

$$I = 3.6\frac{\pi}{6} N_0 \sigma^3 \Gamma\left(\frac{3}{\eta} + 1\right) \tag{69}$$

Equation (69) provides a direct link between rainfall intensity and the parameters of the Weibull distribution, and allows the intercept parameter N_0 to be expressed as:

$$N_0 = \frac{I}{3.6\frac{\pi}{6}\sigma^3 \Gamma\left(\frac{3}{\eta} + 1\right)} \tag{70}$$

By adopting the velocity–diameter relationship proposed by Atlas and Ulbrich (1977), Equation (10), and substituting both the Weibull drop size distribution, Equation (30), and the velocity expression into the expression representing the

rainfall kinetic power per unit area and time, P_n (J m^{-2} h^{-1}), Equation (19), the following analytical expression is obtained:

$$P_n = 10^{-6}\frac{\rho\pi}{12}17.67^2 N_0 \sigma^{4.34}\Gamma\left(\frac{4.34}{\eta}+1\right) \tag{71}$$

Finally, by replacing N_0 with the expression given by Equation (70), a closed-form relationship is obtained:

$$P_n = 6.2735\times10^{-5}\rho\sigma^{1.34}\frac{\Gamma\left(\frac{4.34}{\eta}\right)}{\Gamma\left(\frac{3}{\eta}\right)}I \tag{72}$$

Equation (72) shows that the kinetic power per unit volume of rainfall, P_n/I, depends exclusively on the intrinsic characteristics of precipitation, namely the shape parameter η and scale parameter σ of the Weibull distribution. Rainfall intensity acts only as a scaling factor, confirming that energetic properties cannot be fully described by intensity alone.

Rainfall momentum per unit area and time, M (N m^{-2}), was derived following a similar approach. Specifically, substituting Equations (30) and (10) into Equation (20), the following analytical expression is obtained:

$$M = 10^{-6}\frac{\rho}{3.6}17.67\sigma^{0.67}\frac{\Gamma\left(\frac{3.67}{\eta}+1\right)}{\Gamma\left(\frac{3}{\eta}+1\right)}I \tag{73}$$

According to Equation (73), rainfall momentum depends on rainfall intensity as well as on the Weibull shape parameter η and scale parameter σ, in a form analogous to that derived for kinetic power.

The theoretical relationships for rainfall kinetic power were validated by comparing the values calculated using Equations (72) and (73), hereafter referred to as *calculated* P_n and *calculated* M, with those directly computed from the measured raindrop size distributions, hereafter referred to as *measured* P_n and *measured* M. The latter were obtained by applying Equations (40) and (41) to the raw DSD data and associating each raindrop diameter with the corresponding terminal velocity, calculated according to Equation (10).

Figure 34 shows the comparison between measured and calculated rainfall kinetic power and momentum. In particular, Figure 34a and Figure 34b compare

measured P_n and *calculated* P_n for the Palermo and El Teularet datasets, respectively, while Figure 34c and Figure 34d show the corresponding comparisons for *measured M* and *calculated M*.

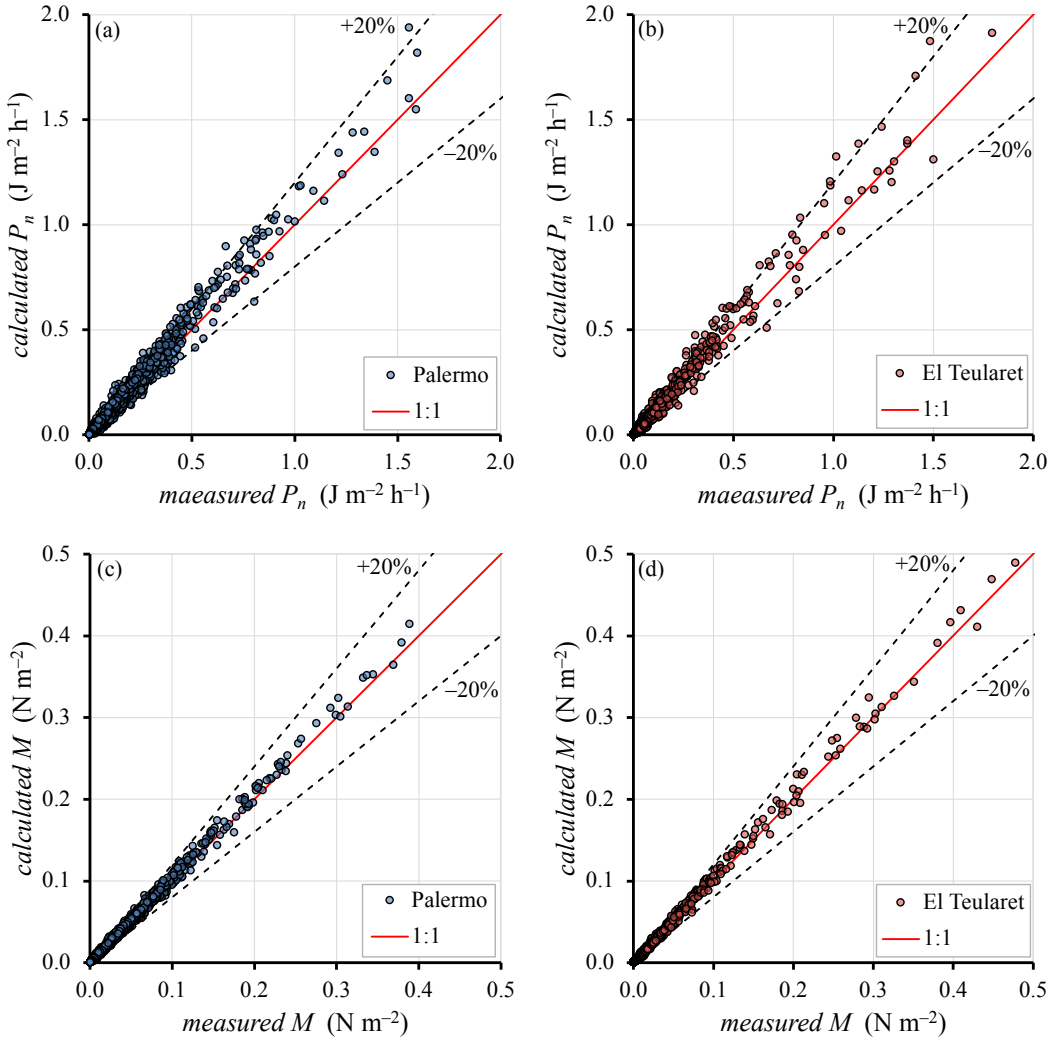

Figure 34. Comparison between measured and calculated rainfall energy-related parameters based on the Weibull-derived theoretical relationships. Panels (a) and (b) show measured versus calculated rainfall kinetic power, P_n, for the Palermo and El Teularet dataset, respectively, where calculated values are obtained from Eq. (72). Panels (c) and (d) report the corresponding comparison for rainfall momentum, M, for the same datasets, with calculated values derived from Eq. (73). The red solid line denotes the 1:1 relationship, while dashed lines indicate ±20% deviation.

For both sites, the comparison shows good agreement between measured and calculated rainfall kinetic power. Many points fall within the ±20% bounds around the 1:1 line (Figure 34a and Figure 34b), and the error metrics in Table 3 indicate a

small overall underestimation (MRE from −3.1% to −4.4%) and MAE values of 8.8% and –12.4% for Palermo and El Teularet, respectively.

A clearer agreement is observed for rainfall momentum. As shown in Figure 34c and Figure 34d, the calculated and measured values closely align along the 1:1 line at both sites, with markedly reduced dispersion compared with P_n. This is supported by the statistical indicators in Table 3, which show very small bias (MRE ≈ −1% to −2%), low MAE (≈ 4-5%), and more than 98% of the estimates within ±20% error at both sites (Table 3).

Overall, the theoretical formulations derived from the Weibull distribution, Equations (72) and (73), yield satisfactory estimates of both rainfall kinetic power and momentum, with an improved agreement in terms of M.

Table 3. Statistical performance indicators for the Weibull-based estimation of rainfall kinetic power, P_n, and rainfall momentum, M, at the Palermo and El Teularet experimental sites, reporting the Mean Relative Error (MRE), Mean Absolute Error (MAE), and the percentage of data characterized by an absolute error (AE) lower than 20%.

	Palermo		El Teularet	
	P_n (J m^{-2} s^{-1})	M (N m^{-2})	P_n (J m^{-2} s^{-1})	M (N m^{-2})
MRE	−3.1 %	−1.1 %	−4.4 %	−1.8 %
MAE	8.8 %	3.8 %	12.4 %	5.3 %
Data with AE<20%	93.0 %	99.3 %	80.7 %	98.1 %

Furthermore, for rainfall intensities exceeding 40 mm h^{-1}, which are the most relevant from an erosive perspective, nearly all rainfall momentum estimates exhibit absolute errors below 20%, reaching 99% at Palermo and 100% at El Teularet (Table 4). These results indicate that, under high-intensity rainfall conditions, the relationships used to estimate rainfall momentum provide more accurate and stable predictions than those based on rainfall kinetic power.

Table 4. Summary statistics for high-intensity rainfall events ($I > 40$ mm h^{-1}) at Palermo and El Teularet. The table reports the total number of available DSDs, the subset characterized by rainfall intensities exceeding 40 mm h^{-1}, and the percentages of kinetic power (P_n) and rainfall momentum (M) estimates with absolute errors (AE) below 20%.

	Palermo	El Teularet
Total number of DSDs	42279	5581
Number of DSDs with $I > 40$ mm h^{-1}	234	105
DSDs with AE (P_n) < 20%	89.3 %	78.1 %
DSDs with AE (M) < 20%	98.7 %	100.0 %

Rainfall kinetic power and rainfall momentum emerge as physically meaningful variables for describing rainfall aggressiveness. An important advantage of the present framework is that the relationships used to estimate P_n and M are analytically derived from the Weibull distribution and are therefore physically based rather than empirical or site-specific.

The present analysis demonstrates that rainfall momentum provides more reliable estimates than kinetic power. This finding supports the hypothesis that descriptors based on rainfall momentum are better suited for the characterization of rainfall erosivity and strengthens the motivation for the development of alternative erosivity indices that explicitly incorporate rainfall momentum rather than relying solely on kinetic energy formulations.

Finally, these results indicate that, in agreement with previous studies (Carollo et al., 2017; Carollo, Ferro, et al., 2018; Serio et al., 2019a, 2019b), the accurate estimation of rainfall energy–related characteristics relies more on the correct representation of a limited number of key descriptors than on the reproduction of the entire raindrop size distribution.

3.2.3 Physical and Statistical Interpretation of the Weibull Shape and Scale Parameters and Sensitivity of Rainfall Energetic Estimates

In Mediterranean rainfall conditions, the Weibull parameters do not exhibit a clear correlation with rainfall intensity (Figure 33). Therefore, starting from the theoretical relationships derived for estimating rainfall kinetic power and momentum, the physical meaning of the Weibull shape and scale parameters was

investigated, together with an assessment of how uncertainties in their estimation propagate into rainfall energetic descriptors.

The shape parameter, η, governs the form of the raindrop size distribution and controls the relative spread of drop diameters around the mean value. This role can be clarified by expressing the coefficient of variation of the Weibull distribution, CV_W (–), as the ratio of the standard deviation, $\sigma_{(D)}$, to the mean diameter, $\mu_{(D)}$, of the DSD, obtained from Equations (35) and (34) for the Weibull distribution:

$$CV_W = \frac{\sigma_{(D)}}{\mu_{(D)}} = \frac{\left[2\eta\Gamma\left(\frac{2}{\eta}\right) - \Gamma^2\left(\frac{1}{\eta}\right)\right]^{0.5}}{\Gamma\left(\frac{1}{\eta}\right)} \quad (74)$$

According to this expression, the coefficient of variation depends exclusively on the shape parameter η, which therefore represents the primary descriptor of the internal variability of the raindrop population. Within the range of η values observed in the present investigation (0.3 – 17.2), the relationship between CV_W and η, shown in Figure 35, is monotonic and can be accurately approximated by a power-law expression, confirming that η uniquely controls the dispersion of drop diameters within the distribution:

$$\eta = 1.06\ CV_W^{-1.054} \quad (75)$$

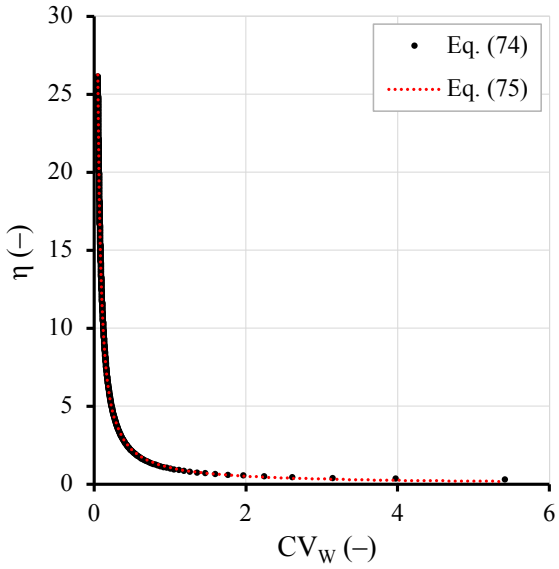

Figure 35. Relationship between the Weibull shape parameter η and the coefficient of variation of the raindrop diameter distribution, CV_W, as obtained from Equations (74) (symbols) and (75) (dotted line).

From a physical perspective, variations in CV_W are associated with microphysical processes governing raindrop formation and breakup, such as aerodynamic drag and surface tension, which regulate the fragmentation of large drops into smaller ones, and therefore the shape of the DSD. Consequently, η can be interpreted as a physically meaningful parameter reflecting the dominant breakup regime of precipitation.

Substituting Equation (75) in Equations (72) and (73) allows the scale parameter σ to be explicitly expressed as a function of rainfall kinetic power and momentum, for a given rainfall intensity and shape parameter:

$$\sigma = \kappa P_n^{\frac{1}{1.34}} \tag{76}$$

$$\sigma = \kappa' M^{\frac{1}{0.67}} \tag{77}$$

where κ (cm $kg^{-\frac{1}{1.34}}$ $s^{\frac{3}{1.34}}$) and κ' (cm $kg^{-\frac{1}{0.67}}$ $m^{\frac{1}{0.67}}$ $s^{\frac{2}{0.67}}$) are functions of η and I.

These expressions demonstrate that the scale parameter is not merely a statistical quantity describing the position of the raindrop size distribution, but a physically meaningful descriptor directly linked to the energetic content of rainfall. Specifically, larger values of σ correspond to raindrop populations with a greater proportion of large diameters, which dominate both the rainfall kinetic power and the rainfall momentum. Accordingly, σ can be interpreted as a direct indicator of the energetic aggressiveness of precipitation.

Equations (76) and (77) further clarify that rainfall intensity alone is insufficient to characterize the energy of rainfall. For a fixed intensity, different combinations of η and σ may result in markedly different kinetic power and momentum values. From this perspective, the Weibull scale parameter acts as the energetic counterpart of the shape parameter: while η governs the internal variability and fragmentation regime of the raindrop population, σ directly controls the magnitude of the energy and momentum transferred to the soil surface. This dual interpretation provides a coherent physical framework that consistently links rainfall microphysics and energetic forcing.

The different sensitivity of rainfall kinetic power and momentum to uncertainties in the Weibull parameters was investigated through a sensitivity analysis of the

ratios P_n/I and M/I. Thus, the first derivatives of Equations (72) and (73) with respect to σ were computed, named $d(P_n/I)/d\sigma$ and $d(M/I)/d\sigma$, respectively.

The patterns of these derivatives, evaluated over the experimental range of σ (0.04–0.30 cm) and for representative minimum, median, and maximum values of η, are shown in Figure 36. The sensitivity of P_n/I to σ increases with increasing σ and assumes its largest values for small η, whereas it becomes negligible for higher η values (Figure 36a). Conversely, the sensitivity of M/I to σ decreases with increasing σ and remains markedly lower than that of P_n/I over the entire range of σ (Figure 36b). This result highlights that rainfall momentum is intrinsically less sensitive to uncertainties in estimating the Weibull scale parameter.

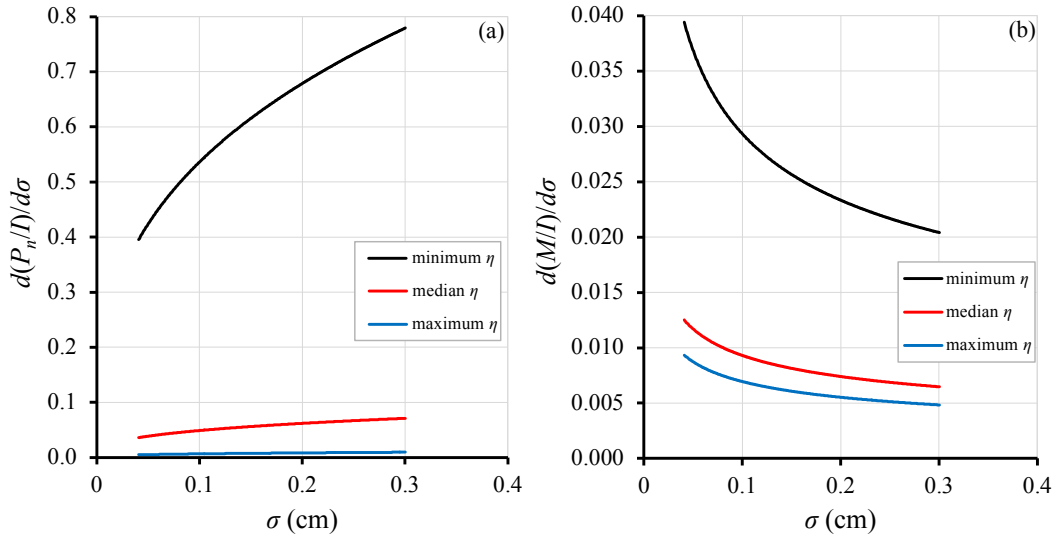

Figure 36. Sensitivity of the rainfall energy-related parameters (P_n, M) to the Weibull scale parameter, σ, for representative values of the shape parameter, η (minimum, median, and maximum). Panel (a) shows the first derivative of the kinetic power per unit rainfall depth, $d(P_n/I)/d\sigma$, while panel (b) reports the corresponding derivative of the rainfall momentum per unit rainfall depth, $d(M/I)/d\sigma$.

A complementary sensitivity analysis was performed with respect to the shape parameter η. Fixed relative variations of η (±1%, ±5%, and ±10%) were imposed, and the resulting variations in P_n/I and M/I were computed using Equations (72) and (73), respectively, and named $\Delta P_n/I$ and $\Delta M/I$.

Owing to the functional form of these equations, the relative variations of both energetic indices are independent of σ, and therefore the results are valid across the entire experimental range of the scale parameter. The results, reported in Figure 37, show that both $\Delta(P_n/I)$ and Δ(M/I) decrease as η increases, with the magnitude of

the variation being directly proportional to the imposed perturbation of η. However, for any given variation in η, the corresponding variation in $\Delta(M/I)$ is systematically smaller than that observed for $\Delta(P_n/I)$ and tends to become negligible for η values greater than approximately 5. This further confirms that rainfall momentum is less sensitive to uncertainties in the shape of the raindrop size distribution than kinetic power.

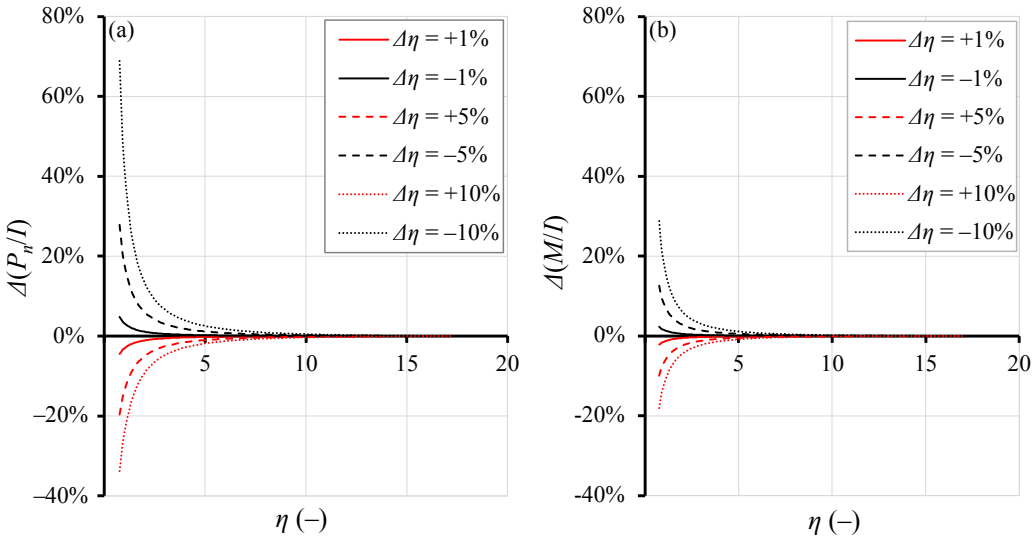

Figure 37. Sensitivity of the rainfall energetic parameters to variations in the Weibull shape parameter, η. Panel (a) shows the relative variation of the kinetic power per unit rainfall depth, Δ(Pn/I), while panel (b) reports the corresponding relative variation of the rainfall momentum per unit rainfall depth, Δ(M/I), obtained by imposing fixed perturbations of η (±1%, ±5%, and ±10%).

3.2.4 Performance Comparison Between Weibull and Gamma Distributions in Estimating Rainfall Energy-Related Properties

To further assess the robustness of the Weibull-based framework adopted in this study, its performance was compared with that of the Gamma distribution, which has been widely used in the literature to describe raindrop size distributions and to derive theoretical relationships for estimating rainfall energetic characteristics (Section 1.2.3.2).

The Gamma distribution, as given in Equation (11), was fitted to each measured DSD collected at the Palermo and El Teularet experimental sites. The distribution parameters were estimated using the same Method of Moments adopted for the Weibull distribution (Section 2.1.2.2), with D_0 and D_{50}, computed according to

Equations (14) and (15). The methodological consistency between the two approaches allowed a direct comparison of their respective performances.

The reliability of the Gamma distribution in reproducing the observed DSDs was evaluated by computing, for each distribution, the coefficient of determination (R^2), Equation (61). Table 5 lists the number of observed DSDs and the percentage of distributions with $R^2 > 0.8$ for the Gamma and Weibull fits, including intense rainfall conditions ($I > 40$ mm h^{-1}). The comparison between the fitting performances shows that the two distributions provide similar results at both experimental sites. In particular, at the Palermo site, more than 99% of the DSDs are characterized by R^2 values greater than 0.8 for both distributions, while at El Teularet, this percentage is approximately 92%. These results indicate that both distributions are equally capable of reproducing the large dataset measured at Palermo and El Teularet experimental sites.

Table 5. Number of observed drop size distributions (DSDs) at Palermo and El Teularet, and percentage of DSDs adequately reproduced by the Gamma and Weibull distributions. Percentages refer to cases with a coefficient of determination $R^2 > 0.8$, and to the subset of intense rainfall events ($I > 40$ mm h^{-1}).

		Gamma distribution		Weibull distribution	
Observed DSDs		DSDs with $R^2 > 0.8$	DSDs with $I > 40$ mm h^{-1} and $R^2 > 0.8$	DSDs with $R^2 > 0.8$	DSDs with $I > 40$ mm h^{-1} and $R^2 > 0.8$
Palermo	42279	99.3 %	99.8 %	99.5 %	99.9 %
El Teularet	5581	92.2%	99.5 %	99.2 %	99.7 %

The comparison was then extended to the estimation of rainfall energy–related characteristics. Figure 38 reports, for both experimental sites, the comparison between measured values of rainfall kinetic power and momentum and those calculated using the relationship derived from the Gamma distribution, Equations (24) and (25), and the Weibull one, Equations (72) and (73). The results show that both distributions provide good estimates of P_n and M, with data points generally clustered around the line of perfect agreement.

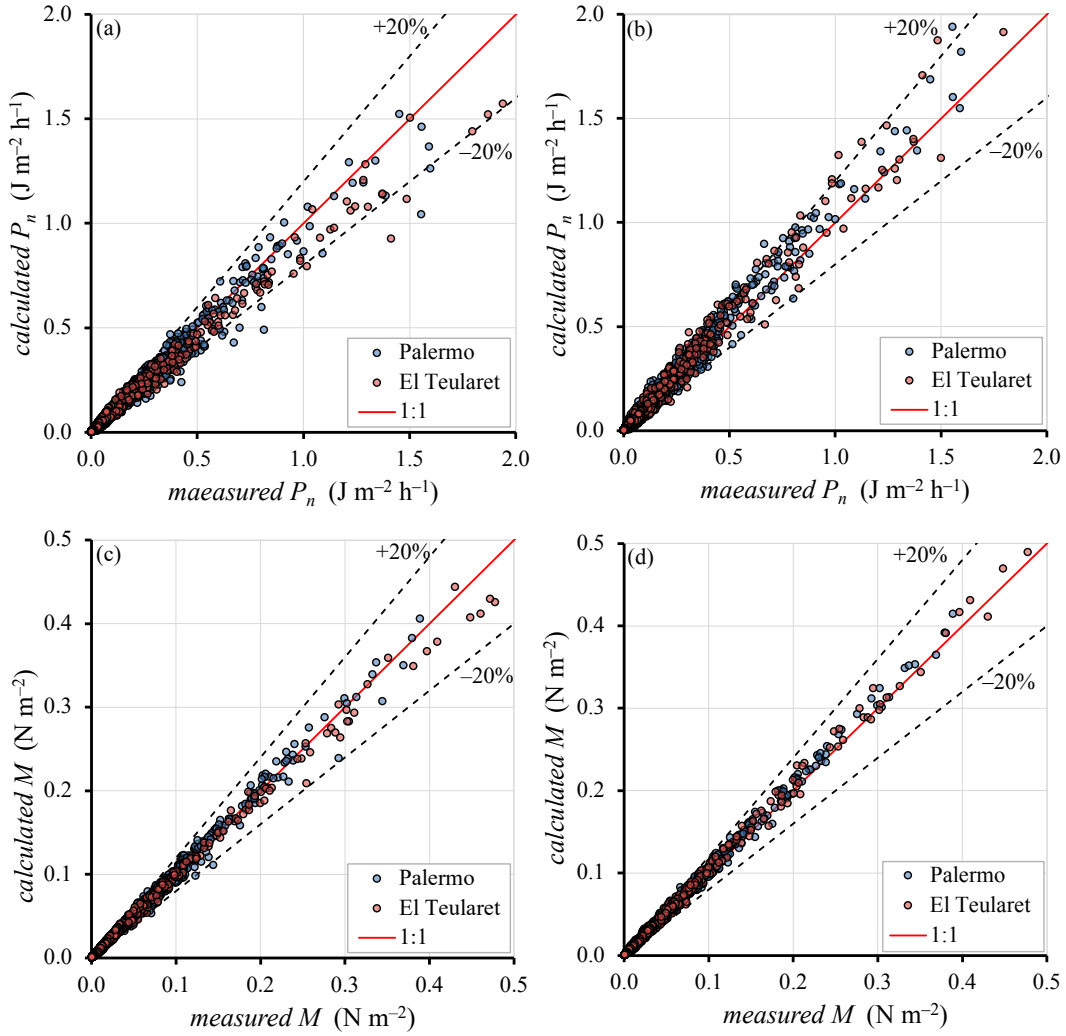

Figure 38. Comparison between measured and calculated values of rainfall kinetic power (P_n, top panels) and rainfall momentum (M, bottom panels) for both experimental sites (Palermo and El Teularet). Calculated values are obtained using the Gamma relationships (Eqs. (24) and (25), left panels) and the corresponding relationships derived from the Weibull distribution (Eqs. (72) and (73), right panels). The red solid line denotes the 1:1 relationship, while the black solid lines indicate ±20% deviation from perfect agreement.

A quantitative assessment of estimation accuracy, summarized in Table 6, indicates that slight underestimation of both kinetic power and momentum is generally observed for both sets of relationships. The only notable exception is represented by the estimation of rainfall momentum at the El Teularet site using the relationship derived from the Gamma distribution, which exhibits a positive MRE. Overall, however, the error metrics indicate that the predictive capabilities of the relationships derived from the Weibull and Gamma distributions are essentially equivalent for the analyzed datasets (Table 6).

Table 6. Performance of Gamma- and Weibull-based relationships in estimating rainfall kinetic power (Pn) and momentum (M) at the Palermo and El Teularet sites. For each variable and distribution, the mean relative error (MRE) and the percentage of drop size distributions (DSDs) with absolute error (AE) below 20% are reported.

		Palermo		El Teularet	
	Observed DSDs	42279		5581	
	Distribution	Gamma	Weibull	Gamma	Weibull
P_n	MRE	−2.4%	−3.1%	−3.1%	−4.4%
	% of DSDs with AE < 20%	97.2%	93.0%	90.0%	80.8%
M	MRE	−1.7%	−1.1%	8.8%	−9.4%
	% of DSDs with AE < 20%	99.2%	99.3%	99.0%	93.7%

Therefore, while both distributions can be effectively used to estimate rainfall kinetic power and momentum in Mediterranean environments with equivalent performances, the Weibull distribution is preferred because its shape and scale parameters are directly linked to physically interpretable characteristics of the drop size distribution, such as the variability of drop diameters and the energetic content of precipitation.

3.3 Advances in the Patented Method for Measuring Rainfall Energetic Characteristics Using the Weibull Distribution

The analyses presented in Section 3.2 demonstrated that the Weibull distribution accurately represents Mediterranean DSDs and enables reliable estimation of rainfall kinetic power and momentum through the analytical relationships of Equations (72) and (73). These findings constitute the scientific basis for significant advancements in a patented method of instrumentation (Patent No. 102018000010691) aimed at the direct measurement of rainfall energetic characteristics using low-cost.

According to the patented measurement method, P_n and M can be related to two easily measurable quantities, i.e., rainfall intensity and the number of raindrop impacts, N_{imp} (–). Under the simplifying assumption that all drops within a sampling interval have the same equivalent volume, the mean volume diameter D_m can be estimated as:

$$D_m = \sqrt[3]{\frac{I}{N_{imp}\frac{\pi}{6}}} \tag{78}$$

Substituting Equation (68) into Equation (78), the expression becomes:

$$D_m = \sigma \sqrt[3]{\Gamma\left(\frac{3}{\eta}+1\right)} \tag{79}$$

which expresses that the mean volume diameter is theoretically related to the shape and the scale parameters of the Weibull distribution.

To further improve the measurement method for rainfall energy characteristics, the distribution of rainfall momentum, $M_{(D)}dD$, corresponding to all droplets with diameter in the range (D, D+dD), is explicitly considered. Since the terminal velocity of a drop is estimated using Equation (10), the momentum distribution can be expressed in general form as:

$$M_{(D)}dD = N_{(D)}\rho\frac{\pi}{6\times 10^6}D^3 17.67 D^{0.67} dD \tag{80}$$

If the DSD follows a Weibull distribution, Equation (80) can be rewritten as:

$$M_{(D)}dD = N\rho\frac{\pi}{6\times10^6}D^3 17.67D^{0.67}\frac{\eta}{\sigma}\left(\frac{D}{\sigma}\right)^{\eta-1}\exp\left[-\left(\frac{D}{\sigma}\right)^{\eta}\right]dD \qquad (81)$$

According to Equation (81), the rainfall momentum distribution is fully determined by the raindrop diameter and the Weibull parameters η and σ.

The momentum of a single raindrop, M_D, defined as the product of the drop mass and its fall velocity obtained from Equation (10), results in:

$$M_D = \rho\frac{\pi}{6\times10^6}17.67D^{3.67} \qquad (82)$$

from which the raindrop diameter can be expressed as:

$$D = \left(\frac{6\times10^{-6}}{17.67\pi\rho}M_{(D)}\right)^{\frac{1}{3.67}} \qquad (83)$$

If a device capable of measuring the momentum of individual raindrops impacting a surface is available, the sample mean diameter $\mu'_{(D)}$, referred to the detected momentum distribution, can be obtained as:

$$\mu'_{(D)} = \frac{\sum_{i=1}^{N} M_D\left(\frac{6\times10^{-6}}{17.67\pi\rho}M_D\right)^{\frac{1}{3.67}}}{M} \qquad (84)$$

in which M represents the sum of the momentum of all drops recorded during the sampling time interval.

Considering the theoretical momentum distribution given by Equation (81), the corresponding theoretical mean diameter $\mu_{(D)}$ can be computed as:

$$\mu_{(D)} = \frac{\int_0^\infty DM_{(D)}dD}{\int_0^\infty M_{(D)}dD} = \frac{\int_0^\infty D^{4.67}\frac{\eta}{\sigma}\left(\frac{D}{\sigma}\right)^{\eta-1}\exp\left[-\left(\frac{D}{\sigma}\right)^{\eta}\right]dD}{\int_0^\infty D^{3.67}\frac{\eta}{\sigma}\left(\frac{D}{\sigma}\right)^{\eta-1}\exp\left[-\left(\frac{D}{\sigma}\right)^{\eta}\right]dD} = \sigma\frac{\Gamma\left(\frac{4.67}{\eta}+1\right)}{\Gamma\left(\frac{3.67}{\eta}+1\right)} \qquad (85)$$

The estimation of the Weibull parameters can therefore be performed by solving the system constituted by Equations (79) and (85). Specifically, by dividing the two equations, one obtains:

$$\frac{D_m}{\mu_{(D)}} = \frac{\sqrt[3]{\Gamma\left(\frac{3}{\eta}+1\right)}}{\Gamma\left(\frac{4.67}{\eta}+1\right)}\Gamma\left(\frac{3.67}{\eta}+1\right) \qquad (86)$$

Equation (86) highlights that the ratio $D_m/\mu_{(D)}$ is a function of the sole shape parameter η. In the range of practical interest for rainfall applications

($0.25 \leq \eta \leq 10$), this function is monotonic and therefore invertible. For practical implementation, the inverse function of Equation (86) can be accurately approximated by the empirical relationship:

$$\eta = 0.53 + \tan\frac{\frac{D_m}{\mu_{(D)}} - 0.15}{0.5593} \tag{87}$$

which reproduces the exact inversion with a mean absolute error of approximately 1.8%.

Consequently, adopting the Method of Moments (MM), the scale parameter σ is obtained imposing $\mu_{(D)} = \mu'_{(D)}$, i.e., Equation (85), while the shape parameter η is estimated using Equation (87) by setting $D_m/\mu_{(D)} = (I/(N\,\pi/6))^{1/3}/\mu'_{(D)}$, where $(I/(N\,\pi/6))^{1/3}$ is the definition of D_m (Equation (78).

The reliability of the theoretically deduced relationships for estimating rainfall kinetic power and momentum from the Weibull distribution, Equations (72) and (73), using η and σ parameters obtained through the abovementioned Method of Moments, was evaluated using the same disdrometric datasets previously analyzed in Section 3.2.

These calculated values were compared with measured P_n and *M values* obtained from the observed DSDs, using Equations (35) and (36), with terminal fall velocity determined using Equation (10).

The results of this comparison are summarized in Figure 39, which shows scatter plots of measured versus calculated P_n and M values for the Palermo and El Teularet experimental sites.

The proposed approach demonstrated a very good level of agreement, with only a slight systematic overestimation and most estimates exhibiting absolute errors of 10% or less (Table 7). Specifically, better performance was observed for rainfall momentum estimates, confirming the trend already highlighted in Figure 34 using a different methodological approach.

These results confirm both the validity of Equations (72) and (73), theoretically derived from the Weibull distribution, and the accuracy of the new procedure for estimating the Weibull parameters from simplified measurements.

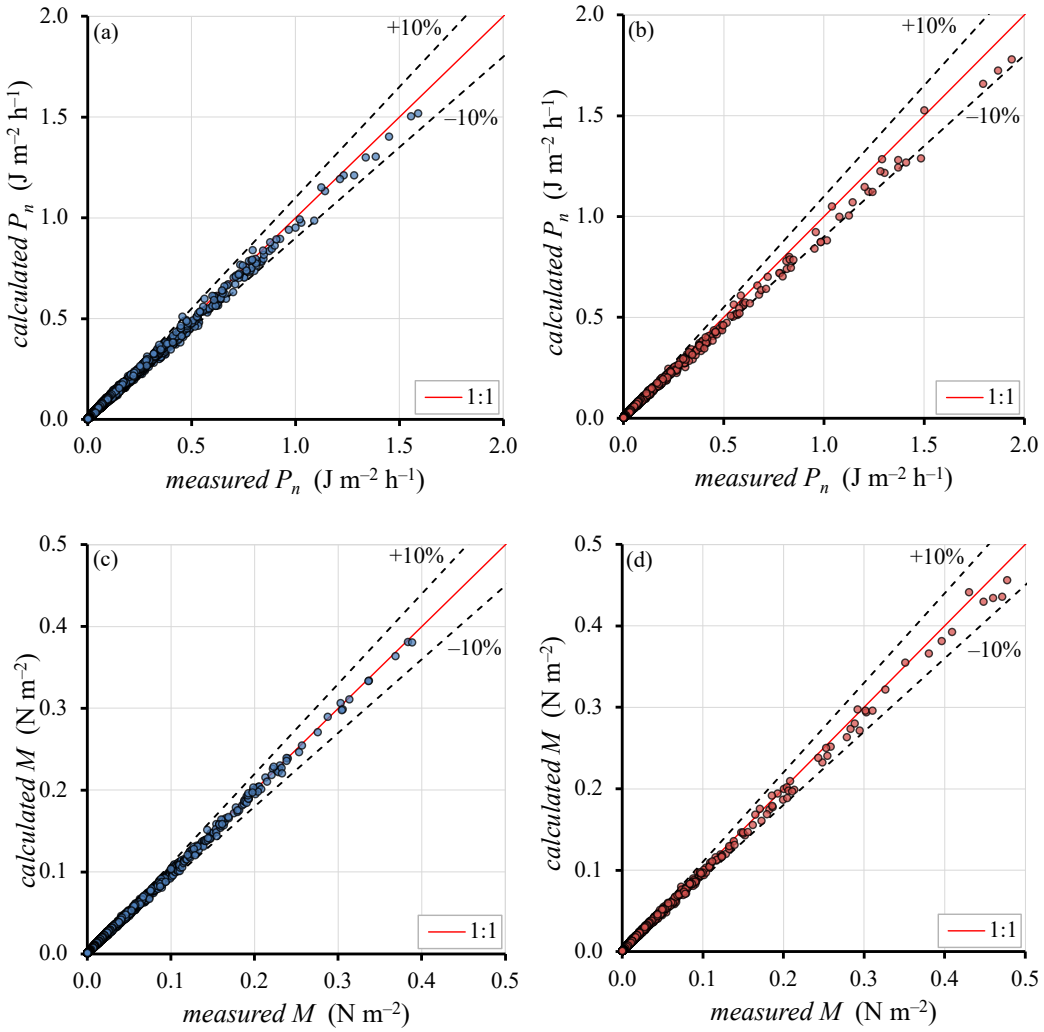

Figure 39. Comparison between measured and calculated values of rainfall kinetic power (P_n, panels a–b) and rainfall momentum (M, panels c–d) for the Palermo (a, c) and El Teularet (b, d) experimental sites. Calculated P_n and M values are obtained from Equations (72) and (73), respectively, with Weibull parameters derived from the Method of Moments described in the present section. The red solid line denotes the 1:1 relationship, while the black dashed lines indicate ±10% deviation from perfect agreement.

Moreover, comparison with previous investigations using the same disdrometric dataset but employing the Gamma distribution (Carollo et al., 2024d) indicates that estimates of rainfall momentum are consistently more accurate than those of kinetic power, irrespective of the theoretical distribution adopted to describe the DSD.

In other words, the combined knowledge of I, N, and $\mu'_{(D)}$ is sufficient to obtain reliable estimates of rainfall energetic characteristics, regardless of the statistical distribution used to represent the drop size distribution.

Table 7. Error analysis for rainfall kinetic power, P_n (J m^{-2} s^{-1}), and rainfall momentum, M (N m^{-2}), estimated using Equations (72) and (73) with Weibull parameters derived from the Method of Moments described in the present section.

	Palermo		El Teularet	
	P_n (J m^{-2} s^{-1})	M (N m^{-2})	P_n (J m^{-2} s^{-1})	M (N m^{-2})
MRE (%)	7.2%	3.6%	6.2%	3.5%
MAE (%)	7.5%	3.8%	7.5%	4.2%
% of data with AE ≤ 10%	89.0%	95.1%	77.4%	96.5%

To further investigate the method's behavior under different rainfall conditions, the dataset was analyzed by grouping the DSDs into rainfall-intensity classes, with the mean value denoted as I_{mean}. The classes were defined with variable widths: 1 mm h^{-1} for $I \leq 10$; 5 mm h^{-1} for $10 < I \leq 100$; 10 mm h^{-1} for $100 < I \leq 170$; and 20 mm h^{-1} for $170 < I \leq 210$. The MAE associated with the P_n and M estimates was computed for each class, and the results are presented in Table 8.

The analysis indicates that, for the Palermo dataset, the highest errors occur mainly for low-intensity rainfall events with $I < 20$ mm h^{-1}, whereas no significant trend is observed for the El Teularet dataset. However, Table 8 shows that the method's accuracy generally increases for intensities greater than 10 mm h^{-1}, which are more relevant from an erosive point of view. Across all intensity ranges, momentum estimates are systematically more accurate than kinetic power estimates, due to *the* lower sensitivity of M to uncertainties in terminal velocity estimation.

The findings encourage further experimental investigations to verify the assumption that the mean diameter derived from the electrical signal distribution coincides with that derived from the momentum distribution. If this hypothesis is confirmed, the patented instrument will be capable of reproducing the information typically provided by a disdrometer, with the additional advantage of directly measuring the energetic properties of rainfall. This would overcome the main limitations of traditional disdrometers, such as high cost, operational complexity, and limited suitability for large-scale deployment, and could have a substantial impact on soil erosion research, enabling a continuous and capillary monitoring of rainfall erosivity.

Table 8. Variation of the Mean Absolute Error (MAE) in the estimation of rainfall kinetic power, P_n (J m^{-2} s^{-1}), and momentum, M (N m^{-2}), across different mean rainfall intensity classes, I_{mean} (mm h^{-1}), for the Palermo and El Teularet experimental sites.

	Palermo			El Teularet		
I_{mean} (mm h^{-1})	DSDs	MAE M	MAE P_n	DSDs	MAE M	MAE P_n
0.75	7,289	4%	9%	885	4%	8%
1.5	13,840	4%	8%	1,200	4%	8%
2.5	8,134	4%	8%	701	4%	8%
3.5	5,263	4%	7%	478	5%	8%
4.5	3,421	4%	7%	332	4%	7%
5.5	2,484	3%	6%	273	5%	8%
6.5	1,691	3%	6%	247	4%	7%
7.5	1,197	3%	6%	202	5%	7%
8.5	898	3%	6%	177	5%	8%
9.5	654	3%	6%	166	4%	7%
12.5	1,784	3%	5%	441	4%	6%
17.5	708	2%	5%	170	4%	6%
22.5	365	2%	4%	95	3%	5%
27.5	202	2%	4%	54	3%	5%
32.5	125	2%	3%	32	3%	5%
37.5	94	2%	3%	27	3%	6%
42.5	68	2%	4%	19	4%	7%
47.5	49	2%	3%	7	3%	5%
52.5	25	3%	5%	9	4%	6%
57.5	28	2%	4%	10	3%	5%
62.5	16	2%	3%	7	3%	6%
67.5	18	2%	4%	3	5%	9%
72.5	8	2%	4%	–	–	–
77.5	11	2%	4%	6	4%	8%
82.5	12	2%	3%	3	7%	12%
87.5	7	3%	6%	3	5%	9%
92.5	4	2%	4%	3	5%	8%
97.5	9	2%	3%	1	2%	2%
105	8	2%	4%	5	3%	6%
115	9	1%	2%	5	3%	7%
125	5	1%	2%	2	4%	8%
135	2	2%	3%	3	3%	6%
145	4	1%	3%	2	3%	7%
155	2	1%	1%	1	4%	8%
165	2	1%	4%	4	3%	5%
180	2	1%	3%	5	5%	8%
200	1	2%	3%	1	4%	8%

3.4 Characterization of Rainfall Simulators

This section presents a comprehensive characterization of the rainfall simulators employed in this research. The analyses combine traditional volumetric measurements, disdrometric observations, and physically based formulations to evaluate the performance of each simulator with respect to rainfall intensity, spatial uniformity, drop-size distribution, fall velocity, and associated energetic properties.
First, the Kamphorst Simulator is analyzed in detail with respect to its hydraulic behavior, spatial uniformity, and energetic characteristics (Section 3.4.1).
The same experimental framework is extended to two modified configurations of the Kamphorst simulator (Section 3.4.2). This leads to the development of a generalized energetic formulation for drip-type rainfall simulators, demonstrating that their energetic behavior can be consistently described using a limited set of measurable variables, regardless of specific geometric configurations.
Subsequently, the performance of a newly designed pressurized rainfall simulator developed at the University of Palermo is presented in terms of hydraulic response, spatial rainfall distribution, and disdrometric properties (Section 3.4.3). This analysis allows the identification of optimal nozzle configurations for future plot-scale erosion experiments.
Next, the hydrological and energetic behavior of an additional pressurized simulator, capable of simulating raindrops falling at terminal velocity, and installed at the University of León, is characterized (Section 3.4.4).
Additionally, the reliability of the Parsivel^2 optical disdrometer in laboratory applications is critically examined. The instrument performance is evaluated using independent reference measurements (Section 3.4.5).
Finally, the proposed empirical fall velocity relationship is validated and extended to both drip-type and pressurized simulators (Sections 3.4.5 and 3.4.6). Overall, this chapter aims to provide an integrated methodological framework for an easy and reliable characterization of rainfall simulators.

3.4.1 Performance of the Kamphorst rainfall simulator

To assess the spatial uniformity of the rainfall intensity generated by the Kamphorst simulator (KS), the experimental procedure described in Section 2.2 was applied.
For each investigated pressure head condition, H, the Christiansen Uniformity Coefficient, CUC, was computed using Equation (38), averaged over the two experimental runs, and reported in Table 9. In addition, Table 9 also reports the mean simulated rainfall intensity, I_S, obtained by averaging the measurements from the 49 capillary tubes and the two repeated runs for each H value.

Table 9. Christiansen Uniformity Coefficient, CUC (%), and mean simulated rainfall intensity, I_S (mm h^{-1}), of the rainfall generated by the Kamphorst rainfall simulator for different pressure head values, H (cm).

***H* (cm)**	2	3	4	5	6	7	8	9	10	11	12
CUC (%)	96.4	96.7	96.5	96.7	96.6	96.3	98.4	97.3	97.4	98.7	98.6
I_S (mm h^{-1})	231	323	405	472	538	600	661	715	772	822	871

The obtained results consistently show high uniformity, with a mean CUC value of 97.24%, indicating excellent uniformity across the 49 capillary tubes of the KS. Such values are well above the threshold commonly accepted in rainfall simulation experiments to guarantee reproducible and spatially uniform rainfall conditions, equal to 80% according to the literature (Arnaez et al., 2007; Esteves et al., 2000; Iserloh et al., 2013a; Mhaske et al., 2019; Salem and Meselhy, 2021).
Overall, these results demonstrate that variations in pressure head mainly affect the magnitude of rainfall intensity, without compromising the spatial uniformity of the simulated rainfall field.
Furthermore, the comparison between the total volume collected by the 49 capillary tubes during the uniformity tests and the volume measured in the collection tank during the control runs showed no appreciable differences, generally below ±1% and never exceeding 3% across the investigated H range. This confirms that the simulator operates without leakage under the investigated conditions.
In addition, the spatial variability of the simulated rainfall intensity was further analyzed through the thematic maps shown in Figure 40. For each H value, the figure shows the spatial distribution of rainfall intensity measured at the 49 capillary tubes of the KS, expressed as the normalized ratio I_i/I_S, where I_i is the rainfall

intensity of the *i*-th collector. This normalization was introduced to enable a single, consistent color scale across all experimental configurations, thereby enabling direct visual comparison of spatial distribution patterns across different pressure head values, despite substantial differences in I_S (Table 9).

In this normalized representation, values of I_i/I_S close to unity indicate that the rainfall intensity produced by a given capillary tube is consistent with the simulator's mean behavior, whereas deviations from unity reflect local variations in rainfall intensity from the average.

Overall, 92% of the analyzed I_i/I_S values fall within the 0.95–1.05 range, indicating that most of the capillary tubes produce rainfall intensities very close to the mean simulated value. This result is fully consistent with both the visual evidence provided by the thematic maps in Figure 40 and the high CUC values reported in Table 9.

A limited number of capillary tubes, particularly 2, 16, and 31 (Figure 40a), systematically exhibit lower I_i/I_S values across most pressure head configurations, suggesting a reduced local discharge. This behavior is likely attributable to partial occlusion or minor malfunctioning of individual capillary tubes, which may occur given their small diameter and the use of tap water. However, these local anomalies do not affect the overall spatial uniformity of the simulated rainfall.

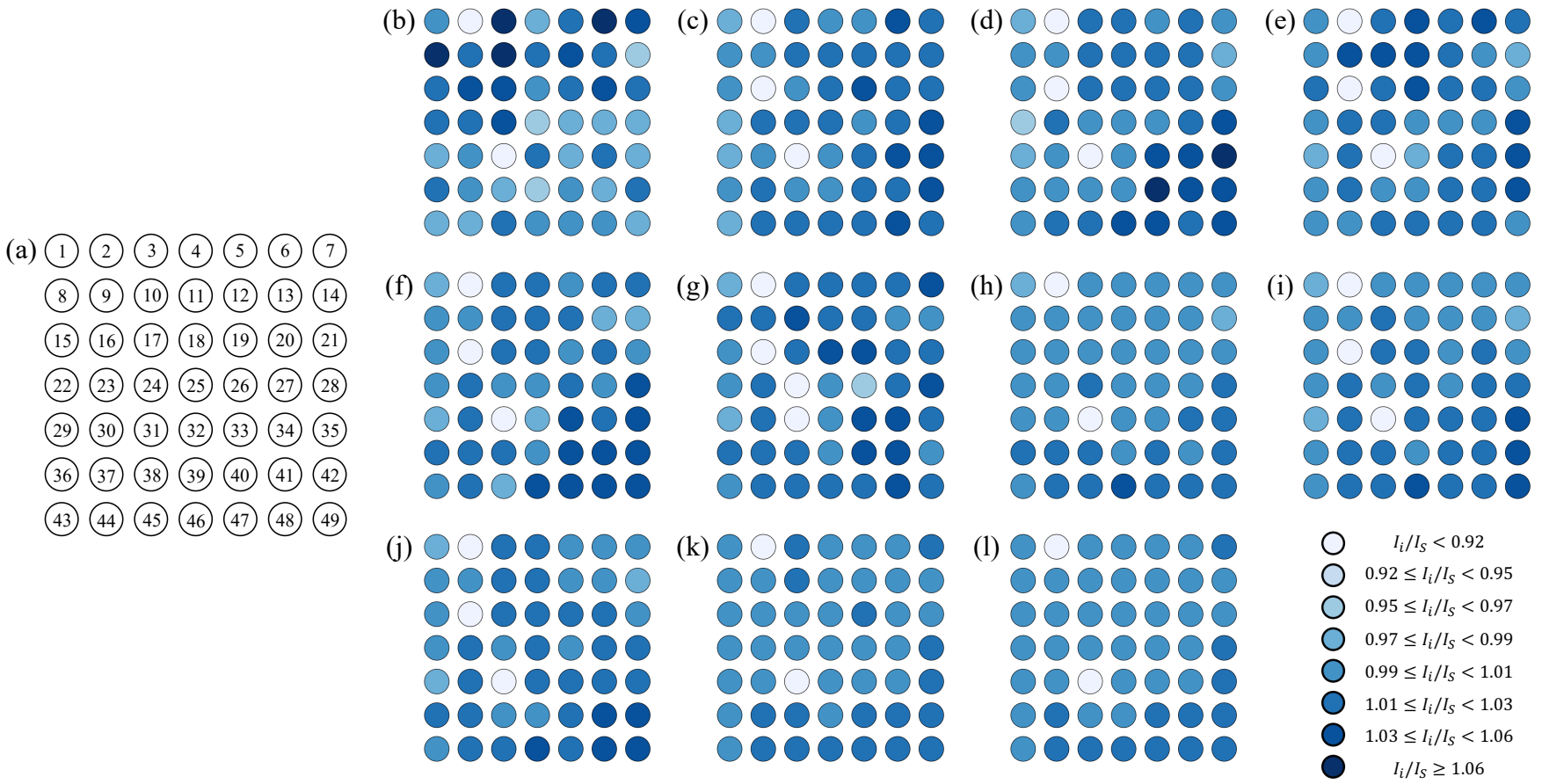

Figure 40. Normalized rainfall intensity (I_i/I_S) spatial distribution measured at the 49 collectors of the KS for different pressure head, H, values. Panel (a) shows the spatial layout of the collectors, while panels (b–l) report the normalized rainfall intensity maps for increasing pressure head values (2–12 cm).

Accordingly, the energetic characterization of the Kamphorst simulator was performed by considering a single capillary tube representative of the mean simulator behavior. In all experiments, capillary tube 25 (Figure 40a) was selected. To investigate the influence of water temperature on raindrop mass, m_D, Figure 41 illustrates the relationship between m_D and H for different water temperatures, T (°C), measured at the outlet of the selected capillary tube.

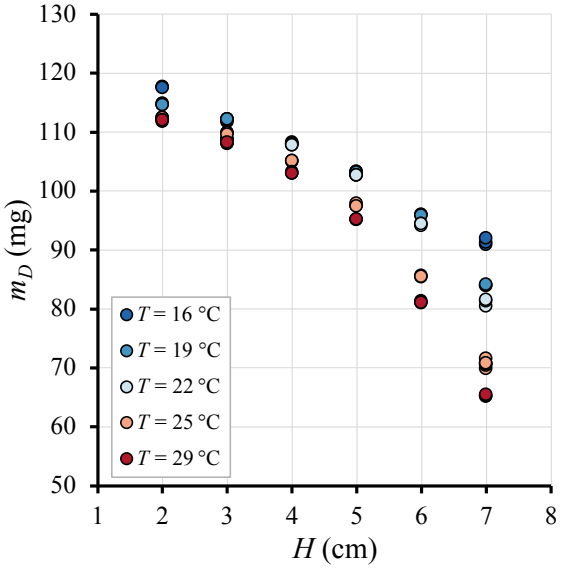

Figure 41. Relationship between the mean raindrop mass, m_D (mg), and the pressure head, H (cm), for different water temperatures, T (°C), conditions.

For a given water temperature, the results show a clear decreasing trend of m_D with increasing pressure head, indicating that higher hydraulic loads lead to the formation of smaller raindrops. In addition, for a fixed pressure head, an increase in water temperature systematically results in lower m_D values. This behavior can be explained physically by the combined effects of pressure head and temperature on the outflow velocity at the capillary tube outlet. An increase in H enhances the hydraulic driving force, while an increase in T reduces water viscosity, both leading to higher discharge velocities and, consequently, to a higher raindrop formation rate and smaller individual drop masses.

The combined effects of H and T on the raindrop mass were further analyzed by examining the relationship between m_D and I_S, as shown in Figure 42. Specifically, Figure 42a plots m_D vs I_S for fixed H values, whereas Figure 42b plots m_D vs I_S for fixed T values.

A clear decreasing trend of m_D with increasing I_S is observed in both panels, with experimental data collapsing onto a common m_D–I_S relationship. This indicates that rainfall intensity effectively integrates the combined influence of pressure head and water temperature on raindrop mass formation, acting as the primary controlling variable.

Furthermore, the (I_S, m_D) pairs suggest the existence of a threshold rainfall intensity of approximately 500 mm h^{-1}, above which the rate of decrease in raindrop mass with increasing rainfall intensity becomes significantly steeper than that observed at lower intensity values.

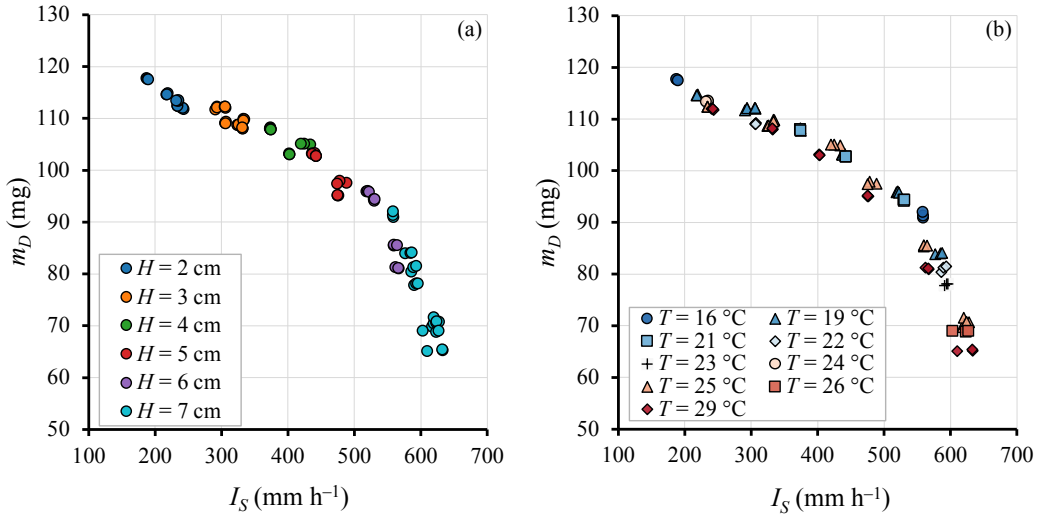

Figure 42. Relationship between the mass of a single raindrop, m_D (mg), and rainfall intensity, I_S (mm h^{-1}), under different pressure head, H (cm), conditions (a), and water temperature, T (°C), conditions (b).

For each investigated pressure head and water temperature, raindrop fall velocities, V_S (m s^{-1}), were measured at different fall heights, h (m), using the photographic method described in Section 2.2.3.3. The reliability of this measurement technique was first assessed by comparing the experimentally measured fall velocities with the theoretical terminal velocities, V_{max} (m s^{-1}), computed using Equation (55), as shown in Figure 43 for three pressure head values (2 cm, 5 cm, and 7 cm).

The experimental (V_{max}, V_S) pairs systematically lie below the 1:1 line, indicating that the measured fall velocities never exceed the corresponding maximum fall velocity. The slight underestimation of V_S relative to V_{max} is physically consistent with the presence of modest, yet non-negligible, aerodynamic drag effects, which

are not accounted for in Equation (55). This confirms both the physical plausibility of the measurements and the reliability of the photographic method.

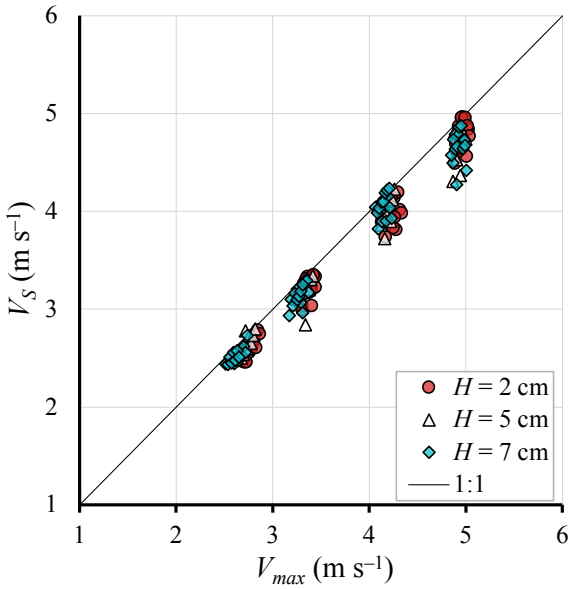

Figure 43. Comparison between measured raindrop fall velocity, V_S (m s^{-1}), and maximum velocity reachable by a body falling free in a vacuum, V_{max} (m s^{-1}), for different pressure head, H (cm), conditions. The solid line represents the 1:1 relationship.

Based on these observations, and for the fall heights investigated in this study, V_S can be expressed by introducing a dimensionless correction factor, ω (–), into Equation (60):

$$V_S = \omega\sqrt{2gh} \tag{88}$$

where ω (–) is a dimensionless coefficient estimated from experimental data. Specifically, the value of ω was determined by fitting Equation (88) to the experimental fall velocity measurements obtained using the photographic technique. The limited variability of ω, which ranges from 0.9490 to 0.9576 across all experimental conditions, justified adopting a constant value equal to the mean, $\omega = 0.9525$.

Moreover, considering the relationship between raindrop mass and rainfall intensity under the hypothesis that all raindrops, N_d (–), have the same mass:

$$m_D = \frac{I_S \rho \sigma t}{N_d} \tag{89}$$

and by substituting Equations (88) and (89) into the original expressions for kinetic power and momentum, defined in Equations (56) and (57), the following relationships are obtained:

$$P_n = N_d P_{n,D} = \frac{g\omega^2 \rho h I_S}{3.6 \times 10^6} \tag{90}$$

$$M = N_d M_D = \frac{\sqrt{2g}\omega \rho h^{0.5} I_S}{3.6 \times 10^6} \tag{91}$$

in which 3.6×10^6 converts I_S from mm h^{-1} to m s^{-1} for dimensional consistency. Equations (90) and (91) demonstrate that, for the investigated operating conditions, the energetic characterization of the KS depends solely on the rainfall intensity and the fall height, independently of the specific hydraulic operating conditions.

Figure 44 presents the comparison between the measured rainfall kinetic power and momentum, denoted as *measured* P_n and *measured* M, and those estimated by Equations (90) and (91), assuming $\omega = 0.9525$, hereafter referred to as *calculated* P_n and *calculated* M, respectively.

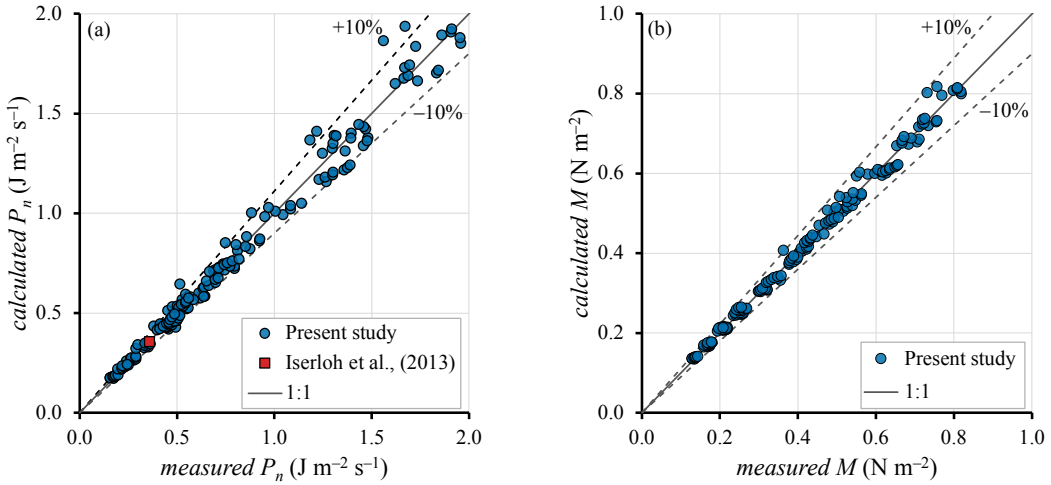

Figure 44. Comparison between measured and calculated rainfall kinetic power, P_n (a), and momentum, M (b). The solid line represents the 1:1 relationship, while the dashed lines indicate ±10% deviation from perfect agreement. The P_n value reported by Iserloh et al. (2013a), measured using a Thies Clima LPM disdrometer under the standard Kamphorst simulator rainshower, is also shown.

The close agreement of the data points with the 1:1 line confirms the reliability of the proposed equations for estimating both the rainfall kinetic power and the rainfall momentum. Most experimental points lie within the ±10% deviation bands, indicating that the simplified energetic formulation captures the dominant physical

processes governing raindrop motion and impact energy over the investigated fall heights.

In addition, Figure 44a includes the measured kinetic power value reported by Iserloh et al. (2013a), under the standard KS operating conditions (I_S equal to 360 mm h^{-1}, drops fall height of 0.40 m) and employing a LPM disdrometer. The overlap of this independent measurement with the present experimental dataset further supports the robustness and transferability of the proposed energetic characterization, confirming that Equations (90) and (91) can be applied reliably across different experimental setups employing the same simulator.

To quantitatively evaluate the accuracy of the proposed formulations, the mean relative error (MRE), mean absolute error (MAE), and the percentage of data with an absolute error (AE) less than or equal to 10% were computed using Equations (59) and (60). The corresponding results are summarized in Table 10.

Table 10. Statistical error metrics for the comparison between measured and calculated rainfall kinetic power (Pn) and momentum (M): mean relative error (MRE), mean absolute error (MAE), and percentage of data with absolute error (AE) ≤ 10%.

	P_n (J m^{-2} s^{-1})	M (N m^{-2})
MRE (%)	0.37%	0.03%
MAE (%)	5.12%	2.54%
% of data with AE ≤ 10%	88.75%	99.38%

The error analysis shows excellent agreement between the measured and calculated values for both energetic variables. In particular, the momentum estimates exhibit very small errors, with an MRE of 0.03% and nearly all data (99.38%) affected by an AE ≤ 10%. The better performance observed for momentum estimates can be attributed to the different dependence of P_n and M on the fall height. While kinetic power scales linearly with h, momentum scales with $\sqrt{h}$, making it less sensitive to uncertainties in fall-velocity estimation. This difference explains the smaller dispersion observed for M compared to P_n.

The I_S measurements collected in the present investigation were also employed to assess the reliability of Equation (43) for estimating rainfall intensity, assuming $\alpha_I = 1.25$.

As shown in Figure 45, the comparison between measured and calculated rainfall intensities reveals a strong agreement, with most data points closely aligned along the 1:1 line. The analysis indicates a slight underestimation of I_S by Equation (43), with a mean relative error of −0.30%. Nevertheless, 90.91% of the measurements exhibit absolute errors less than or equal to ±5%, demonstrating the formulation's high predictive capability over the investigated range of operating conditions.

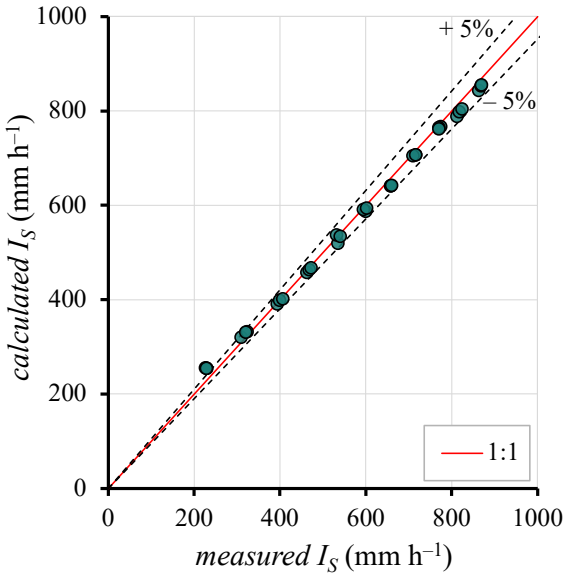

Figure 45. Comparison between measured and calculated rainfall intensity, I_S (mm h^{-1}). Calculated values were obtained using Eq. (43). The solid line represents the 1:1 relationship, while the dashed lines indicate ±5% deviation from perfect agreement.

This behavior is consistent with the findings of Agosta et al. (2022) and supports the use of Equation (43) to estimate rainfall intensity produced by the Kamphorst rainfall simulator, provided that its operating conditions (T and H) and the geometric characteristics of the capillary tubes (d_c and l_c) are known.

Overall, the results presented in this section demonstrate that the Kamphorst rainfall simulator can be fully characterized from both hydraulic and energetic perspectives by measuring only a limited set of variables. This is particularly relevant from an operational standpoint.

3.4.2 From the Modified Kamphorst Simulator to a Generalized Energetic Framework for Drip-Type Rainfall Simulators

Although the KS proved to be a robust and reliable device for laboratory and field investigations, its standard configuration is characterized by the generation of relatively large raindrops and very high rainfall intensities, ranging from approximately 228 mm h^{-1} to 872 mm h^{-1}. Since the experimental conditions investigated for the KS mainly involved variations in water temperature and hydraulic head acting on the capillary tubes, the range of reproducible rainfall intensities remained inherently constrained by the geometric characteristics of the nozzles.

To overcome these limitations and to extend the spectrum of rainfall conditions reproducible in laboratory experiments, two Modified Kamphorst Simulators (MKS and MKS_2) were employed (Section 2.2.1.2). The modification consists of modifying the geometric properties of the capillary tubes while preserving the original hydraulic feeding system and the simulator's spatial layout.

Based on the energetic framework validated for the KS (Section 3.4.1), the same experimental and analytical approach was adopted for the MKS. Given the high spatial uniformity of the rainfall distribution guaranteed by the device, the energetic characterization was carried out by analyzing a single representative capillary tube, in accordance with the procedure previously applied to the original configuration.

Figure 46a compares the relationship between the mean raindrop mass, m_D, and the rainfall intensity, I_S, obtained for the KS, MKS, and MKS_2. As expected, changing the geometric characteristics of the capillary tubes leads to the formation of smaller raindrops and allows the exploration of a wider range of rainfall intensities. Specifically, the MKS configuration enables simulation of lower rainfall intensities than the KS, whereas the MKS_2 configuration produces even more extreme intensity values.

Despite the differences among the three configurations, all datasets exhibit a consistent monotonic decrease of m_D with increasing I_S, specific to each simulator configuration. This result further supports the role of I_S as the primary controlling variable governing raindrop mass, regardless of the simulator's geometric configuration. From a physical perspective, this behavior reflects an increase in

droplet formation frequency at the nozzle outlet with increasing pressure head, leading to the generation of more small droplets within a given sampling time.

Due to the extremely high rainfall intensities associated with the MKS_2 configuration, which exceed the range of interest for the present study, this configuration was not considered in the subsequent analyses.

Figure 46b shows the relationship between the equivalent raindrop diameter, D, derived from m_D using Equations (53) and (54), and the rainfall intensity, I_S, for both the KS and MKS configurations. For the KS, I_S ranges from 188 mm h^{-1} to 633.7 mm h^{-1}, with corresponding D values between 0.50 and 0.61 cm, whereas for the MKS the rainfall intensity spans from 90.4 mm h^{-1} to 358 mm h^{-1}, with D varying between 0.28 and 0.33 cm.

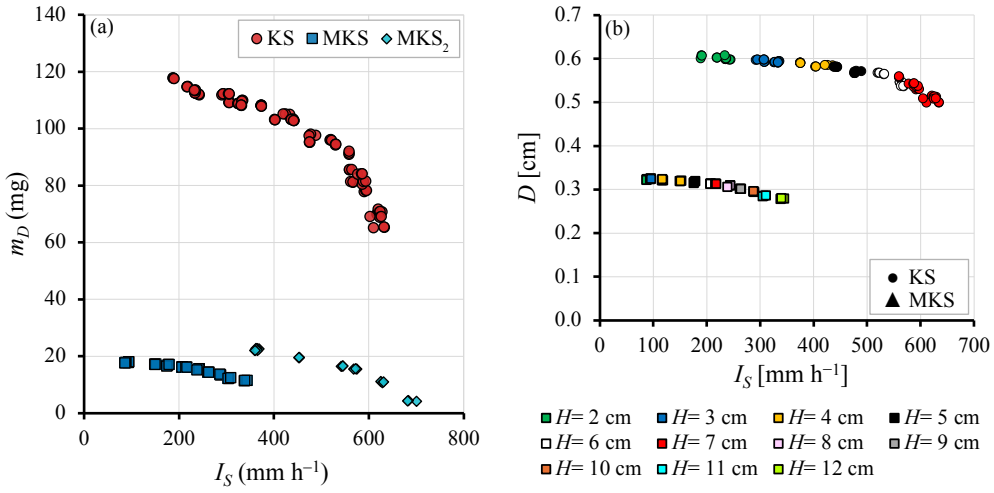

Figure 46. Relationship between the mean raindrop mass, m_D (mg), and rainfall intensity, I_S (mm h^{-1}), for the Kamphorst simulator (KS), and the two Modified Kamphorst Simulator configurations (MKS and MKS_2) (a) and between the equivalent raindrop diameter, D (cm), and I_S (mm h^{-1}) for the KS and MKS configurations.

In both configurations, D exhibits a decreasing trend with increasing rainfall intensity, and this behavior is independent of the applied pressure head. This confirms that the observed variations in raindrop size are primarily controlled by rainfall intensity rather than by the specific hydraulic operating conditions.

For both the KS and MKS configurations, raindrop fall velocity was measured at different fall heights and pressure head values using the photographic technique described in Section 2.2.3.3. To verify the reliability of the measured fall velocities, the experimental values, V_S, were compared with the theoretical maximum velocity

achievable by a body falling freely in a vacuum from the same height, V_{max}, calculated using Equation (55).

Figure 47 shows a comparison of V_S and V_{max} across different pressure head values for both simulators. In all cases, the experimental pairs systematically lie below the 1:1 line, indicating that the measured fall velocities never exceed the theoretical maximum velocity.

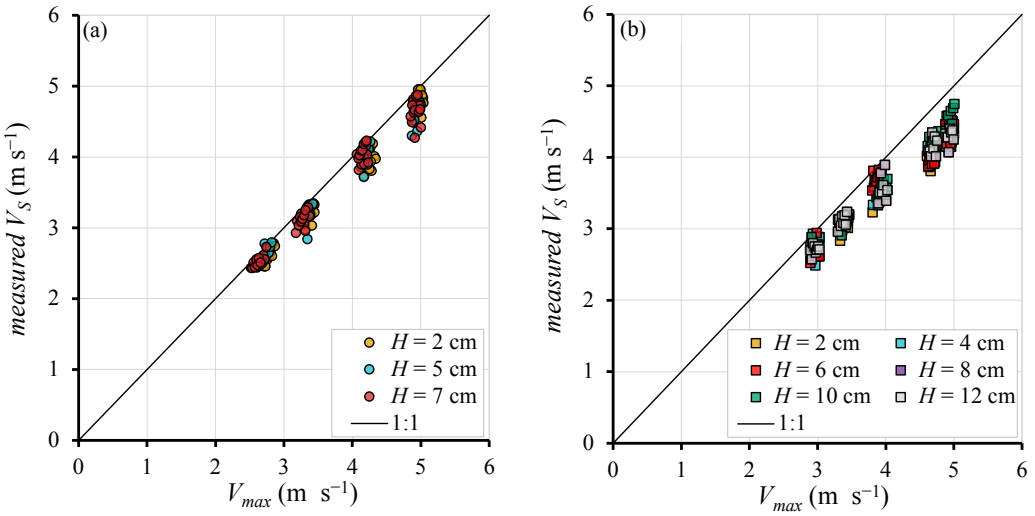

Figure 47. Comparison between measured raindrop fall velocity, measured V_S (m s^{-1}), and the maximum velocity reachable by a body falling free in a vacuum, V_{max} (m s^{-1}), for different pressure head, H (cm), conditions, and for both the Kamphorst Simulator (a) and the Modified Kamphorst Simulator (b). The solid line represents the 1:1 relationship.

This behavior is physically consistent with aerodynamic drag during the raindrop's fall and confirms the reliability of the photographic method for both KS and MKS configurations. Moreover, the similarity of the observed behavior across the two simulators suggests that modifying the capillary tube geometry does not alter the fundamental dynamics governing raindrop fall velocity.

Subsequently, the applicability of Equations (90) and (91), specifically developed for the KS to estimate the rainfall kinetic power and momentum, given only h and I_S, was also tested for the MKS configuration.

Figure 48 compares the measured P_n and M, obtained for both KS and MKS configurations, with those calculated using Equations (90) and (91), respectively. The close agreement of the experimental data with the 1:1 line confirms that these formulations remain valid also for the modified simulator configuration, despite the changes in capillary tube geometry.

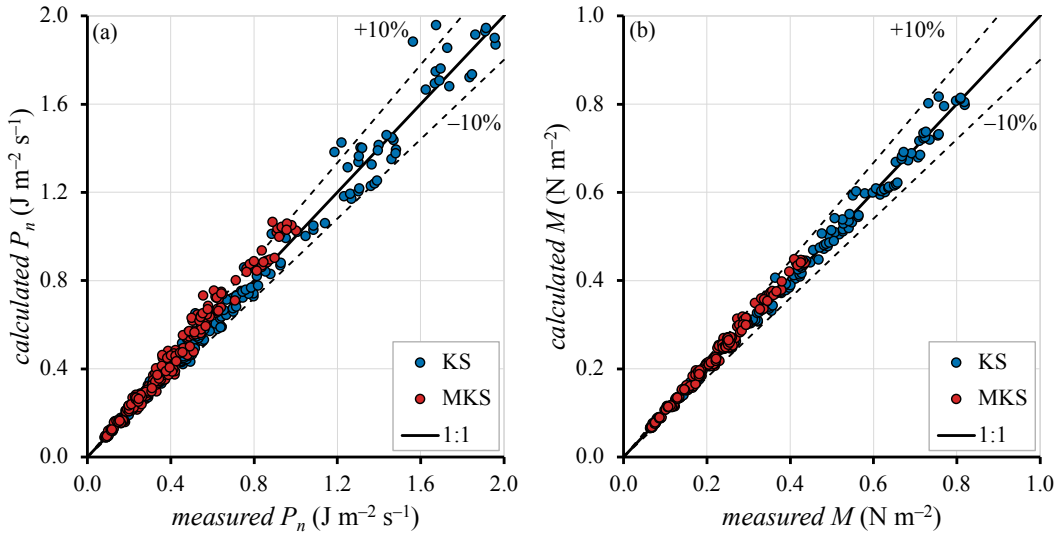

Figure 48. Comparison between measured and calculated rainfall kinetic power, Pn (J m^{-2} s–1), (a), and rainfall momentum, M (N m^{-2}), (b), for the Kamphorst simulator (KS) and the Modified Kamphorst Simulator (MKS). Calculated values were obtained using Equations (80) and (81). The solid line represents the 1:1 relationship, while the dashed lines indicate a ±10% deviation from perfect agreement.

Although an overall good agreement is observed, a slightly systematic overestimation is observed for the MKS with respect to the KS (Table 10), with mean relative error values equal to 8.45% for P_n and 4.15% for M. Nevertheless, consistently with the behavior previously observed for the KS, the errors associated with momentum estimates remain smaller than those related to kinetic power. This difference can be attributed to the quadratic dependence of kinetic power on fall velocity, which amplifies the propagation of uncertainties in V_S compared to momentum, which depends linearly on velocity.

Although Equations (90) and (91) allow an effective energetic characterization of both KS and MKS configurations based solely on rainfall intensity and fall height, a more comprehensive and general framework also requires an explicit characterization of raindrop fall velocity. For this reason, the reliability of the empirical relationship proposed in this work, Equation (52), was tested. This formulation is intended for drip-type rainfall simulators (DRS) and is valid within the calibration range defined by the literature database used in this study (Laws, 1941) (D between 1 mm and 6 mm and h between 0.5 m and 20 m).

The performance of Equation (52) was first evaluated against the calibration dataset (Laws, 1941).

Figure 49 presents the comparison between measured and calculated fall velocities using Equation (52). The points cluster closely around the 1:1 line, indicating the capability of the proposed relationship over the calibration range.

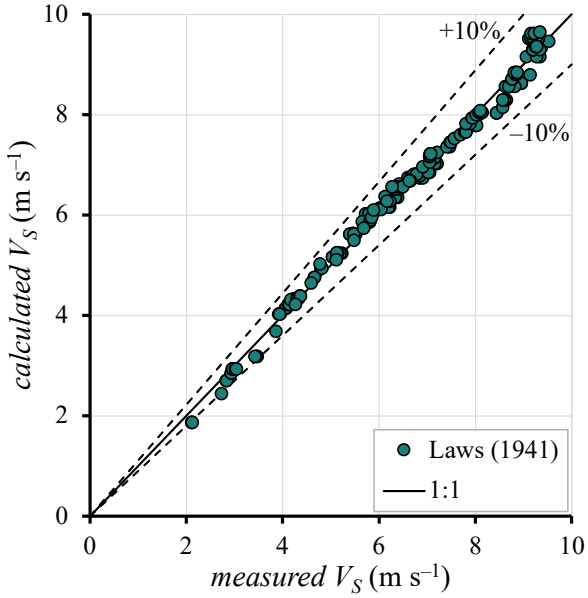

Figure 49. Comparison between measured fall velocity, V_S (m s^{-1}), and those calculated using Equation (52) for the calibration dataset (Laws, 1941). The solid line represents the line of perfect agreement, while the dashed lines denote the ±10% deviation from the 1:1.

To further assess the reliability of Equation (52), the formulation was tested against an independent dataset taken from the literature, namely the measurements reported by Epema and Riezebos (1983), which cover fall heights h ranging from 0.5 m to 13 m and drop diameters D from 0.2 cm to 0.6 cm.

Figure 50 shows the comparison between measured and calculated fall velocities for this dataset. The close agreement observed confirms that the proposed relationship can reliably reproduce raindrop fall velocities measured under different experimental conditions.

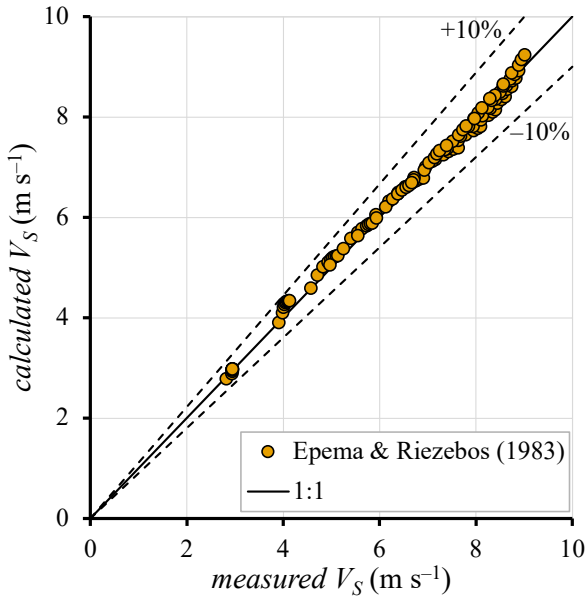

Figure 50. Comparison between measured fall velocity, V_S (m s^{-1}), and those calculated using Equation (52) for an independent literature dataset (Epema and Riezebos, 1983). The solid line represents the line of perfect agreement, while the dashed lines denote the ±10% deviation from the 1:1.

Finally, the reliability of Equation (52) was verified using experimental measurements collected in the present investigation for both KS and MKS. Figure 51 presents the comparison between the measured and calculated V_S values.

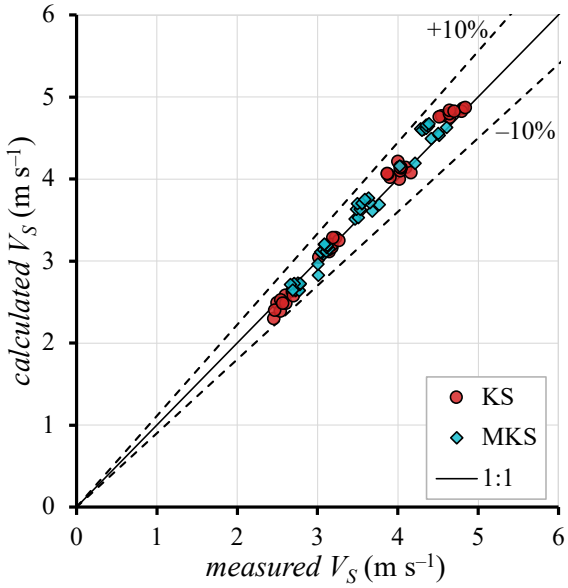

Figure 51. Comparison between measured fall velocity, V_S (m s^{-1}), and those calculated using Equation (52) for the experimental measurements of the present study using a Kamphorst Simulator (KS) and a Modified Kamphorst Simulator (MKS). The solid line represents the line of perfect agreement, while the dashed lines denote the ±10% deviation from the 1:1.

The results show good agreement across the entire range of investigated conditions, confirming that Equation (52) can be applied consistently to both the original and modified Kamphorst simulators.

The accuracy of Equation (52) across different datasets was quantitatively evaluated by computing MRE, MAE, and R^2 using Equations (59), (60), and (61). Moreover, the percentage of data characterized by absolute errors less than or equal to 10% was determined. The results of the error analysis are summarized in Table 11. Overall, the statistical indicators confirm the high reliability of the proposed formulation, with very small bias and a large majority of data points falling within the ±10% error threshold for all considered datasets.

Table 11. Mean Relative Error (MRE), Mean Absolute Error (MAE), percentage of data with Absolute Error (AE) ≤ 10%, and coefficient of determination (R^2) between fall velocities measured in different investigations (Laws, 1941; Epema & Riezebos, 1983) and in the present study using the Kamphorst Simulator (KS) and the Modified Kamphorst Simulator (MKS), and the corresponding values calculated using Equation (52).

	Laws (1941)	Epema and Riezebos (1983)	KS (Present study)	MKS (Present Study)
MRE	0.2%	–0.3%	–0.6%	–1.7%
MAE	2.1%	1.8%	2.4%	3.0%
% of data with AE ≤ 10%	98.0%	100.0%	100.0%	100.0%
R^2	0.9994	0.9997	0.9993	0.9990

The validated fall-velocity formulation was then employed to estimate the rainfall kinetic power and momentum generated by both KS and MKS. Figure 52 compares the measured P_n and M values obtained in the present investigation with those calculated using Equation (52) to estimate V_S. Moreover, Table 12 lists the MRE, MAE, and the percentage of data showing AE less than or equal to 10%.

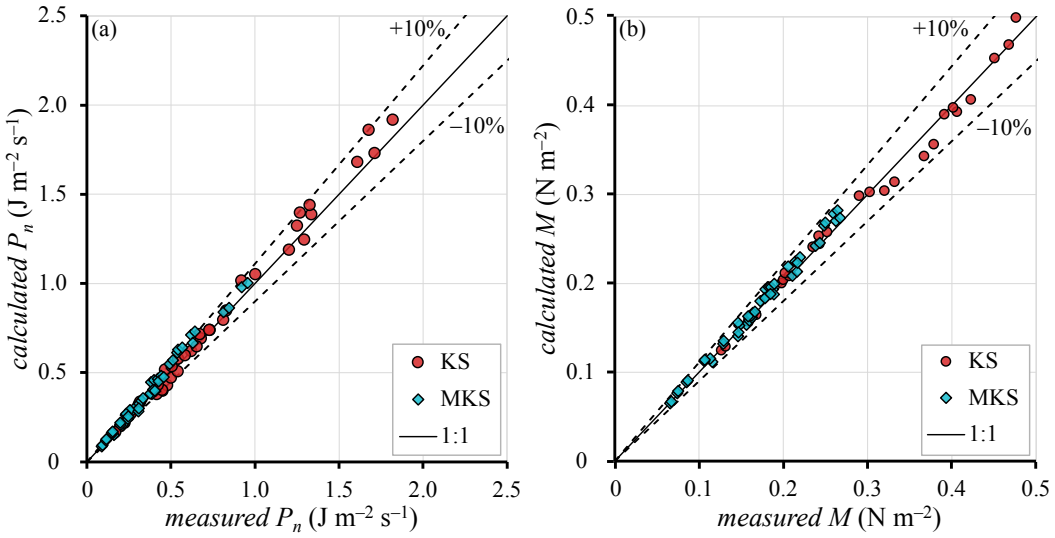

Figure 52.Comparison between measured and calculated rainfall kinetic energy, Pn (J m^{-2} s^{-1}), (a) and momentum, M (N m^{-2}), (b). Calculated values were obtained by applying Equation (52) to estimate the raindrop fall velocity. The solid line represents the line of perfect agreement, while the dashed lines denote the ±10% deviation from the 1:1.

Table 12. Mean Relative Error (MRE), Mean Absolute Error (MAE), and percentage of data with Absolute Error (AE) ≤ 10% obtained from the comparison between measured and calculated rainfall kinetic power, Pn (J m^{-2} s^{-1}), and momentum, M (N m^{-2}), for both the Kamphorst Simulator (KS) and the Modified Kamphorst Simulator (MKS). Calculated values were obtained by applying Equation (52) to estimate the raindrop fall velocity.

	KS		MKS	
	P_n (J m^{-2} s^{-1})	M (N m^{-2})	P_n (J m^{-2} s^{-1})	M (N m^{-2})
MRE	1.2%	0.6%	3.6%	1.7%
MAE	5.0%	2.5%	6.1%	3.0%
% of data with AE ≤ 10%	82.5%	100.0%	80.0%	100.0%

The close agreement of the experimental data with the 1:1 line and the error analysis confirms that the generalized energetic framework is capable of accurately reproducing both rainfall kinetic power and momentum for different simulator configurations. Overall, the KS configuration exhibits better performance than the MKS. Notably, improved results are obtained for both simulators in the estimation of rainfall momentum, with all M measurements characterized by absolute errors ≤ 10%. In contrast, for P_n, the proportion of measurements with AE ≤ 10% decreases to 82.5% for KS and 80.0% for MKS.

Overall, the results demonstrate that, once the fall height is set by the operator and the raindrop diameter is known, the proposed fall velocity relationship, Equation (52), allows raindrop velocity to be reliably estimated without direct velocity measurements. This, in turn, enables a complete volumetric and energetic characterization of drip-type rainfall simulators, since rainfall intensity, kinetic power, and momentum can all be consistently derived from a limited set of measurable variables.

3.4.3 A New Portable Rainfall Simulator for Soil Erosion Investigations

This section presents and discusses the results related to the design and hydraulic characterization of a new portable pressurized rainfall simulator developed for plot-scale soil erosion and hydrological investigations.

At first, the technological variability of the selected nozzle models was verified employing two distinct nozzles (hereafter referred to as n_1 and n_2) for each model, and the obtained pressure–discharge (P_S–Q) relationships were tested against the manufacturer-provided ones, summarized by Equation (44).

Figure 53 presents the comparison between the experimental P_S–Q of n_1 and n_2 and the characteristic curves suggested by the manufacturer. Experimental data are largely overlapping for all nozzle models, indicating a high degree of technological consistency and repeatability of the hydraulic behavior within each model.

However, non-negligible discrepancies can be observed between experimental and expected (P_S, Q) pairs. These discrepancies are quantitatively summarized in Table 13, which reports the MRE and the MAE, obtained using Equations (59) and (60), and the percentage of measurements affected by AE lower than or equal to 10%. The error analysis indicates that overall, and for pressures below 2.5 bar, the manufacturer's curves tend to underestimate the actual Q. This behavior can be explained by the fact that the nozzles were intentionally operated outside the P_S range suggested by the manufacturer to generate rainfall composed of distinguishable single droplets (Section 2.2.1.4).

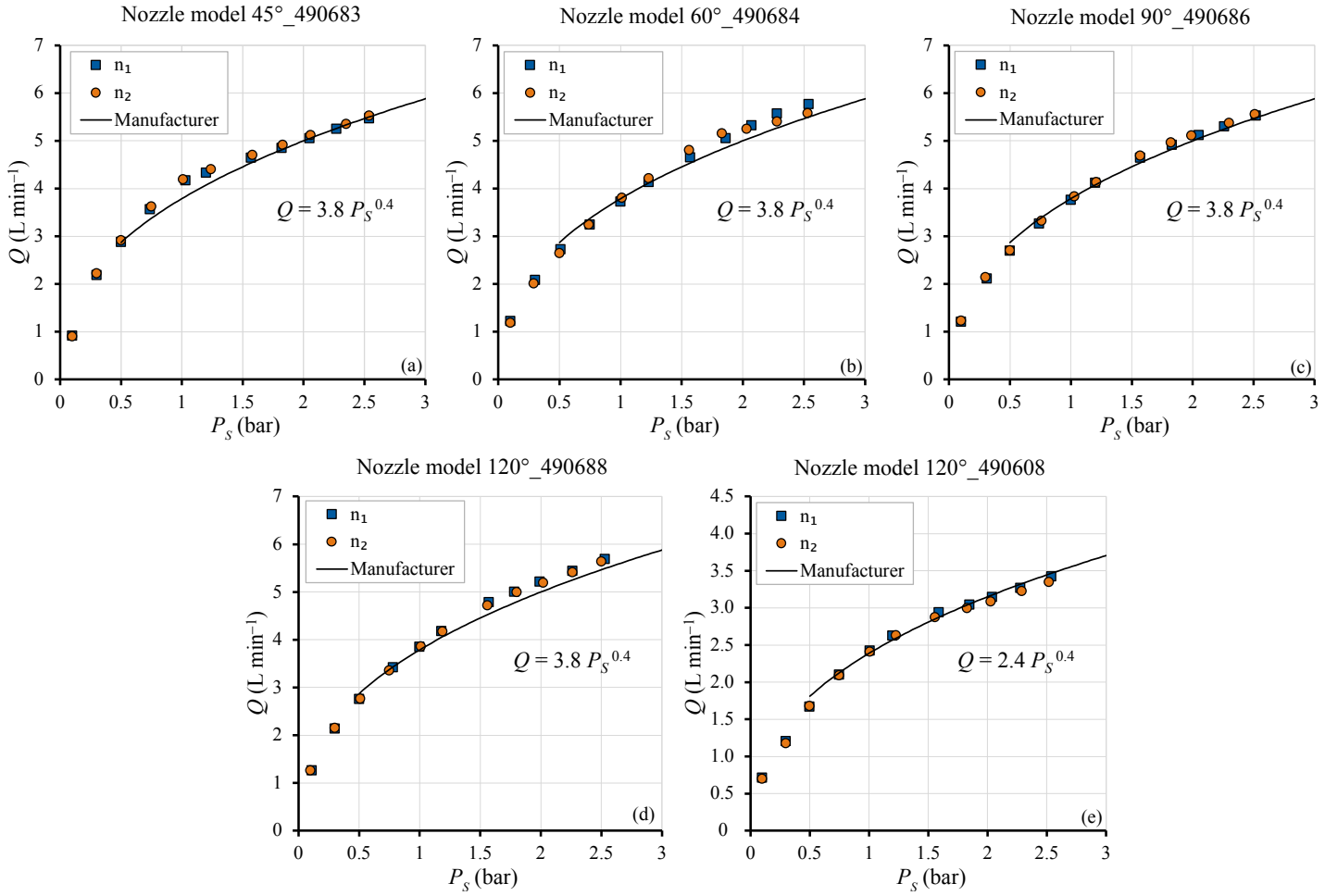

Figure 53. Comparison between experimentally measured pressure–flow-rate (P_S–Q) relationships and manufacturer-provided characteristic curves for the five tested nozzle models: 45°_490683 (a), 60°_490684 (b), 90°_490686 (c), 120°_490688 (d), and 120°_490608 (e).

These results clearly indicate the need for a recalibration of the characteristic curves based on experimental data. The recalibration led to the identification of different pressure–discharge relationships depending on the nozzle model.

For the high-flow-rate nozzles with spray angles equal to 60°, 90°, and 120° (models 490684, 490686, and 490688), the experimental data were satisfactorily described by a power-law relationship of the form:

$$Q = 3.73\ P_S^{\,0.48} \tag{92}$$

Similarly, for the low-flow-rate nozzle with a spray angle of 120° (model 490608), the P_S–Q relationship was also represented by a power-law function

$$Q = 2.26\ P_S^{\,0.49} \tag{93}$$

Conversely, the 45° high-flow-rate nozzle (model 490683) exhibited a markedly different hydraulic behavior, and its experimental P_S–Q relationship was better reproduced by a logarithmic function:

$$Q = 1.44 \ln P_S + 4.06 \tag{94}$$

The use of these calibrated relationships resulted in a substantial reduction of estimation errors for all nozzle models, as documented by the improved statistical indices reported in Table 13.

Table 13. Reliability of the characteristic curves suggested by the manufacturer, Equation (44), and those calibrated on experimental data, Equations (92), (93), and (94). Reported values include the mean relative error (MRE), the mean absolute error (MAE), and the percentage of data with absolute errors (AE) less than or equal to 10%.

	Manufacturer characteristic curves, Equation (44)		Calibration on experimental data, Equations (92), (93), and (94)		
Nozzle Type	High Q	Low Q	High Q		Low Q
Spray angle	45°, 60°, 90°, 120°	120°	45°	60°, 90°, 120°	120°
MRE	–1.7%	–5.1%	0.8%	0.1%	0.3%
MAE	5.6%	5.4%	3.9%	1.8%	4.3%
% of data with AE ≤ 10%	86.4%	86.4%	90.9%	100.0%	100.0%

From a methodological perspective, this finding highlights a potential source of uncertainty that may affect rainfall simulator studies if manufacturer data are used without experimental validation, particularly outside the calibrated range.

The performance of the rainfall simulator was than evaluated in terms of rainfall intensity and spatial uniformity. The analysis was first conducted within the central circular sampling area with a diameter of 60 cm (Figure 21b), calculating the average rainfall intensity, I_S, and the Christiansen Uniformity Coefficient (CUC), Equation (38). The corresponding results are summarized in Table 14.

Table 14. Rainfall intensity, I_S (mm h^{-1}), and Christiansen Uniformity Coefficient, CUC (%), within the central circular sampling are of 60 cm in diameter. Values are reported for both tested nozzles (n_1 and n_2) and each nozzle model and operating pressure, P_S (bar).

Spray Angle and Nozzle Model	Nozzle Type	Nozzle n.	P_S (bar)	I_S (mm h^{-1})	CUC (%)
45°_490683	High *Q*	n_1	1.00	186.9	91.5
			1.50	247.0	91.7
		n_2	1.03	209.1	91.4
			1.50	253.1	90.2
60°_490684	High *Q*	n_1	1.02	327.4	66.5
			1.54	321.4	72.4
		n_2	1.02	164.2	91.8
			1.52	176.3	92.2
90°_490686	High *Q*	n_1	0.25	130.6	93.9
			0.51	85.4	95.6
		n_2	0.25	132.6	91.0
			0.52	83.1	95.4
120°_490688	High *Q*	n_1	0.26	64.6	92.1
			0.52	60.6	96.2
		n_2	0.26	55.3	97.1
			0.53	55.2	97.2
120°_490608	Low *Q*	n_1	0.26	62.1	73.5
			0.54	68.9	90.9
		n_2	0.25	44.7	88.1
			0.51	51.6	95.6

The results indicate that nozzle models characterized by wide spray angles generally produced rainfall distributions with good to excellent uniformity within the reference plot. In particular, the 120° and 90° nozzle models exhibited CUC

values typically exceeding 90% for the investigated pressure levels, except for the 120°_490608 model operating at low P_S. These uniformity levels are fully consistent with the criteria commonly adopted in rainfall simulation studies for hydrological and erosion applications (Iserloh et al., 2013a).

In contrast, nozzle models with narrower spray angles showed a more variable behavior. For the 60° nozzle, marked differences were observed between nominally identical nozzles (n_1 and n_2) in both average rainfall intensity and uniformity. This result highlights a significant technological variability for this nozzle model, which affects not only the hydraulic response but also the spatial distribution of rainfall. Moreover, the rainfall intensities generated by the 60° nozzle were generally very high, exceeding typical values adopted in erosion experiments, thus limiting its applicability for plot-scale investigations.

Although the CUC values of the 45° nozzle model resulted relatively high, they also produced high rainfall intensities within the reference plot. Consequently, this nozzle configuration is less suitable for controlled rainfall simulation aimed at reproducing realistic erosive conditions.

An additional aspect emerging from Table 14 is the limited influence of operating pressure on the average rainfall intensity for some nozzle models, particularly those characterized by wide spray angles, and it becomes especially pronounced for the 90° nozzles, which exhibit highly stable rainfall intensity values across the investigated pressure range. Overall, for 90° and 120° models, changes in pressure primarily affected the spatial redistribution of rainfall rather than producing a proportional variation in I_S. This behavior further supports the conclusion that, for the proposed simulator, rainfall intensity is more effectively controlled by selecting the nozzle model than by adjusting the operating pressure alone.

Therefore, the analysis conducted in the reference plot demonstrates that the proposed rainfall simulator can produce spatially uniform rainfall conditions suitable for soil erosion experiments. In particular, the results identify wide spray-angle nozzles as the most reliable configurations for achieving realistic rainfall intensities and high uniformity at the plot scale.

The spatial distribution of the simulated rainfall was further investigated over the entire wetted area. This analysis was carried out to evaluate how rainfall intensity

and spatial uniformity vary with distance from the nozzle axis, providing additional insight into the suitability of different nozzle configurations for plot-scale erosion experiments.

Rainfall spatial variability was analyzed using two complementary approaches, consistent with the methodology described in Section 2.2.1.4. First, I_S was evaluated by progressively increasing the radius of circular sampling areas centered below the nozzle. Second, the CUC was computed over concentric rings, defined as annular areas bounded by two successive radii, thereby isolating local radial variability independently of the cumulative averaging effect associated with circular areas. The results of these analyses are illustrated in Figure 54, where I_S and CUC are reported as functions of distance for the different nozzle models, operating pressures, and tested nozzles (n_1 and n_2).

The analysis based on circular areas (Figure 54a, c, e, g, and i) reveals a gradual decrease in average rainfall intensity with increasing distance from the nozzle axis. This behavior reflects the progressive inclusion of peripheral regions characterized by lower rainfall intensities. However, nozzle models characterized by wide spray angles (90° and 120°) (Figure 54a, c, e) exhibit less sensitivity of I_S to distance within the 30 cm radius wetted area compared to those with narrower spray angles (60° and 45°) (Figure 54g, i). Indeed, narrow spray-angle configurations are characterized by rainfall intensities that are largely concentrated near the nozzle axis and decrease sharply with increasing distance, resulting in a highly non-uniform radial distribution.

A distinctive behavior is observed for the 45° nozzle model, which is the only configuration exhibiting an increasing trend of I_S with distance from the nozzle axis over part of the wetted area. This counterintuitive pattern reflects the highly concentrated jet structure, further confirming the unsuitability of this configuration for plot simulation.

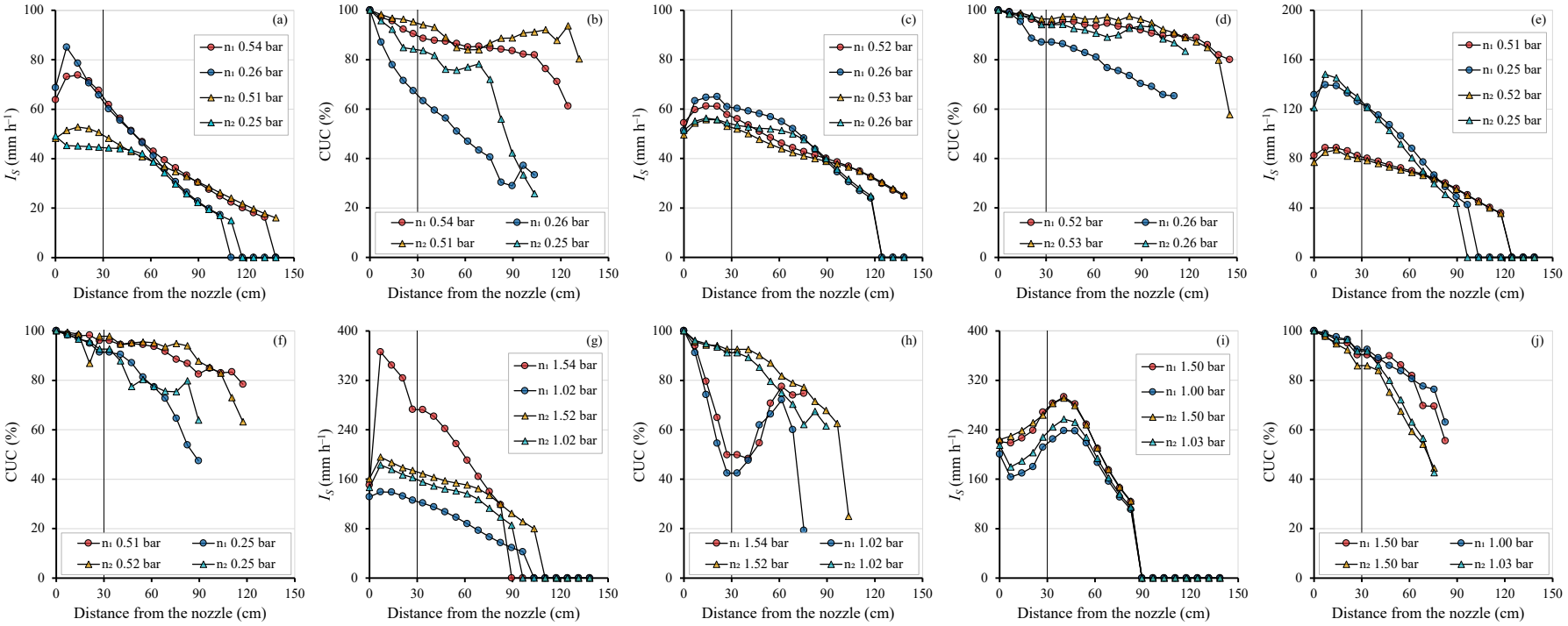

Figure 54. Radial variation of average rainfall intensity, I_S (mm h^{-1}), and Christiansen Uniformity Coefficient, CUC (%), as a function of distance from the nozzle axis for the tested nozzle models. Panels (a–b) refer to the 120°_490608 nozzle model, (c–d) to the 120°_490688 nozzle model, (e–f) to the 90°_490686 nozzle model, (g–h) to the 60°_490684 nozzle model, and (i–j) to the 45°_490683 nozzle model. For each nozzle, I_S is evaluated over circular sampling areas (upper panels), while CUC is computed over concentric rings (lower panels). In each panel, results are reported for the two tested nozzles (n_1 and n_2) and the corresponding operating pressure values, P_S (bar). The solid black vertical line at 30 cm denotes the radius of the central sampling area adopted for plot-scale analyses.

The concentric-ring analysis shows that CUC values remain high across a broad range of distances, especially for wide-spray-angle, high-flow-rate nozzle models (120°_490688, 90°_490686) (Figure 54d, f), which maintain elevated uniformity levels even beyond the reference plot radius. An additional systematic behavior is the positive effect of operating pressure on rainfall uniformity. For most nozzle models, increasing P_S results in higher CUC values, indicating a more homogeneous redistribution of rainfall as droplet dispersion increases with pressure.

In contrast, nozzle models with narrower spray angles (60°_490684, 45°_490683) (Figure 54h, j) exhibit markedly different patterns, with CUC values rapidly decreasing with increasing distance. The low-flow-rate 120° nozzle (model 120°_490608) (Figure 54b) exhibits intermediate behavior, characterized by greater sensitivity to operating pressure, with reduced uniformity at low P_S values and improved spatial homogeneity at higher pressures. This finding suggests that although this nozzle model can be used for rainfall simulation, its operational range is more restricted than that of high-flow-rate, wide-angle nozzles.

Additionally, the 90° nozzle model exhibits the lowest technological variability among the tested configurations, as demonstrated by the close agreement between n_1 and n_2 in terms of both rainfall intensity and CUC across the entire wetted area.

In addition to the radial analyses based on circular areas and concentric rings, the spatial variability of rainfall intensity was further investigated using GIS tools to generate thematic maps over the wetted area. Figure 55 shows an example of the spatial distribution of rainfall intensity for the high–flow–rate nozzles with spray angles of 120° and 90°, operated at test pressures of 0.53 and 0.52 bar, respectively, which were among the configurations exhibiting the best overall rainfall simulation performance.

The maps highlight that, within the simulator plot area, the two nozzle models generate different ranges of rainfall intensity while maintaining a relatively homogeneous spatial distribution of I_S. For both configurations, a decreasing trend in rainfall intensity with increasing distance from the nozzle is observed, consistently with the results of the radial analyses.

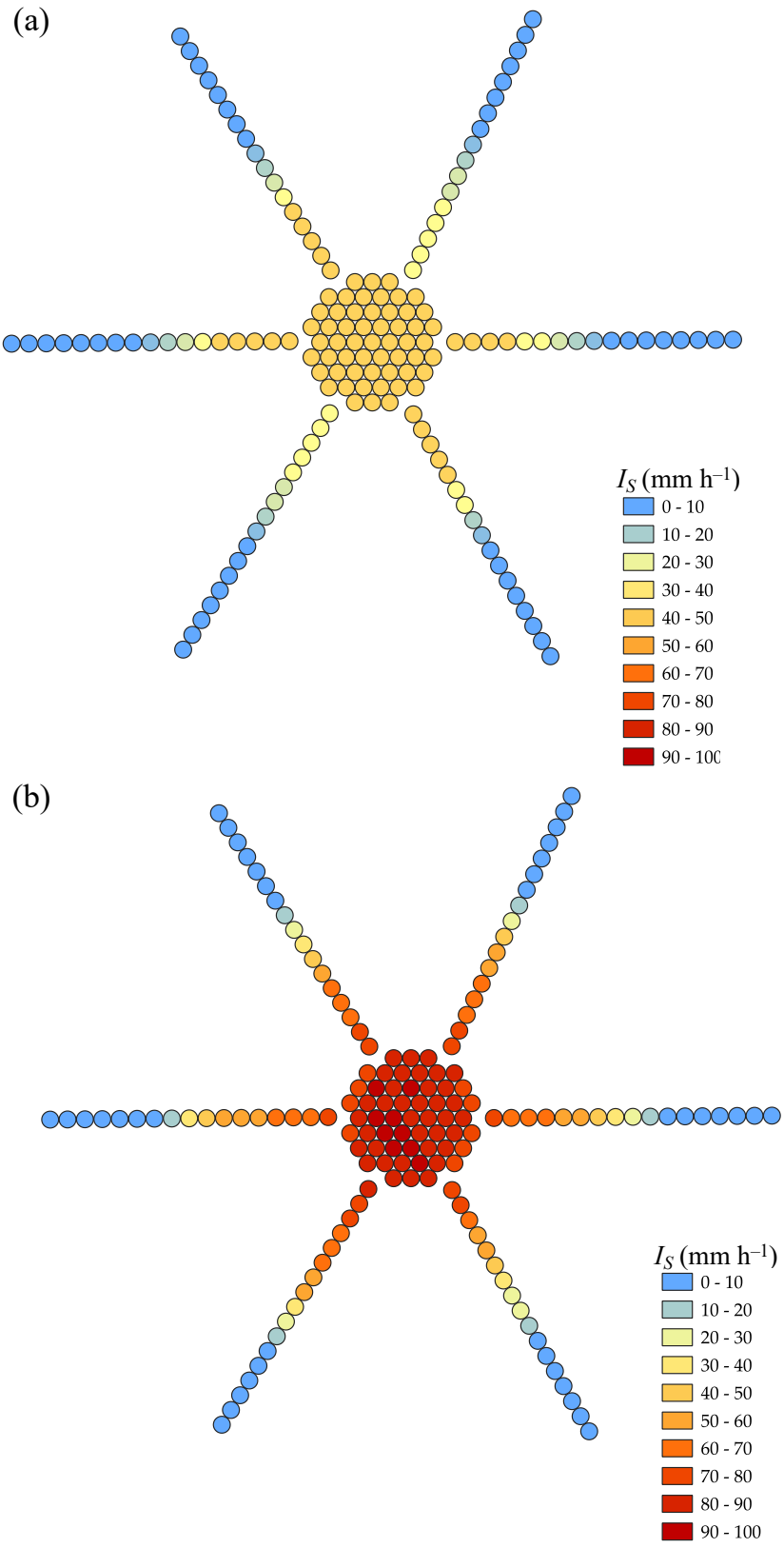

Figure 55. Example of the spatial distribution of rainfall intensity, I_S (mm h^{-1}), produced by the 120°_490688 nozzle operated at a test pressure of 0.53 bar (a) and the 90°_490686 nozzle operated at a test pressure of 0.52 bar (b).

Overall, the combined use of circular-area, concentric-ring, and GIS-based spatial analyses confirms that nozzle geometry plays a dominant role in controlling the spatial distribution of simulated rainfall. Nozzle models with wide spray angles, particularly those with 90° and 120°, provide the most favorable combination of rainfall intensity, spatial uniformity, and spatial stability across the wetted area, effectively minimizing edge effects and enhancing the representativeness of the imposed rainfall forcing at the plot scale.

In accordance with the experimental protocol described in Section 2.2.3.4, the disdrometric characterization of the Palermo PRS was carried out at the present stage for a single nozzle configuration, namely the 120°_490608 model. Additional measurement campaigns are planned to apply the same disdrometric methodology to other nozzle models identified here as hydraulically and spatially suitable, thereby broadening the energetic and microphysical characterization of the PRS.

Unlike volumetric measurements, which covered the entire wetted area, the disdrometric characterization focused on the central portion of the rainfall pattern, spatially consistent with the 60 cm diameter reference area previously identified as the most homogeneous zone of the simulator.

For each sampled position with the Parsivel^2 optical disdrometer, rainfall intensity, I_{OTT} (mm h^{-1}), kinetic power, $P_{n,OTT}$ (J m^{-2} s^{-1}), and momentum, M_{OTT} (N m^{-2}), were derived from the raw PSVDs applying Equations (46), (47), and (48), respectively. In addition, the drop size distribution measured at each sampling position was used to compute several statistical descriptors of drop diameter, including the mean of the diameter, $\mu_{(D)}$ (cm), the standard deviation, $\sigma_{(D)}$ (cm), the median volume diameter, D_0 (cm), and the median diameter, D_{50} (cm).

This approach allows the spatial variability of rainfall properties to be analyzed not only in terms of intensity but also in terms of energy-related characteristics and statistical descriptors directly relevant to soil erosion processes.

Table 15 lists the CUC values, computed using Equation (38), for all the above-mentioned rainfall variables and statistical parameters. The CUC indicates a high degree of spatial uniformity across all rainfall variables derived from disdrometric measurements. For both operating pressures, CUC values largely exceed the commonly accepted threshold of 80% for rainfall simulation experiments in open-

field and laboratory conditions (Esteves et al., 2000; Iserloh et al., 2013a; Mhaske et al., 2019; Salem and Meselhy, 2021), confirming the good spatial performance of the tested nozzle configuration across the sampled surface, also from a disdrometric perspective.

Table 15. Christiansen Uniformity Coefficient (CUC, %) values computed from disdrometric measurements for the two investigated operating pressures, P_S =0.26 bar and P_S =0.51 bar. CUC values are reported for rainfall intensity, I_{OTT}, kinetic power, $P_{n,OTT}$, momentum, M_{OTT}, mean drop diameter $\mu_{(D)}$, standard deviation of drop diameter $\sigma_{(D)}$, volumetric median diameter D_0, and median diameter D_{50}.

	CUC (%)	
	P_S = 0.26 bar	P_S = 0.51 bar
I_{OTT} (mm h^{-1})	90.9 %	94.0 %
$P_{n,OTT}$ (J m^{-2} s^{-1})	85.5 %	88.5 %
M_{OTT} (N m^{-2})	88.0 %	93.8 %
$\mu_{(D)}$ (cm)	97.5 %	99.5 %
$\sigma_{(D)}$ (cm)	88.3 %	95.3 %
D_0 (cm)	88.2 %	93.5 %
D_{50} (cm)	97.7 %	99.5 %

As previously observed in the volumetric analyses, an increase in operating pressure from 0.26 bar to 0.51 bar generally improves uniformity, as reflected by higher CUC values across all investigated variables. This behavior can be attributed to enhanced droplet dispersion at higher pressures, which promotes a more homogeneous spatial redistribution of rainfall properties.

The spatial variability of rainfall properties derived from disdrometric measurements is illustrated in Figure 56–Figure 62. For each investigated variable, thematic maps were generated using a GIS to provide a graphical representation of its spatial distribution within the reference sampling area. Specifically, Figure 56, Figure 57, and Figure 58 show, for the two employed operating conditions, the spatial distribution of normalized I_{OTT}, $P_{n,OTT}$, and M_{OTT}, respectively. Figure 59, Figure 60, Figure 61, and Figure 62 present the spatial distribution of normalized statistical descriptors of the drop size distribution, namely $\mu_{(D)}$, $\sigma_{(D)}$, D_0, and D_{50}. All variables are expressed in normalized form by dividing the measured value at each sampling position (X) by the corresponding spatial mean value ($\bar{X}$) computed

over all sampling locations, consistent with the approach adopted in Section 3.4.1. This normalization enables direct comparison of spatial patterns, independent of differences in absolute magnitude between operating pressures and the investigated variables.

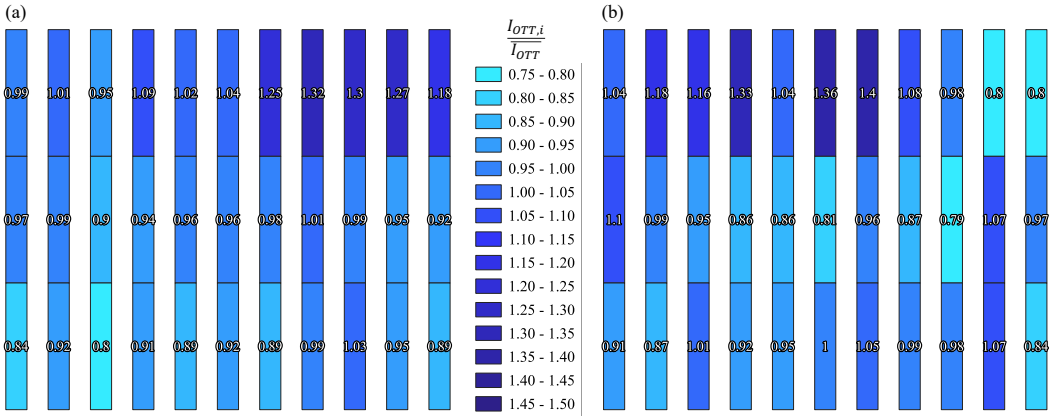

Figure 56. Spatial distribution of normalized rainfall intensity, I_{OTT} (mm h^{-1}), derived from disdrometric measurements for the nozzle model 120°_490608. Values are expressed as the ratio between the rainfall intensity of the i-th position $I_{OTT,i}$ and the mean value over the entire area $\overline{I_{OTT}}$. Results are shown for pressures of 0.26 bar (a) and 0.51 bar (b).

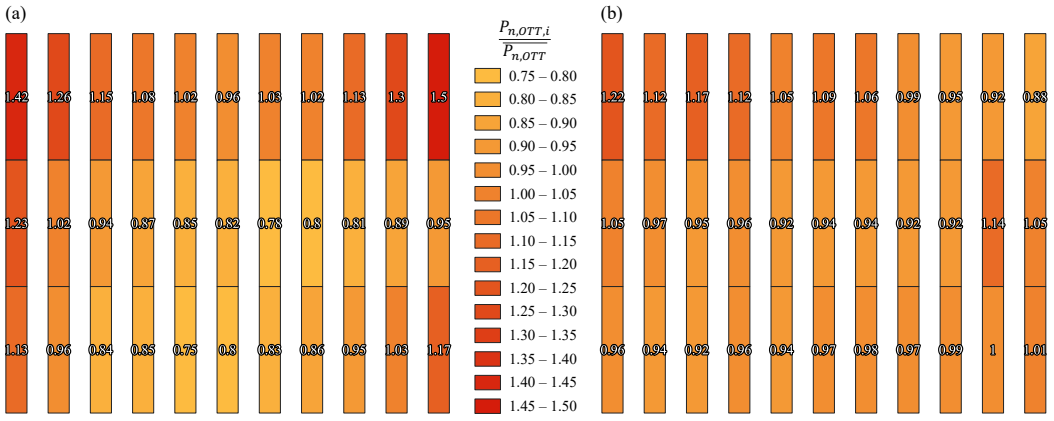

Figure 57. Spatial distribution of normalized rainfall kinetic power, $P_{n,OTT}$ (J m^{-2} s^{-1}), derived from disdrometric measurements for the nozzle model 120°_490608. Values are expressed as the ratio between the kinetic power of the i-th position $P_{n,OTT,i}$ (J m^{-2} s^{-1}), and the mean value over the entire area $\overline{P_{n,OTT}}$. Results are shown for pressures of 0.26 bar (a) and 0.51 bar (b).

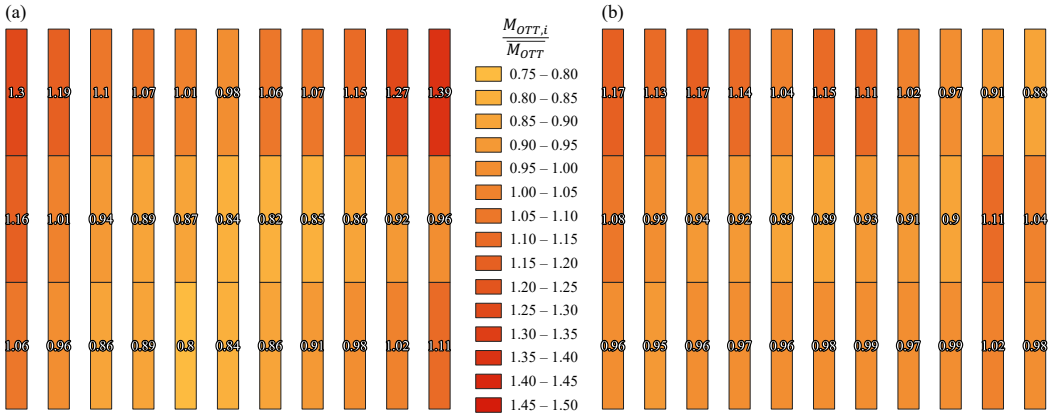

Figure 58. Spatial distribution of normalized rainfall momentum, M_{OTT} (N m^{-2}), derived from disdrometric measurements for the nozzle model 120°_490608. Values are expressed as the ratio between the momentum of the i-th position $M_{OTT,i}$ and the mean value over the entire area $\overline{M_{OTT}}$. Results are shown for pressures of 0.26 bar (a) and 0.51 bar (b).

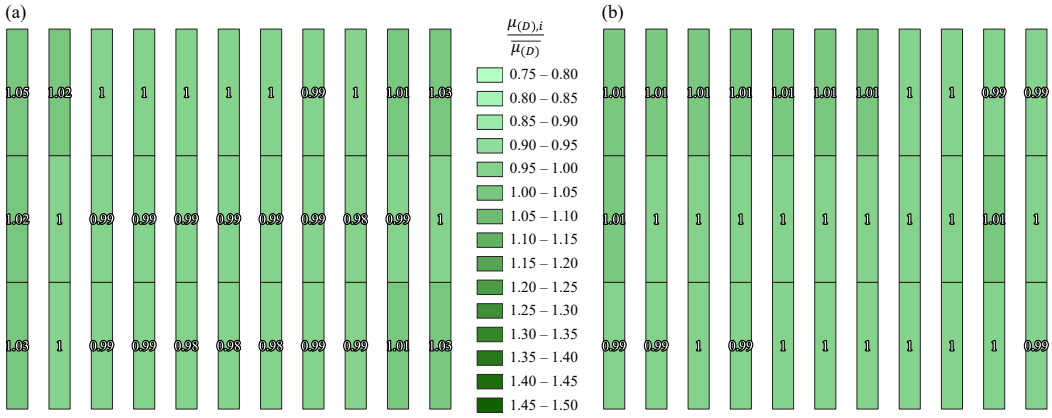

Figure 59. Spatial distribution of normalized mean drop diameter, $\mu_{(D)}$ (cm), derived from disdrometric measurements for the nozzle model 120°_490608. Values are expressed as the ratio between the mean drop diameter of the i-th position $\mu_{(D),i}$ and the mean value over the entire area $\overline{\mu_{(D)}}$. Results are shown for pressures of 0.26 bar (a) and 0.51 bar (b).

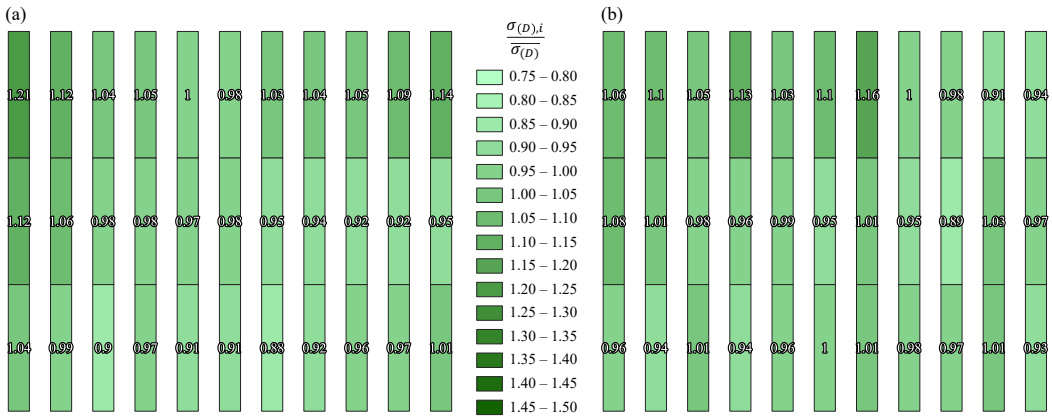

Figure 60. Spatial distribution of normalized diameter standard deviation $\sigma_{(D)}$ derived from disdrometric measurements for the nozzle model 120°_490608. Values are expressed as the ratio between the diameter standard deviation of the i-th position $\sigma_{(D),i}$ and the mean value over the entire area $\overline{\sigma_{(D)}}$. Results are shown for pressures of 0.26 bar (a) and 0.51 bar (b).

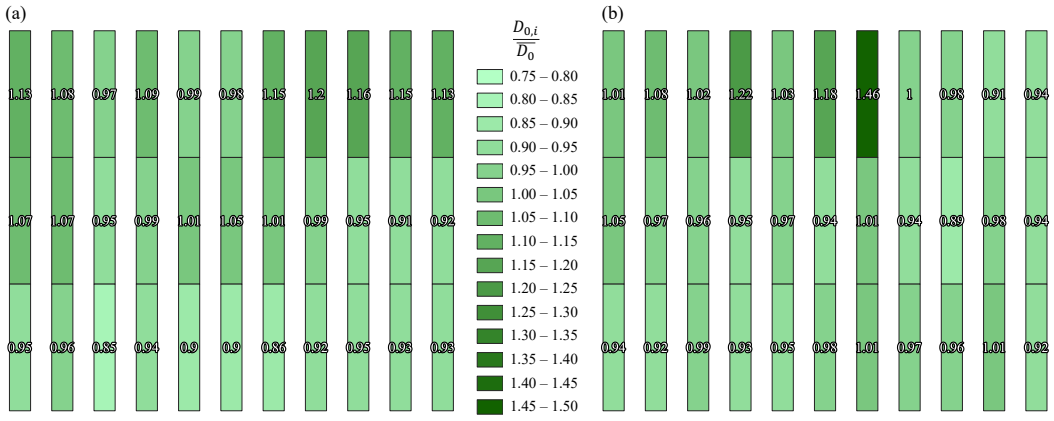

Figure 61. Spatial distribution of normalized median volume diameter, D_0 (cm), derived from disdrometric measurements for the nozzle model 120°_490608. Values are expressed as the ratio between the median volume diameter of the i-th position $D_{0,i}$ and the mean value over the entire area $\overline{D_0}$. Results are shown for pressures of 0.26 bar (a) and 0.51 bar (b).

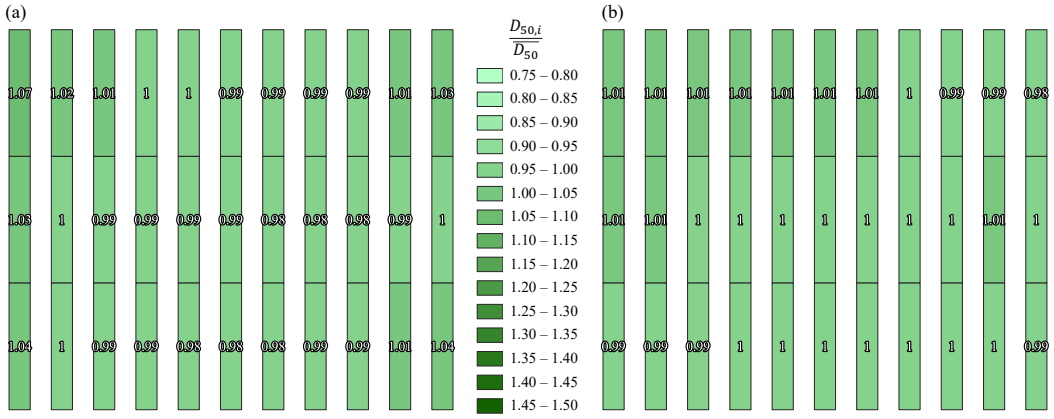

Figure 62. Spatial distribution of normalized median diameter, D_{50} (cm), derived from disdrometric measurements for the nozzle model 120°_490608. Values are expressed as the ratio between the median diameter of the i-th position $D_{50,i}$ and the mean value over the entire area $\overline{D_{50}}$. Results are shown for pressures of 0.26 bar (a) and 0.51 bar (b).

Figure 56–Figure 62 further supports the quantitative results summarized in Table 15 and provide additional insight into the uniformity of the simulated rainfall properties: (i) for all investigated variables, an improvement in spatial uniformity is generally observed with increasing operating pressure; (ii) apart from a few localized deviations, the areas exhibiting lower uniformity, typically associated with both darker and lighter color tones, are mainly located near the corners of the sampled domain; (iii) a higher degree of spatial uniformity can be observed for rainfall momentum compared to kinetic power, reflecting the different sensitivity of these variables to local fluctuations in drop size and velocity; (iv) the results in

terms of rainfall intensity within the central portion investigated with both volumetric and disdrometric methodologies is consistent, confirming the agreement of the two independent measurement approaches; (v) the statistical descriptors of drop diameter exhibit the most homogeneous spatial patterns, particularly in terms of $\mu_{(D)}$ and D_{50}.

Overall, the disdrometric results confirm that the tested nozzle configuration exhibits reliable, reproducible spatial performance, supporting its suitability for further deployment in open-field experiments and enabling the transition from controlled laboratory investigations to full-scale erosion studies.

3.4.4 Characterization of the Pressurized Rainfall Simulator of León

This section presents the results obtained during the research period carried out at the University of León, aimed at the comprehensive characterization of a pressurized rainfall simulator originally designed for studies on the erosion and weathering of stone-based heritage surfaces.

As for the Palermo PRS, the characterization was conducted combining a traditional volumetric calibration based on rain collectors with a disdrometric analysis performed using an optical Parsivel^2 disdrometer. This methodology enabled the simultaneous assessment of rainfall intensity, its spatial uniformity, and the associated energetic parameters, namely rainfall kinetic power and momentum.

Figure 63 presents the spatial distribution of rainfall intensity obtained from the volumetric calibration of the simulator for the three experimental treatments, which differ in collector geometry and simulation duration. Each value represents the average of three repeated simulations performed under identical operating conditions.

The maps clearly show a non-uniform rainfall pattern over the entire wetted area of 1.8 m × 1.8 m, characterized by lower intensities along the outer portions of the plot and markedly higher values concentrated in the central zone. When the analysis is restricted to the central 1.2 m × 1.2 m area, the spatial variability is reduced and the rainfall field appears more homogeneous, albeit with higher mean intensities.

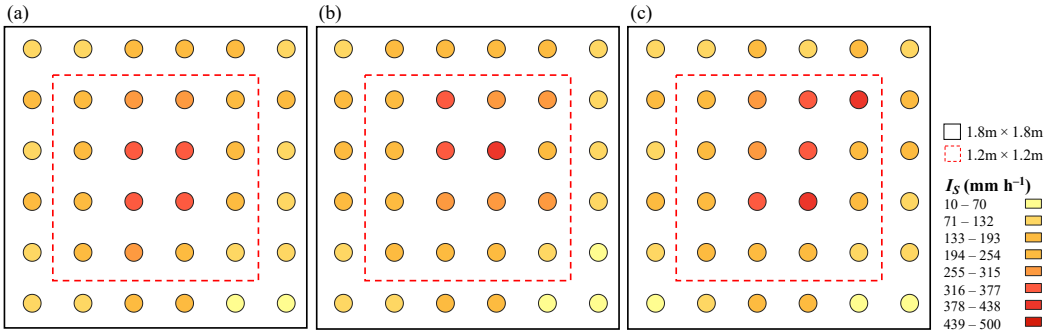

Figure 63. Spatial distribution of simulated rainfall intensity, I_S (mm h^{-1}), for the three characterization treatments (T) employed in this investigation: plastic vessels for 5 minutes (T1) (a), plastic cups for 5 minutes (T2) (b), and plastic cups for 10 minutes (T3) (c).

This behavior can be attributed to the simulator's structural configuration, which consists of a dense array of drippers and minisprinklers arranged to generate a wide drop-size spectrum. Moreover, the superposition of droplets originating from multiple emitters enhances the rainfall intensity in the central area, whereas a smaller number of active sources influences peripheral locations.

Table 16 reports, for each treatment, the mean rainfall intensity, the corresponding standard deviation, and the Christiansen Uniformity Coefficient computed over both the full wetted area and the reduced central area. While the mean rainfall intensity remains remarkably consistent across treatments, substantial differences emerge in spatial uniformity. Across the full sampling surface, the CUC values indicate a relatively low degree of homogeneity, whereas values increase significantly when only the central area is considered, reaching levels commonly regarded as acceptable for small-scale experimental studies.

Table 16. Mean simulated rainfall intensity, I_S (mm h^{-1}), standard deviation, and Christiansen Uniformity Coefficient, CUC (%) for the three characterization treatments, plastic vessels for 5 minutes (T1), plastic cups for 5 minutes (T2), and plastic cups for 10 minutes (T3), evaluated for both the 1.8 m × 1.8 m and the 1.2 m × 1.2 m sampling areas.

	Mean I_S (mm h^{-1})	Standard Deviation	CUC (%)	Mean I_S (mm h^{-1})	Standard Deviation	CUC (%)
Treatment	Full wetted area of 1.8 m × 1.8 m			Central wetted area of 1.2 m × 1.2 m		
T1	183.1	87.2	61.7	256.9	66.6	79.5
T2	181.8	91.0	59.9	252.9	71.0	77.6
T3	182.9	108.3	55.9	257.6	98.1	68.4

Indeed, the mean CUC over the three treatments in the 1.2 m × 1.2 m area, equal to 75.16%, is consistent with uniformity coefficients widely accepted in the literature, typically close to or slightly below 80%, especially when simulator design prioritizes the reproduction of realistic drop velocity characteristics over perfect spatial uniformity (Fernández-Raga et al., 2022).

To further assess whether the observed differences in rainfall intensity were statistically meaningful, a two-factor analysis of variance was conducted. Table 17 presents the results of the two-way ANOVA performed to assess the effects of spatial position and treatment (accounting for both collector type and simulation duration) on the measured rainfall intensity. The analysis confirmed that rainfall-intensity variability is primarily controlled by spatial position within the plot, whereas neither collector type nor simulation duration yields statistically significant differences. This result supports the use of a single representative rainfall intensity value at each location, obtained by averaging across the different volumetric treatments.

Table 17. Results of the two-factor analysis of variance (ANOVA) performed to evaluate the influence of two main factors on simulated rainfall intensity: (i) characterization treatment; (ii) spatial position of the rain collectors within the sampling grid. The table reports the sum of squares (SQ), degrees of freedom (df), mean squares (MQ), F-value, p-value, and critical F-value (F-critical) for each source of variation.

Source of variation	SQ	df	MQ	F-value	p-Value	F-Critical
Rain collector position	2,496,505	35	71,328	59.14	6.4×10^{-92}	1.48
Treatments	107	2	54	0.04	0.96	3.04
Interaction	197,798	70	2,826	2.34	1.4×10^{-6}	1.36
Intragroup	260,497	216	1,206	–	–	–
Total	2,954,908	323	–	–	–	–

Once the reliability of the volumetric calibration had been established, the rainfall intensity values obtained from the disdrometric technique (I_{OTT}, mm h^{-1}) were compared with the mean intensity derived from the three volumetric treatments. Figure 64 presents, for each of the 16 fixed positions of the 1.2 m × 1.2 m area, the comparison between I_{OTT} and I_S. The comparison reveals a systematic underestimation of rainfall intensity by the disdrometric measurements, with most

data points lying below the 1:1 agreement line and a substantial fraction exceeding ±20% relative deviation.

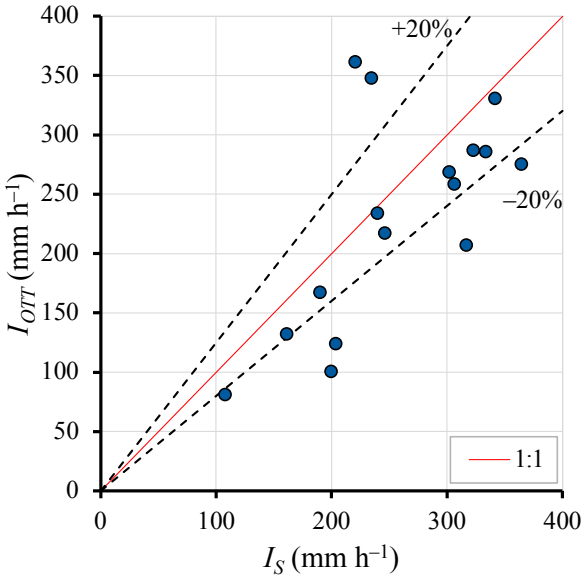

Figure 64. Comparison between simulated rainfall intensity obtained from volumetric measurements, I_S (mm h^{-1}), and using the Parsivel^2 disdrometer I_{OTT} (mm h^{-1}), in the 1.2 m × 1.2 m wetted area. The solid line represents the 1:1 agreement, while dashed lines indicate the ±20% deviation range.

This discrepancy is consistent with previous findings reported for optical disdrometers operating under high-intensity rainfall conditions (Angulo-Martínez et al., 2018) and can be explained by a combination of factors. Instrumental limitations, such as the partial interception of drops at the laser beam margins and the misclassification of overlapping particles, tend to bias disdrometric estimates toward lower intensities. Furthermore, the sampling area of the disdrometer (5.4×10^{-3} m^2) is considerably smaller than that of the rain collectors (9.3×10^{-3} m^2 for p_v, 9.6×10^{-3} m^2 for p_c). This difference makes disdrometric measurements more sensitive to local spatial variability within a rainfall field that is not perfectly uniform, thereby amplifying point-scale discrepancies between the two methods.

To provide a spatial interpretation of the differences between the two measurement techniques, the thematic map produced by GIS-based interpolation of volumetric and disdrometric measurements is presented in Figure 65. The coherent spatial overlay of rain collector positions and the disdrometer location, combined with a consistent color scale, allows for an immediate visual comparison between the two datasets.

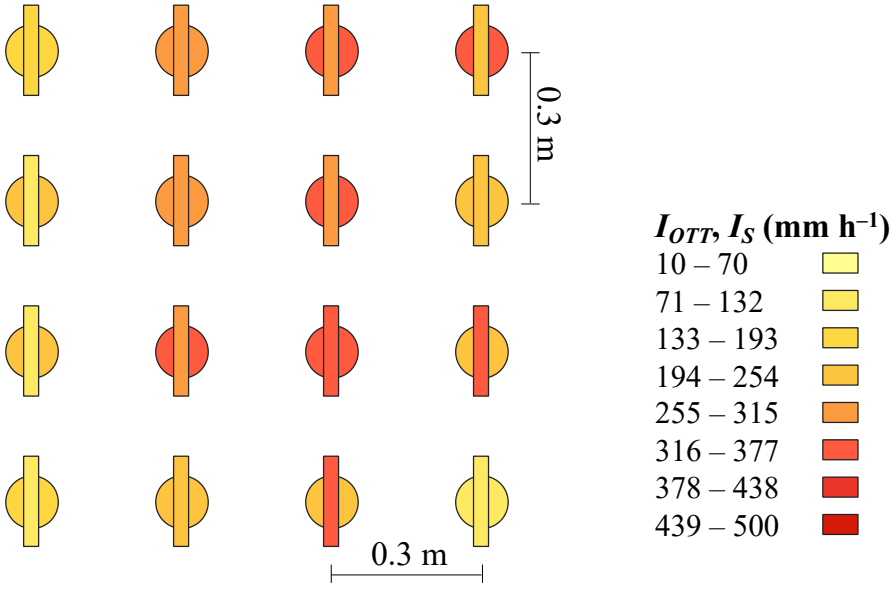

Figure 65. Spatial comparison of rainfall intensity obtained from disdrometric, I_{OTT} (mm h^{-1}), and volumetric, I_S (mm h^{-1}), measurements.

The map clearly shows that comparable rainfall-intensity values are observed only at a limited number of locations, whereas, in general, the intensities derived from disdrometric measurements appear less uniformly distributed than those obtained from the rain collectors. This visual impression is confirmed by the quantitative evaluation based on the CUC, listed in Table 18.

Table 18. Summary of the mean values and Christiansen Uniformity Coefficient, CUC (%), in terms of rainfall intensity measured with the volumetric method, I_S (mm h^{-1}), and with the disdrometer, I_{OTT} (mm h^{-1}), as well as of rainfall kinetic power, Pn (J m^{-2} s^{-1}) and momentum, M (N m^{-2}), over the 1.2 m × 1.2 m wetted area.

	I_S (mm h^{-1})	I_{OTT} (mm h^{-1})	$P_{n,OTT}$ (J m^{-2} s^{-1})	M_{OTT} (N m^{-2})
Mean value	255.8	229.6	1.54	0.39
CUC (%)	75.7	61.1	61.5	65.0

Despite similar mean rainfall intensities recorded over the 1.2 × 1.2 m area using the volumetric and disdrometric calibrations, the uniformity levels differ substantially, with a CUC of 75.7% for I_S and 61.1% for I_{OTT}.

These discrepancies are consistent with findings reported in the literature, which highlight that the number, spatial arrangement, and physical characteristics of rainfall collectors, such as their size and shape, directly influence the representation of rainfall distribution over an experimental surface (Green and Pattison, 2022).

The assessment of simulator performance was further extended by analyzing the spatial distribution of energy-related variables derived from disdrometric measurements, namely rainfall kinetic power, $P_{n,OTT}$, and momentum, M_{OTT}, as shown in Figure 66.

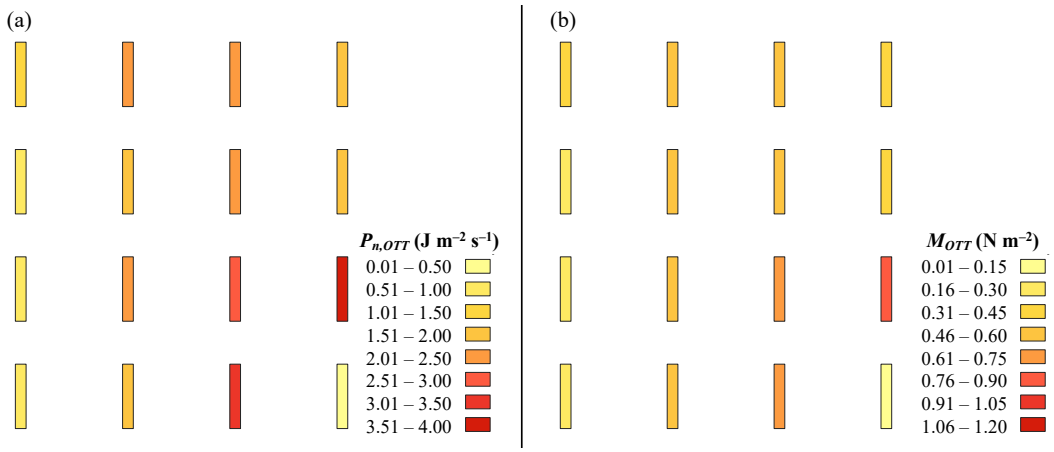

Figure 66. Spatial distribution of rainfall kinetic power, Pn (J m^{-2} s^{-1}), and momentum, M (N m^{-2}), obtained from disdrometric measurements.

The spatial patterns of the energetic parameters closely mirror those observed for I_{OTT}. Moreover, rainfall momentum exhibits slightly greater spatial uniformity than kinetic power (Table 18). This difference reflects the distinct dependence of the two parameters on fall velocity: while momentum scales linearly with velocity, kinetic power scales with the square of velocity, thereby amplifying local variations in drop dynamics. Therefore, spatial heterogeneity in the drop size and velocity distributions has a stronger impact on kinetic power than on momentum.

The magnitude of the obtained values indicates that the simulator can generate rainfall events characterized by high erosive potential. However, the uniformity coefficients calculated for both energetic parameters remain comparable to those derived for disdrometric rainfall intensity, highlighting that, when assessed through point-based disdrometric measurements, the simulator exhibits limited spatial uniformity even within the central area.

Such limited uniformity, however, does not necessarily represent a critical drawback. As discussed by Fernández-Raga et al. (2022), non-uniform rainfall fields can still be effectively exploited for experimental purposes when their spatial patterns are properly characterized. Specifically, the wetted area can be subdivided into zones with relatively homogeneous conditions based on the maps obtained

from volumetric and disdrometric calibrations. Within each subzone, rainfall intensity and associated energetic parameters exhibit limited variability, enabling tests to be performed on well-defined, reduced portions of the surface under consistent boundary conditions. The presence of areas characterized by different levels of intensity and energy provides the opportunity to investigate material responses under a range of controlled impact conditions using the same simulator configuration. By systematically assigning samples to specific subzones, or by rotating them among zones, it becomes possible to design experiments that either isolate a given energy level or integrate the effects of multiple conditions in a reproducible manner. This approach enables the intrinsic spatial variability of the simulator to be transformed from a limitation into a practical experimental resource.

3.4.5 Assessment of Parsivel² Reliability Under Laboratory Conditions and Extension of the Empirical Fall Velocity Relationship to Pressurized Rainfall Simulators

In the previous sections, both drip-type and pressurized rainfall simulators were characterized from a hydrological and energetic perspective using volumetric and disdrometric measurements. In particular, Sections 3.4.3 and 3.4.4 presented the experimental analysis of two pressurized devices, namely the Palermo PRS and the León PRS, highlighting their rainfall-intensity fields and drop-size distributions as measured by the Parsivel² optical disdrometer. However, these investigations were limited to the direct interpretation of disdrometric outputs and did not address the instrument's reliability under laboratory conditions, nor the applicability of empirical formulations for estimating raindrop fall velocity.

Although the Parsivel² disdrometer is widely used for natural rainfall monitoring, its performance in controlled environments, characterized by relatively low fall heights and non-terminal fall conditions, requires specific verification. Moreover, for simulated rainfall, direct measurement of raindrop fall velocity may be limited by instrumentation, making alternative estimation approaches potentially more robust.

For these reasons, the present section is devoted to a systematic evaluation of the Parsivel² reliability and to the development and validation of an empirical

relationship for estimating raindrop fall velocity as a function of drop diameter and fall height. Specifically, the analysis is structured in three main steps.

First, the accuracy of the Parsivel^2 is assessed under controlled conditions using drip-type rainfall simulators. Single drops were isolated, and reference measurements of diameter and fall velocity were carried out through weighing and photographic techniques described in previous chapters. This phase enables testing the instrument response in an ideal configuration and quantifying potential biases. Table 19 reports the experimental dataset used for this purpose, including the range of drop diameters and fall heights considered for both the Modified Kamphorst Simulator (MKS) and the Drop Generator (DG).

Table 19. Experimental dataset used for testing the reliability of the Parsivel^2 disdrometer with drip-type rainfall simulators: drop diameters, D (cm), and corresponding fall heights, h (m), considered for the Modified Kamphorst Simulator (MKS) and the Drop Generator (DG).

	D (cm)	h (m)
MKS	0.33	0.27; 0.58; 1.08; 1.75; 2.32; 2.34
DG	0.51	0.24; 0.59; 1.21; 1.79; 2.35
	0.57	0.22; 0.57; 2.32
	0.63	1.75; 2.33

Second, the validated approach is extended to the pressurized rainfall simulator developed in Palermo. In this case, Parsivel^2 measurements are compared with independent estimates obtained from the proposed empirical fall velocity formulation, Equation (52), to verify the consistency of the disdrometric data also in more complex rainfall fields.

Finally, once the empirical relationship has been tested and validated, its applicability is further investigated by applying it to the León pressurized rainfall simulator presented in Section 3.4.4. This final step enables the evaluation of the robustness of the formulation over a wider range of experimental conditions and fall heights, thereby assessing its general validity for the energetic characterization of different types of laboratory rainfall simulators.

Figure 67 presents the comparison between the reference measurements and the corresponding Parsivel^2 outputs for drip-type simulators. Specifically, Figure 67a

shows the relationship between the measured number of raindrops, N (–), and those detected by the Parsivel^2 disdrometer, N_{OTT} (–), while Figure 67b reports the comparison between the raindrop diameters obtained through the weighing technique, D (cm), and those measured by the Parsivel^2, D_{OTT} (cm).

The analysis of Figure 67a indicates that the Parsivel^2 disdrometer provides an overall good performance in terms of the number of raindrops under the explored controlled conditions. Most experimental points are distributed close to the line of perfect agreement, with only a limited number of data falling outside the ±10% error bounds.

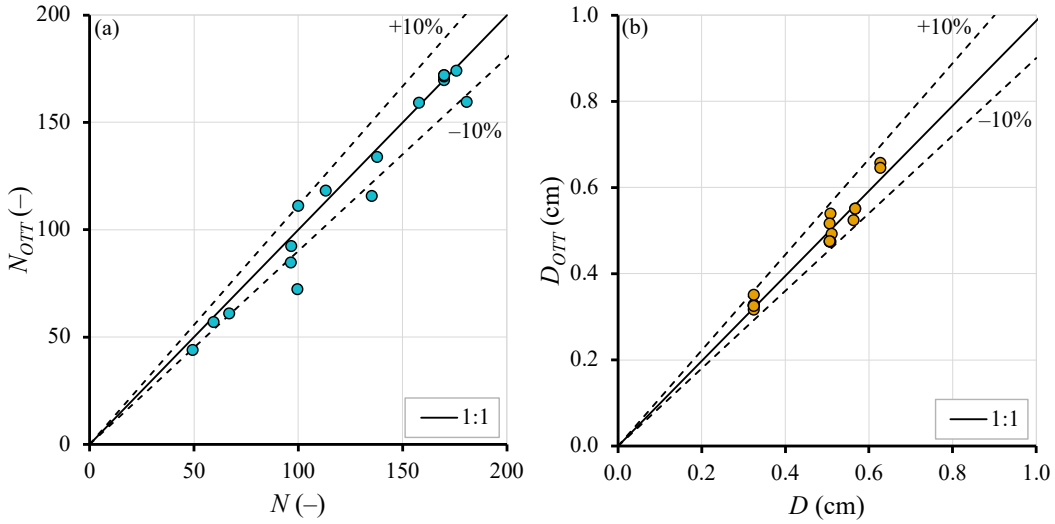

Figure 67. Relationship between raindrop diameters obtained through the weighing technique, D (cm), and those measured by the Parsivel^2, D_{OTT} (cm) (a), and between the measured number of raindrops, N (–), and those detected by the Parsivel^2, N_{OTT} (–) (b). In both panels, the line of perfect agreement (1:1) and the ±10% error ranges are shown.

A more detailed and quantitative evaluation of these discrepancies is provided in Table 20, where the error statistics are reported for two distinct diameter ranges, 0.33 cm and 0.51–0.63 cm. The results show that the instrument exhibits very high accuracy for smaller diameters, while a moderate underestimation of drop counts is observed for larger droplets.

Regarding the raindrop diameters, Figure 67b shows better behavior. All experimental points lie within the ±10% error range and are closely distributed around the 1:1 line, demonstrating that the Parsivel^2 can accurately determine the equivalent diameter of raindrops produced by drip-type simulators. This finding is

further confirmed by the error statistics summarized in Table 20, which indicate very low MRE and MAE values for both diameter ranges considered.

Table 20. Reliability of the Parsivel² disdrometer in measuring raindrop diameter, D (cm), and number of raindrops, N (–), for drip-type simulators, expressed in terms of Mean Relative Error (MRE), Mean Absolute Error (MAE), and percentage of measurements affected by an Absolute Error (AE) ≤ 10%, for two diameter ranges (0.28–0.33 cm and 0.51–0.63 cm).

	N (–)		*D* (cm)	
Drop diameter range (cm)	0.33	0.51-0.63	0.33	0.51-0.63
MRE (%)	0.25	–7.72	0.86	–2.02
MAE (%)	0.76	10.44	1.93	4.69
% of data with AE ≤ 10%	100	100	100	100

Overall, the Parsivel² provides reliable measurements of raindrop diameters across all investigated experimental conditions, while its ability to accurately measure the number of drops depends on the considered diameter range, with greater underestimation observed for larger droplets. Such behavior is consistent with the known limitations of optical disdrometers (Angulo-Martínez et al., 2018; Saha and Testik, 2023), which may have difficulty in correctly detecting large and fast-moving drops due to margin faller effects and partial beam interception. However, since drops with diameters larger than about 0.5 cm are relatively rare in natural rainfall, this bias is generally considered of limited practical relevance for standard operational applications.

The performance of the Parsivel² disdrometer was then evaluated with respect to rainfall-intensity estimation. Figure 68 compares rainfall intensity values obtained using three different approaches: the reference weighing technique, I_S, the intensity values calculated from the raw DSD measured by the Parsivel² through Equation (46), I_{OTT}, and the intensity values directly provided by the Parsivel² summary data file, I_{sum} (mm h^{-1}).

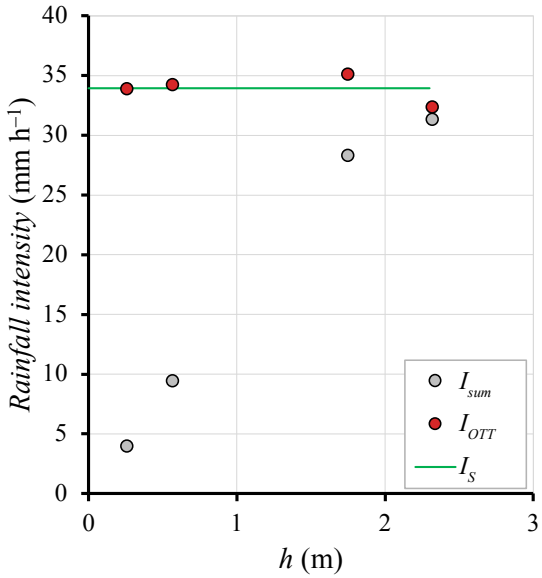

Figure 68. Comparison between rainfall intensity values obtained using three different approaches: weighing technique, I_S (mm h^{-1}), intensity calculated from Parsivel² raw Drop Size Distribution, I_{OTT} (mm h^{-1}), and intensity values provided in the Parsivel² summary data file, I_{sum} (mm h^{-1}), as a function of raindrop fall height, h (m).

The comparison shows that, for a given fall height, the intensity values computed from the raw DSD are in strong agreement with those obtained from the weighing technique. In contrast, the intensity values reported in the Parsivel² summary output differ significantly from the reference measurements, with greater errors at lower fall heights.

This result suggests that the internal algorithm used by the Parsivel² software to compute rainfall intensity may implicitly assume terminal-velocity conditions or apply corrections that are not suitable for subterminal laboratory conditions. Consequently, for simulated rainfall experiments characterized by limited fall heights, it is advisable to compute rainfall intensity directly from the raw DSD data rather than relying on the values provided in the instrument summary files.

Concerning the fall velocity of simulated raindrops, three different estimates were obtained for the drip-type simulators: values measured through the photographic technique, V_S (m s^{-1}); values measured by the Parsivel² disdrometer, $V_{S,OTT}$ (m s^{-1}); and values calculated using the empirical relationship given in Equation (52), denoted as $V_{S,calc}$. For the pressurized rainfall simulator analyzed in the following paragraphs, the photographic technique was not employed due to practical

limitations, mainly the difficulty of isolating individual droplets and the need for high-speed imaging systems.

Figure 69 plots the comparison between the reference technique, V_S, and the velocity measured by the Parsivel^2 disdrometer, $V_{S,OTT}$. The figure clearly shows a systematic underestimation of fall velocity by the disdrometer, as most experimental points lie below the line of perfect agreement. This behavior is confirmed by the error statistics summarized in Table 21, which indicate a Mean Relative Error of –14.9% and show that only 29.4% of the measurements have an absolute error below 10%.

Similar underestimations of drop velocities have been widely documented in the literature for the same instrument operating under natural rainfall conditions (Angulo-Martínez et al., 2018; Saha and Testik, 2023). These studies reported that the Parsivel^2 tends to underestimate drop velocities, particularly for larger and faster droplets, mainly due to intrinsic limitations of the optical measuring principle, including the finite thickness of the laser beam, the internal processing algorithm, and margin-faller effects. The present results confirm that such limitations also affect measurements performed under controlled laboratory conditions with simulated rainfall.

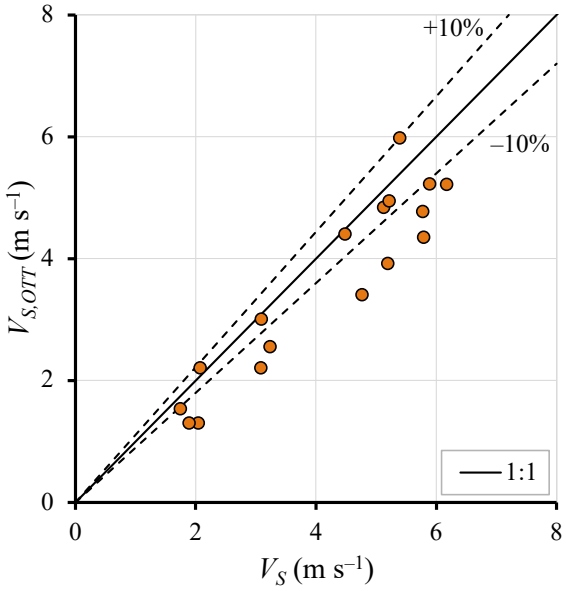

Figure 69. Comparison between the fall velocity of individual raindrops measured using the weighing technique, V_S (m s^{-1}), and that measured by the Parsivel^2 disdrometer $V_{S,OTT}$ (m s^{-1}). The solid line represents the 1:1 line, while the dashed lines indicate the ±10% error bounds.

Table 21. Statistical error metrics for the comparison of drop fall velocities obtained from three techniques: photographic method, V_S (m s^{-1}), Parsivel² disdrometer, $V_{S,OTT}$ (m s^{-1}), and estimated using Equation (46), $V_{S,calc}$ (m s^{-1}). Mean Relative Error (MRE), Mean Absolute Error (MAE), and the percentage of data with Absolute Error (AE) less than or equal to 10% are reported for each considered pair and for both the Drip-type Rainfall Simulators (DRS) and the Pressurized Rainfall Simulator (PRS) installed in Palermo.

	DRS			Palermo PRS	
Pair	V_S vs $V_{S,OTT}$	V_S vs $V_{S,calc}$	$V_{S,calc}$ vs $V_{S,OTT}$	$V_{S,calc}$ vs $V_{S,OTT}$ P_S = 0.26 bar	$V_{S,calc}$ vs $V_{S,OTT}$ P_S = 0.51 bar
MRE (%)	–14.9 %	1.5 %	–16.4 %	–14.7 %	–24.6 %
MAE (%)	16.8%	4.3 %	17.8 %	14.7 %	24.6 %
% of data with AE ≤ 10%	29.4 %	88.2 %	17.6 %	25.0 %	13.3 %

Although the empirical relationship, Equation (52), was already been validated in Section 3.4.2 using fall velocity measurements obtained with the photographic technique, the verification was repeated in this section in order to account for the different experimental conditions considered in the present analysis. In particular, the current dataset includes a wider range of fall heights and an additional drip-type simulator (DG), thus extending the applicability of the equation beyond the conditions originally investigated.

Figure 70 reports the comparison between V_S and $V_{S,calc}$. The results show a very good agreement between measured and calculated velocities, with the experimental points closely distributed around the 1:1 line. The error metrics summarized in Table 21 indicate a slight overestimation by the empirical equation (MRE = 1.5%), while 88.2% of the data fall within the ±10% error range. These outcomes confirm the reliability of Equation (52) for estimating the fall velocity of single raindrops generated by drip-type simulators under subterminal conditions.

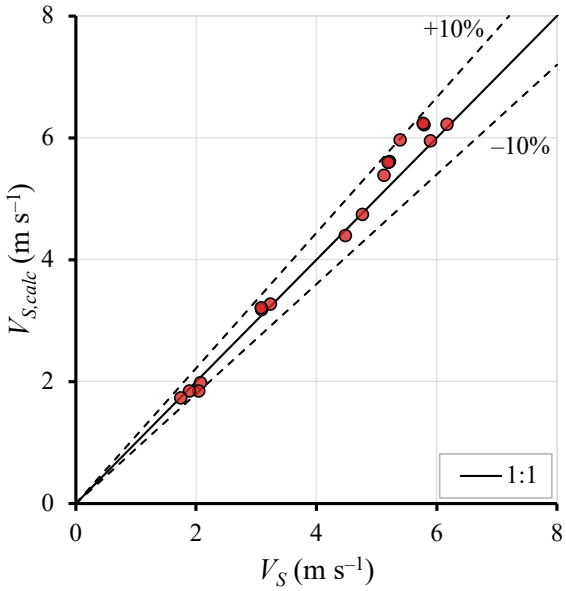

Figure 70. Comparison between the fall velocity of individual raindrops measured using the photographic technique, V_S (m s^{-1}), and that estimated using Equation (52), $V_{S,calc}$ (m s^{-1}). The solid line denotes the 1:1 line, while the dashed lines indicate the ±10% error bounds.

Given the demonstrated accuracy of Equation (52), a further comparison was conducted between the velocities measured by the Parsivel^2 and those calculated from the empirical relationship. The results are presented in Figure 71, which plots $V_{S,calc}$ against $V_{S,OTT}$. The figure again reveals a clear and systematic underestimation of fall velocity by the disdrometer, with error statistics very similar to those obtained in Figure 69.

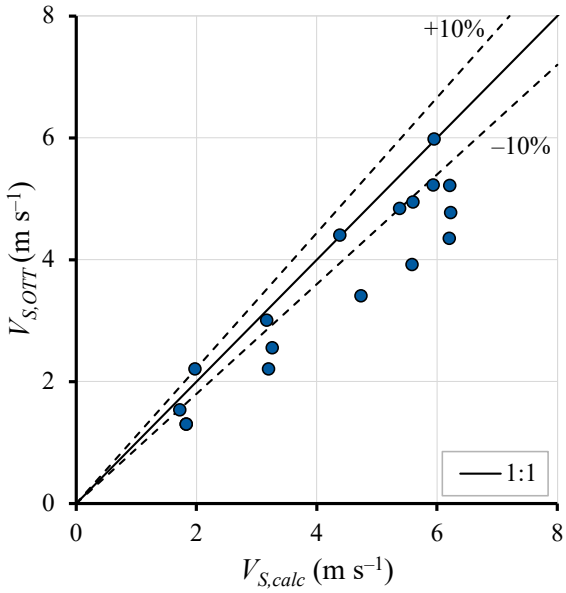

Figure 71. Comparison between the fall velocity of individual raindrops estimated using Equation (46), $V_{S,calc}$ (m s^{-1}), and that measured by the Parsivel^2 disdrometer, $V_{S,OTT}$ (m s^{-1}). The solid line denotes the 1:1 line, while the dashed lines indicate the ±10% error bounds.

Overall, these analyses indicate that, for drip-type rainfall simulators, the DSDs measured by the Parsivel^2 can be reliably used for estimating raindrop diameter, drop count, and rainfall intensity, while the fall velocity should preferably be derived from Equation (52) rather than from the direct measurements provided by the disdrometer.

For the pressurized rainfall simulator, the analysis was carried out at two operating pressures, 0.26 bar and 0.51 bar, corresponding to rainfall intensities of 50.5 mm h^{-1} and 41.3 mm h^{-1}, respectively. Figure 72 shows the DSDs measured by the Parsivel^2 for the two considered pressure levels. The comparison shows that increasing the operating pressure shifts the DSD toward smaller diameters. In particular, at both pressures, the instrument recorded drop diameters starting at approximately 0.03 cm, while 90% of the detected drops were concentrated within diameter classes up to 0.094 cm at 0.25 bar and 0.081 cm at 0.51 bar. This performance is consistent with the physical behavior of pressurized nozzles, where higher pressures promote greater water-jet atomization, producing more droplets of smaller size.

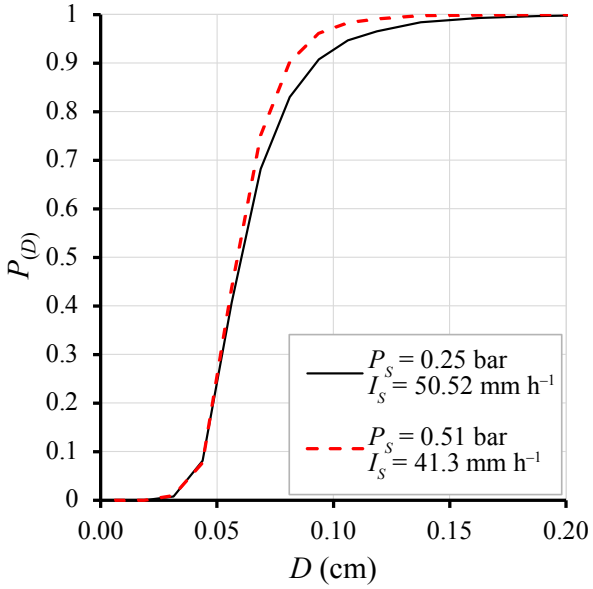

Figure 72. Drop Size Distributions measured by the Parsivel² disdrometer for the pressurized rainfall simulator of Palermo operating at two different pressure levels, P_S (bar): 0.25 bar, corresponding to a simulated rainfall intensity, I_S (mm h^{-1}), of 50.5 mm h^{-1}, and 0.51 bar, corresponding to an I_S of 41.3 mm h^{-1}.

The fall velocity analysis for the pressurized simulator is reported in Figure 73, which compares the velocities measured by the Parsivel², $V_{S,OTT}$, with those calculated using Equation (52), $V_{S,calc}$, for both pressure levels.

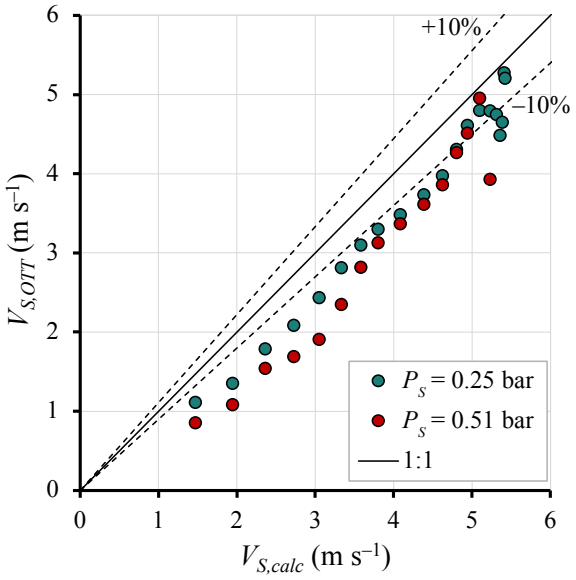

Figure 73. Comparison between raindrop fall velocities calculated using Equation (52), $V_{S,calc}$ (m s^{-1}), and those measured by the Parsivel² disdrometer, $V_{S,OTT}$ (m s^{-1}), for the pressurized rainfall simulator of Palermo operating at two different pressure levels (0.25 bar and 0.51 bar). The solid line represents the line of perfect agreement (1:1), while the dashed lines indicate the ±10% error bounds.

The figure clearly shows that, as observed with the drip-type simulators, the Parsivel^2 systematically underestimates raindrop fall velocities relative to those estimated using Equation (52). The magnitude of this underestimation increases with increasing pressure: the Mean Relative Error is equal to –14.7% for 0.26 bar and reaches –24.6% for 0.51 bar, while the percentage of measurements within the ±10% error range decreases from 25.0% to 13.3%, as summarized in Table 21.

These results demonstrate that the limitations of the Parsivel^2 disdrometer in measuring fall velocity are not limited to isolated drops produced by drip-type systems but become even more pronounced under the dense, dynamic conditions generated by pressurized simulators. The greater underestimation observed at higher pressures can reasonably be attributed to the increasing concentration of small, fast-moving droplets, which enhances the likelihood of double detections, overlapping particles within the laser beam, and misclassification by the internal processing algorithm. Similar issues have been reported in previous studies conducted under natural rainfall conditions, where high rainfall intensities were shown to amplify biases in optical disdrometer measurements (Angulo-Martínez et al., 2018; Saha and Testik, 2023).

Moreover, for pressurized simulators, additional sources of uncertainty may arise from the complex trajectories droplets follow leaving the nozzle. Unlike drip-type systems, where drops fall almost vertically with negligible initial velocity, droplets generated by nozzles may exhibit non-negligible horizontal and vertical velocity components at the moment of formation. Although Equation (52) was originally developed for raindrops falling with null initial velocity, its applicability to the pressurized rainfall simulator can be inferred from the experimental evidence. The comparisons shown in Figure 73 reveal a systematic underestimation of fall velocity by the Parsivel^2 disdrometer, with a magnitude comparable to that observed for the drip-type simulators, particularly at a pressure of 0.26 bar.

These findings allow the definition of a clear methodological framework for the characterization of simulated rainfall under subterminal conditions. The Parsivel^2 disdrometer can be effectively employed for the measurement of Drop Size Distributions and for the computation of rainfall intensity from raw data, while the estimation of raindrop fall velocity should preferably be performed using

Equation (52), which proved to be more reliable than the direct velocity outputs provided by the instrument. The applicability of this approach has been demonstrated for both drip-type simulators and for the pressurized simulator installed in Palermo.

3.4.6 Validation of the Empirical Fall Velocity Relationship Under Terminal Fall Conditions

The analyses presented in Sections 3.4.2 and 3.4.5 demonstrated that Equation (52) can be reliably used to estimate raindrop fall velocity under subterminal laboratory conditions, for both drip-type and pressurized rainfall simulators. A further step is to verify whether the same relationship remains valid when applied to experimental configurations characterized by much higher fall heights, in which drops are expected to reach terminal velocity.

This opportunity is provided by the León rainfall simulator, which operates with a drop height of 10 m. Under these conditions, the influence of the initial velocity imparted by the emitters can be considered negligible, and raindrops are assumed to approach terminal fall velocity before reaching the ground.

Figure 74 presents the comparison between the fall velocities estimated using Equation (52), $V_{S,calc}$, and those measured by the Parsivel^2 disdrometer, $V_{S,OTT}$, including all available experimental datasets: drip-type rainfall simulators (DRS), the Palermo pressurized rainfall simulator (PRS), and the León PRS.

The analysis reveals that the experimental points obtained from the León simulator substantially overlap with those previously observed for both the drip-type simulators and the Palermo pressurized simulator. This result indicates that, despite different operating principles and experimental setups, the Parsivel^2's velocity underestimation remains consistent across all devices. However, as fall velocities increase, the experimental points tend to approach the 1:1 line more closely.

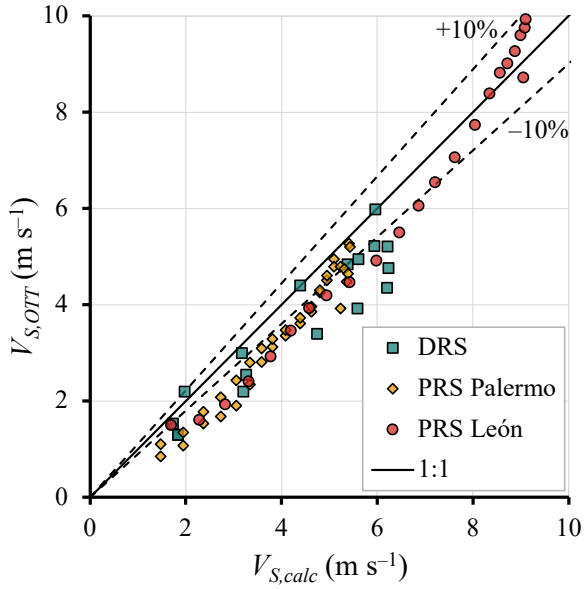

Figure 74. Comparison between raindrop fall velocities estimated using Equation (57), $V_{S,calc}$ (m s^{-1}), and those measured by the Parsivel² disdrometer, $V_{S,OTT}$ (m s^{-1}), for all investigated experimental configurations: drip-type simulators (DRS), Palermo pressurized simulator (PRS), and León pressurized simulator. The solid line represents the line of perfect agreement (1:1), while the dashed lines indicate the ±10% error bounds.

These results demonstrate once again the reliability of Equation (52) under a variety of experimental conditions: DRS, PRS, subterminal velocity, and terminal velocity. Accordingly, since the León PRS operates under conditions in which raindrops are expected to reach terminal velocity, an additional validation step can be performed. In this specific configuration, the fall velocities measured with the Parsivel^2 disdrometer can be compared both with those estimated using Equation(52), developed for simulated rainfall conditions as it explicitly accounts for both drop diameter and velocity, and with those obtained from empirical relationships traditionally adopted for natural rainfall under terminal conditions, namely those proposed by Ferro (2001), Equation (21), and (Atlas et al., 1973), Equation (58), in which fall velocity depends solely on drop diameter.

Figure 75 presents this comparison, in which velocities calculated using the three formulations, $V_{(D)}$, are plotted against velocities measured by the Parsivel^2 disdrometer for the León simulator, $V_{S,OTT}$.

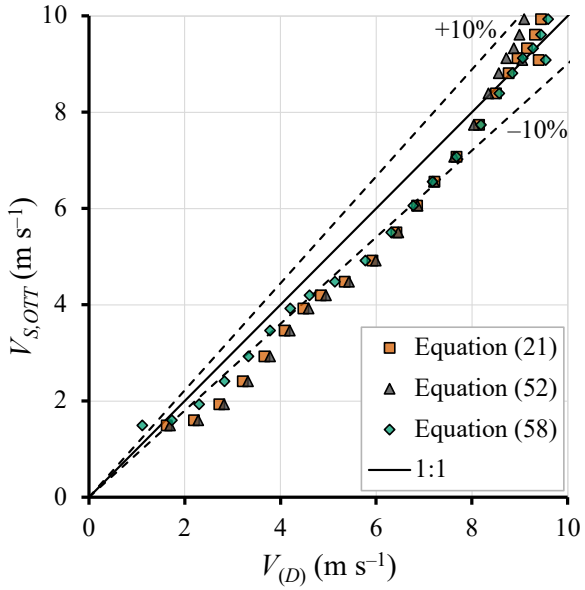

Figure 75. Comparison between raindrop fall velocities measured by the Parsivel² disdrometer, $V_{S,OTT}$ (m s^{-1}), and those estimated, $V_{(D)}$ (m s^{-1}), using three different predictive relationships, Equation (21) (Ferro, 2001), Equation (52) proposed in this investigation, and Equation (58) (Atlas et al., 1973). The solid line represents the line of perfect agreement (1:1), while the dashed lines indicate the ±10% error bounds.

The close agreement observed between the velocity estimates obtained from Equation (52) and those derived from both Atlas et al. (1973) and Ferro (2001) relationships corroborates the objectives for which Equation (52) was conceived, namely, to provide a versatile and reliable tool for estimating raindrop fall velocity over a wide range of experimental configurations. Indeed, under terminal conditions, it produces estimates fully consistent with those obtained from well-established relationships in the literature, while under subterminal conditions, its explicit dependence on both drop diameter and fall height allows for a straightforward application to any laboratory setup. Such flexibility makes Equation (52) particularly suitable for the energetic characterization of simulated rainfall, where fall heights and experimental configurations may vary considerably.

4 CONCLUSIONS

4.1 Natural Rainfall

4.1.1 Rainfall Erosivity and Soil Loss Measurement at the Sparacia Experimental Site

When the classical USLE approach is applied at the event scale, the rainfall erosivity index R_e has limited capability to explain the variability of measured event soil loss at the Sparacia experimental site, even when rainfall kinetic energy is derived from disdrometric observations rather than empirical intensity–energy relationships. This indicates that the main limitation of the USLE formulation at the site is not solely related to rainfall energy estimation, but also to the use of a single event-scale intensity descriptor, such as I_{30}, to represent erosive forcing under complex rainfall events.

The proposed R_e^* index, which aggregates rainfall kinetic power and intensity at the measurement temporal resolution, showed markedly improved correlation with event soil loss for both investigated slope gradients. This result demonstrates that explicitly accounting for intra-event variability provides a more consistent representation of rainfall erosivity at the event scale. A residual scatter persists for very high soil loss events, likely associated with increased uncertainty in plot measurements during long sequences of erosive rainfall and with additional controlling factors beyond rainfall erosivity alone.

These findings contribute to the achievement of Objective 1 of the thesis (Section 1.4) and encourage further investigation of this research area by extending the current database of concurrent measurements of soil loss and disdrometric rainfall characteristics to further validate the applicability of the proposed R_e^* index.

4.1.2 Analysis of Natural Rainfall Properties Using the Weibull Distribution

An extensive dataset of DSDs measured at the Palermo and El Teularet sites confirmed that the Weibull distribution provides a reliable representation of natural rainfall DSD across a wide range of intensities, I. The accurate reproduction of both median diameter, D_{50}, and median volume diameter, D_0, demonstrates that key descriptors controlling rainfall kinetic power are consistently captured.

Based on the validated Weibull framework, analytical relationships were derived to express rainfall kinetic power, P_n, and momentum, M, as explicit functions of the Weibull scale and shape parameters. These relationships show that P_n/I and M/I depend primarily on intrinsic precipitation properties rather than on rainfall intensity alone, confirming that bulk intensity cannot fully describe the erosive potential of rainfall.

Comparison with values computed directly from measured DSDs demonstrated good predictive capability for kinetic power and even higher accuracy and robustness for rainfall momentum at both experimental sites. Sensitivity analyses further indicated that momentum is intrinsically less affected by uncertainties in Weibull parameters than kinetic power. Although the Weibull and Gamma distributions provided comparable accuracy in reproducing DSDs and energetic variables, the Weibull formulation is preferable because its parameters have clear physical interpretations related to drop-size variability and precipitation energy content.

Overall, the results support the use of Weibull-based descriptors for rainfall erosivity characterization in Mediterranean environments and suggest that rainfall momentum may represent a more stable indicator of erosive forcing than kinetic power. These findings contribute to the achievement of Objective 2 of the thesis (Section 1.4) and encourage further validation of the proposed framework across a wider range of climatic conditions.

4.1.3 Advances in the Patented Method for Measuring Rainfall Energetic Characteristics Using the Weibull Distribution

Building on the analytical framework associated with the Weibull distribution, this study also advanced a patented measurement method that enables the estimation of rainfall energetic characteristics from three directly measurable quantities: rainfall intensity, drop concentration, and the mean diameter derived from the raindrop momentum distribution, $m'_{(D)}$. The proposed formulation allows the Weibull parameters to be retrieved from simplified measurements and subsequently used to estimate P_n and M. Consistent with previous analyses, rainfall momentum estimates

showed higher accuracy and lower sensitivity to measurement uncertainty than kinetic power across rainfall-intensity ranges, particularly for erosive events.

The findings indicate that the combined knowledge of these three variables is sufficient to reconstruct rainfall energetic properties independently of the specific statistical distribution adopted to describe the DSD. This supports the feasibility of the patented device concept, which aims to directly measure rainfall energy characteristics without requiring full disdrometric measurements.

If the underlying assumption that the mean diameter derived from the electrical signal distribution, generated by piezoelectric sensing of individual raindrop impacts, coincides with that obtained from the momentum distribution is experimentally confirmed, the instrument will be capable of reproducing disdrometer information while directly providing rainfall energetic variables at larger spatial scales. Such capability could substantially improve rainfall erosivity monitoring and soil erosion modeling. These findings contribute to the achievement of Objective 3 of the thesis (Section 1.4) and support further efforts aimed at completing prototype development and validating the method across several rainfall regimes.

4.2 Simulated Rainfall

4.2.1 Rainfall Simulator Characterization

As widely recognized, drip-type (DRS) and pressurized (PRS) rainfall simulators require different approaches to achieve a complete and reliable characterization of their properties. Drip-type simulators generate individual raindrops with nearly uniform volumetric and energetic characteristics determined solely by the imposed operating conditions (fall height, capillary geometry, hydraulic head, and water temperature).

Therefore, the rainfall produced by DRSs can be described through simplified formulations based on a limited set of measurable variables. For instance, for the KS and MKS simulators, empirical relationships were established to estimate rainfall kinetic power and momentum as functions only of rainfall intensity and fall height, demonstrating that their energetic behavior can be consistently reproduced without direct measurements of drop velocity or full DSD characterization.

In contrast, PRSs generate complex spray jets characterized by intrinsic spatial variability controlled primarily by nozzle geometry (spray angle and discharge type) and operating pressure. Under these conditions, volumetric characterization using rain collectors alone is insufficient to describe simulated rainfall properties. The integration of volumetric calibration with spatially distributed disdrometric measurements enables a comprehensive characterization of pressurized simulators, allowing the spatial variability of rainfall intensity, kinetic power, momentum, and DSD statistical descriptors to be quantified and related to simulator configuration.

Together, the simplified energetic characterization developed for drip-type simulators and the integrated volumetric–disdrometric approach adopted for pressurized simulators provide a comprehensive framework for describing the main properties of simulated rainfall, including its spatial variability, kinetic power, momentum, and DSD statistical descriptors. These results contribute to the achievement of Objective 4 of the thesis (Section 1.4).

4.2.2 Raindrop Fall Velocity under Simulated Rainfall Conditions

Fall-velocity measurements obtained for DRSs using the photographic technique enabled the validation of an empirical relationship proposed in this work, Equation (52), which expresses raindrop fall velocity as a function of fall height and drop diameter.

The proposed formulation proved highly reliable against the calibration database (Laws, 1941), independent literature data (Epema and Riezebos, 1983), and the experimental datasets obtained with KS, MKS, and DG simulators.

Additional analyses performed under pressurized rainfall simulators further demonstrated the robustness of the proposed formulation. In particular, the comparison between velocities derived from disdrometric measurements and those predicted by Equation (52) showed that the relationship remains applicable under experimental conditions different from those for which it was originally calibrated. The formulation proved suitable not only for the sub-terminal fall-velocity regimes typical of drip-type simulators but also under terminal fall-velocity conditions generated by the pressurized rainfall simulator operating at the León experimental facility.

Overall, the velocity measurements obtained through photographic techniques for drip-type simulators and disdrometric measurements under pressurized simulators provided consistent evidence supporting the validity of the proposed formulation across a wide range of experimental configurations. These results contribute to the achievement of Objective 5 of the thesis (Section 1.4).

4.2.3 Evaluation of the Parsivel^2 Disdrometer under Laboratory Conditions

The performance of the Parsivel^2 optical disdrometer was evaluated under controlled laboratory conditions to assess its reliability for characterizing simulated rainfall. Indeed, laboratory environments differ significantly from natural rainfall conditions for which the instrument was originally designed, particularly because simulated rainfall often occurs under subterminal fall-velocity regimes.

The analyses confirmed the systematic underestimation of raindrop fall velocity reported in the literature for natural rainfall measurements. This behavior was

observed under both drip-type and pressurized rainfall simulators, indicating that the instrument's limitations extend beyond natural rainfall conditions.

Moreover, under subterminal fall-velocity conditions, the instrument's synthetic parameters may introduce additional uncertainties. This behavior is mainly due to the instrument's internal processing algorithms, which are calibrated for natural rainfall regimes, potentially leading to biased estimates when applied to laboratory rainfalls under subterminal-velocity conditions. Therefore, rainfall descriptors such as rainfall intensity, kinetic power, and momentum should preferably be derived directly from the raw DSD measurements.

The results also indicate that the Parsivel^2 provides reliable information on key microphysical properties of simulated rainfall, particularly drop counts and drop diameter.

The comparable underestimation of fall velocity observed across DRS and PRS devices further supports the use of the proposed fall-velocity formulation, Equation (52), as a consistent reference for estimating drop velocity and related energetic variables under simulated rainfall conditions. In other words, fall velocity calculated by Equation (52) can be applied to measured DSDs while disregarding the velocity distribution provided by the Parsivel^2. This approach is consistent with procedures commonly adopted in the literature for natural rainfall.

Overall, these analyses contribute to the achievement of Objective 6 of the thesis (Section 1.4) by providing a comprehensive assessment of Parsivel^2 performance for the characterization of simulated rainfall generated by both drip-type and pressurized rainfall simulators.

Further investigations would be useful to improve the understanding of Parsivel^2 behavior under laboratory rainfall conditions. Additional experimental campaigns could compare disdrometric measurements obtained under pressurized rainfall simulators with independent velocity measurements derived from advanced photographic techniques, which are difficult to obtain due to the complex operating environment of PRSs. Additional comparisons with alternative optical disdrometers could also help clarify the extent to which the observed biases are instrument-specific or intrinsic to disdrometric measurements under simulated rainfall conditions.

4.3 Future perspectives

The advancement of the patented measurement method logically leads to the development and experimental validation of a prototype device for direct measurement of rainfall energy. Once available, the prototype should first be tested and calibrated under controlled laboratory conditions, where rainfall properties can be reproduced with high repeatability and low variability. In this context, DRSs represent an ideal reference environment, as they generate rainfall with known drop size, fall velocity, and energetic characteristics. Such conditions enable initial verification of the instrument response and the consistency of the estimated energetic parameters with independent reference measurements.

Subsequently, the prototype should be evaluated under pressurized simulated rainfall, characterized by higher drop arrival frequency and greater variability. These tests will allow verification of the instrument's capability to reproduce rainfall energetic parameters and DSD-related descriptors under more complex rainfall conditions. In this phase, comparisons with reliable disdrometric measurements will be essential to assess the accuracy of the energetic parameters estimated by the prototype and to verify the consistency of the proposed measurement principle under different simulated rainfall configurations.

Finally, once the instrument performance has been validated under laboratory conditions, field experiments under natural rainfall events will represent a crucial step for assessing its applicability in real atmospheric conditions. Such testing will enable assessment of instrument performance under stochastic variability and external disturbances, such as wind or variable impact dynamics of big and small drops, which may affect piezoelectric sensing systems. Progressive refinement of hardware and automated acquisition software will be required to ensure reliable long-term operation and data quality in open-field conditions.

Overall, this staged validation pathway provides a physically consistent framework for scaling the patented measurement concept toward operational rainfall erosivity monitoring and soil erosion research applications.

ACKNOWLEDGMENTS

The author gratefully acknowledges that the laboratory rainfall experiments conducted at the University of León were carried out during his six-month research stay under the supervision of Prof. María Fernández-Raga. He also thanks Dr. Carlos del Blanco Alegre for his collaboration on ongoing comparative analyses of disdrometer measurements of natural rainfall, closely related to this research but still in progress at the time of writing.

The author further acknowledges his participation in the Erasmus+ Program (zero-grant modality) of the University of Palermo (D.R. No. 848/2025). He also thanks Dr. Maria Angela Serio for collecting the DSD data at the El Teularet experimental station during her research stay at the University of Valencia under the supervision of Prof. Artemi Cerdà.

A PERSONAL NOTE

A PhD is a long and winding journey, marked by highs and lows, achievements and discouragements. Beyond representing the highest level of academic education, it is an experience that allows one to grow both professionally and personally, in ways that few other paths can offer.
I believe I have changed greatly over the past three years. It is certainly the result of hard work, determination, and ambition. Qualities I began to develop throughout this journey and that I hope will continue to guide me in my future.

And like every voyager embarking on a long trip, it is only right to thank all those who shared this path with me toward my destination. Each of you has played an important role in my academic and personal growth.
I would therefore like to express my deepest gratitude to Professors Ferro, Di Stefano, Carollo, and Pampalone, as well as Doctors Serio, Palmeri, Nicosia, and Guida. In different ways, you have all been fundamental points of reference for me. You have given me invaluable advice since the very first day, and I hope I will be able to make the best possible use of everything you have taught me. I would also like to thank Antonino, with whom I shared part of this PhD experience, and Stefania, who, for six months, was my *pain in the neck*, but who at the same time gave me many laughs and provided invaluable help during experimental activities.

Long voyages also require stops along the way. Moments to rest, experience new things, meet new people, and engage with different ways of working. In my case, I had the fortune of spending six incredible months in León. I would therefore like to thank María for her warm welcome and constant support, together with Gabriél, Carlos, and Ángel.
I am also grateful to all the people who stood by me during the moments of leisure and lightheartedness that made my time in León so special: Oliver, Milena, David, Adrián, Laura, Ana, María, Paula, and Selva.

Having had the fortune of working within such a stimulating research group and the opportunity to live such positive experiences abroad has been of enormous value. Yet none of this would have meant the same without the support of my wonderful

family, of whom I am immensely proud for the values they have passed on to me, and my lifelong friends, Nino and Totò. I am truly fortunate to have you in my life.

Finally, thank you to the most important person in my life, Cristina, who for more than ten years has stood by my side through every moment, sharing with me joys, sacrifices, fears, and achievements. Thank you for being there even during the most difficult times, and for the patience, support, and love you have never failed to give me. I hope we will soon be able to fulfill all the dreams we share.

REFERENCES

Abudi, I., Carmi, G., Berliner, P., 2012. Rainfall simulator for field runoff studies. J. Hydrol. (Amst). 454–455. https://doi.org/10.1016/j.jhydrol.2012.05.056

Adams, J.E., Kirkham, D., Nielsen, D.R., 1957. A Portable Rainfall-Simulator Infiltrometer and Physical Measurements of Soil in Place. Soil Science Society of America Journal 21. https://doi.org/10.2136/sssaj1957.03615995002100050004x

Adirosi, E., Porcù, F., Montopoli, M., Baldini, L., Bracci, A., Capozzi, V., Annella, C., Budillon, G., Bucchignani, E., Zollo, A.L., Cazzuli, O., Camisani, G., Bechini, R., Cremonini, R., Antonini, A., Ortolani, A., Melani, S., Valisa, P., Scapin, S., 2023. Database of the Italian disdrometer network. Earth Syst. Sci. Data 15, 2417–2429. https://doi.org/10.5194/essd-15-2417-2023

Agosta, M., Bagarello, V., Caltabellotta, G., Carollo, F.G., Vaccaro, G., Pampalone, V., 2022. Theoretical prediction of rainfall intensity for a small rainfall simulator, in: 2022 IEEE Workshop on Metrology for Agriculture and Forestry, MetroAgriFor 2022 - Proceedings. https://doi.org/10.1109/MetroAgriFor55389.2022.9965068

Aksoy, H., Unal, N.E., Cokgor, S., Gedikli, A., Yoon, J., Koca, K., Inci, S.B., Eris, E., 2012. A rainfall simulator for laboratory-scale assessment of rainfall-runoff-sediment transport processes over a two-dimensional flume. Catena (Amst). 98, 63–72. https://doi.org/10.1016/j.catena.2012.06.009

Alewell, C., Borrelli, P., Meusburger, K., Panagos, P., 2019. Using the USLE: Chances, challenges and limitations of soil erosion modelling. International Soil and Water Conservation Research 7, 203–225. https://doi.org/10.1016/j.iswcr.2019.05.004

Alonge, A., Afullo, T.J.O., 2012. Seasonal Analysis and Prediction of Rainfall Effects in Eastern South Africa at Microwave Frequencies. Progress In Electromagnetics Research B 40, 279–303. https://doi.org/10.2528/PIERB12020305

Alves Sobrinho, T., Gómez-Macpherson, H., Gómez, J.A., 2008. A portable integrated rainfall and overland flow simulator. Soil Use Manag. 24. https://doi.org/10.1111/j.1475-2743.2008.00150.x

Amerman, C.R., 1979. Rainfall Simulation as a Research Tool in Infiltration, in: Proceedings of Rainfall Simulator Workshop. United States Department of Agriculture, Science and Education Administration, Agricultural Reviews and Manuals, Western Series, no. 10, Oakland (California), July 1979, Tucson, Arizona, pp. 85–89.

Angulo-Martínez, M., Barros, A.P., 2015. Measurement uncertainty in rainfall kinetic energy and intensity relationships for soil erosion studies: An evaluation using PARSIVEL disdrometers in the Southern Appalachian Mountains. Geomorphology 228, 28–40. https://doi.org/10.1016/j.geomorph.2014.07.036

Angulo-Martínez, M., Beguería, S., Kyselý, J., 2016. Use of disdrometer data to evaluate the relationship of rainfall kinetic energy and intensity (KE-I). Science of The Total Environment 568, 83–94. https://doi.org/10.1016/j.scitotenv.2016.05.223

Angulo-Martínez, M., Beguería, S., Latorre, B., Fernández-Raga, M., 2018. Comparison of precipitation measurements by OTT Parsivel^2 and Thies LPM optical disdrometers. Hydrol. Earth Syst. Sci. 22, 2811–2837. https://doi.org/10.5194/hess-22-2811-2018

Arnaez, J., Lasanta, T., Ruiz-Flaño, P., Ortigosa, L., 2007. Factors affecting runoff and erosion under simulated rainfall in Mediterranean vineyards. Soil Tillage Res. 93, 324–334. https://doi.org/10.1016/j.still.2006.05.013

Arnold, J.G., Srinivasan, R., Muttiah, R.S., Williams, J.R., 1998. Large Area Hydrologic Modeling and Assessment Part I: Model Development. JAWRA Journal of the American Water Resources Association 34, 73–89. https://doi.org/10.1111/j.1752-1688.1998.tb05961.x

Arunrat, N., Sereenonchai, S., Kongsurakan, P., Hatano, R., 2022. Assessing Soil Organic Carbon, Soil Nutrients and Soil Erodibility under Terraced Paddy

Fields and Upland Rice in Northern Thailand. Agronomy 12, 537. https://doi.org/10.3390/agronomy12020537

ASABE Standard, 2014. Design and Installation of Microirrigation Systems.

ASTM D6459-19; Advancing Standards Transforming Markets (ASTM), 2019. Test Method for Determination of Rolled Erosion Control Product (RECP) Performance in Protecting Hillslopes from Rainfall-Induced Erosion. https://doi.org/10.1520/D6459-19

Atlas, D., Srivastava, R.C., Sekhon, R.S., 1973. Doppler radar characteristics of precipitation at vertical incidence. Reviews of Geophysics 11, 1–35. https://doi.org/10.1029/RG011i001p00001

Atlas, D., Ulbrich, C.W., 1977. Path- and Area-Integrated Rainfall Measurement by Microwave Attenuation in the 1–3 cm Band. Journal of Applied Meteorology 16, 1322–1331. https://doi.org/10.1175/1520-0450(1977)016<1322:PAAIRM>2.0.CO;2

Bagarello, V., Baiamonte, G., Ferro, V., Giordano, G., 1996. Contributo alla valutazione dei fattori elementari dell'erosione negli studi a scala di bacino (Evaluating Soil Erosion Factors for Watershed Studies), in: Quaderni Di Idronomia Montana – Sviluppi Recenti Delle Ricerche Sull'erosione e Sul Suo Controllo. Associazione Italiana di Idronomia, Bari, 17-18 Febbraio 1994, pp. 47–82.

Bagarello, V., Di Piazza, G. V., Ferro, V., Giordano, G., 2008. Predicting unit plot soil loss in Sicily, south Italy. Hydrol. Process. 22, 586–595. https://doi.org/10.1002/hyp.6621

Bagarello, V., Di Stefano, C., Ferro, V., Pampalone, V., 2018. Comparing theoretically supported rainfall-runoff erosivity factors at the Sparacia (South Italy) experimental site. Hydrol. Process. 32, 507–515. https://doi.org/10.1002/hyp.11432

Bagarello, V., Ferro, V., Giordano, G., 2010. Testing alternative erosivity indices to predict event soil loss from bare plots in Southern Italy. Hydrol. Process. 24, 789–797. https://doi.org/10.1002/hyp.7538

Bagarello, V., Ferro, V., Pampalone, V., 2020. A comprehensive analysis of Universal Soil Loss Equation-based models at the Sparacia experimental area. Hydrol. Process. 34, 1545–1557. https://doi.org/10.1002/hyp.13681

Bagarello, V., Ferro, V., Pampalone, V., 2013. A new expression of the slope length factor to apply USLE-MM at Sparacia experimental area (Southern Italy). Catena (Amst). 102, 21–26. https://doi.org/10.1016/j.catena.2011.06.008

Battany, M.C., Grismer, M.E., 2000. Development of a portable field rainfall simulator for use in hillside vineyard runoff and erosion studies. Hydrol. Process. 14. https://doi.org/10.1002/(sici)1099-1085(20000430)14:6<1119::aid-hyp8>3.0.co;2-o

Beard, K. V., 1976. Terminal Velocity and Shape of Cloud and Precipitation Drops Aloft. J. Atmos. Sci. 33, 851–864. https://doi.org/10.1175/1520-0469(1976)033<0851:TVASOC>2.0.CO;2

Benavidez, R., Jackson, B., Maxwell, D., Norton, K., 2018. A review of the (Revised) Universal Soil Loss Equation ((R)USLE): with a view to increasing its global applicability and improving soil loss estimates. Hydrol. Earth Syst. Sci. 22, 6059–6086. https://doi.org/10.5194/hess-22-6059-2018

Bharali, B., 2021. Rate of infiltration for different soil textures using rainfall simulator and Green–Ampt model. ISH Journal of Hydraulic Engineering 27, 70–76. https://doi.org/10.1080/09715010.2019.1576549

Birt, L.N., Persyn, R.A., Smith, P.K., 2007. Evaluation of an indoor nozzle-type rainfall simulator. Appl. Eng. Agric. 23.

Biswas, S., Kranz, W.L., Shapiro, C.A., Snow, D.D., Bartelt-Hunt, S.L., Mamo, M., Tarkalson, D.D., Zhang, T.C., Shelton, D.P., van Donk, S.J., Mader, T.L., 2017. Effect of rainfall timing and tillage on the transport of steroid hormones in

runoff from manure amended row crop fields. J. Hazard. Mater. 324, 436–447. https://doi.org/10.1016/j.jhazmat.2016.11.009

Blanchard, D.C., 1967. From raindrops to volcanoes: Adventures with sea surface meteorology. Anchor Books, Doubleday & Company, Inc., Garden City, New York.

Blanchard, D.C., 1953. Raindrop Size-Distribution in Hawaiian Rains. Journal of Meteorology 10, 457–473. https://doi.org/10.1175/1520-0469(1953)010<0457:RSDIHR>2.0.CO;2

Blanchard, D.C., 1952. Raindrop Size Distribution and Associated Phenomena in Hawaiian Rains. https://doi.org/10.21236/AD0009370

Blanquies, J., Hallock, B., Scharff, M., 2003. The design and construction of a rainfall simulator, in: International Erosion Control Association (IECA), 34th Annual Conference and Expo.

Boardman, J., Vandaele, K., 2023. Soil erosion and runoff: The need to rethink mitigation strategies for sustainable agricultural landscapes in western Europe. Soil Use Manag. 39, 673–685. https://doi.org/10.1111/sum.12898

Boardman, J., Vandaele, K., Evans, R., Foster, I.D.L., 2019. Off-site impacts of soil erosion and runoff: Why connectivity is more important than erosion rates. Soil Use Manag. 35, 245–256. https://doi.org/10.1111/sum.12496

Boix-Fayos, C., de Vente, J., 2023. Challenges and potential pathways towards sustainable agriculture within the European Green Deal. Agric. Syst. 207, 103634. https://doi.org/10.1016/j.agsy.2023.103634

Borrelli, P., Alewell, C., Alvarez, P., Anache, J.A.A., Baartman, J., Ballabio, C., Bezak, N., Biddoccu, M., Cerdà, A., Chalise, D., Chen, S., Chen, W., De Girolamo, A.M., Gessesse, G.D., Deumlich, D., Diodato, N., Efthimiou, N., Erpul, G., Fiener, P., Freppaz, M., Gentile, F., Gericke, A., Haregeweyn, N., Hu, B., Jeanneau, A., Kaffas, K., Kiani-Harchegani, M., Villuendas, I.L., Li, C., Lombardo, L., López-Vicente, M., Lucas-Borja, M.E., Märker, M., Matthews, F., Miao, C., Mikoš, M., Modugno, S., Möller, M., Naipal, V.,

Nearing, M., Owusu, S., Panday, D., Patault, E., Patriche, C.V., Poggio, L., Portes, R., Quijano, L., Rahdari, M.R., Renima, M., Ricci, G.F., Rodrigo-Comino, J., Saia, S., Samani, A.N., Schillaci, C., Syrris, V., Kim, H.S., Spinola, D.N., Oliveira, P.T., Teng, H., Thapa, R., Vantas, K., Vieira, D., Yang, J.E., Yin, S., Zema, D.A., Zhao, G., Panagos, P., 2021. Soil erosion modelling: A global review and statistical analysis. Science of The Total Environment 780, 146494. https://doi.org/10.1016/j.scitotenv.2021.146494

Bosio, R., Cagninei, A., Poggi, D., 2023. Large Laboratory Simulator of Natural Rainfall: From Drizzle to Storms. Water (Basel). 15, 2205. https://doi.org/10.3390/w15122205

Boulange, J., Malhat, F., Jaikaew, P., Nanko, K., Watanabe, H., 2019. Portable rainfall simulator for plot-scale investigation of rainfall-runoff, and transport of sediment and pollutants. International Journal of Sediment Research 34, 38–47. https://doi.org/10.1016/j.ijsrc.2018.08.003

Bowen, E.G., Davidson, K.A., 1951. A raindrop spectrograph. Quarterly Journal of the Royal Meteorological Society 77, 445–449. https://doi.org/10.1002/qj.49707733311

Bowyer-Bower, T.A.S., Burt, T.P., 1989. Rainfall simulators for investigating soil response to rainfall. Soil Technology 2, 1–16. https://doi.org/10.1016/S0933-3630(89)80002-9

Braimoh, A.K., Vlek, P.L.G., 2008. Impact of Land Use on Soil Resources, in: Braimoh, A.K., Vlek, P.L.G. (Eds.), Land Use and Soil Resources. Springer Netherlands, Dordrecht, pp. 1–7. https://doi.org/10.1007/978-1-4020-6778-5_1

Brawn, D., Upton, G., 2008. On the measurement of atmospheric gamma drop-size distributions. Atmospheric Science Letters 9, 245–247. https://doi.org/10.1002/asl.198

Breure, A.M., Lijzen, J.P.A., Maring, L., 2018. Soil and land management in a circular economy. Science of The Total Environment 624, 1125–1130. https://doi.org/10.1016/j.scitotenv.2017.12.137

Bringi, V.N., Chandrasekar, V., Hubbert, J., Gorgucci, E., Randeu, W.L., Schoenhuber, M., 2003. Raindrop Size Distribution in Different Climatic Regimes from Disdrometer and Dual-Polarized Radar Analysis. J. Atmos. Sci. 60, 354–365. https://doi.org/10.1175/1520-0469(2003)060<0354:RSDIDC>2.0.CO;2

Bringi, V.N., Huang, G.-J., Munchak, S.J., Kummerow, C.D., Marks, D.A., Wolff, D.B., 2012. Comparison of Drop Size Distribution Parameter (D0) and Rain Rate from S-Band Dual-Polarized Ground Radar, TRMM Precipitation Radar (PR), and Combined PR–TMI: Two Events from Kwajalein Atoll. J. Atmos. Ocean. Technol. 29, 1603–1616. https://doi.org/10.1175/JTECH-D-11-00153.1

Brown, L.C., Foster, G.R., 1987. storm Erosivity Using Idealized Intensity Distributions. Transactions of the ASAE 30, 379–386. https://doi.org/10.13031/2013.31957

Bryan, R.B., 2000. Soil erodibility and processes of water erosion on hillslope. Geomorphology 32, 385–415. https://doi.org/10.1016/S0169-555X(99)00105-1

Bubenzer, G.D., 1979. Rainfall Characteristics Important for Simulation, in: Proceedings of Rainfall Simulator Workshop. United States Department of Agriculture, Science and Education Administration, Agricultural Reviews and Manuals, Western Series, no. 10, Oakland (California), July 1979, Tucson, Arizona.

Búrdalo-Salcedo, G., Rodríguez, I., Fernández-Raga, M., Fernández-Raga, S., Rodríguez-Fernández, C., González-Domínguez, J.M., 2023. Adaptation of a Standard Method for Water Absorption Testing of Stone Materials: The Case of a Hydrophilic Protective Coating. Materials 16, 4228. https://doi.org/10.3390/ma16124228

Campbell Scientific, Inc., 2015. PWS100 Present Weather Sensor Instruction Manual. Logan, UT.

Campos, E.F., 1999. On measurements of drop size distribution. Topics in Meteorology and Oceanography 6, 24–30.

Caracciolo, C., Napoli, M., Porcù, F., Prodi, F., Dietrich, S., Zanchi, C., Orlandini, S., 2012. Raindrop Size Distribution and Soil Erosion. Journal of Irrigation and Drainage Engineering 138, 461–469. https://doi.org/10.1061/(ASCE)IR.1943-4774.0000412

Caracciolo, C., Prodi, F., Battaglia, A., Porcu', F., 2006. Analysis of the moments and parameters of a gamma DSD to infer precipitation properties: A convective stratiform discrimination algorithm. Atmos. Res. 80, 165–186. https://doi.org/10.1016/j.atmosres.2005.07.003

Carbone, R.E., Nelson, L.D., 1978. The Evolution of Raindrop Spectra in Warm-Based Convective Storms as Observed and Numerically Modeled. J. Atmos. Sci. 35, 2302–2314. https://doi.org/10.1175/1520-0469(1978)035<2302:TEORSI>2.0.CO;2

Carollo, F.G., Caruso, R., Di Stefano, C., Ferro, V., Pampalone, V., Serio, M.A., 2026. Measurement method of rainfall energetic characteristics using the Weibull drop size distribution. J. Hydrol. (Amst). 664, 134368. https://doi.org/10.1016/j.jhydrol.2025.134368

Carollo, F.G., Caruso, R., Ferro, V., Serio, M.A., 2024a. Characterizing the Kamphorst rainfall simulator for soil erosion investigations. J. Hydrol. (Amst). 643, 132025. https://doi.org/10.1016/j.jhydrol.2024.132025

Carollo, F.G., Caruso, R., Serio, M.A., Pampalone, V., 2024b. A Novel Approach for Measuring the Energetic Characteristics of Drip-Type Rainfall Simulators, in: 2024 IEEE International Workshop on Metrology for Agriculture and Forestry (MetroAgriFor). Institute of Electrical and Electronics Engineers (IEEE), Padua, Italy, pp. 528–532. https://doi.org/10.1109/MetroAgriFor63043.2024.10948871

Carollo, F.G., Di Stefano, C., Ferro, V., Pampalone, V., Sanzone, F., 2016a. Testing a new sampler for measuring plot soil loss. Earth Surf. Process. Landf. 41, 867–874. https://doi.org/10.1002/esp.3866

Carollo, F.G., Ferro, V., 2015. Modeling Rainfall Erosivity by Measured Drop-Size Distributions. J. Hydrol. Eng. 20. https://doi.org/10.1061/(ASCE)HE.1943-5584.0001077

Carollo, F.G., Ferro, V., Serio, M.A., 2018a. Predicting rainfall erosivity by momentum and kinetic energy in Mediterranean environment. J. Hydrol. (Amst). 560. https://doi.org/10.1016/j.jhydrol.2018.03.026

Carollo, F.G., Ferro, V., Serio, M.A., 2017. Reliability of rainfall kinetic power–intensity relationships. Hydrol. Process. 31. https://doi.org/10.1002/hyp.11099

Carollo, F.G., Ferro, V., Serio, M.A., 2016b. Estimating rainfall erosivity by aggregated drop size distributions. Hydrol. Process. 30, 2119–2128. https://doi.org/10.1002/hyp.10776

Carollo, F.G., Nicosia, A., Palmeri, V., Pampalone, V., Serio, M.A., Ferro, V., 2023. Measuring Rainfall Kinetic Power in Two Sicilian Experimental Areas by Drop-Size Distribution Data. Land (Basel). 12, 418. https://doi.org/10.3390/land12020418

Carollo, F.G., Serio, M.A., Caruso, R., 2025. Rainfall Energy Characteristics of a Modified Kamphorst Simulator, in: Sartori, L., Tarolli, P., Guerrini, L., Zuecco, G., Pezzuolo, A. (Eds.), Biosystems Engineering Promoting Resilience to Climate Change - AIIA 2024 - Mid-Term Conference. Springer, Cham, Padua, Italy, pp. 138–145. https://doi.org/10.1007/978-3-031-84212-2_18

Carollo, F.G., Serio, M.A., Ferro, V., Cerdà, A., 2018b. Characterizing rainfall erosivity by kinetic power - Median volume diameter relationship. Catena (Amst). 165, 12–21. https://doi.org/10.1016/j.catena.2018.01.024

Carollo, F.G., Serio, M.A., Pampalone, V., Ferro, V., 2024c. The unit plot of the Universal soil loss equation (USLE): Myth or reality? J. Hydrol. (Amst). 632, 130880. https://doi.org/10.1016/j.jhydrol.2024.130880

Carollo, F.G., Serio, M.A., Pampalone, V., Ferro, V., 2024d. Advances in a measurement method of rainfall kinetic power and momentum affecting soil erosion processes. Hydrol. Process. 38. https://doi.org/10.1002/hyp.15172

Caruso, R., Serio, M.A., Búrdalo-Salcedo, G., Carollo, F.G., Ortiz-Marqués, A., Ferro, V., Fernández-Raga, M., 2025. Integrated Approach to Assess Simulated Rainfall Uniformity and Energy-Related Parameters for Erosion Studies. Water (Basel). 17, 3429. https://doi.org/10.3390/w17233429

Caton, P.G.F., 1966. A study of raindrop-size distributions in the free atmosphere. Quarterly Journal of the Royal Meteorological Society 92, 15–30. https://doi.org/10.1002/qj.49709239103

Centeri, C., 2022. Soil Water Erosion. Water (Basel). 14, 447. https://doi.org/10.3390/w14030447

Cerdá, A., 1997. Rainfall drop size distribution in the Western Mediterranean basin, València, Spain. Catena (Amst). 30, 169–182. https://doi.org/10.1016/S0341-8162(97)00019-2

Cerdà, A., Ibáñez, S., Calvo, A., 1997. Design and operation of a small and portable rainfall simulator for rugged terrain. Soil Technology 11. https://doi.org/10.1016/S0933-3630(96)00135-3

Cevasco, A., Diodato, N., Revellino, P., Fiorillo, F., Grelle, G., Guadagno, F.M., 2015. Storminess and geo-hydrological events affecting small coastal basins in a terraced Mediterranean environment. Science of The Total Environment 532, 208–219. https://doi.org/10.1016/j.scitotenv.2015.06.017

Chandrasekar, V., Bringi, V.N., 1987. Simulation of Radar Reflectivity and Surface Measurements of Rainfall. J. Atmos. Ocean. Technol. 4, 464–478. https://doi.org/10.1175/1520-0426(1987)004<0464:SORRAS>2.0.CO;2

Chigier, N., 1983. Drop size and velocity instrumentation. Prog. Energy Combust. Sci. 9, 155–177. https://doi.org/10.1016/0360-1285(83)90008-4

Chouksey, A., Lambey, V., Nikam, B., Aggarwal, S., Dutta, S., 2017. Hydrological Modelling Using a Rainfall Simulator over an Experimental Hillslope Plot. Hydrology 4, 17. https://doi.org/10.3390/hydrology4010017

Christiansen, J.E., 1942. Irrigation by Sprinkling. University of California College of Agriculture Agricultural Experiment Station Berkeley, California BULLETIN 6.

Clarke, M.A., Walsh, R.P.D., 2007. A portable rainfall simulator for field assessment of splash and slopewash in remote locations. Earth Surf. Process. Landf. 32. https://doi.org/10.1002/esp.1526

Cottenot, L., Courtemanche, P., Nouhou-Bako, A., Darboux, F., 2021. A rainfall simulator using porous pipes as drop former. Catena (Amst). 200, 105101. https://doi.org/10.1016/j.catena.2020.105101

Covert, A., Jordan, P., 2009. A portable rainfall simulator: techniques for understanding the effects of rainfall on soil erodibility. Streamline 13.

De Marchi, G., 1950. Idraulica. Basi scientifiche e applicazioni tecniche. Hoepli, Milan.

De Ploey, J., 1981. Crusting and time-dependent rainwash mechanisms on loamy soil. Soil conservation: problems and prospects.

De Roo, A.P.J., Offermans, R.J.E., Cremers, N.H.D.T., 1996. LISEM: A Single-Event, Physically Based Hydrological and Soil Erosion Model For Drainage Basins. II: Sensitivity Analysis, Validation and Application. Hydrol. Process. 10, 1119–1126. https://doi.org/10.1002/(SICI)1099-1085(199608)10:8<1119::AID-HYP416>3.0.CO;2-V

Defant, A., 1905. Gesetzmässigkeiten in der Verteilung der Verschiedenen Tropfenggrössen bei Regenfällen, Wiener Sitzungsber. Mathematisch-Wissenschaftliche Klasse 114, 585–646.

Depietri, A., 2025. The Sustainable Use of Healthy Soil as a Cornerstone of the One Health Approach: An Analysis of European Public Strategies and Market-Based Environmental Protection Tools, in: Antonelli, G., Penna, F.,

Chaturvedi, E., Cilento, A. (Eds.), Planetary Health - Laws, Policies and Science on the “One Health” Approach. Springer Nature Switzerland, Cham, pp. 19–41. https://doi.org/10.1007/978-3-031-90621-3_2

Dhakal, A.S., Sidle, R.C., 2004. Distributed simulations of landslides for different rainfall conditions. Hydrol. Process. 18, 757–776. https://doi.org/10.1002/hyp.1365

Di Stefano, C., Nicosia, A., Pampalone, V., Ferro, V., 2023. Soil loss tolerance in the context of the European Green Deal. Heliyon 9, e12869. https://doi.org/10.1016/j.heliyon.2023.e12869

Dingle, A.N., Hardy, K.R., 1962. The description of rain by means of sequential raindrop-size distributions. Quarterly Journal of the Royal Meteorological Society 88, 301–314. https://doi.org/10.1002/qj.49708837709

Donnadieu, G., 1980. Comparison of Results Obtained with the VIDIAZ Spectropluviometer and the Joss-Waldvogel Rainfall Disdrometer in a “Rain of a Thundery Type.” J. Appl. Meteorol. Climatol. 19, 593–597. https://doi.org/10.1175/1520-0450(1980)019<0593:COROWT>2.0.CO;2

Eckley, C.S., Branfireun, B., 2009. Simulated rain events on an urban roadway to understand the dynamics of mercury mobilization in stormwater runoff. Water Res. 43, 3635–3646. https://doi.org/10.1016/j.watres.2009.05.022

Eigel, J.D., Moore, I.D., 1983. A Simplified Technique for Measuring Raindrop Size and Distribution. Transactions of the ASAE 26, 1079–1084. https://doi.org/10.13031/2013.34080

Eigenbrodt GmbH & Co., 2007. Meteorological Sensors: Optical Disdrometer ODM 470. Königsmoor, Germany.

Eijkelkamp, 2022. Rainfall simulator – Operating instructions. Giesbeek.

Epema, G.F., Riezebos, H.T., 1983. Fall velocity of waterdrops at different heights as a factor influencing erosivity of simulated rain. Catena Suppl. 4, 1–17.

Esteves, M., Planchon, O., Lapetite, J.M., Silvera, N., Cadet, P., 2000. The 'EMIRE' large rainfall simulator: design and field testing. Earth Surf. Process. Landf. 25, 681–690. https://doi.org/10.1002/1096-9837(200007)25:7<681::AID-ESP124>3.0.CO;2-8

Etheridge, J.A., 2023. Construction and Calibration of Large-Scale Rainfall Simulators. Auburn University, Auburn, Alabama.

European Environment Agency, 2024. The State of Soils in Europe – Fully evidenced, spatially organised assessment of the pressures driving soil degradation. Publications Office of the European Union, Luxembourg. https://doi.org/https://data.europa.eu/doi/10.2760/7007291

Farres, P.J., 1987. The dynamics of rainsplash erosion and the role of soil aggregate stability. Catena (Amst). 14. https://doi.org/10.1016/S0341-8162(87)80009-7

Fazlina, M.I.S., Azhar, A.T.S., Aziman, M., 2018. Design, Operation and Construction of a Large Rainfall Simulator for the Field Study on Acidic Barren Slope. Civil Engineering Journal 4, 1851–1857. https://doi.org/10.28991/cej-03091119

Feingold, G., Levin, Z., 1986. The Lognormal Fit to Raindrop Spectra from Frontal Convective Clouds in Israel. Journal of Climate and Applied Meteorology 25, 1346–1363.

Fernández-Raga, M., Cabeza-Ortega, M., González-Castro, V., Peters, P., Commelin, M., Campo, J., 2021. The Use of High-Speed Cameras as a Tool for the Characterization of Raindrops in Splash Laboratory Studies. Water (Basel). 13, 2851. https://doi.org/10.3390/w13202851

Fernández-Raga, M., Palencia, C., Keesstra, S., Jordán, A., Fraile, R., Angulo-Martínez, M., Cerdà, A., 2017. Splash erosion: A review with unanswered questions. Earth. Sci. Rev. 171, 463–477. https://doi.org/10.1016/j.earscirev.2017.06.009

Fernández-Raga, M., Palencia, C., Tomás, C., Calvo, A.I., Castro, A., Fraile, R., 2011. Rain research with disdrometers: a bibliometric review. Atmospheric

Measurement Techniques Discussions 4, 6041–6068. https://doi.org/10.5194/amtd-4-6041-2011

Fernández-Raga, M., Rodríguez, I., Caldevilla, P., Búrdalo, G., Ortiz, A., Martínez-García, R., 2022. Optimization of a Laboratory Rainfall Simulator to Be Representative of Natural Rainfall. Water (Basel). 14, 3831. https://doi.org/10.3390/w14233831

Ferro, V., 2001. Tecniche di misura e monitoraggio dei processi erosivi, in: Bagarello, V., Ferro, V., Giordano, G. (Eds.), Quaderni Di Idronomia Montana – Trasporto Di Acqua e Sedimenti a Scala Di Versante. Editoriale Bios, Cosenza, Italy, pp. 63–128.

Ferro, V., Porto, P., 2000. Sediment Delivery Distributed (SEDD) Model. J. Hydrol. Eng. 5, 411–422. https://doi.org/10.1061/(ASCE)1084-0699(2000)5:4(411)

Foster, G.R., 2005. Science documentation: Revised Universal Soil Loss Equation, Version 2 (RUSLE 2). Washington, D.C.

Foster, G.R., Yoder, D.C., Weesies, G.A., Toy, T.J., 2001. The Design Philosophy Behind RUSLE2: Evolution of an Empirical Model, in: Ascough II, J.C., Flanagan, D.C. (Eds.), Soil Erosion Research for the 21st Century: Proceedings of the International Symposium. American Society of Agricultural and Biological Engineers (ASABE), St. Joseph, MI, pp. 95–98. https://doi.org/10.13031/2013.3211

Fraile, R., Castro, A., Fernández-Raga, M., Palencia, C., Calvo, A.I., 2013. Error in the Sampling Area of an Optical Disdrometer: Consequences in Computing Rain Variables. The Scientific World Journal 2013. https://doi.org/10.1155/2013/369450

Fu, B., Wang, Y., Xu, P., Yan, K., 2012. Assessment of the performance of WEPP in purple soil area with simulated rainfall experiments. J. Mt. Sci. 9, 570–579. https://doi.org/10.1007/s11629-012-2194-z

Fu, Z., Dong, X., Zhou, L., Cui, W., Wang, J., Wan, R., Leng, L., Xi, B., 2020. Statistical Characteristics of Raindrop Size Distributions and Parameters in

Central China During the Meiyu Seasons. Journal of Geophysical Research: Atmospheres 125. https://doi.org/10.1029/2019JD031954

Fuchs, N., Petrjanoff, I., 1937. Microscopic Examination of Fog-, Cloud- and Rain-Droplets. Nature 139, 111–112. https://doi.org/10.1038/139111b0

García-Orenes, F., Cerdà, A., Mataix-Solera, J., Guerrero, C., Bodí, M.B., Arcenegui, V., Zornoza, R., Sempere, J.G., 2009. Effects of agricultural management on surface soil properties and soil–water losses in eastern Spain. Soil Tillage Res. 106, 117–123. https://doi.org/10.1016/j.still.2009.06.002

García-Ruiz, J.M., Beguería, S., Lana-Renault, N., Nadal-Romero, E., Cerdà, A., 2017. Ongoing and Emerging Questions in Water Erosion Studies. Land Degrad. Dev. 28, 5–21. https://doi.org/10.1002/ldr.2641

García-Ruiz, J.M., Beguería, S., Nadal-Romero, E., González-Hidalgo, J.C., Lana-Renault, N., Sanjuán, Y., 2015. A meta-analysis of soil erosion rates across the world. Geomorphology 239, 160–173. https://doi.org/10.1016/j.geomorph.2015.03.008

Garg, K., Nayar, S.K., 2007. Vision and Rain. Int. J. Comput. Vis. 75, 3–27. https://doi.org/10.1007/s11263-006-0028-6

Gatidis, C., Schleiss, M., Unal, C., Russchenberg, H., 2020. A Critical Evaluation of the Adequacy of the Gamma Model for Representing Raindrop Size Distributions. J. Atmos. Ocean. Technol. 37, 1765–1779. https://doi.org/10.1175/JTECH-D-19-0106.1

Gires, A., Bruley, P., Ruas, A., Schertzer, D., Tchiguirinskaia, I., 2020. Disdrometer measurements under Sense-City rainfall simulator. Earth Syst. Sci. Data 12, 835–845. https://doi.org/10.5194/essd-12-835-2020

Green, D., Pattison, I., 2022. Christiansen uniformity revisited: Re-thinking uniformity assessment in rainfall simulator studies. Catena (Amst). 217, 106424. https://doi.org/10.1016/j.catena.2022.106424

Grossklaus, M., Uhlig, K., Hasse, L., 1998. An Optical Disdrometer for Use in High Wind Speeds. J. Atmos. Ocean. Technol. 15, 1051–1059. https://doi.org/10.1175/1520-0426(1998)015<1051:AODFUI>2.0.CO;2

Gunn, R., Kinzer, G.D., 1949. The Terminal Velocity of Fall for Water Droplets in Stagnant Air. Journal of Meteorology 6. https://doi.org/10.1175/1520-0469(1949)006<0243:ttvoff>2.0.co;2

Gunn, R.E.S., Marshall, J.S., 1955. The Effect of Wind Shear on Falling Precipitation. J. Atmos. Sci. 12, 339–349. https://doi.org/10.1175/1520-0469(1955)012<0339:TEOWSO>2.0.CO;2

Hall, M.J., 1970. Use of the Stain Method in Determining the Drop-Size Distributions of Coarse Liquid Sprays. Transactions of the ASAE 13, 0033–0037. https://doi.org/10.13031/2013.38528

Hall, R.L., Calder, I.R., 1993. Drop size modification by forest canopies: Measurements using a disdrometer. Journal of Geophysical Research: Atmospheres 98, 18465–18470. https://doi.org/10.1029/93JD01498

Hamed, Y., Albergel, J., Pépin, Y., Asseline, J., Nasri, S., Zante, P., Berndtsson, R., El-Niazy, M., Balah, M., 2002. Comparison between rainfall simulator erosion and observed reservoir sedimentation in an erosion-sensitive semiarid catchment. Catena (Amst). 50, 1–16. https://doi.org/10.1016/S0341-8162(02)00089-9

Hou, Z., Liu, G., Shen, E., Qiang, H., Zhang, Q., Guo, Z., Abd Elbasit, M.A.M., Song, K., Zhao, X., 2026. Global rainfall simulator studies: review, challenge and perspective. J. Hydrol. (Amst). 669, 135075. https://doi.org/https://doi.org/10.1016/j.jhydrol.2026.135075

Hudson, N.W., 1965. The influence of rainfall on the mechanics of soil erosion: with particular reference to Southern Rhodesia. MSc. Thesis.

Humphry, J.B., Daniel, T.C., Edwards, D.R., Sharpley, A.N., 2002. A portable rainfall simulator for plot-scale runoff studies. Appl. Eng. Agric. 18. https://doi.org/10.13031/2013.7789

Imeson, A.C., 1977. A simple field-portable rainfall simulator for difficult terrain. Earth Surface Processes 2. https://doi.org/10.1002/esp.3290020414

Iserloh, T., Fister, W., Seeger, M., Willger, H., Ries, J.B., 2012. A small portable rainfall simulator for reproducible experiments on soil erosion. Soil Tillage Res. 124, 131–137. https://doi.org/10.1016/j.still.2012.05.016

Iserloh, T., Ries, J.B., Arnáez, J., Boix-Fayos, C., Butzen, V., Cerdà, A., Echeverría, M.T., Fernández-Gálvez, J., Fister, W., Geißler, C., Gómez, J.A., Gómez-Macpherson, H., Kuhn, N.J., Lázaro, R., León, F.J., Martínez-Mena, M., Martínez-Murillo, J.F., Marzen, M., Mingorance, M.D., Ortigosa, L., Peters, P., Regüés, D., Ruiz-Sinoga, J.D., Scholten, T., Seeger, M., Solé-Benet, A., Wengel, R., Wirtz, S., 2013a. European small portable rainfall simulators: A comparison of rainfall characteristics. Catena (Amst). 110, 100–112. https://doi.org/10.1016/j.catena.2013.05.013

Iserloh, T., Ries, J.B., Cerdà, A., Echeverría, M.T., Fister, W., Geißler, C., Kuhn, N.J., León, F.J., Peters, P., Schindewolf, M., Schmidt, J., Scholten, T., Seeger, M., 2013b. Comparative measurements with seven rainfall simulators on uniform bare fallow land. Zeitschrift für Geomorphologie, Supplementary Issues 57, 11–26. https://doi.org/10.1127/0372-8854/2012/S-00085

Isidoro, J.M.G.P., Green, D., Iserloh, T., de Lima, J.L.M.P., Pattison, I., Marzen, M., Silveira, A., Stirling, R., 2022. Towards harmonization in the use of rainfall simulators – On the pursuit of better and more comparable experimental results, in: 18th Biennial Conference of the Euromediterranean Network of Experimental and Representative Basins. Portoferraio, Italy.

Issaka, S., Ashraf, M.A., 2017. Impact of soil erosion and degradation on water quality: a review. Geology, Ecology, and Landscapes 1, 1–11. https://doi.org/10.1080/24749508.2017.1301053

Janapati, J., Seela, B.K., Lin, P.-L., Lan, C.-H., Tu, C.-C., Kumar, U., Huang, M.-Q., 2023. An assessment of rainfall kinetic energy functional relationships with GPM DPR. J. Hydrol. (Amst). 617, 128754. https://doi.org/10.1016/j.jhydrol.2022.128754

Jayawardena, A.W., Rezaur, R.B., 2000. Drop size distribution and kinetic energy load of rainstorms in Hong Kong. Hydrol. Process. 14, 1069–1082. https://doi.org/10.1002/(SICI)1099-1085(20000430)14:6<1069::AID-HYP997>3.0.CO;2-Q

Johannsen, L.L., Zambon, N., Strauss, P., Dostal, T., Neumann, M., Zumr, D., Cochrane, T.A., Blöschl, G., Klik, A., 2020a. Comparison of three types of laser optical disdrometers under natural rainfall conditions. Hydrological Sciences Journal 65, 524–535. https://doi.org/10.1080/02626667.2019.1709641

Johannsen, L.L., Zambon, N., Strauss, P., Dostal, T., Neumann, M., Zumr, D., Cochrane, T.A., Klik, A., 2020b. Impact of Disdrometer Types on Rainfall Erosivity Estimation. Water (Basel). 12, 963. https://doi.org/10.3390/w12040963

Joss, J., Waldvogel, A., 1967. A spectrograph for raindrops with automatic interpretation. Pure Appl. Geophys. 68, 240.

Kamphorst, A., 1987. A small rainfall simulator for the determination of soil erodibility. Netherlands Journal of Agricultural Science 35, 407–415. https://doi.org/10.18174/njas.v35i3.16735

Kathiravelu, G., Lucke, T., Nichols, P., 2016. Rain Drop Measurement Techniques: A Review. Water (Basel). 8, 29. https://doi.org/10.3390/w8010029

Kavian, A., Mohammadi, M., Cerda, A., Fallah, M., Abdollahi, Z., 2018. Simulated raindrop's characteristic measurements. A new approach of image processing tested under laboratory rainfall simulation. Catena (Amst). 167, 190–197. https://doi.org/10.1016/j.catena.2018.04.034

Keesstra, S., Geissen, V., Mosse, K., Piiranen, S., Scudiero, E., Leistra, M., van Schaik, L., 2012. Soil as a filter for groundwater quality. Curr. Opin. Environ. Sustain. 4, 507–516. https://doi.org/10.1016/j.cosust.2012.10.007

Keesstra, S.D., Chenu, C., Munkholm, L.J., Cornu, S., Kuikman, P.J., Thorsøe, M.H., Besse-Lototskaya, A., Visser, S.M., 2024. European agricultural soil

management: Towards climate-smart and sustainability, knowledge needs and research approaches. Eur. J. Soil Sci. 75, e13437. https://doi.org/10.1111/ejss.13437

Ketema, A., Dwarakish, G.S., 2021. Water erosion assessment methods: a review. ISH Journal of Hydraulic Engineering 27, 434–441. https://doi.org/10.1080/09715010.2019.1567398

Kimble, J.M., Follett, R.F., Stewart, B.A. (Eds.), 2000. Assessment Methods for Soil Carbon, 1st Edition. ed. CRC Press, Boca Raton. https://doi.org/10.1201/9781482278644

Kincaid, D.C., Solomon, K.H., Oliphant, J.C., 1996. Drop Size Distributions for Irrigation Sprinklers. Transactions of the ASAE 39, 839–845. https://doi.org/10.13031/2013.27568

Kinnell, P.I.A., 2025. Comparing WEPP with USLE based models: The role of bare fallow runoff and soil loss plots. Soil Tillage Res. 248, 106413. https://doi.org/10.1016/j.still.2024.106413

Kinnell, P.I.A., 1997. Runooff ratio as a factor in the empirical modelling of soil erosion by individual rainstorms. Australian Journal of Soil Research 35, 1–14. https://doi.org/10.1071/S95085

Kinnell, P.I.A., Risse, L.M., 1998. USLE-M: Empirical Modeling Rainfall Erosion through Runoff and Sediment Concentration. Soil Science Society of America Journal 62, 1667–1672. https://doi.org/10.2136/sssaj1998.03615995006200060026x

Koch, T., Chifflard, P., Aartsma, P., Panten, K., 2024. A review of the characteristics of rainfall simulators in soil erosion research studies. MethodsX 12, 102506. https://doi.org/10.1016/j.mex.2023.102506

Kohl, R.A., 1974. Drop Size Distribution from Medium-Sized Agricultural Sprinklers. Transactions of the ASAE 17, 690–693. https://doi.org/10.13031/2013.36938

Lal, R., 2003. Soil erosion and the global carbon budget. Environ. Int. 29, 437–450. https://doi.org/10.1016/S0160-4120(02)00192-7

Lal, R., 2001. Soil degradation by erosion. Land Degrad. Dev. 12, 519–539. https://doi.org/10.1002/ldr.472

Lal, R., Ahmadi, M., Bajracharya, R.M., 2000. Erosional impacts on soil properties and corn yield on Alfisols in central Ohio. Land Degrad. Dev. 11, 575–585. https://doi.org/10.1002/1099-145X(200011/12)11:6<575::AID-LDR410>3.0.CO;2-N

Lang, R.D., 1992. Accuracy of two sampling methods used to estimate sediment concentrations in runoff from soil-loss plots. Earth Surf. Process. Landf. 17, 841–844. https://doi.org/10.1002/esp.3290170809

Lanza, L.G., Merlone, A., Cauteruccio, A., Chinchella, E., Stagnaro, M., Dobre, M., Garcia Izquierdo, M.C., Nielsen, J., Kjeldsen, H., Roulet, Y.A., Coppa, G., Musacchio, C., Bordianu, C., Parrondo, M., 2021. Calibration of non-catching precipitation measurement instruments: A review. Meteorological Applications 28. https://doi.org/10.1002/met.2002

Lascelles, B., Favis-Mortlock, D.T., Parsons, A.J., Guerra, A.J.T., 2000. Spatial and temporal variation in two rainfall simulators: Implications for spatially explicit rainfall simulation experiments, in: Earth Surface Processes and Landforms. Wiley, Hoboken, NJ, USA. https://doi.org/10.1002/1096-9837(200007)25:7<709::AID-ESP126>3.0.CO;2-K

Lassu, T., Seeger, M., Peters, P., Keesstra, S.D., 2015. The Wageningen Rainfall Simulator: Set-up and Calibration of an Indoor Nozzle-Type Rainfall Simulator for Soil Erosion Studies. Land Degrad. Dev. 26, 604–612. https://doi.org/10.1002/ldr.2360

Laws, J.O., 1941. Measurements of the fall-velocity of water-drops and raindrops. Eos, Transactions American Geophysical Union 22, 709–721. https://doi.org/10.1029/TR022i003p00709

Laws, J.O., Parsons, D.A., 1943. The relation of raindrop-size to intensity. Eos, Transactions American Geophysical Union 24, 452–460. https://doi.org/10.1029/TR024i002p00452

Lazarus, R.R., Wan Jaafar, W.Z., Alengaram, U.J., Hin, L.S., 2023. Overview of the research gaps in the rainfall simulator study. Soil Science Society of America Journal 87, 1231–1248. https://doi.org/10.1002/saj2.20590

Lechler GmbH, 2016. Axial-flow full cone nozzles – Series 490. Metzingen, Germany.

Lee, G., Bringi, V., Thurai, M., 2023. The Retrieval of Drop Size Distribution Parameters Using a Dual-Polarimetric Radar. Remote Sens. (Basel). 15, 1063. https://doi.org/10.3390/rs15041063

Leh, M., Bajwa, S., Chaubey, I., 2013. IMPACT OF LAND USE CHANGE ON EROSION RISK: AN INTEGRATED REMOTE SENSING, GEOGRAPHIC INFORMATION SYSTEM AND MODELING METHODOLOGY. Land Degrad. Dev. 24, 409–421. https://doi.org/10.1002/ldr.1137

Lempio, G.E., Bumke, K., Macke, A., 2007. Measurement of solid precipitation with an optical disdrometer. Advances in Geosciences 10, 91–97. https://doi.org/10.5194/adgeo-10-91-2007

Levin, L.M., 1961. Исследования по физике грубодисперсных аэрозолей (Studies in the physics of roughly dispersed aerosols). Izdatel'stvo Akademii Nauk SSSR. English Translation: Translation No. 815, 1963, U.S. Army Biological Laboratories, Fort Detrick, Frederick, Maryland, Mosca.

Li, Z., Fang, H., 2016. Impacts of climate change on water erosion: A review. Earth. Sci. Rev. 163, 94–117. https://doi.org/10.1016/j.earscirev.2016.10.004

Lim, Y.S., Kim, J.K., Kim, J.W., Park, B.I., Kim, M.S., 2015. Analysis of the relationship between the kinetic energy and intensity of rainfall in Daejeon, Korea. Quaternary International 384, 107–117. https://doi.org/10.1016/j.quaint.2015.03.021

Liu, X.C., Gao, T.C., Liu, L., 2013. A comparison of rainfall measurements from multiple instruments. Atmos. Meas. Tech. 6, 1585–1595. https://doi.org/10.5194/amt-6-1585-2013

Loch, R.J., Robotham, B.G., Zeller, L., Masterman, N., Orange, D.N., Bridge, B.J., Sheridan, G., Bourke, J.J., 2001. A multi-purpose rainfall simulator for field infiltration and erosion studies. Australian Journal of Soil Research 39. https://doi.org/10.1071/SR00039

Löffler-Mang, M., Joss, J., 2000. An Optical Disdrometer for Measuring Size and Velocity of Hydrometeors. J. Atmos. Ocean. Technol. 17, 130–139. https://doi.org/10.1175/1520-0426(2000)017<0130:AODFMS>2.0.CO;2

Lowe, E.J., 1892. Rain drops. Quarterly Journal of the Royal Meteorological Society 18, 242–245. https://doi.org/10.1002/qj.4970188404

Lu, M., Wang, H., Sharma, A., Zhang, J., 2025. A stochastic rainfall model for reliability analysis of rainfall-induced landslides. Georisk: Assessment and Management of Risk for Engineered Systems and Geohazards 19, 30–44. https://doi.org/10.1080/17499518.2024.2359957

Luk, S., Abrahams, A.D., Parsons, A.J., 1993. Sediment sources and sediment transport by rill flow and interrill flow on a semi-arid piedmont slope, southern Arizona. Catena (Amst). 20, 93–111. https://doi.org/10.1016/0341-8162(93)90031-J

Luk, S. hung, 1985. Effect of antecedent soil moisture content on rainwash erosion. Catena (Amst). 12. https://doi.org/10.1016/0341-8162(85)90005-0

Ma, G., Li, G., Mu, X., Hou, W., Ren, Y., Yang, M., 2022. Effect of raindrop splashes on topsoil structure and infiltration characteristics. Catena (Amst). 212, 106040. https://doi.org/10.1016/j.catena.2022.106040

Majoro, F., Wali, U.G., Munyaneza, O., Naramabuye, F.-X., Mukamwambali, C., 2020. On-site and Off-site Effects of Soil Erosion: Causal Analysis and Remedial Measures in Agricultural Land - a Review. Rwanda Journal of

Engineering, Science, Technology and Environment 3. https://doi.org/10.4314/rjeste.v3i2.1

Manning, C.J.W., 2021. Rainfall Simulator construction and Evaluation of Erosion Control Practices (Master's Thesis). Auburn University, Auburn, Alabama.

Manning, C.J.W., Faulkner, B., Donald, W.N., Perez, M.A., 2023. Comparison of Erosion Control Products Using an ASTM D6459 Rainfall Simulator: Insights and Suggestions. Journal of Irrigation and Drainage Engineering 149. https://doi.org/10.1061/JIDEDH.IRENG-9935

Mariotte, E., 1686. Traité du mouvement des eaux et des autres corps fluides. Estienne Michallet, Paris.

Markowitz, A.H., 1976. Raindrop Size Distribution Expressions. Journal of Applied Meteorology 15, 1029–1031. https://doi.org/10.1175/1520-0450(1976)015<1029:RSDE>2.0.CO;2

Marshall, J.S., Palmer, W.McK., 1948. The distribution of raindrops with size. Journal of Meteorology 5, 166–167.

Martínez-Mena, M., Abadia, R., Castillo, V., Albaladejo, J., 2001. Diseño experimental mediante lluvia simulada para el estudio de los cambios en la erosión del suelo durante la tormenta. Revista C & G 15.

Martinez-Mena, M., Castillo, V., Albaladejo, J., 2001. Hydrological and erosional response to natural rainfall in a semi-arid area of south-east Spain. Hydrol. Process. 15, 557–571. https://doi.org/10.1002/hyp.146

Martínez-Murillo, J.F., Nadal-Romero, E., Regüés, D., Cerdà, A., Poesen, J., 2013. Soil erosion and hydrology of the western Mediterranean badlands throughout rainfall simulation experiments: A review. Catena (Amst). 106, 101–112. https://doi.org/10.1016/j.catena.2012.06.001

Mason, B.J., Ramanadham, R., 1953. A photoelectric raindrop spectrometer. Quarterly Journal of the Royal Meteorological Society 79, 490–495. https://doi.org/10.1002/qj.49707934204

McCarthy, E.L., 1934. Mariotte's Bottle. Science (1979). 80, 100–100. https://doi.org/10.1126/science.80.2065.100

Meshesha, D.T., Tsunekawa, A., Haregeweyen, N., 2018. Application of an optical disdrometer to characterize simulated rainfall and measure drop-size distribution. Hydrological Sciences Journal 63, 1574–1587. https://doi.org/10.1080/02626667.2018.1521522

Meyer, L.D., 1994. Rainfall Simulators for Soil Erosion Research, in: R. Lal (Ed.), Soil Erosion Research Methods. Routledge, Abingdon, UK, pp. 83–104.

Meyer, L.D., 1988. Rainfall simulators for soil conservation research, in: Lal, R. (Ed.), Soil Erosion Research Methods. Soil & Water Conservation Societ, Ankeny, Iowa, USA., pp. 75–95.

Meyer, L.D., 1979. Methods for Attaining Desired Rainfall Characteristics in Rainfall Simulators, in: Proceedings of Rainfall Simulator Workshop. United States Department of Agriculture, Science and Education Administration, Agricultural Reviews and Manuals, Western Series, no. 10, Oakland (California), July 1979, Tucson, Arizona, pp. 35–44.

Mhaske, S.N., Pathak, K., Basak, A., 2019. A comprehensive design of rainfall simulator for the assessment of soil erosion in the laboratory. Catena (Amst). 172, 408–420. https://doi.org/10.1016/j.catena.2018.08.039

Midha, V.-K., S, S.-K., Sharma, A., 2017. Biodegradable Geomeshes for Rainsplash Erosion Control. Journal of Fiber Bioengineering and Informatics 10, 155–161. https://doi.org/10.3993/jfbim00241

Mineo, C., Ridolfi, E., Moccia, B., Napolitano, F., Russo, F., 2020. On the reliability of gamma distributed dsds for modelling kinetic energy of rainfall. Irrigation and Drainage 69, 1176–1191. https://doi.org/10.1002/ird.2507

Mineo, C., Ridolfi, E., Moccia, B., Russo, F., Napolitano, F., 2019. Assessment of Rainfall Kinetic-Energy–Intensity Relationships. Water (Basel). 11, 1994. https://doi.org/10.3390/w11101994

Mitasova, H., Hofierka, J., Zlocha, M., Iverson, L.R., 1996. Modelling topographic potential for erosion and deposition using GIS. International journal of geographical information systems 10, 629–641. https://doi.org/10.1080/02693799608902101

Montanarella, L., 2020. Soils and the European Green Deal. Italian Journal of Agronomy 15, 1761. https://doi.org/10.4081/ija.2020.1761

Montanarella, L., Panagos, P., 2021. The relevance of sustainable soil management within the European Green Deal. Land use policy 100, 104950. https://doi.org/10.1016/j.landusepol.2020.104950

Montanarella, L., Vargas, R., 2012. Global governance of soil resources as a necessary condition for sustainable development. Curr. Opin. Environ. Sustain. 4, 559–564. https://doi.org/10.1016/j.cosust.2012.06.007

Morgan, R.P.C., 2005. Soil Erosion and Conservation, 3rd Edition. ed. Blackwell Publishing, Oxford.

Morgan, R.P.C., Quinton, J.N., Smith, R.E., Govers, G., Poesen, J.W.A., Auerswald, K., Chisci, G., Torri, D., Styczen, M.E., 1998. The European Soil Erosion Model (EUROSEM): a dynamic approach for predicting sediment transport from fields and small catchments. Earth Surf. Process. Landf. 23, 527–544. https://doi.org/10.1002/(SICI)1096-9837(199806)23:6<527::AID-ESP868>3.0.CO;2-5

Mualem, Y., Assouline, S., 1989. Modeling soil seal as a nonuniform layer. Water Resour. Res. 25, 2101–2108. https://doi.org/10.1029/WR025i010p02101

Mueller, E.A., Sims, A.L., 1968a. Raindrop Distributions at Bogor, Indonesia (Technical Report ECOM-02071-RR5). Fort Monmouth, N.J.

Mueller, E.A., Sims, A.L., 1968b. Raindrop Distributions at Corvallis, Oregon (Technical Report ECOM-02071-RR6). Fort Monmouth, N.J.

Mueller, E.A., Sims, A.L., 1967a. Raindrop Distributions at Island Beach, New Jersey (Technical Report ECOM-02071-RR2). Fort Monmouth, N.J.

Mueller, E.A., Sims, A.L., 1967b. Raindrop Distributions at Majuro Atoll, Marshall Islands (Technical Report ECOM-02071-RR1). Fort Monmouth, N.J.

Mueller, E.A., Sims, A.L., 1967c. Raindrop Distribution at Woody Island, Alaska (Technical Report ECOM-02071-RR4). Fort Monmouth, N.J.

Mueller, E.A., Sims, A.L., 1967d. Raindrop Distributions at Franklin, North Carolina (Technical Report ECOM-02071-RR3). Fort Monmouth, N.J.

Mueller, E.A., Sims, A.L., 1966. Radar cross sections from drop size spectra. Urbana, Illinois.

Mullan, D., 2013. Managing Soil Erosion in Northern Ireland: A Review of Past and Present Approaches. Agriculture 3, 684–699. https://doi.org/10.3390/agriculture3040684

Musa, J.J., Otuaro, E.A., Dada, P.O., Adewumi, J.K., Kuti, I.A., Adams-Suberu, J., 2021. Validation of Universal Soil Loss Equation for Selected Soil Locations in Northcentral Nigeria Using a Rainfall Simulator. AgricEngInt: CIGR Journal 23, 21–30.

Mutchler, C.K., 1971. Splash Droplet Production by Waterdrop Impact. Water Resour. Res. 7, 1024–1030. https://doi.org/10.1029/WR007i004p01024

Mutchler, C.K., Hansen, L.M., 1970. Splash of a Waterdrop at Terminal Velocity. Science (1979). 169, 1311–1312. https://doi.org/10.1126/science.169.3952.1311

Mutchler, C.K., Larson, C.L., 1971. Splash Amounts from Waterdrop Impact on a Smooth Surface. Water Resour. Res. 7, 195–200. https://doi.org/10.1029/WR007i001p00195

Nadal-Romero, E., Lasanta, T., Regüés, D., Lana-Renault, N., Cerdà, A., 2011. Hydrological response and sediment production under different land cover in abandoned farmland fields in a Mediterranean mountain environment. Boletín de la Asociación de Geógrafos Españoles 55, 303–323.

Nadal-Romero, E., Regüés, D., 2009. Detachment and infiltration variations as consequence of regolith development in a Pyrenean badland system. Earth Surf. Process. Landf. 34. https://doi.org/10.1002/esp.1772

Nash, J.E., Sutcliffe, J.V., 1970. River flow forecasting through conceptual models part I — A discussion of principles. J. Hydrol. (Amst). 10, 282–290. https://doi.org/10.1016/0022-1694(70)90255-6

Navas, A., Alberto, F., Machín, J., Galán, A., 1990. Design and operation of a rainfall simulator for field studies of runoff and soil erosion. Soil Technology 3, 385–397. https://doi.org/10.1016/0933-3630(90)90019-Y

Naves, J., Anta, J., Suárez, J., Puertas, J., 2020. Development and Calibration of a New Dripper-Based Rainfall Simulator for Large-Scale Sediment Wash-Off Studies. Water (Basel). 12, 152. https://doi.org/10.3390/w12010152

Neal, J.H., 1938. The Effect of the Degree of Slope and Rainfall Characteristics on Runoff and Soil Erosion. Soil Science Society of America Journal 2. https://doi.org/10.2136/sssaj1938.036159950002000c0083x

Nearing, M.A., Xie, Y., Liu, B., Ye, Y., 2017. Natural and anthropogenic rates of soil erosion. International Soil and Water Conservation Research 5, 77–84. https://doi.org/10.1016/j.iswcr.2017.04.001

Neff, E.L., 1979. Why rainfall simulation?, in: Proceedings of Rainfall Simulator Workshop. United States Department of Agriculture, Science and Education Administration, Agricultural Reviews and Manuals, Western Series, no. 10, Oakland (California), July 1979, Tucson, Arizona, pp. 3–7.

Neuper, M., Ehret, U., 2019. Quantitative precipitation estimation with weather radar using a data- and information-based approach. Hydrol. Earth Syst. Sci. 23, 3711–3733. https://doi.org/10.5194/hess-23-3711-2019

Norton, L.D., 1987. Micromorphological study of surface seals developed under simulated rainfall. Geoderma 40. https://doi.org/10.1016/0016-7061(87)90018-8

Nyssen, J., Vandenreyken, H., Poesen, J., Moeyersons, J., Deckers, J., Haile, M., Salles, C., Govers, G., 2005. Rainfall erosivity and variability in the Northern Ethiopian Highlands. J. Hydrol. (Amst). 311, 172–187. https://doi.org/10.1016/j.jhydrol.2004.12.016

Nystuen, J.A., 2001. Listening to Raindrops from Underwater: An Acoustic Disdrometer. J. Atmos. Ocean. Technol. 18, 1640–1657. https://doi.org/10.1175/1520-0426(2001)018<1640:LTRFUA>2.0.CO;2

Ochou, A.D., Nzeukou, A., Sauvageot, H., 2007. Parametrization of drop size distribution with rain rate. Atmos. Res. 84, 58–66. https://doi.org/10.1016/j.atmosres.2006.05.003

Ogden, C.B., van Es, H.M., Schindelbeck, R.R., 1997. Miniature Rain Simulator for Field Measurement of Soil Infiltration. Soil Science Society of America Journal 61, 1041–1043. https://doi.org/10.2136/sssaj1997.03615995006100040008x

Olver, F., 1997. Asymptotics and Special Functions, 1st ed. A K Peters/CRC Press, New York. https://doi.org/10.1201/9781439864548

Osman, K.T., 2014. Soil Erosion by Water, in: Soil Degradation, Conservation and Remediation. Springer Netherlands, Dordrecht, pp. 69–101. https://doi.org/10.1007/978-94-007-7590-9_3

OTT Hydromet GmbH, 2016. Operating instructions - Present Weather Sensor OTT Parsivel^2 [WWW Document]. https://www.ott.com/download/operating-instructions-present-weather-sensor-ott-parsivel2-with-screen-heating-3/.

Palmeri, V., Guida, G., Lucchese, A., Nicosia, A., Ferro, V., 2025. Rainfall Impact Experiments on a Clay Soil Covered by Rock Fragments. Water (Basel). 17, 3387. https://doi.org/10.3390/w17233387

Pampalone, V., Autovino, D., Serio, M.A., Bagarello, V., Ferro, V., 2025. Use of the Calibrated Curve Number and a Runoff-Driven <scp>USLE</scp> Model to Estimate Event Soil Loss From Sparacia (Sicily, Southern Italy) Plots. Hydrol. Process. 39. https://doi.org/10.1002/hyp.70205

Pampalone, V., Nicosia, A., Palmeri, V., Serio, M.A., Ferro, V., 2023. Rill and Interrill Soil Loss Estimations Using the USLE-MB Equation at the Sparacia Experimental Site (South Italy). Water (Basel). 15, 2396. https://doi.org/10.3390/w15132396

Panagos, P., Borrelli, P., Meusburger, K., Alewell, C., Lugato, E., Montanarella, L., 2015. Estimating the soil erosion cover-management factor at the European scale. Land use policy 48, 38–50. https://doi.org/10.1016/j.landusepol.2015.05.021

Panagos, P., Jones, A., Lugato, E., Ballabio, C., 2025. A Soil Monitoring Law for Europe. Global Challenges 9, 2400336. https://doi.org/10.1002/gch2.202400336

Panagos, P., Karydas, C.G., Gitas, I.Z., Montanarella, L., 2012. Monthly soil erosion monitoring based on remotely sensed biophysical parameters: a case study in Strymonas river basin towards a functional pan-European service. Int. J. Digit. Earth 5, 461–487. https://doi.org/10.1080/17538947.2011.587897

Park, S.-G., Kim, H.-L., Ham, Y.-W., Jung, S.-H., 2017. Comparative Evaluation of the OTT PARSIVEL2 Using a Collocated Two-Dimensional Video Disdrometer. J. Atmos. Ocean. Technol. 34, 2059–2082. https://doi.org/10.1175/JTECH-D-16-0256.1

Pasqualucci, F., 1982. The variation of drop-size distribution in convective storms: A comparison between theory and radar measurements. Geophys. Res. Lett. 9, 839–841. https://doi.org/10.1029/GL009i008p00839

Pérez-Latorre, F.J., de Castro, L., Delgado, A., 2010. A comparison of two variable intensity rainfall simulators for runoff studies. Soil Tillage Res. 107, 11–16. https://doi.org/10.1016/j.still.2009.12.009

Pimentel, D., Harvey, C., Resosudarmo, P., Sinclair, K., Kurz, D., McNair, M., Crist, S., Shpritz, L., Fitton, L., Saffouri, R., Blair, R., 1995. Environmental and Economic Costs of Soil Erosion and Conservation Benefits. Science (1979). 267, 1117–1123. https://doi.org/10.1126/science.267.5201.1117

Poesen, J., Ingelmo-Sanchez, F., Mucher, H., 1990. The hydrological response of soil surfaces to rainfall as affected by cover and position of rock fragments in the top layer. Earth Surf. Process. Landf. 15. https://doi.org/10.1002/esp.3290150707

Pruppacher, H.R., Klett, J.D., 2010. Cloud Particle Interactions. pp. 568–616. https://doi.org/10.1007/978-0-306-48100-0_14

Pruppacher, H.R., Klett, J.D., 1978. Cloud Particle Interactions-Collision, Coalescence, and Breakup, in: Microphysics of Clouds and Precipitation. Springer Netherlands, Dordrecht, pp. 464–503. https://doi.org/10.1007/978-94-009-9905-3_14

Quinn, N.W., 1981. Properties of transformed simulated rainfall under a corn canopy at different growth stages and row widths. Iowa State University of Science and Technology.

Raupach, T.H., 2016. Variability of the raindrop size distribution across scales in Mediterranean rainfall: characterisation and stochastic simulation. Ecole Polytechnique Fédérale de Lausanne.

Regmi, T.P., Thompson, A.L., 2000. Rainfall Simulator for Laboratory Studies. Appl. Eng. Agric. 16, 641–647. https://doi.org/10.13031/2013.5380

Regüés, D., Gallart, F., 2004. Seasonal patterns of runoff and erosion responses to simulated rainfall in a badland area in Mediterranean mountain conditions (Vallcebre, Southeastern Pyrenees). Earth Surf. Process. Landf. 29. https://doi.org/10.1002/esp.1067

Renard, K.G., Foster, G.R., Weesies, G.A., McCool, D.K., Yoder, D.C., 1997. Predicting soil erosion by water: a guide to conservation planning with the Revised Universal Soil Loss Equation (RUSLE). Washington, D.C.

Richards, J., Zhao, G., Zhang, H., Viles, H., 2019. A controlled field experiment to investigate the deterioration of earthen heritage by wind and rain. Herit. Sci. 7, 51. https://doi.org/10.1186/s40494-019-0293-7

Ricks, M.D., Horne, M.A., Faulkner, B., Zech, W.C., Fang, X., Donald, W.N., Perez, M.A., 2019. Design of a Pressurized Rainfall Simulator for Evaluating Performance of Erosion Control Practices. Water (Basel). 11, 2386. https://doi.org/10.3390/w11112386

Ries, J.B., Iserloh, T., Seeger, M., Gabriels, D., 2013. Rainfall simulations - Constraints, needs and challenges for a future use in soil erosion research. Zeitschrift fur Geomorphologie 57. https://doi.org/10.1127/0372-8854/2013/S-00130

Ries, J.B., Seeger, M., Iserloh, T., Wistorf, S., Fister, W., 2009. Calibration of simulated rainfall characteristics for the study of soil erosion on agricultural land. Soil Tillage Res. 106, 109–116. https://doi.org/10.1016/j.still.2009.07.005

Rodrigo-Comino, J., 2021. Precipitation : earth surface responses and processes. Elsevier, Amsterdam, Netherlands.

Rodríguez, I., Ortiz, A., Caldevilla, P., Giganto, S., Búrdalo, G., Fernández-Raga, M., 2023. Comparison between the Effects of Normal Rain and Acid Rain on Calcareous Stones under Laboratory Simulation. Hydrology 10, 79. https://doi.org/10.3390/hydrology10040079

Rončević, V., Živanović, N., Radulović, L., Ristić, R., Sadeghi, S.H., Fernández-Raga, M., Prats, S.A., 2025. Design, Calibration, and Performance Evaluation of a High-Fidelity Spraying Rainfall Simulator for Soil Erosion Research. Water (Basel). 17, 1863. https://doi.org/10.3390/w17131863

Rončević, V., Živanović, N., van Boxel, J.H., Iserloh, T., Štrbac, S., 2023. Dripping Rainfall Simulators for Soil Research—Performance Review. Water (Basel). 15, 1314. https://doi.org/10.3390/w15071314

Rose, C.W., 1960. Soil detachment caused by rainfall. Soil Sci. 89, 28–35.

Roth, C.H., Meyer, B., Frede, H.-G., 1985. A portable rainfall simulator for studying factors affecting runoff, infiltration and soil loss. Catena (Amst). 12, 79–85. https://doi.org/10.1016/S0341-8162(85)80006-0

Saber, A.N., Somjunyakul, P., Ok, J., Watanabe, H., 2019. Rainfall-Runoff Simulation of Radioactive Cesium Transport by Using a Small-Scale Portable Rainfall Simulator. Water Air Soil Pollut. 230, 226. https://doi.org/10.1007/s11270-019-4268-9

Saco, P.M., McDonough, K.R., Rodriguez, J.F., Rivera-Zayas, J., Sandi, S.G., 2021. The role of soils in the regulation of hazards and extreme events. Philosophical Transactions of the Royal Society B: Biological Sciences 376, 1–10. https://doi.org/10.1098/rstb.2020.0178

Saha, A., Lee, J.D., Basu, S., Kumar, R., 2012. Breakup and coalescence characteristics of a hollow cone swirling spray. Physics of Fluids 24. https://doi.org/10.1063/1.4773065

Saha, R., Testik, F.Y., 2023. Assessment of OTT Parsivel^2 Raindrop Fall Speed Measurements. J. Atmos. Ocean. Technol. 40, 557–573. https://doi.org/10.1175/JTECH-D-22-0091.1

Salem, H.M., Meselhy, A.A., 2021. A portable rainfall simulator to evaluate the factors affecting soil erosion in the northwestern coastal zone of Egypt. Natural Hazards 105, 2937–2955. https://doi.org/10.1007/s11069-020-04432-8

Salles, C., Poesen, J., Sempere-Torres, D., 2002. Kinetic energy of rain and its functional relationship with intensity. J. Hydrol. (Amst). 257, 256–270. https://doi.org/10.1016/S0022-1694(01)00555-8

Sanchez-Moreno, J.F., Mannaerts, C.M., Jetten, V., Löffler-Mang, M., 2012. Rainfall kinetic energy–intensity and rainfall momentum–intensity relationships for Cape Verde. J. Hydrol. (Amst). 454–455, 131–140. https://doi.org/10.1016/j.jhydrol.2012.06.007

Sander, J., 1975. Rain attenuation of millimeter waves at λ = 5.77, 3.3, and 2 mm. IEEE Trans. Antennas Propag. 23, 213–220. https://doi.org/10.1109/TAP.1975.1141059

Sauvageot, H., Lacaux, J.-P., 1995. The Shape of Averaged Drop Size Distributions. J. Atmos. Sci. 52, 1070–1083. https://doi.org/10.1175/1520-0469(1995)052<1070:TSOADS>2.0.CO;2

Schiettecatte, W., Ke Jin, Yao, Y., Cornelis, W.M., Junjie Lu, Huijun Wu, Verbist, K., Dianxiong Cai, Gabriels, D., Hartmann, R., 2005. Influence of simulated rainfall on physical properties of a conventionally tilled loess soil. Catena (Amst). 64, 209–221. https://doi.org/10.1016/j.catena.2005.08.017

Sekhon, R.S., Srivastava, R.C., 1971. Doppler Radar Observations of Drop-Size Distributions in a Thunderstorm. J. Atmos. Sci. 28, 983–994. https://doi.org/10.1175/1520-0469(1971)028<0983:DROODS>2.0.CO;2

Sekine, M., Lind, G., 1982. Rain Attenuation of Centimeter, Millimeter and Submillimeter Radio Waves, in: 12th European Microwave Conference, 1982. IEEE, pp. 584–589. https://doi.org/10.1109/EUMA.1982.333124

Sempere Torres, D., Porrà, J.M., Creutin, J.-D., 1994. A General Formulation for Raindrop Size Distribution. Journal of Applied Meteorology 33, 1494–1502.

Serio, M.A., Carollo, F.G., Caruso, R., Ferro, V., 2024. Guidelines for the Energetic Characterization of a Portable Drip-Type Rainfall Simulator for Soil Erosion Research. Water (Basel). 16, 2100. https://doi.org/10.3390/w16152100

Serio, M.A., Carollo, F.G., Ferro, V., 2019a. Raindrop size distribution and terminal velocity for rainfall erosivity studies. A review. J. Hydrol. (Amst). https://doi.org/10.1016/j.jhydrol.2019.06.040

Serio, M.A., Carollo, F.G., Ferro, V., 2019b. A method for evaluating rainfall kinetic power by a characteristic drop diameter. J. Hydrol. (Amst). 577, 123996. https://doi.org/10.1016/j.jhydrol.2019.123996

Serio, M.A., Caruso, R., Carollo, F.G., Bagarello, V., Ferro, V., Nicosia, A., 2025. The Hydraulic Assessment of a New Portable Rainfall Simulator Using Different Nozzle Models. Water (Basel). 17, 1765. https://doi.org/10.3390/w17121765

Sheppard, B.E., Joe, P.I., 1994. Comparison of Raindrop Size Distribution Measurements by a Joss-Waldvogel Disdrometer, a PMS 2DG Spectrometer, and a POSS Doppler Radar. J. Atmos. Ocean. Technol. 11, 874–887. https://doi.org/10.1175/1520-0426(1994)011<0874:CORSDM>2.0.CO;2

Simelane, M.P.Z., Soundy, P., Maboko, M.M., 2024. Effects of Rainfall Intensity and Slope on Infiltration Rate, Soil Losses, Runoff and Nitrogen Leaching from Different Nitrogen Sources with a Rainfall Simulator. Sustainability 16, 4477. https://doi.org/10.3390/su16114477

Smith, P., 2012. Soils and climate change. Curr. Opin. Environ. Sustain. 4, 539–544. https://doi.org/10.1016/j.cosust.2012.06.005

Testik, F.Y., Barros, A.P., Bliven, L.F., 2011. Toward a Physical Characterization of Raindrop Collision Outcome Regimes. J. Atmos. Sci. 68, 1097–1113. https://doi.org/10.1175/2010JAS3706.1

Thies CLIMA, 2010. Laser Precipitation Monitor - Instruction for Use [WWW Document]. https://www.thiesclima.com/en/db/dnl/5.4110.xx.x00_laser_precipitation_monitor_eng.pdf.

Tiller, M., Reading, L., Miska, M., Egodawatta, P., 2025. Analysis of square pattern spray nozzles for use in a portable field rainfall simulator. Catena (Amst). 250, 108796. https://doi.org/10.1016/j.catena.2025.108796

Tokay, A., Kruger, A., Krajewski, W.F., 2001. Comparison of Drop Size Distribution Measurements by Impact and Optical Disdrometers. Journal of Applied Meteorology 40, 2083–2097. https://doi.org/10.1175/1520-0450(2001)040<2083:CODSDM>2.0.CO;2

Tokay, A., Short, D.A., 1996. Evidence from Tropical Raindrop Spectra of the Origin of Rain from Stratiform versus Convective Clouds. Journal of Applied Meteorology 35, 355–371. https://doi.org/10.1175/1520-0450(1996)035<0355:EFTRSO>2.0.CO;2

Tokay, A., Wolff, D.B., Petersen, W.A., 2014. Evaluation of the New Version of the Laser-Optical Disdrometer, OTT Parsivel^2. J. Atmos. Ocean. Technol. 31, 1276–1288. https://doi.org/10.1175/JTECH-D-13-00174.1

Torri, D., Regüés, D., Pellegrini, S., Bazzoffi, P., 1999. Within-storm soil surface dynamics and erosive effects of rainstorms. Catena (Amst). 38. https://doi.org/10.1016/S0341-8162(99)00059-4

Uijlenhoet, R., 2001. Raindrop size distributions and radar reflectivity–rain rate relationships for radar hydrology. Hydrol. Earth Syst. Sci. 5, 615–628. https://doi.org/10.5194/hess-5-615-2001

Uijlenhoet, R., Stricker, J.N.M., 1999. Dependence of rainfall interception on drop size – a comment. J. Hydrol. (Amst). 217, 157–163. https://doi.org/10.1016/S0022-1694(99)00004-9

Ulbrich, C.W., 1983. Natural Variations in the Analytical Form of the Raindrop Size Distribution. Journal of Climate and Applied Meteorology 22, 1764–1775. https://doi.org/10.1175/1520-0450(1983)022<1764:NVITAF>2.0.CO;2

van Boxel, J.H., 1998. Numerical model for the fall speed of raindrops in a rainfall simulator, in: Gabriels, D., Cornelis, W.M. (Eds.), Workshop on Wind and Water Erosion. International Centre for Eremology, University of Ghent, Ghent, Belgium, pp. 77–85.

van Dijk, A.I.J.M., Bruijnzeel, L.A., Rosewell, C.J., 2002. Rainfall intensity–kinetic energy relationships: a critical literature appraisal. J. Hydrol. (Amst). 261, 1–23. https://doi.org/10.1016/S0022-1694(02)00020-3

Van Oost, K., Govers, G., Desmet, P., 2000. Evaluating the effects of changes in landscape structure on soil erosion by water and tillage. Landsc. Ecol. 15, 577–589. https://doi.org/10.1023/A:1008198215674

Vergni, L., Todisco, F., Vinci, A., 2018. Setup and calibration of the rainfall simulator of the Masse experimental station for soil erosion studies. Catena (Amst). 167, 448–455. https://doi.org/10.1016/j.catena.2018.05.018

Verheijen, F.G.A., Jones, R.J.A., Rickson, R.J., Smith, C.J., 2009. Tolerable versus actual soil erosion rates in Europe. Earth. Sci. Rev. 94, 23–38. https://doi.org/10.1016/j.earscirev.2009.02.003

Waldvogel, A., 1974. The N0 Jump of Raindrop Spectra. J. Atmos. Sci. 31, 1067–1078. https://doi.org/10.1175/1520-0469(1974)031<1067:TJORS>2.0.CO;2

Walling, D.E., 1990. Linking the field to the river: sediment delivery from agricultural land, in: Boardman, J., Foster, I.D.L., Dearing, J.A. (Eds.), Soil Erosion on Agricultural Land. John Wiley and Sons, Chichester, Sussex, England, pp. 129–152.

Weibull, W., 1951. A Statistical Distribution Function of Wide Applicability. J. Appl. Mech. 18, 293–297. https://doi.org/10.1115/1.4010337

Westbrook, C.D., Hogan, R.J., O'Connor, E.J., Illingworth, A.J., 2010. Estimating drizzle drop size and precipitation rate using two-colour lidar measurements. Atmos. Meas. Tech. 3, 671–681. https://doi.org/10.5194/amt-3-671-2010

Wickerts, S., 1982. Drop size distribution in rain. Stockholm.

Wiesner, J., 1895. Beiträge zur Kenntniss des tropischen Regens (About Contributions to the knowledge of the tropical rain). Sitzungsberichte der Kaiserlichen Akademie der Wissenschaften. Mathematisch-Naturwissenschaftliche Classe 104, 1397–1434.

Wilken, F., Baur, M., Sommer, M., Deumlich, D., Bens, O., Fiener, P., 2018. Uncertainties in rainfall kinetic energy-intensity relations for soil erosion modelling. Catena (Amst). 171, 234–244. https://doi.org/10.1016/j.catena.2018.07.002

Williams, J.R., Berndt, H.D., 1977. Sediment Yield Prediction Based on Watershed Hydrology. Transactions of the ASAE 20, 1100–1104. https://doi.org/10.13031/2013.35710

Williams, J.R., Renard, K.G., Dyke, P.T., 1983. EPIC: A new method for assessing erosion's effect on soil productivity. J. Soil Water Conserv. 38, 381–383. https://doi.org/10.1080/00224561.1983.12436327

Wilm, H.G., 1943. The application and measurement of artificial rainfall on types FA and F infiltrometers. Eos, Transactions American Geophysical Union 24. https://doi.org/10.1029/TR024i002p00480

Winder, P., Paulson, K.S., 2012. The measurement of rain kinetic energy and rain intensity using an acoustic disdrometer. Meas. Sci. Technol. 23, 015801. https://doi.org/10.1088/0957-0233/23/1/015801

Wischmeier, W.H., 1955. Punched cards record runoff and soil-loss data. Agricultural Engineering 36, 664–666.

Wischmeier, W.H., Smith, D.D., 1978. Predicting rainfall erosion losses: a guide to conservation planning. U.S. Department of Agriculture, Science and Education Administration (Agriculture Handbook No. 537), Washington, D.C.

Yan, K., Chen, H., Hu, L., Huang, K., Huang, Y., Wang, Z., Liu, B., Wang, J., Guo, S., 2023. A review of video-based rainfall measurement methods. WIREs Water 10, e1678. https://doi.org/10.1002/wat2.1678

Yin, H., Zheng, F., Duan, H.-F., Savic, D., Kapelan, Z., 2023. Estimating Rainfall Intensity Using an Image-Based Deep Learning Model. Engineering 21, 162–174. https://doi.org/10.1016/j.eng.2021.11.021

Zemke, J.J., 2017. Set-up and calibration of a portable small scale rainfall simulator for assessing soil erosion processes at interrill scale. Cuadernos de Investigación Geográfica 43, 63–81. https://doi.org/10.18172/cig.3129

Zeng, Y., Yang, L., Tong, Z., Jiang, Y., Abulikemu, A., Lu, X., Li, X., 2024. Seasonal Variations in the Rainfall Kinetic Energy Estimation and the Dual-Polarization Radar Quantitative Precipitation Estimation Under Different Rainfall Types in the Tianshan Mountains, China. Remote Sens. (Basel). 16, 3859. https://doi.org/10.3390/rs16203859

Zhang, T., Wei, W., Zheng, L., Chen, Y., 2022. Characteristics and Variations of Raindrop Size Distribution in Chengdu of the Western Sichuan Basin, China. Atmosphere (Basel). 14, 76. https://doi.org/10.3390/atmos14010076

Živanović, N., Rončević, V., Spasić, M., Ćorluka, S., Polovina, S., 2022. Construction and calibration of a portable rain simulator designed for the in situ research of soil resistance to erosion. Soil and Water Research 17, 158–169. https://doi.org/10.17221/148/2021-SWR

Zöbisch, M.A., Klingspor, P., Oduor, A.R., 1996. The accuracy of manual runoff and sediment sampling from erosion plots. J. Soil Water Conserv. 51, 231–233. https://doi.org/10.1080/00224561.1996.12457073

LIST OF SYMBOLS AND UNITS

A	Annual average soil loss of the USLE model, Eq. (1)	$\frac{\text{t}}{\text{ha yr}}$
a	Coefficient of Eq. (44) depending on flow rate	$\frac{\text{L}}{\text{min bar}^{0.4}}$
A_e	Event soil loss, Eq. (2)	$\frac{\text{t}}{\text{ha}}$
$A_{e,c}$	Calculated event soil loss	$\frac{\text{t}}{\text{ha}}$
$A_{e,m}$	Measured event soil loss	$\frac{\text{t}}{\text{ha}}$
a_h	Coefficient of Eqs. (21) and (49) depending on the drop fall height	cm
A_{KS}	Sampling area of the Kamphorst rainfall simulator	m^2
A_{ODM}	Sampling area of the ODM 470 optical disdrometer	m^2
A_{OTT}	Effective sampling area of the Parsivel^2 optical disdrometer	m^2
C	Land cover and management factor of the USLE model, Eq. (1)	–
c_n	Number of capillary tubes	–
CUC	Christiansen uniformity coefficient, Eq. (38)	%
CV_W	Coefficient of Variation of the Weibull distribution	–
D	Raindrop diameter	cm
D_0	Median volume diameter of the drop size distribution	cm
D_{50}	Median diameter of the drop size distribution	cm
d_c	Diameter of the capillary tube	m
df	Degrees of freedom, index of ANOVA test	–
D_g	Geometric mean diameter of the Lognormal distribution, Eq. (26)	cm
D_i	Mean diameter of the *i*-th diameter class	mm
D_m	Mean volume diameter	cm
D_{OTT}	Raindrop diameter measured by the Parsivel^2 optical disdrometer	cm
F-critical	Critical value of the F distribution at the selected significance level and degrees of freedom, used as the threshold for the ANOVA test	–
F-value	F-statistic of the ANOVA test	–
g	Acceleration due to gravity	$\frac{\text{m}}{\text{s}^2}$
H	Pressure head on the capillary tube	cm
h	Raindrop fall height	m
H_I	Opening of the Kamphorst simulator's aeration tube	cm
h_e	Accumulated rainfall depth of an erosive event measured in the *e*-th interval	mm

I	Rainfall intensity	$\frac{\text{mm}}{\text{h}}$
I_{30}	Maximum 30-minute rainfall intensity	$\frac{\text{mm}}{\text{h}}$
I_c	Rainfall intensity of the i-th rainfall collector employed to determine the CUC	$\frac{\text{mm}}{\text{h}}$
I_e	Rainfall intensity of an erosive event measured in the e-th interval	$\frac{\text{mm}}{\text{h}}$
I_i	Rainfall intensity at the i-th sampling position	$\frac{\text{mm}}{\text{h}}$
I_{mean}	Mean rainfall intensity within a given intensity range	$\frac{\text{mm}}{\text{h}}$
I_{ODM}	Rainfall intensity measured by the ODM 470 disdrometer	$\frac{\text{mm}}{\text{h}}$
I_{OTT}	Rainfall intensity measured by the OTT Parsivel^2 disdrometer	$\frac{\text{mm}}{\text{h}}$
I_S	Mean simulated rainfall intensity	$\frac{\text{mm}}{\text{h}}$
I_{sum}	Rainfall intensity value directly reported in the Parsivel^2 output file, based on the instrument's internal processing	$\frac{\text{mm}}{\text{h}}$
K	Soil erodibility factor of the USLE model, Eq. (1)	$\frac{\text{t ha h}}{\text{ha MJ mm}}$
L	Slope-length factor of the USLE model, Eq. (1)	–
l_c	Length of the capillary tube	m
L_{OTT}	Parsivel^2 laser beam length	m
M	Rainfall momentum per unit time and area	$\frac{\text{N}}{\text{m}^2}$
$M_{(D)}dD$	Distribution of rainfall momentum in the diameter interval (D, $D + dD$)	$\frac{\text{N}}{\text{m}^2}$
M_D	Rainfall momentum of a single drop	$\frac{\text{N}}{\text{m}^2}$
m_D	Mass of a single drop	kg
M_i	Rainfall momentum at the i-th sampling position	$\frac{\text{N}}{\text{m}^2}$
M_{ODM}	Rainfall momentum derived by ODM 470 raw DSD	$\frac{\text{N}}{\text{m}^2}$
M_{OTT}	Rainfall momentum derived by Parsivel^2 raw PSVD	$\frac{\text{N}}{\text{m}^2}$
MQ	Mean sqauares, index of ANOVA test	Square of the unit of the analyzed variable

N	Total number of terms over which a summation is performed; it denotes the size of the sample, dataset, or discretization domain, depending on the context	–
$N_{(D)}$	Number of raindrops per unit area and time	$\frac{1}{\text{cm m}^2\text{s}}$
$N_{(D)V}$	Number of raindrops per unit volume of air	$\frac{1}{\text{cm m}^3}$
N_0	Intercept parameter of: • Gamma distribution referred to the unit of area and time, Eq. (11) • Weibull distribution, Eq. (30)	$\frac{1}{\text{m}^3}$
$N_{0,V}$	Intercept parameter of: • Exponential distribution, Eq. (6) • Gamma distribution referred to the unit volume of air, Eq. (9)	• $\frac{1}{\text{m}^3\ \text{cm}}$ • $\frac{1}{\text{m}^3\ \text{cm}^{-\mu_V}}$
n_c	• Number of collectors employed to determine the CUC, Eq. (38) • Number of capillary tubes of the Kamphorst rainfall simulator	–
N_d	Total number of drops	–
N_{DSD}	Number of DSDs	–
N_e	Number of erosive events	–
N_i	Number of drops in the *i*-th diameter class	–
N_{ij}	Number of drops in the *i*-th diameter and *j*-th velocity class	–
N_{imp}	Total number of raindrop impacts	–
N_{OTT}	Total number of drops recorded by the Parsivel^2 optical disdrometer	–
N_T	Drop concentration parameter of the Lognormal distribution, Eq. (26)	$\frac{1}{\text{m}^3}$
P	Soil conservation practices factor of the USLE model, Eq. (1)	–
p-value	Probability associated with the observed F-statistic under the null hypothesis	–
$P_{(D)}$	Theoretical probability that the raindrop diameter is less than D	–
$P_{(D),i}$	Measured probability that the raindrop diameter is less than D	–
P_n	Rainfall kinetic power per unit time and area	$\frac{\text{J}}{\text{m}^2\text{s}}$
$P_{n,D}$	Rainfall kinetic power of a single drop	$\frac{\text{J}}{\text{m}^2\text{s}}$
$P_{n,e}$	Kinetic energy of an erosive event measured in the *e*-th interval	$\frac{\text{MJ}}{\text{ha h}}$
$P_{n,i}$	Rainfall kinetic power at the *i*-th sampling position	$\frac{\text{J}}{\text{m}^2\text{s}}$
$P_{n,ODM}$	Rainfall kinetic power derived by ODM 470 raw DSD	$\frac{\text{J}}{\text{m}^2\text{s}}$

$P_{n,OTT}$	Rainfall kinetic power derived by Parsivel^2 raw PSVD	$\frac{\mathrm{J}}{\mathrm{m^2 s}}$
P_n/I	Rainfall kinetic power per unit volume of rainfall	$\frac{\mathrm{MJ}}{\mathrm{ha\ mm}}$
P_S	Hydraulic pressure	bar
Q	Flow rate	$\frac{\mathrm{L}}{\mathrm{min}}$
R	Rainfall erosivity factor of the USLE model, Eq. (1)	$\frac{\mathrm{MJ\ mm}}{\mathrm{h\ ha\ yr}}$
R_e	Rainfall erosivity factor of a single rainfall event, Eq. (3)	$\frac{\mathrm{MJ\ mm}}{\mathrm{h\ ha}}$
R_e^*	Alternative rainfall erosivity factor of a single rainfall event, Eq. (65)	$\frac{\mathrm{MJ\ mm}}{\mathrm{h\ ha}}$
s	Coefficient of Eq. (64)	–
S	Slope-steepness factor of the USLE model, Eq. (1)	–
SQ	Sum of squares, index of ANOVA test	Square of the unit of the analyzed variable
t	Sampling time	s
T	Water temperature	°C
$V_{(D)}$	Raindrop terminal velocity	$\frac{\mathrm{m}}{\mathrm{s}}$
V_h	Coefficient of Eqs. (21) and (49) depending on the drop fall height	$\frac{\mathrm{m}}{\mathrm{s}}$
V_j	Fall velocity of the j-th velocity class	$\frac{\mathrm{m}}{\mathrm{s}}$
V_{max}	Theoretical maximum velocity of a body in free fall in a vacuum starting from rest	$\frac{\mathrm{m}}{\mathrm{s}}$
vol_D	Volume of a single drop	$\mathrm{m^3}$
V_S	Fall velocity of a single drop	$\frac{\mathrm{m}}{\mathrm{s}}$
$V_{S,OTT}$	Fall velocity of a single drop measured by the Parsivel^2 disdrometer	$\frac{\mathrm{m}}{\mathrm{s}}$
W_{OTT}	Parsivel^2 laser beam width	m
x_c	Calculated or estimated value of the generic x variable, derived from empirical relationships, theoretical models, or instrument measurements under evaluation, used in statistical performance indices, Eqs. (59)–(63)	Same as the analyzed variable
x_m	Measured (reference) value of the generic x variable, adopted as the benchmark for the computation of statistical performance indices, Eqs. (59)–(63)	Same as the analyzed variable

α	• Coriolis coefficient, denoted as α_1 at the inlet section of the capillary tube and as α_2 at the outlet section, Eq. (43) • Significance level for the ANOVA statistical analysis	–
η	Shape parameter of the Weibull distribution, Eq. (30)	–
κ	Dimensional coefficient of Equation (76) dependent on η and I	$\frac{\text{cm s}^{\frac{3}{1.34}}}{\text{kg}^{\frac{1}{1.34}}}$
κ'	Dimensional coefficient of Equation (77) dependent on η and I	$\frac{\text{cm m}^{\frac{1}{0.67}}\text{s}^{\frac{2}{0.67}}}{\text{kg}^{\frac{1}{0.67}}}$
Λ	Scale parameter of the Gamma distribution referred to the unit of area and time, Eq. (11)	$\frac{1}{\text{cm}}$
Λ_V	Scale parameter of: • Exponential Distribution, Eq. (6) • Gamma Distribution referred to the unit volume of air, Eq. (9)	$\frac{1}{\text{cm}}$
μ	Shape parameter of the Gamma distribution referred to the unit of area and time, Eq. (11)	–
$\mu'_{(D)}$	Sampled mean of the diameters	cm
$\mu_{(D)}$	Mean of the diameters within the drop size distribution	cm
μ_V	Shape parameter of: • Exponential Distribution, Eq. (6) • Gamma Distribution referred to the unit volume of air, Eq. (9)	–
ρ	Water density	$\frac{\text{kg}}{\text{m}^3}$
σ	Scale parameter of the Weibull distribution, Eq. (30)	cm
$\sigma_{(D)}$	Standard deviation of the diameters within the drop size distribution	cm
σ_c	Sampling area of a single capillary tube	m^2
σ_g	Geometric standard deviation of the Lognormal distribution, Eq. (26)	–
σ_W	Standard deviation of the diameters within the drop size distribution	cm
φ	Water dynamic viscosity	$\frac{\text{kg}}{\text{m s}}$
ω	Coefficient of Eq. (88)	–

ABBREVIATIONS

ANOVA	Analysis of Variance
ASABE	American Society of Agricultural and Biological Engineers
CAD	Computer-Aided Design
CUC	Christiansen Uniformity Coefficient
CV	Computer Vision
DCPS	Data Converter and Power Supply
DEM	Digital Elevation Model
DG	Drop Generator
DL	Deep Learning
DoD	Digital elevation model of Difference
DRS	Drip-type Rainfall Simulator
DSD	Drop Size Distribution
EPIC	Erosion-Productivity Impact Calculator
EU	European Union
EUROSEM	European Soil Erosion Model
FPS	Frame Per Second
GASEMT	Global Applications of Soil Erosion Modelling Tracker
GIS	Geographical Information System
HDPE	High Density Polyethylene
HFR	High Flow Rate
IRSS	Infrared Sensor System
JWD	Joss-Waldvogel Disdrometer
KS	Kamphorst rainfall Simulator
LFR	Low Flow Rate
LISEM	Limburg Soil Erosion Model
LPM	Laser Precipitation Monitor
MKS	Modified Kamphorst rainfall Simulator
ML	Maximum Likelihood method
MM	Method of Moments
MUSLE	Modified Universal Soil Loss Equation
NSEI	Nash–Sutcliffe Efficiency Index
ODM	Optical Disdrometer (Eigenbrodt GmbH & Co. disdrometer)
Parsivel	Particle Size Velocity (OTT Hydromet GmbH disdrometer)
p_c	Plastic cup
PRS	Pressurized Rainfall Simulator

PSVD	Particle Size and Velocity Distribution
p_v	Plastic vessel
RMSE	Root Mean Square Error
RUSLE	Revised Universal Soil Loss Equation
SEDD	Sediment Delivery Distributed
SWAT	Soil and Water Assessment Tool
T	Experimental treatment
USLE	Universal Soil Loss Equation
USPED	Unit Stream Power-based Erosion Deposition
WaTEM/SEDEM	Water and Tillage Erosion Model/Sediment Delivery Model
WEPP	Water Erosion Prediction Project